Institute of Applied Problems of Physics, NAS Republic of Armenia, Department of Physics Yerevan State University, State Engineering University of Armenia, National Research Laboratory after A.I. Alikhanyan, Lebedev Physical Institute of RAS, A.M. Prokhorov General Physics Institute of RAS.

International Conference On Electron, Positron, Neutron and X – Ray Scattering Under External Influences

Yerevan-Meghri, Armenia

18-22 October 2011

Proceedings

Yerevan 2012

UDC 53:06

International Conference on Electron, Positron, Neutron and X-Ray Scattering Under External Influences

The refereed Proceedings of the "International Conference on Electron, Positron, Neutron and X-Ray Scattering Under External Influences" are published by decision of the Scientific Council of the Institute of Applied Problems of Physics, NAS RA.

ISBN 978-99941-2-710-8

Contents

Invitation talk

Section I
Time – spatial control of characteristics of the channelled particles radiation with and without acoustic fields.

Section II
Time – spatial control of characteristic of X – ray and optical transition radiation with and without acoustic influences.

Section III
Time – spatial control of characteristic of the parametric X – ray radiation (PXR) with and without acoustic influences.

Section IV
Time-spatial control of characteristic of the coherent bremsstrahlung with and without acoustic influences.

Section V
Time – spatial control of characteristic X – ray radiation by external influences

Section VI
Control of characteristic of plasma by acoustic fields.

Section VII
Technologies of New Basic Elements of X-Ray Optics

Section VIII
Related Problems of Acoustophysics and Solid State Physics

Invitation talk

Radiation by relativistic electrons at large formation lengths of radiation process

N. F. Shul'ga *, S. V. Trofymenko

*Akhiezer Institute for Theoretical Physics of National Science Centre "Kharkov Institute of Physics and Technology", 1 Akademicheskaya Str., 61108 Kharkov, Ukraine, *Phone: +38 (057) 335 64 62, E-mail: shulga@kipt.kharkov.ua*

Abstract

The evolution in space and time of localized high-energy wave packets, which take place in process of bremsstrahlung by ultra relativistic electrons is considered. It is shown that high energies make stabilizing influence upon the motion of such packets and that the lengths within which their dispersion and reconstruction into the packets of diverging waves occurs can be macroscopic. In this case the problem of measurement of radiation characteristics in the pre-wave zone arises, which consists in dependence of the results of measurements on the detector's size and its position relative to the region of packet formation. In this case, in particular, the ultra relativistic electron can be in 'half-bare' state with considerably suppressed low frequency Fourier-components of the field around it during long period of time.

1. Introduction

A lot of high-energy physical processes develop within large domains of space along the direction of particle motion (see, for example monographs [1-4] and references in them). In the case of electromagnetic processes the size of these domains can substantially exceed sometimes not only interatomic distances of substance but the size of experimental facility (detectors) as well [1, 2, 4-13]. Essential in this case is the fact that interaction of particles with atoms and experimental facility situated within such domains and outside them can substantially differ. Such situation arises, for example, when considering long-wave radiation in processes of bremsstrahlung and transition radiation by ultra relativistic electrons. Therefore, it is necessary to know what happens within such regions and what the peculiarities of evolution of such processes in space and time are. In the present paper some results of investigation of this problem in relation to the radiation process at the instantaneous change of an ultra relativistic electron trajectory are presented.

The considered problem is closely related to the problem of study of the behavior of localized high-energy wave packets. Therefore, firstly, we will consider some peculiarities of the behavior of such wave packets drawing special attention to the questions of their stability and reconstruction into the packets of diverging waves. Further we show that the discussed wave packets naturally arise in the process of bremsstrahlung at the instantaneous scattering of an ultra relativistic electron to a large angle.

The consideration is made on the basis of classical electrodynamics. In this case the moving electron is considered as a charge with its own coulomb field moving together with it. At the instantaneous scattering the perturbation of this field occurs. This perturbation is treated here as appearance of a packet of free plane electromagnetic waves, which reconstructs then into a packet of diverging waves. For ultra relativistic particles, however, this does not happen at once. The length within which this process develops has a name of the coherence length of the radiation process [1, 2]. It is $2\gamma^2$ times larger than the length λ of the considered radiated waves (γ is here the electrons Lorentz-factor). We show that within this length the field around the electron substantially differs from the coulomb one. This leads, in particular, to the fact that the bremsstrahlung characteristics in this case substantially depend on both the detector's size and its position relative to the scattering point.

2. High energy wave packets

The general solution of the wave equation can be presented in the form of a wave packet, which spatially disperses in course of time. In semiclassical approximation such packet does not disperse. It moves according to the laws of classical mechanics (see, for example [2, 14]). It is going beyond the semiclassical approximation that leads to the packet dispersion. The high-energy wave packets are of special interest because the speed of their dispersion decreases with the increase of their energy. Let us pay attention to some peculiarities of dispersion of such packets. Significant here is the fact that characteristic features of this dispersion are similar for all fields. Therefore it is sufficient to consider just scalar field.
The general solution of the wave equation

$$\left(\frac{\partial^2}{\partial t^2} - \nabla^2 - m^2\right)\varphi(\vec{r},t) = 0 \qquad (1)$$

for a scalar particle with the mass m can be written in the following form of the expansion of the field $\varphi(\vec{r},t)$ over plane waves:

$$\varphi(\vec{r},t) = \int \frac{d^3\kappa}{(2\pi)^3} e^{i(\vec{\kappa}\vec{r} - \omega t)} C_{\vec{\kappa}}\,, \qquad (2)$$

where $\omega = \sqrt{\vec{\kappa}^2 + m^2}$ and $C_{\vec{\kappa}}$ - are the expansion coefficients. Here and further we will use the system of units in which the speed of light c and the Plank constant $\hbar$ equal unit.

Let us consider the dispersion of the wave packet, which at the initial moment of time coincides with the Gaussian packet modulated by the plane wave with large value of the momentum $\vec{p}$ [2, 15]. Moreover we will assume that the initial widths of the packet $a_{\parallel}$ and $a_{\perp}$ parallel and perpendicular to the particle momentum $\vec{p}$ are different. For such packet at the initial moment of time the field $\varphi(\vec{r},t)$ has the following form:

$$\varphi(\vec{r},t) = e^{i\vec{p}\vec{r} - \frac{z^2}{2a_{\parallel}^2} - \frac{\vec{\rho}^2}{2a_{\perp}^2}}, \qquad (3)$$

where z and $\vec{\rho}$ are the coordinates parallel and orthogonal to $\vec{p}$. At the moment of time t this packet will be defined by the relation (2) with

$$C_{\vec{\kappa}} = (2\pi)^{3/2} a_{\parallel} a_{\perp}^2 e^{-\frac{(p-\kappa_z)^2 a_{\parallel}^2}{2} - \frac{\kappa_{\perp}^2 a_{\perp}^2}{2}}. \qquad (4)$$

We can write the obtained expression for the field $\varphi(\vec{r},t)$ in the form

$$\varphi(\vec{r},t) = A e^{i(\vec{p}\vec{r} - \varepsilon t)} I(\vec{r},t) \qquad (5)$$

in which $A = a_{\parallel} a_{\perp}^2$, $\varepsilon = \sqrt{\vec{p}^2 + m^2}$ and

$$I(\vec{r},t) = (2\pi)^{-3/2} \int d^3\kappa e^{i(\vec{\kappa}-\vec{p})\vec{r} - \frac{(p-\kappa_z)^2 a_{\parallel}^2}{2} - \frac{\kappa_{\perp}^2 a_{\perp}^2}{2} - i(\omega_k - \varepsilon)t}. \qquad (6)$$

Having made in this expression the variable substitution $\vec{\kappa} = \vec{p} + \vec{q}$ we find that

$$I(\vec{r},t)=(2\pi)^{-3/2}\int d^3q e^{i\vec{q}\vec{r}-\frac{q_z^2a_\parallel^2}{2}-\frac{q_\perp^2a_\perp^2}{2}-i(\omega_{\vec{p}+\vec{q}}-\varepsilon)t}. \qquad (7)$$

In the case of large energies it is possible to make the expansion over $|\vec{q}|/p$ in the quantity $(\omega_{\vec{p}+\vec{q}}-\varepsilon)$ in (7). Having preserved the quadratic terms of expansion we obtain

$$\omega_{\vec{p}+\vec{q}}-\varepsilon\approx vq_z+\frac{q_z^2}{2\varepsilon\gamma^2}+\frac{q_\perp^2}{2\varepsilon}, \qquad (8)$$

where $v=p/\varepsilon$ and $\gamma=(1-v^2)^{-1/2}$. Substituting this expression into (6) after simple calculations we obtain

$$I(\vec{r},t)=\frac{1}{\sqrt{a_\parallel^2+i\frac{t}{\varepsilon\gamma^2}}}\ \frac{1}{a_\perp^2+i\frac{t}{\varepsilon}}\ \exp\left\{-\frac{(z-vt)^2}{2\left(a_\parallel^2+i\frac{t}{\varepsilon\gamma^2}\right)}-\frac{\rho^2}{2\left(a_\perp^2+i\frac{t}{\varepsilon}\right)}\right\}. \qquad (9)$$

The formula (9) can be written in the following form as well:

$$I(\vec{r},t)=A(t)\exp\left\{i\alpha(\vec{r},t)-\frac{(z-vt)^2}{2\Delta_\parallel^2(t)}-\frac{\rho^2}{2\Delta_\perp^2(t)}\right\}, \qquad (10)$$

in which $A(t)$ is a slowly changing quantity

$$A(t)=\frac{1}{\left(a_\perp^2+i\frac{t}{\varepsilon}\right)\sqrt{a_\parallel^2+i\frac{t}{\varepsilon\gamma^2}}}, \qquad (11)$$

$\alpha(\vec{r},t)$ is the real phase

$$\alpha(\vec{r},t)=\frac{(z-vt)^2}{2}\frac{t/\varepsilon\gamma^2}{a_\parallel^4+\left(t/\varepsilon\gamma^2\right)^2}+\frac{\rho^2}{2}\frac{t/\varepsilon}{a_\perp^4+\left(t/\varepsilon\right)^2}, \qquad (12)$$

$\Delta_\parallel(t)$ and $\Delta_\perp(t)$ are the longitudinal and transverse widths of the packet at the moment of time t

$$\Delta_\parallel^2(t)=a_\parallel^2+\left(\frac{t}{a_\parallel\varepsilon\gamma^2}\right)^2, \qquad \Delta_\perp^2(t)=a_\perp^2+\left(\frac{t}{a_\perp\varepsilon}\right)^2. \qquad (13)$$

In the case of $a_\parallel=a_\perp$ the obtained above formulae coincide with the corresponding result of the paper [15].

The formulae (13) show that in longitudinal and transverse directions the squares of the widths of the packet $\Delta_\parallel^2(t)$ and $\Delta_\perp^2(t)$ grow with time proportionally to t^2m^4/ε^6 and t^2/ε^2. In nonrelativistic case these quantities do not depend on the particle energy ($t^2/\varepsilon^2=t^2/m^2$). In relativistic case the quantities t^2m^4/ε^6 and t^2/ε^2 are substantially smaller than the corresponding values for nonreativistic particles. Let us note that the additional factor m^4/ε^4 exists for longitudinal direction in $\Delta_\parallel^2(t)$. It leads to the substantial decrease of the speed of the packet

dispersion in this direction compared to the speed of the packet dispersion in transverse direction. Thus the relativistic effects do the stabilizing influence upon the wave packets.

Now let us consider high energy packets of free electromagnetic waves. Scalar and vector potentials of such packets are the solutions of the wave equation (1) with $m = 0$. Therefore in order to analyze the peculiarities of dispersion of such packets we can use the previous formulae assuming that all the terms in them containing the Lorentz-factor γ equal zero. In this case for scalar potential we find that

$$\varphi(\vec{r},t) = Ae^{i(\vec{k}\vec{r}-\omega t)} I(\vec{r},t), \qquad (14)$$

where $\vec{k}$ and ω are the wave vector and the frequency of the electromagnetic wave and

$$I(\vec{r},t) = A(t)\exp\left\{ i\alpha_k(\vec{r},t) - \frac{(z-t)^2}{2\Delta_\parallel^2} - \frac{\rho^2}{2\Delta_\perp^2} \right\}. \qquad (15)$$

Here

$$A(t) = \frac{1}{a_\parallel\left(a_\perp^2 + it/\omega\right)}, \quad \alpha(\vec{r},t) = \frac{\rho^2}{2}\frac{t/\omega}{a_\perp^4 + \left(t/\omega\right)^2}, \qquad (16)$$

and

$$\Delta_\parallel^2(t) = a_\parallel^2, \qquad \Delta_\perp^2(t) = a_\perp^2 + \left(t/a_\perp\omega\right)^2.$$

The obtained formulae show that the initially Gaussian packet does not disperse in the direction parallel to the $\vec{k}$ vector. In transverse direction the square of the packet widths grows proportionally to $(t/\omega)^2$. Thus the speed of the packet dispersion decreases with the increase of the wave frequency ω.

When considering a process of radiation by relativistic electrons it is often necessary to deal with packets, which are constructed of plane waves with wave vectors, which directions are close to the direction of a given vector $\vec{k}$. Such wave packets differ somehow from the ones considered above. Let us consider some peculiarities of dispersion of such packets assuming for simplicity that at the initial moment of tome $t = 0$ the distribution of the waves over the wave vectors is Gaussian relative to the given vector $\vec{k}$ [16]. For such distribution in the initial moment of time the scalar potential $\varphi_k(\vec{r},0)$ has the following form:

$$\varphi_k(\vec{r},0) = \frac{1}{\pi\overline{\Delta}_\vartheta^2}\int d^2\vartheta e^{-\vartheta^2/\overline{\Delta}_\vartheta^2} e^{i\vec{k}\vec{r}}, \qquad (17)$$

where ϑ is the angle between the packet wave vector and the wave vector $\vec{k}$, $\overline{\Delta}_\vartheta^2$ is the average value of the square of the angle ϑ, $\overline{\Delta}_\vartheta^2 << 1$.

The coefficients $C_{\vec{q}}$ of the Fourier expansion (2) for such initial packet have the following form

$$C_{\vec{q}} = (2\pi)^3 \int \frac{d^2\vartheta}{\pi\overline{\Delta}_\vartheta^2} e^{-\vartheta^2/\overline{\Delta}_\vartheta^2} \delta(\vec{k}-\vec{q}), \qquad (18)$$

in which $\delta(\vec{k}-\vec{q})$ is the delta-function. As a result we come to the following expression for the scalar potential

$$\varphi_k(\vec{r},t)=\frac{1}{1+ikz\overline{\Delta}_\vartheta^2/2}e^{ik(z-t)-\frac{(k\rho/2)^2\overline{\Delta}_\vartheta^2}{1+ikz\overline{\Delta}_\vartheta^2/2}}, \qquad (19)$$

where z and $\vec{\rho}$ are the coordinates parallel and orthogonal to $\vec{k}$.

The given expression for the wave packet has the same structure as the corresponding expression for the packet (14). If the substitutions $(t/a_\perp^2\varepsilon)\to(\omega\ z\overline{\Delta}_\vartheta^2/2)$ and $a_\parallel^2\to\infty$ are made in the latter expression the both formulae for the wave packet will become identical.

The formula (19) shows that for $\omega\ z\overline{\Delta}_\vartheta^2/2<<1$

$$\left\langle\varphi_k(\vec{r},t)\right\rangle\approx\exp\left\{i\omega(z-t)-\left(\frac{\omega\rho}{2}\right)^2\overline{\Delta}_\vartheta^2\right\}, \qquad (20)$$

and for $\omega\ z\overline{\Delta}_\vartheta^2/2>>1$

$$\left\langle\varphi_k(\vec{r},t)\right\rangle\approx-\frac{2i}{\omega\ z\overline{\Delta}_\vartheta^2}\exp\left\{i\omega(z-t)+i\omega\frac{\rho^2}{2z}-\frac{\rho^2}{z^2\overline{\Delta}_\vartheta^2}\right\}. \qquad (21)$$

For $z>>\rho$ the latter formula can be written in the form of a diverging wave

$$\left\langle\varphi_k(\vec{r},t)\right\rangle\approx-\frac{2i}{\omega\ r\overline{\Delta}_\vartheta^2}\exp\left\{i\omega(r-t)-\frac{\rho^2}{z^2\overline{\Delta}_\vartheta^2}\right\}, \qquad (22)$$

where $r=\sqrt{z^2+\rho^2}\approx z+\rho^2/2z$. Thus on distances z from the center of the initial packet, which satisfy the condition

$$\omega\ z\overline{\Delta}_\vartheta^2/2<<1 \qquad (23)$$

the form of the packet (19) coincides with the form of the packet at $t=0$. Only on the distances, which satisfy the condition

$$\omega\ z\overline{\Delta}_\vartheta^2/2>>1 \qquad (24)$$

the transformation of the packet (19) to the packet of spherical diverging waves occurs.

Let us note that in the theory of radiation of electromagnetic waves by a moving electron the spatial region in which the formation of spherical diverging waves occurs has a name of the wave zone (see for example [17]). In particular, for nonrelativistic charged particles the wave zone begins on distances from the radiation region, which exceed the length of the radiated wave λ. However, the condition (24) shows that for $\overline{\Delta}_\vartheta^2<<1$ the wave zone formation occurs not on distances $z>>\lambda$ as in the case of a nonrelativistic particle but on distances

$$z>>2\lambda/\overline{\Delta}_\vartheta^2, \qquad (25)$$

which are much larger than the wave length $\lambda=1/\omega$. For sufficiently small values of $\overline{\Delta}_\vartheta^2$ the length $z=2\lambda/\overline{\Delta}_\vartheta^2$ can reach macroscopic size.

3. The electromagnetic field structure at an electron instantaneous scattering. The 'half-bare' electron

The electromagnetic wave packets similar to the ones considered above arise, for example, in the process of bremsstrahlung by relativistic electron at its instantaneous scattering to a large angle. Let us consider some peculiarities of evolution of such packets and of formation of radiation by relativistic electron in the wave and the pre wave zones.

In classical electrodynamics electromagnetic field around an electron is defined by a retarded solution of the Maxwell equations. For a particle, which moves along the trajectory $\vec{r}(t)$ vector and scalar potentials of such field have the following form:

$$\left\{ \vec{A} \ , \ \varphi \right\} = e \int_{-\infty}^{+\infty} \frac{dt'}{\left|\vec{r} - \vec{r}(t')\right|} \left\{ \vec{v}(t') \ , \ 1 \right\} \delta(t' - t - \left|\vec{r} - \vec{r}(t')\right|), \quad (26)$$

in which $\vec{v}(t)$ is the electron velocity. The Fourier-expansion of the potentials (26) can be presented in the next form:

$$\left\{ \vec{A} \ , \ \varphi \right\} = -\frac{e}{2\pi^2} \mathrm{Im} \int \frac{d^3k}{k} e^{-i(kt - \vec{k}\vec{r})} \int_{-\infty}^{t} dt' \left\{ \vec{v}(t') \ , \ 1 \right\} e^{i(kt' - \vec{k}\vec{r}(t'))} . \quad (27)$$

In the case of a uniform particle motion with the velocity $\vec{v}$ along the z axis (27) leads to the following expressions for the potentials:

$$\vec{A}_{\vec{v}}(\vec{r},t) = \frac{e}{2\pi^2} \mathrm{Re} \int \frac{d^3k}{k} \frac{\vec{v}}{ck - \vec{k}\vec{v}} e^{i(\vec{k}\vec{r} - \vec{k}\vec{v}t)} , \quad (28)$$

$$\varphi_{\vec{v}}(\vec{r},t) = \frac{e}{2\pi^2} \mathrm{Re} \int \frac{d^3k}{k} \frac{1}{ck - \vec{k}\vec{v}} e^{i(\vec{k}\vec{r} - \vec{k}\vec{v}t)} .$$

After integration in (28) over $\vec{k}$ we find that

$$\vec{A}_v(\vec{r},t) = \frac{e\vec{v}}{\sqrt{\rho^2\gamma^{-2} + (z - vt)^2}} , \qquad \varphi_v(\vec{r},t) = \frac{e}{\sqrt{\rho^2\gamma^{-2} + (z - vt)^2}} . \quad (29)$$

These formulae represent the coulomb potential of an electron, which moves uniformly with the velocity $\vec{v}$. Here $\gamma = E/m$ is the particle's Lorentz-factor and ρ is the absolute value of the coordinate $\vec{\rho}$ of the observation point in the plane orthogonal to the z axis. The formula (29) for $\varphi(\vec{r},t)$ shows that the equipotential surfaces of the field of the particle, which moves uniformly straightforward are the ellipsoids flattened in the direction of particle motion.

Another rather interesting situation occurs at the instantaneous change of the electron velocity from the value $\vec{v}$ to the value $\vec{v}'$ at the moment of time $t = 0$. In this case before the scattering ($t < 0$) the potentials $\vec{A}(\vec{r},t)$ and $\varphi(\vec{r},t)$ of the field around the electron are the own coulomb field (29) of a uniformly moving electron. After the scattering ($t > 0$), according to (27), we find that

$$\vec{A}(\vec{r},t) = \frac{e}{2\pi^2} \mathrm{Re} \int \frac{d^3k}{k} \left\{ \frac{\vec{v}'}{k - \vec{k}\vec{v}'} \left[1 - e^{-i(k - \vec{k}\vec{v}')t} \right] e^{-i\vec{k}\vec{v}'t} + \frac{\vec{v}}{k - \vec{k}\vec{v}} e^{-ikt} \right\} e^{i\vec{k}\vec{r}} , \quad (30)$$

$$\varphi(\vec{r},t)=\frac{e}{2\pi^2}\,\mathrm{Re}\int\frac{d^3k}{k}\left\{\frac{1}{k-\vec{k}\vec{v}'}\left[1-e^{-i(k-\vec{k}\vec{v}')t}\right]e^{-i\vec{k}\vec{v}'t}+\frac{1}{k-\vec{k}\vec{v}}e^{-ikt}\right\}e^{i\vec{k}\vec{r}}\,.$$

The integration over $\vec{k}$ gives in this case:

$$\vec{A}(\vec{r},t)=\vec{A}_{\vec{v}'}(\vec{r},t)\theta(t-r)+\vec{A}_{\vec{v}}(\vec{r},t)\theta(r-t)\,, \qquad (31)$$

$$\varphi(\vec{r},t)=\varphi_{\vec{v}'}(\vec{r},t)\theta(t-r)+\varphi_{\vec{v}}(\vec{r},t)\theta(r-t)\,.$$

where $(\vec{A}_{\vec{v}},\varphi_{\vec{v}})$ and $(\vec{A}_{\vec{v}'},\varphi_{\vec{v}'})$ are respectively the coulomb potentials of the particles, which uniformly move in the directions of z and z' axis.

The expressions (29) show that before the scattering moment the total field around the electron coincides with its own coulomb field, which moves with the velocity $\vec{v}$ together with the electron. After the scattering, according to (30) and (31), the total field around the electron breaks into two parts represented by two items in the considered expressions.

The first items in braces in (30) correspond to the nonequilibrium field, which the scattered electron has already managed to rebuild around itself by the moment of time t. This field consists of the own coulomb field of the electron, which moves along the z' axis with the velocity $\vec{v}'$ (the first items in square brackets in (30) correspond to it) and the packet of free waves, which moves in the same direction (it is described by the second item in square brackets). There is substantial interference between these fields due to which (as the first items in (31) show) the total field vanishes in the region $r>t$, which the signal about the electron scattering at the moment of time $t=0$ has not yet reached. Inside the sphere of radius $r=t$ the total field coincides with the equilibrium coulomb field of the electron.

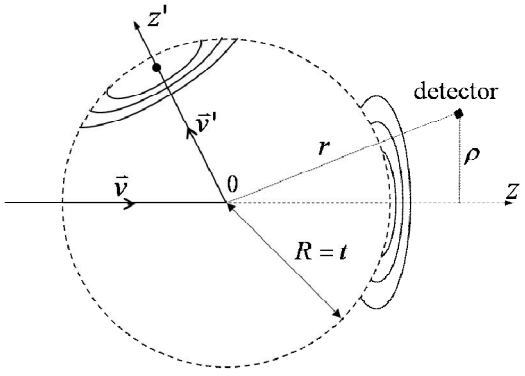

Fig.1. The picture of total field after instantaneous scattering of an electron to a large angle

The second items in braces in (30) describe the field, which as though `tears away' from the electron at the scattering moment. It is a packet of free electromagnetic waves, which moves in the direction of the initial electron's velocity $\vec{v}$ and gradually transforms into bremsstrahlung. This field is different from zero outside the sphere $r=t$ and vanishes inside it.

The equipotential surfaces of the scalar potential of the field around the electron after its scattering to a large angle are presented on Fig. 1.

The behavior of certain Fourier-components of the nonequilibrium field of the electron after its scattering and of the field 'torn away' from the electron at its scattering is of special interest. According to (30), the values of $\vec{k}$, which make contribution to each item of the nonequilibrium field of the electron has directions close to the direction of the electron's final velocity $\vec{v}'$. During the period of time $t<(k-\vec{k}\vec{v}')^{-1}$, however, both of these items substantially cancel each other due to the interference. Therefore the coulomb field, which corresponds to the scattered electron, does not appear instantly. Namely, during the period of time $t\le(k-\vec{k}\vec{v}')^{-1}$ the Fourier components with wave vector $\vec{k}$ are nearly absent in the field around the scattered electron.

As the main contribution to the coulomb field is made by $\vec{k}$ with directions close to the direction of the velocity $\vec{v}$ this period of time is defined by the relation $t \le 2\gamma^2 / k$. Figuratively speaking we can say that after the scattering during such period of time the electron is in 'half-bare' state, which means without considerable part of its field. Such state of electron with nonequilibrium field manifests itself during further scatterings of the electron, which causes different effects of bremsstrahlung suppression during an electron's motion in substance, such as Landau-Pomeranchuk-Migdal effect [18-20], the effect of radiation suppression in thin layer of substance (TSF-effect [21-23]), etc. Recently the series of detailed experimental investigations of these effects at ultra high energies was performed on SLAC [24, 25] and CERN[26, 27] accelerators, which confirmed the main theoretical predictions.

The notion of a 'half-bare' electron was introduced in the paper of E.L. Feinberg [28, 29] who studied the time evolution of the state vector of the system 'electron + photon' after the scattering of a fast electron to a large angle on atom. The classical theory of this effect was given in [2, 22, 30].

Let us note that during the period of time $t = 2\gamma^2 / \omega$ the electron covers the distance

$$l_C = 2\gamma^2 v / \omega \qquad (32)$$

In the theory of radiation by relativistic electrons the length l_C has a name of the coherence length of the radiation process [1,2]. Within this length the interference effects in radiation are significant. For ultra relativistic electrons in the region of small frequencies of radiated waves the length l_C can have macroscopic size, which exceeds not only interatomic distance of the substance but the size of the experimental facility as well. Indeed, in the millimeter range of the waves radiated by electrons with the energy of $50Mev$ the coherence length is $l_C = 20m$. It means that within such length after scattering the electron is in 'half-bare' state, which means that the Fourier-components of the corresponding wavelengths are absent in the field around the electron.

The field, which 'tears away' from the electron at its scattering (the second items in braces in (30)) has the structure similar to the one, which has the packet of free waves considered above. Therefore the main peculiarities of the reconstruction of the 'torn away' field to the field of radiation will be the same as the considered above peculiarities of the wave packets evolution.

4. The problem of measurement of bremsstrahlung characteristics

The results presented above show that for ultra relativistic electrons the radiation formation process develops on large distances along the initial and final directions of the electron motion, which can be of macroscopic size. In this case a detector, which registers the radiation characteristics can be situated both in the wave zone (which means on large distances $r \to \infty$ from the scattering point) and in the pre wave zone (which means on within the coherence length l_C of the radiation process). Let us show that the results of measurements can substantially differ in these cases. For this purpose let us consider the peculiarities of the formation of radiation from the 'torn-away' field on different distances from the scattering point [31]. The consideration will be made for a point detector situated in the point with coordinates $\vec{r} = (\vec{\rho}, z)$. Here the z axis is parallel to the vector of the electron's initial velocity and $\vec{\rho}$ are the coordinates in the orthogonal plane. In this case by the point detector we mean the detector, which measures the characteristics of electromagnetic waves (wave packet), which fall on a small element of surface situated in the point with the coordinates $\vec{r} = (\vec{\rho}, z)$ and seen at solid angle do from the scattering point.

Making in the second item in the expression (30) for scalar potential the variable substitution $k_z \to k$ by $k_z = \sqrt{k^2 - q^2}$ (k_z and q are respectively the components of the wave vector $\vec{k}$ along the z - axis and orthogonal to it) and denoting $k = \omega$, it is possible to present the Fourier-expansion of the `torn-away' field scalar potential in the following form:

$$\varphi(\vec{r},t) = \frac{e}{\pi v^2}\int_{-\infty}^{+\infty} d\omega\ e^{-i\omega t}\int_0^{|\omega|} dq\,\frac{qJ_0(q\rho)}{q^2+\omega^2/v^2\gamma^2}Q(z), \qquad (33)$$

where

$$Q(z) = \frac{\omega\cos\left(z\sqrt{\omega^2-q^2}\right)}{\sqrt{\omega^2-q^2}} + iv\sin\left(z\sqrt{\omega^2-q^2}\right) \qquad (34)$$

and $\rho = |\vec{\rho}|$.

In (33) and (34) the square root $\sqrt{\omega^2-q^2}$ is considered to be a single-valued branch of the analytical function, which is equal to $\left|\sqrt{\omega^2-q^2}\right|$ for $\omega > q$ and $-\left|\sqrt{\omega^2-q^2}\right|$ for $\omega < -q$.

In ultra relativistic case ($\gamma >> 1$) the range of q, which make the main contribution to the integral (33) is $q \le \omega/\gamma << \omega$ and it is possible to expand the square roots $\sqrt{\omega^2-q^2}$ in (34) in the small factor q/ω. Let us leave the items proportional to the second power of q/ω in the arguments of sine and cosine, while in the other parts of the expression (34) neglect them. Moreover the integration over q can be extended to the region $0 < q < \infty$. This leads to the following expression for the `torn-away' field potential in ultra relativistic case:

$$\varphi(\vec{r},t) = \frac{e}{\pi}\int_{-\infty}^{+\infty} d\omega\int_0^{+\infty} dq\,\frac{qJ_0(q\rho)}{q^2+\omega^2/v^2\gamma^2}e^{i\omega(z-t)-iq^2z/2\omega}. \qquad (35)$$

In Lorentz gauge potentials $\vec{A}(\vec{r},t)$ and $\varphi(\vec{r},t)$ satisfy the equation

$$div\vec{A} + \frac{\partial\varphi}{\partial t} = 0. \qquad (36)$$

If we know $\varphi(\vec{r},t)$, we can derive the vector potential component A_z from this equation ($\vec{A}_\perp = 0$ in this case). In the considered case the vector potential equals to the scalar one up to the neglected items of the order of $(q/\omega)^2$.

In order to determine the total energy radiated in the direction of a small area $d\vec{s} = \vec{n}r^2 do$ situated in the point $\vec{r} = (\vec{\rho}, z)$ we can calculate the flux of the Poynting vector through this area during the whole time of the particle motion

$$d\mathcal{E} = \frac{r^2 do}{4\pi}\int dt\left(\vec{E}\times\vec{H}\right)\vec{n}$$

where do is the element of solid angle in the direction of radiation $\vec{n} = \vec{r}/r$. The fields $\vec{E}$ and $\vec{H}$ in this expression are the fields of the packet of free electromagnetic waves (the field 'torn-away'

from the electron at its scattering). They are related to scalar φ and vector $\vec{A}$ potentials of the radiation field by

$$\vec{E} = -\frac{\partial \vec{A}}{\partial t} - \nabla\varphi \quad \vec{H} = \nabla \times \vec{A}. \tag{37}$$

Proceeding to the Fourier-expansions of the fields φ and $\vec{A}$ over frequency ω we obtain the following expression for the radiation spectral-angular density:

$$\frac{d\mathcal{E}}{d\omega do} = \frac{r^2}{4\pi^2}\left[\vec{E}_\omega(\vec{r}) \times \vec{H}_{-\omega}(\vec{r})\right] \vec{n}, \tag{38}$$

in which $\omega \geq 0$.

With the use of the Maxwell equation $\vec{H}_\omega = (-i/\omega)\nabla \times \vec{E}_\omega$, the radiation spectral-angular density can be expressed in the terms of Fourier-component of the electric field alone:

$$\frac{d\mathcal{E}}{d\omega do} = -\frac{ir^2}{\omega}\left[\vec{E}_\omega \times (\nabla \times \vec{E}_{-\omega}(\vec{r}))\right] \cdot \vec{n}. \tag{39}$$

Let us note that the formulae (38) and (39) are valid for arbitrary distances from the scattering point. Therefore they can be used for radiation consideration both in the wave and the pre wave zones. In the wave zone (which means in the region $r \to \infty$) they can be considerably simplified. Therefore, firstly, let us dwell on the consideration of this case.

On large distances from the scattering point ($r \to \infty$) a Fourier-component of the field of the radiation waves $\vec{E}_\omega(\vec{r})$ reconstructs into a packet of diverging waves, which amplitude is proportional to the factor $r^{-1}\exp(i\omega r)$. The action of the Hamilton operator ∇ in (39) upon $\vec{E}_{-\omega}$ in this case can be applied only to the factor $\exp(i\omega r)$:

$$\nabla \times \vec{E}_{-\omega} = i\omega \ \vec{n} \times \vec{E}_{-\omega}. \tag{40}$$

As a result we obtain the following expression for the radiation spectral-angular density for $r \to \infty$:

$$\frac{d\mathcal{E}}{d\omega do} = \frac{r^2}{4\pi^2}\left|\vec{E}_\omega(\vec{r})\right|^2. \tag{41}$$

Let us note that the formula (41) is valid on large distances from the scattering point ($r \to \infty$). While proceeding from (39) to (41) we took into account that $\vec{n}\vec{E}_\omega = 0$. This relation directly comes from the expression of Fourier-components of electric and magnetic fields in terms of potentials $\varphi_\omega(\vec{r})$ and $\vec{A}_\omega(\vec{r})$

$$\vec{E}_\omega = -\nabla\varphi_\omega(\vec{r}) + i\omega \ \vec{A}_\omega(\vec{r}), \qquad \vec{H}_\omega = \nabla \times \vec{A}_\omega(\vec{r}), \tag{42}$$

where $\varphi_\omega(\vec{r})$ and $\vec{A}_\omega(\vec{r})$ are defined from the expression (35).

In the case of ultrarelativistic particle in the region of characteristic for this process small radiation angles $\vartheta << 1$ the 'torn-away' electric field can be considered as transverse having only $E_\perp$ component orthogonal to z axis. In this case the formula (41) for the radiation spectral-angular density has the following form:

$$\frac{d\mathcal{E}}{d\omega do} = \frac{r^2}{4\pi^2}\left|E_{\omega\perp}(\vec{r})\right|^2. \qquad (43)$$

Using (35) we can derive the electric field Fourier-component orthogonal to z axis. Substituting it into (43) for the spectral-angular distribution of bremsstrahlung we achieve:

$$\frac{d\mathcal{E}}{d\omega do} = \left(\frac{ez}{\pi}\right)^2 \left| \int_0^\infty dq \frac{q^2 J_1(q\rho)}{q^2 + \omega^2 / v^2\gamma^2} e^{-i\frac{q^2 z}{2\omega}} \right|^2. \qquad (44)$$

For large distances from the scattering point, namely in the wave zone of the radiation process ($z >> 2\gamma^2/\omega$) the integral in (44) can be calculated with the use of stationary phase method [32]. It leads to the well known expression for radiation distribution from the bremsstrahlung theory [1,4,33]:

$$\frac{d\mathcal{E}}{d\omega do} = \frac{e^2}{\pi^2}\frac{\vartheta^2}{\left(\vartheta^2 + \gamma^{-2}\right)^2}, \qquad (45)$$

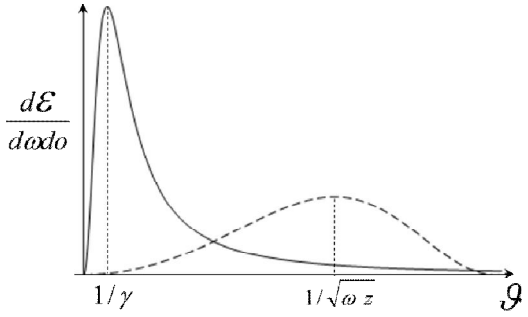

Fig. 2. Bremsstrahlung angular distribution given by a point detector in the wave zone (solid curve) and in the pre-wave zone (dashed curve) for a certain frequency ω

where $\vartheta = \rho / z$ is the angle between the direction of radiation and the z axis. As we can see from (45) in the wave zone the radiation is mainly concentrated within characteristic angles $\vartheta \approx 1/\gamma$. The schematic form of the bremsstrahlung angular distribution in the wave zone is presented on the Fig. 2 by the solid curve. For ultra high energies of the radiating particle in the region of characteristic small angles of radiation the expression (43) (and hence the expression (44)) is valid for the description of radiation spectral-angular density on small distances from the scattering point as well (in particular, in the pre-wave zone ($z << 2\gamma^2/\omega$) of the radiation process). Indeed, as the electric field can be considered transverse in this case than $\vec{E}_\omega = -\nabla\varphi_\omega = -\partial\varphi_\omega / \partial\vec{\rho}$. The equality of $\varphi_\omega(\vec{r})$ and $A_\omega(\vec{r})$ leads to the following expression for the magnetic field:

$$\vec{H}_\omega = \nabla \times \vec{A}_\omega = \nabla\varphi_\omega \times \vec{e}_z,$$

where $\vec{e}_z$ is a unit vector in the direction of z axis. Taking into account the orthogonality of $\nabla\varphi_\omega$ and $\vec{e}_z$ for the absolute value of the magnetic field we obtain $\left|\vec{H}_\omega\right| = \left|\nabla\varphi_\omega\right|$, which is equal to the absolute value of the electric field. Moreover, these fields are orthogonal ($\vec{E}_\omega \vec{H}_\omega = \nabla\varphi_\omega(\nabla\varphi_\omega \times \vec{e}_z) = 0$). Taking into account the fact that the magnetic field $\vec{H}(\vec{r},t)$ is the real function, which leads to the relation $\vec{H}_{-\omega} = \vec{H}^*_\omega$, we can present the general expression (38) in the following form:

$$\frac{d\mathcal{E}}{d\omega do} = \frac{r^2}{4\pi^2}\left[E_{\omega\perp}E^*_{\omega\perp}(\vec{r})\right]\vec{e}_z\vec{n}\ ,$$

which coincides with (43) at small angles between $\vec{e}_z$ and $\vec{n}$. Now let us consider radiation in the pre-wave zone on the basis of this formula.

In the pre-wave zone ($z << 2\gamma^2/\omega$) of the radiation process it is not possible to use the stationary phase method for the analysis of radiation characteristics. Here, making the substitutions $q = \omega\ x/\gamma$ and $\rho = z\vartheta$, we can present the integral (44) in the form:

$$\frac{d\mathcal{E}}{d\omega do} = \left(\frac{e\omega\ z}{\pi\gamma}\right)^2 \left|I_1 - I_2\right|^2, \qquad (46)$$

where

$$I_1 = \int_0^{+\infty} dx J_1(\omega\ z\gamma^{-1}x\vartheta)e^{-i\frac{\omega\ z}{2\gamma^2}x^2}\ ,$$

$$I_2 = \int_0^{+\infty} dx \frac{J_1(\omega\ z\gamma^{-1}x\vartheta)}{x^2+1}e^{-i\frac{\omega\ z}{2\gamma^2}x^2}\ .$$

In the case $\gamma >> 1$ the absolute value of the integral I_2 is negligibly small comparing to the corresponding value of I_1 and for spectral-angular density of bremsstrahlung in the pre-wave zone we obtain:

$$\frac{d\mathcal{E}}{d\omega do} = \left(\frac{e\omega\ z}{\pi}\right)^2 \left|I_1\right|^2 = \frac{4e^2}{\pi^2}\frac{1}{\vartheta^2}\sin^2\left(\frac{\omega\ z\vartheta^2}{4}\right). \qquad (47)$$

From (47) we can conclude that in the pre-wave zone the radiation is mainly concentrated within angles $\vartheta \approx 2/\sqrt{\omega\ z}$, which exceed the characteristic angles $\vartheta \approx 1/\gamma$ of the wave zone. Therefore in the pre-wave zone ($z << 2\gamma^2/\omega$) the point detector gives broader angular distribution of radiation (dashed curve on Fig. 2) than in the wave zone ($z >> 2\gamma^2/\omega$). Moreover this distribution depends on the frequency ω of the radiated waves.

By the point detector we mean here the detector of the smaller size $\delta\rho$ than the transversal radiation length of the process $l_T \approx \gamma/\omega$, which is the characteristic transversal distance on which at the moment of time $t = 0$ the Fourier harmonics of frequency ω are concentrated in the wave packet (35). Such detector registers the radiation of frequency ω, which falls on a small domain of space, where the detector is situated.

The measurements, however, can be made by the extended detector of the larger size than the characteristic transversal length of the radiation process, so that $\delta\rho >> l_T$. Such detector registers not only the waves of frequency ω, which fall on the small element of surface with coordinates $\vec{\rho}$ and z, as the point detector does, but all the electromagnetic waves of frequency ω, which propagate in the direction of wave vector $\vec{k}$ ($\left|\vec{k}\right| = \omega$). In order to calculate the bremsstrahlung spectral-angular distribution, which is registered by an extensive detector, which is a plate of large size, we need to integrate the expression (44) over the entire considered plate and express the obtained result in the form of an integral over the directions of wave vectors of radiated waves. The

integrand in this case will be nothing else than the required distribution. In our case after performing the procedures described above we can present the expression (44) in the following form:

$$\frac{d\mathcal{E}}{d\omega do_\gamma} = \frac{e^2}{\pi^2} \frac{\vartheta_\gamma^{\,2}}{\left(\vartheta_\gamma^{\,2} + \gamma^{-2}\right)^2}, \tag{48}$$

where $\vartheta_\gamma = q/\omega$ is the angle between the direction of the wave vector $\vec{k}$ and the z axis. Hence the bremsstrahlung spectral-angular distribution obtained by the extended detector coincides with the one (45) obtained by the point detector in the wave zone. But unlike the case with point detector this distribution does not depend on the distance from the scattering point and is the same both in the wave and the pre-wave zones.

5. Conclusion

The behavior of localized high-energy electromagnetic wave packets, which take place in process of bremsstrahlung by relativistic electrons has been considered. It is shown that with the increase of the energy the stabilization of characteristics of motion of such packets takes place, which consists in substantial decrease of the speed of their dispersion. Essential here is the fact that at high energies the lengths on which the reconstruction of the form of such packets into packets of diverging waves takes place can reach macroscopic size, which can exceed the size of experimental facility. In this case both the size of the used detector and its position relative to the region of the wave packet formation become essential for measurements.

Such situation takes place, for example, after the sharp scattering of an electron to a large angle. It is shown that as a result of such scattering the electron's own coulomb field tears away from it and turns into a localized packet of free electromagnetic waves, which transforms into a packet of diverging waves on large distance from the scattering point. For ultra relativistic electrons such transformation of certain Fourier-harmonics of the packet field takes place within the coherence length of the radiation process, which substantially exceeds the length of the considered wave of radiation. In the case of low-frequency radiation this coherence length can be macroscopic. It gives birth to the problem of bremsstrahlung characteristics measurement by different detectors, which consists in the dependence of the results of measurement on the detector's size and its position relative to the scattering point. The analogous effect takes place also for backward transition radiation of relativistic electron on thin metallic plate [8, 10, 31, 34-35].

In the final direction of the electron motion (after the scattering) certain Fourier-components of the field around it do not appear at once. The regeneration of these Fourier-components occurs within the coherence length of the radiation process $l_C \approx 2\gamma^2/\omega$. In this case during a long period of time the ultra relativistic electron is in 'half-bare' state without a certain part of Fourier-components of its field. Such state of electron manifests itself, for example, during further collisions of the electron with atoms of a substance, which causes different effects of bremsstrahlung suppression (Landau-Pomeranchuk-Migdal effect, the effect of radiation suppression in thin layer of substance – TSF-effect, etc.). The 'half-bare' state of the scattered electron should also manifest itself in the process of further transition radiation by such electron [31, 34, 36].

References

1. Ter-Mikaelyan M.L. (1972) High-Energy Electromagnetic Processes in media. New York: Wiley.

2. Akhiezer A.I., Shul'ga N.F. (1996) High Energy Electrodynamics in Matter. Amsterdam: Gordon and Breach Publ. 388 p.
3. Dokshitzer Yu. L., Khoze V.A., Mueller A.H. and Troyan S.I. (1991) Basics of Perturbative QCD. Gif sur Yvette Cedex: Editions Frontiers. 274p.
4. Garibyan G.M., Shi Y. (1983) X-Ray transition radiation. Yerevan: Publ. of Acad. of Sc. of Arm. SSR, 320p. (in Russian)
5. Ginzburg V.L., Tsytovich V.N. (1984) Transition Radiation and Transition Scattering. Bristol: Adam Hilger.
6. Rullhusen P., Artru X., Dhez P. (1998) Novel radiation sources using relativistic electrons. Singapore: World Scientific Publ. 202p.
7. Shibata Y., Hasebe S., Ishiki K., et al. (1995) Observation of coherent diffraction radiation from bunched electrons passing through a circular aperture in the millimeter- and submillimeter- wave length regions. Phys. Rev. 52 E: 6737.
8. Dobrovolsky S.N., Shul'ga N.F. (2003) Transversal spatial distribution of transition radiation by relativistic electron in formation zone by the dotted detector. Nucl. Instrum. Methods B. 201: 123-132.
9. Gorham P. et al. (2000) Radio-frequency measurements of coherent transition and Cherenkov radiation: implication for high energy neutrino detection. Phys. Rev. 62 E: 8590-8605.
10. Verzilov V. A. (2000) Transition radiation in the pre-wave zone. Phys. Lett. 273 A: 135-140.
11. Akhiezer A.I., Shul'ga N.F., Fomin S.P. (2005) Landau-Pomeranchuk-Migdal Effect . Physics Reviews (Edited by I. M. Khalatnikov), Cambridge Sci. Publ., Printed in UK. 22: 1-215.
12. Potylitsyn A.P. (2011) Electromagnetic Radiation of Electrons in Periodic Structures. Berlin: Springer. 213p.
13. Naumenko G.N., Potylitsyn A.P., Sukhih L. G. et. al. (2009) Macroscopic effect of shadow of electromagnetic field of relativistic electrons. JETP Letters. 90, iss. 2: 105-110.
14. Miller W. (1974) Classical Limit Quantum Mechanics and the Theory of Molecular Collisions. New York: Wiley. p. 69-177.
15. Blokhintsev D.I. (1967) In the book: High-Energy Physics and Elementary Particles Theory. Kiev: Nauk. Dumka. p. 778.
16. Shul'ga N.F., Syshchenko V.V., Shul'ga S.N. (2009) On the motion of high-energy wave packets and transition radiation by "half-bare" electron. Phys. Lett. 374 A: 331-334.
17. Landau L.D., Lifshitz E.M. (1987) The Classical Theory of Fields. Oxford: Pergamon.
18. Landau L.D., Pomeranchuk I.Ya. (1953) Electron-cascade processes at ultra-high energies. Dokl. Acad. Nauk. SSSR. 92: 735.
19. Migdal A.B. (1956) Bremsstrahlung and pair production in condensed media at high energies. Phys. Rev. 103: 1811.
20. Akhiezer A.I., Shul'ga N.F. (1987) Influence of multiple scattering on the radiation of relativistic particles in amorphous and crystalline media. Sov. Phys. Usp. 30: 197-219.
21. Ternovsky F.F. (1961) On the theory of radiative processes in piece wise homogeneous media. Sov. Phys. JETP. 12: 123.
22. Shul'ga N.F., Fomin S.P. (1978) Suppression of radiation in an amorphous medium and a crystal. JETP Letters. 27: 117-120.
23. Fomin S.P., Shul'ga N.F. (1986) On space-time evolution of the process of ultra relativistic electron radiation in thin layer of substance. Phys. Lett. 114 A, №3: 148-152.
24. Anthony P. et.al. (1997) Bremsstrahlung suppression due to LPM and dielectric effects in a variety of targets. Phys. Rev. 12 D: 1286.

25. Klein S. (1998) Suppression of bremsstrahlung and pair production due to environmental factors. Rev. of Mod. Phys. 71: 1501.
26. Thomsen H.D., Esberg J., Kirsebom K. et. al. (2009) On the Macroscopic Formation Length for GeV Photons. Phys. Lett. 672 B: 323-327.
27. Thomsen H.D., Esberg J., Andersen K.K. et. al. (2010) Distorted Coulomb field of the scattered electron. Phys. Rev. 81 D: 18.
28. Feinberg E.L. (1966) Consecutive interactions at high energies. Sov Phys. JETP 23: 132.
29. Feinberg E.L. (1972) The problems of theoretical physics: paper collection dedicated to the memory of I.Y. Tamm. Moscow: Nauka. p. 248 (in Russian).
30. Akhiezer A.I., Shul'ga N.F. (1982) Radiation of relativistic particles in single crystals. Sov. Phys. Usp. 25: 541-564.
31. N.F. Shul'ga, S.V. Trofymenko, V.V. Syshchenko (2011) On transition radiation and bremsstrahlung by relativistic electron with nonequilibrium field. JETP Letters. 93, iss. 1: 3-7.
32. Bleistein N., Handelsman R. (1986) Asymptotic Expansions of Integrals. New York: Holt, Dover Publications. 425p.
33. Bolotovsky B.M., Serov A.V. (2009) Peculiarities of transition radiation field. Sov. Phys. Usp. 179: 517-524 (in Russian).
34. N.F. Shul'ga, S.V. Trofymenko, V.V. Syshchenko (2010) The Space-Time Evolution of the Process of Transition Radiation by Relativistic Electron. Jornal of Kharkiv National University №916, phys. series "Nuclei, Particles, Fields" iss. 3(47): 23-41.
35. N.F. Shul'ga, S.V. Trofymenko, V.V. Syshchenko (2011) On transition radiation by relativistic electron. Il Nuovo Cimento. 34 C, iss. 4: 327-334.
36. N.F. Shul'ga, S.V. Trofymenko, V.V. Syshchenko (2012) The prewave zone effect in transition radiation and bremsstrahlung by relativistic electron. Problems of atomic science and technology №1 series: Nuclear Physics Investigations. 57: 134-138.

The study of recrystallization of "silicon-on-sapphire" structures in case of amorphization by means of beam of silicon ions

P.A. Alexandrov*, K.D. Demakov*, S.G. Shemardov*, Yu.Yu. Kuznetsov*, A.A.Romanov**

**Scientific & Research Center "Kurchatov Institute", Moscow, Russia.*
***«Angstrom», Zelenograd, Russia*

Silicon films on the sapphire substrates were obtained by recrystallization from the interface "silicon–sapphire". An amorphous layer was formed by means of ion implantation with silicon ions having the energy of 90-150 keV. X-ray rocking curve was used to evaluate the crystalline perfection of silicon films. After recrystallization the silicon layer consisted of two parts with different structural quality. Recrystallized structures of silicon on sapphire have highly perfect upper layer (for the production of microelectronic devices) and the bottom layer with a large number of defects adjacent to the sapphire substrate.

1. Introduction

Modern development of micro- and nano-electronics leds to a widespread usage as substrates for creation of electronic circuits the structures "silicon on insulator" (SOI), which include also the heteroepitaxial films "silicon-on-sapphire" (SOS). However, the high concentration of dislocations, microtwins and other crystalline imperfections in the epitaxial silicon layer, especially near the interface silicon–sapphire, during epitaxy from the gaseous phase, require the use of additional methods for improving the structure of silicon layer.

The usage of solid-phase recrystallization (SPR) process is one of such methods. At the first stage is carried out an amorphization (as a rule, by the implantation of silicon ions) of epitaxial layer with the exception of its small near the surface part, which is hereinafter used as a seed of SPR-process for the subsequent temperature annealing [1-3]. Our latest studies, presented for publication, indicate that high-quality Si-films can be obtained by carrying out SPR from the "silicon–sapphire" interface [4,8]. In case of amorphization of epitaxial SOS-structure with silicon ions (implantation energy is 150 keV, dose is $7{,}5\cdot10^{14}$ Si^{+}/cm^{2}, the implantation temperature of about 0^{0}C) and during the subsequent recrystallization (550^{0}C in half an hour) and annealing (1000^{0}C in 1 hour) there is observed the minimal presence of defects of the silicon layer (FWHM – the width of X-ray rocking curve, decreased from the values ~1400-1500" in the initial epitaxial structures up to ~550-600" in the recrystallized samples).

The SOS-plates with diameter of 100 mm were amorphized by us for above-mentioned parameters (and not as indicated in [5]) and submitted to the Scientific&Research Institute of Measuring Systems (SRIMS, Nizhny Novgorod) for carrying out the recrystallization and creation of testing structures. The authors observed a significant improvement in electrophysical parameters of testing chips (the electron mobility is increased up to 300-700 cm2/V·s from the initial 20-100 cm2/V·s, by an order of magnitude is reduced the consumption current, by two orders of magnitude is decreased the leakage current, and percentage of the yield rate of suitable chips is increased as 3 times, etc.)

However, our recent studies, as well as studies conducted abroad have shown that improving the structural quality of epitaxial film leads to a significant reduction in radiation resistance of chips – one of the most important properties of SOS-structures [6,7]. On the other hand, the use of SPR from the interface allows obtaining the silicon films with sharply differing presence of defects in thickness. The varying the thickness of the seed layer in a wide range leads to the fact that

amorphization and, respectively, recrystallization occur only in the upper part of the epitaxial film. Herewith remains a layer adjacent to the silicon–sapphire interface, which is practically not subjected to the ion impact, the layer, which poor structural quality and, respectively, the arising leakage currents significantly reduce the radiation impact. At the same time, the structural quality improving in the upper part of epitaxial silicon layer allows to improve the electrical characteristics of chips. Thus, such structure of SOS, with a perfect interface layer and relatively defective layer, which is adjacent to the sapphire substrate, undoubtedly is of interest.

In presented work is proposed the original method and investigated the presence of defects by the depth of the silicon layer obtaining in SPR from the silicon–sapphire interface in case of different thicknesses of the "seed" layer.

2. Experimental technique

The amorphization of SOS-plates having 100 mm diameter was carried out on the IBS-100 (Ion-Beam Setup). The implantation energy of silicon ions is varied from 90 keV to 150 keV, while keeping the implantation dose ~$7{,}5\cdot10^{14}$ per sm^2. Other parameters of implantation and recrystallization are mentioned above. The presence of defects of recrystallized silicon layer was measured by the method of two-crystal Bragg diffraction. The wavelength of X-ray was 1,54Å. Since at this wavelength the value of extinction is much greater than the thickness of the silicon layer, the width of the X-ray rocking curve is an integral feature of the entire layer.

To study the structure of the Si-film by the depth the authors proposed a method of stepwise amorphization from the surface with subsequent X-ray measurements. Since the amorphous material does not affect the X-ray diffraction measurements (it is simply not visible), then in case of sequential amorphization from the surface of investigated sample the width of the X-ray rocking curve (FWHM) characterizes the quality of the remaining silicon film, and the integrated intensity (area under the rocking curve) determines the thickness of the crystalline layer of recrystallized SOS-structures. Amorphization of the recrystallized SOS-structures was also carried out by the implantation of silicon ions. The initial energy of implantation was 50 keV. Implantation dose was $7{,}5\cdot10^{14}$ per sm^2. On the surface of recrystallized film was formed an amorphous layer having thickness ~1000Å. To increase the sharpness of the interface between crystal and amorphous material and to reduce the impact of the transition layer on the structural parameters the sample was subjected to short-term low-temperature annealing (450^0C for 1 min.). X-ray measurements determined the quality and thickness of the remaining single-crystalline silicon layer. At the next stage the implantation energy is increased, and all operations are repeated.

3. The experimental results

Figure 1 shows the integral characteristics of the silicon layer quality of SOS-structures after carrying the SPR-process. The first stage of process (amorphization of Si-layer) was held by different energies (90-150 keV). The amorphization dose is the same in all cases (7,5·1014 per см2) and for energy of 150 keV corresponds to the minimal presence of defects of silicon layer of recrystallized SOS-structure and, consequently, to the practically complete amorphization of the epitaxial layer at the first stage of SPR. The amorphization energy reducing leads to a simultaneous decrease in the thickness of amorphizated layer and to shifting it toward the surface. Herewith more and more part of the silicon film, which adjacent to the sapphire substrate, is not exposed to the influence of ion beam. This figure shows that the decrease in amorphization energy is accompanied by a simultaneous increase in the values of FWHM. However, even for the amorphization energy of 90 keV there is a significant improvement of the integral values of FWHM (up to 800"), indicating the possible improvements of structure also in the initially non-amorphizated areas of silicon film during SPR.

Figure 2 shows the study of silicon film structure depending to the depth by means of the methodic described above. The investigations are carried out for three samples: the epitaxial Si-

layer and two recrystallized samples with energies of amorphization 90 and 150 keV at the first phase of SPR. In the latter case, there is amorphizated almost the entire epitaxial layer, and at energy of 90 keV – about 2000 Å.

As was to be expected, the studies have shown an extremely poor quality of the epitaxial film in comparison with the recrystallized samples. FWHM of 1000Å Si-layer, which adjacent to the sapphire substrate, is 2500". This confirms the impossibility of using epitaxial films with a thickness less than 3000Å in microelectronics. Huge changes in the structure of a recrystallized sample 1 (energy of amorphization is 150 keV) against this background demonstrate all the advantages of SPR-process. There is formed slightly imperfect (600-800"), on the whole depth practically silicon layer. As already mentioned above, the huge advantages of using such a structure (followed by thinning, decreasing in the size of microcircuits, increasing of the packing density and speed, etc.) encounter a serious obstacle in the form of low radiation resistance.

In the recrystallized sample 2, the structural changes occur not only initially in the amorphizated layer (~2000Å from the surface of the sample), but also in the layer adjacent to the sapphire substrate (~1000Å), don't being subjected the exposure of ions. The redistribution of tensions in the film, the diffusion and annihilation processes occurring during recrystallization, should lead to some improvement in the layer structure, although initially it had not been subjected to amorphization. Sample 2 has the silicon layer with very non-uniform quality: a high-quality surface and highly defective one adjacent to the sapphire substrate. If with the first layer are associated the significant improvements of electrical characteristics of the chips, the leakage currents associated with the second layer, a few worsen them, however, increasing the radiation resistance. Such a compromise structure allows keeping the radiation resistance by a significant improvement of many parameters of electrical chips.

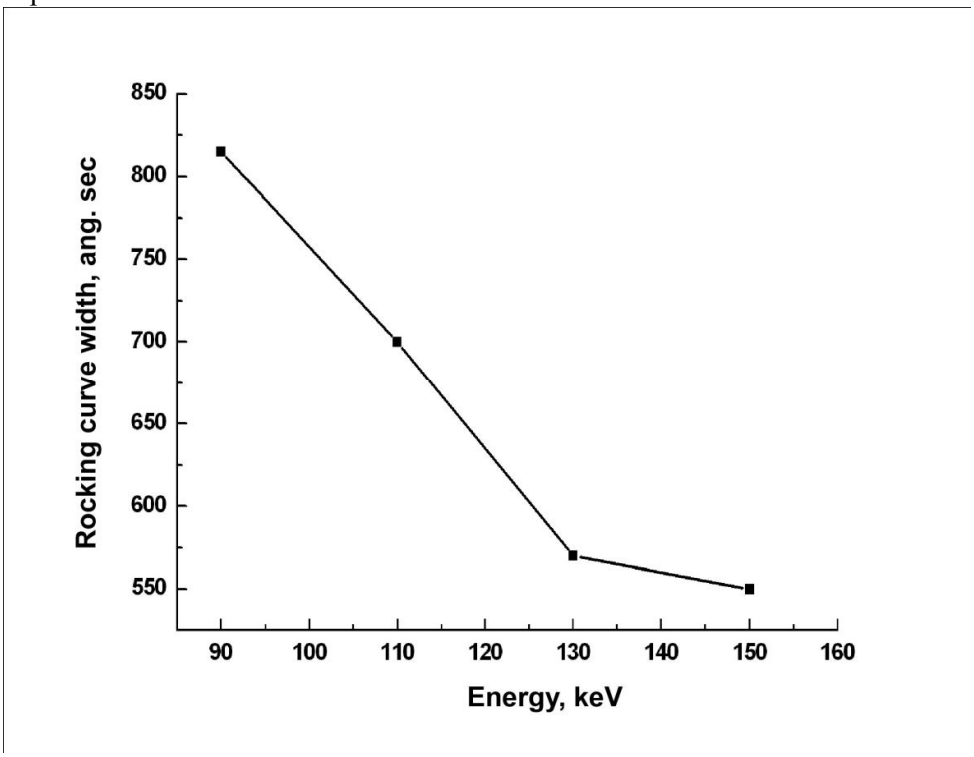

Fig. 1. The dependence of the rocking curve width of X-ray diffraction (FWHM) of the SOS-structure silicon layer of recrystallized samples on the initial energy of amorphization.

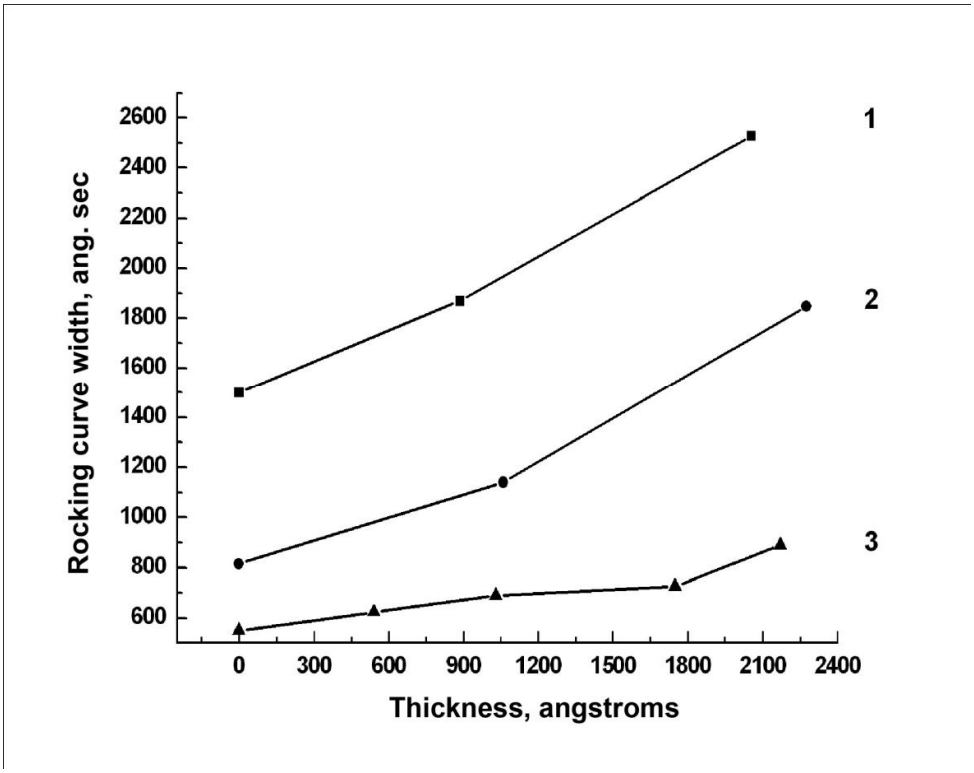

Fig. 2. The presence of defects of recrystallized silicon film of SOS-structure by the thickness in case of various initial amorphization energies:
1 – 0 keV (initial epitaxial layer), 2 – 90 keV, 3 – 150 keV.
The thickness of the silicon layer is about 3000 angstroms.
Zero thickness corresponds to the Si-film surface.

4. Conclusions

The results presented here testify that the optimization of parameters of SPS-process allows obtaining SOS-structures with significantly better electrophysical characteristics, while maintaining their radiation resistance.

References

1. P.A. Alexandrov, K.D. Demakov, S.G. Shemardov, Yu.Yu. Kuznetsov. *Nano- and Microsystem Technology*, **3**, 54 (2008).
2. P.A. Alexandrov, K.D. Demakov, S.G. Shemardov, Yu.Yu. Kuznetsov. *PTS*[1], **43** (5), 627 (2009).
3. M.L. Burgener, R.E. Reedy. *United States Patent*, No. 5416043, (1995).
4. PA Alexandrov, KD Demakov, SG Shemardov, Y. Kuznetsov. *PTS*, *44* (10), 1433 (2010).
5. VM Vorotyntsev, EL Shobolov, VA Gerasimov. *PTS*, **45** (12), 1662 (2011).
6. T.Liu et al. 9th European Conference Radiation and its Effects on *Components and Systems*. (Deauville, France) [10-14 September, (2007)].
7. PA Alexandrov, KD Demakov, SG Shemardov, Y. Kuznetsov. *Unpublished materials*.

P.A.Aleksandrov, K.D.Demakov, S.G.Shemardov, Yu.Yu.Kuznetsov. *Patent Russia*, № 2427941, (2011).

[1] Physics and Technology of Semiconductors.

Lienard-Wiechert Potentials For an Arbitrary Trajectory of the Charge

B.M.Bolotvskii

A moving point charge is convenient to describe with the aid of potentials of Liénard – Wiechert. Let's assume that the motion of a point charged particle has the form $\boldsymbol{r} = \boldsymbol{r}(\boldsymbol{t})$. In all textbooks on electrodynamics is expression for the scalar and vector potentials for Lienard-Wiechert specified. Law of motion. The scalar potential has the form:

$$\varphi(x_0, y_0, z_0) = \frac{q}{\left(R - \frac{vR}{c}\right)_{t=t'}} \tag{1}$$

Here $(x_0, y_0, z_0) = r_0$ - coordinates of the observation point, t - time, q – value charge, v (t) - its speed, $R = 0_r - r(t)$ - the distance from the charge to the observation point. With all quantities in the right side are not taken at the time of observation t′, and at an earlier time t0 Which is determined from the delay

$$t - t' = \frac{|r_0 - r(t')|}{c}, \tag{2}$$

The vector potential in Lorentz gauge differs from the scalar multiplier $v(t'/c)$ on the right side of (1):

$$A(x_0, y_0, z_0, t) = \frac{qv(t')}{c\left(R - \frac{vR}{c}\right)_{t=t'}}, \tag{3}$$

In the derivation of (1) and (3) for the Liénard – Wiechert potentials implicitly assumed that the delay equation (2) has a unique root t 0. Indeed, if the rate od charge does not exceed the phase velocity of light, the retardation equation has a single root. However, there are real cases, where the equation delay has two or more roots. For example when the speed is equal uniformly moving charge exceeds the speed of light (in the case of the Vavilov – Cherenkov radiation), the equation has two roots of delay. Which one should substitute the right side of (1) and (3)? In any case, based on expressions (1) and (3) we do not get the correct expressions for the fields of superluminal charge. It is obvious that one should determine the kind of Liénard – Wiechert potentials for the case when the equation of lat has several roots.

Let's suppose that the equation of the lag (2) formula $t'_1, t'_2, t'_3, \ldots, t'_n$. Then from Maxwell's equations yield the following expressions for the Liénard – Wiechert potentials:

$$\varphi(x_0, y_0, z_0, t) = \sum_i \frac{q}{\left(R - \frac{vR}{c}\right)_{t'_i}}, \tag{4}$$

$$A(x_0, y_0, z_0, t) = \sum_i \frac{q}{c\left(R - \frac{vR}{c}\right)_{t'_i}}, \tag{5}$$

The summation is conducted over all the roots of retardation. The term of the sum number i has the argument formula $t' = t'_i$.

Formation and Choice of Variants of Intellectual Systems of Automatic Identification on the Basis of Morphological, Hierarchical and Indistinct Models

A.R. Mkrtchyan[1], A.H. Mkrtchyan[1], A.S. Baghdasaryan[2], V.V. Butenko[2], S.A. Baghdasaryan[2], A.G. Kashchenko[2], G.A. Kashchenko[2], R.V.Semenov[2]

1) Institute of Applied Problems of Physics of NAS RA, Hr. Nersisyan str. 25, Yerevan, 0014, Armenia, 2) FSUP SRIR, Concern «Constellation» Russia, Moscow, Voronezh, bas@niir.ru

In the course of the development of system of automatic identification constantly become complicated. Along with it market strategy of development of a society in the conditions of a competition imposes rigid restrictions on quality and designing terms. Therefore there is a contradiction between constantly increasing complexity of considered systems and requirements of improvement of quality of designing and reduction of its terms. In such conditions traditional methods of designing often appear inefficient. One of approaches to elimination of this contradiction is working out of methodology of designing of systems of radio-frequency identification (RFID) on the basis of application of methods of an artificial intellect, in particular, by construction of expert systems.

The report purpose is working out of a technique of the decision of problems of formation and a choice of variants of difficult RFID systems from a set alternative interchangeable, but various components under the characteristics.

Designing of any systems, in particular RFID systems, includes three basic stages: formation of set of possible variants; an estimation of set of the generated variants and its truncation at the expense of removal of the worst variants; decision-making on a choice from set of not worst variants (Pareto set) best variant.

One of the basic stages in the course of the decision of a considered problem is formation of set of possible variants. The approach which it is more accurate in comparison with a traditional method of the morphological analysis Is offered defines procedure of an exception of the worst variants. Besides, at a stage of formation of set of possible variants the variants constructed of incompatible components are rejected. The remained variants are estimated on set of quantitative, qualitative and interval criteria.

For the decision of a problem of a choice of the best variant the approach based on use of the modified method of the analysis of hierarchies (MAH), allowing to define optimum layout structure of RFID system is offered. Initial data for modified MAH, a variant of system applied at configuration, are: technical requirements to developed system; library of alternative variants interchangeable a component from which it is supposed to carry out system construction as a whole. Modified MAH and a method of reception of a vector of priorities differs from classical MAH in the way of formation of indistinct matrixes of paired comparisons. Offered in the report modified MAH on the basis of indistinct expert estimations represents synthesis classical MAH and methods of indistinct sets. It is caused by that subjective and qualitative knowledge of expert can be formalized with use of the models constructed on the basis of indistinct sets.

The technique of a choice of a variant of system generally includes following basic steps:

1. In each class of components by means of modified MAH components of one class in decreasing order of preferences are ranged.
2. In componential structure of system expert includes not less certain quantity of the objects having the maximum rating in the class. And this quantity can change depending on definitive results of a choice.

3. By means of a compatibility matrix compatibility of various variants of synthesized system is checked.

4. In each class of components the set of the worst components is cut.

5. By means of morphological model the set of possible variants of RFID systems is formed of set of compatible not worst components.

6. By means of modified MAH the variants of RFID systems received on a step 5, are ranged again on set of private criteria.

The considered approaches are used at the decision of problems of formation and a choice of an optimum variant of construction of intellectual system of automatic identification for management of transportation of cargoes on railway transportation.

———

Work is executed at support of the grant of the Russian Fund of basic researches: 11-07-13141-ofi -m-2011-RZHD.

Pre-Conceptual Design of the New Accelerator Complex at A.I. Alikhanian National Science Laboratory (ANSL)

R H Avakian

Alikhanyan National Research Laboratory, Yerevan, Republic of Armenia

A new accelerator complex is proposed to build at ANSL intended both for cancer particle therapy and for scientific investigations in nuclear physics. It will be based on hi-tech accelerator and irradiation technology developments, realized and tested at the accelerator complex of Gesellschaft für Schwerionenforschung (GSI) and Heidelberg Ion Therapy Center (HIT). The new complex will be capable of providing a variety of clinically interesting ions for treating patients as well as clinical studies.

The guiding line of disposition of HIT accelerator complex in ANSL is its cost-efficiency based on the buildings and other ANSL existing capabilities, including:

- Buildings which can be used for both for bulky equipment installation and for clinic purposes.
- Powerful power supply and power communications more than enough for HIT facility supply.
- Radiation shielding facility.
- Bulky equipment and instrumentation for installation, maintenance and repair purposes.
- Cryogenic facility.
- The presence of specialists with corresponding education and experience.

The new complex will also serve as a base for development of future experimental program to be carried out at ANSL in the field of nuclear physics using the technical capabilities of this accelerator complex.

Introduction

Radiotherapy using proton beams (proton therapy) is rapidly taking an important role among the techniques used in cancer therapy. Up to now 73.800 patients had been treated for cancer by proton beams in the 37 proton therapy facilities operating in the world. While comparing to the now classical ***I***ntensity-***M***odulated ***R***adiation ***T***herapy (IMRT), and for a similar dose to the tumor, proton therapy provides a lower integral dose to the healthy organs surrounding the tumor. It is generally accepted that any reduction of the dose to healthy organs reduces the probability of radiation induced complications and of secondary malignancies.

From clinical studies in the USA and Japan it was estimated that about 25.000 to 30.000 non-curable patients – especially those with tumors in the brain and base of the skull region, sarcoma and prostate carcinoma – would be cured in case of application of heavy charged particles, i.e. protons and ions, in radiation therapy.

The main goal of radiation therapy is to deliver an effective dose as large as possible to a given target volume, while the surrounding healthy tissue as well as the skin in the entrance and exit channels should be spared as much as possible. Conventional irradiation by photons is limited by its unfavorable depth dose profile.

When an energetic heavy charged particle penetrates matter it is slowed down mainly by numerous ionizing collisions with the atomic electrons of the medium. The probability for such collisions increases with decreasing particle energy. Therefore ion beams loose a large fraction of their initial kinetic energy in a relatively narrow region at the end of their path - the so-called Bragg

peak. On the other hand, the dose deposition in the entrance channel (plateau) is relatively low. This particular behavior creates the inverse dose profile which is unique for ion beams.

The energy deposition is quantitatively characterized by the ***L***inear ***E***nergy ***T***ransfer (LET) defined as the energy dE deposited to an absorber per unit path length of the particle trajectory dx**.** This quantity is proportional to the square of the particle atomic number *Z* and inversely proportional to the square of the particle velocity. The LET is one of the important factors which determine the biological effectiveness of a given radiation.

The position of the Bragg peak in depth can be adjusted by the energy of the incoming ion; hence the maximum of the energy deposition can be located precisely to the tumor. In order to cover an extended target volume, several Bragg peaks with different initial energies have to be overlaid. This leads to a reduced peak to plateau ratio, but the resulting depth dose profile is still by far better than that for protons.

Besides proton beam therapy, which is progressively becoming an accepted part of radiation therapy, interest is growing for another form of radiotherapy using ions heavier than protons.

For ions heavier than protons and helium, the favorable physical selectivity is additionally enhanced by a higher biological effectiveness which is expected to be an important advantage for the treatment of radiation resistant tumors. By proper selection of the ion species (e.g. carbon), the biological effectiveness can be controlled in such a way, that it remains low in the plateau region of the Bragg curve and is elevated in the Bragg-peak region. This enhances the peak-to-plateau ratio in terms of the biological dose and enables to deliver a higher biological dose to the tumor while lowering the dose delivered to surrounding healthy tissue.

Carbon ions have, even to a higher degree, the ballistic selectivity of protons. In addition, carbon ions stopping in the body exhibit a very high LET. From this high LET results a very high Relative Biological Efficiency (RBE). This high RBE allows carbon ions to treat efficiently tumors who are radio-resistant and which are difficult to treat with photons or protons. In Fig. 1 the comparison of the depth dose profiles of proton, electron and carbon-ion beams is presented.

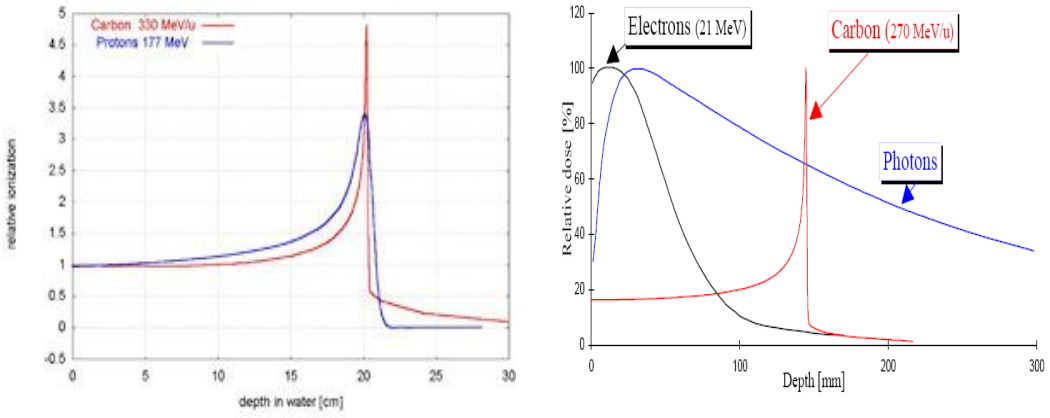

Fig. 1: Comparison of the depth dose profiles of proton and carbon (left), and electron, photon and carbon-ion (right) beams. Photon energy ??. The inverse dose profile (Bragg curve) is typical for ion beams.

The well focused pencil-like charged particle beams with an adjustable spot size can be formed and scanned over the treatment field following precisely the tumor contours. By variation of the beam intensity and scanning speed together with a variation of the beam energy, any desired dose distribution within the target volume can be generated. The dynamic scanning is therefore an ideal technique for 3D-conformal tumor irradiation.

The use of ion beams in radiation therapy offers the unique possibility of PET monitoring (PET = Positron Emission Tomography) of the irradiation procedure. When the beam penetrates through the tissue, positron emitting isotopes are generated by nuclear fragmentation of the primary ions. Some of these positron emitting fragments which differ from the primary particles just by the loss of one or two neutrons (e.g. ^{11}C, ^{10}C in the case of carbon beam) stop nearly in the same region as the primary particles. The stopping point of a positron emitter can be identified with the aid of positron emission tomography, which can be applied even during the irradiation. In this way, the dose localization can be monitored in-situ and the correctness of the irradiation procedure can be verified.

A new ANSL Accelerator Complex (ANSLAC) is proposed to build based on previously developed and operated accelerator complex at HIT. The layout of accelerator complex at HIT is sketched in Fig. 2. This facility consists of two ion sources, low energy transport lines, Linear Accelerator (LINAC), injection line to synchrotron, synchrotron, high energy extraction beam lines from synchrotron, two horizontal treatment beam lines and rotating treatment beam line. The main parameters of accelerator complex at HIT are collected in Table 1.

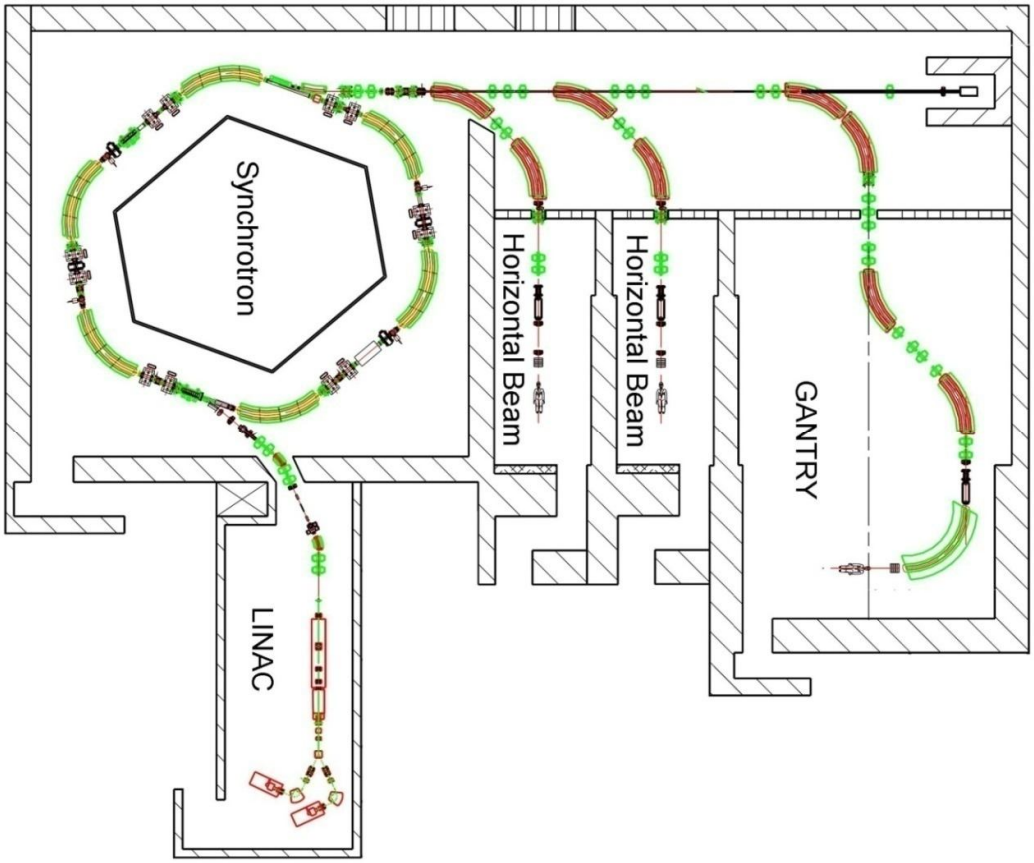

Fig. 2: HIT facility.

Table 1. Overview of HIT basic design and essentials specifications

Particle species	protons, He, C, O
Type of accelerator	Synchrotron (common for all particle species)
Beam energy	50 - 430 MeV/u
Beam intensity [particles per synchrotron cycle]	protons: $4 \cdot 10^{10}$ He: $1 \cdot 10^{10}$ C: $1 \cdot 10^{9}$ O: $5 \cdot 10^{8}$
Treatment rooms	1 fixed-horizontal-beam treatment room 2 gantry rooms
Beam delivery technique	Energy and intensity variation from the accelerator plus magnetic raster scanning
Gantry type	Barrel-like 360° rotating gantry for 1.0 - 6.6 Tm beams, magnetic scanning upstream the bend-down dipole, isocentric geometry, normal conducting magnets
Treatment field	20 x 20 cm^2
PET	In-situ verification of the irradiation procedure
Number of patients per year	≈ 1,000
Building area	≈ 70 x 60 m^2
Design and construction period	≈ 5 years

1. ANSLAC as Ion Therapy Facility

The guiding line of disposition of Heidelberg accelerator complex in ANSL is based mainly on the available buildings and other capabilities existing at ANSL. Particularly, the existing infrastructure of ANSL, the knowledge and experience in construction and exploitation of the existing electron synchrotron ARUS including vacuum and beam-line components, experience of developing and constructions of particles detectors and more complex devises, preparation of the personal for radiobiological control, safety work with radiation materials will be very helpful.The layout of proposed ANSLAC is sketched in Fig. 3. The two ion sources and heavy ion LINAC will be disposed on the underground floor inside the four-storey building of the Eastern Experimental Hall (EEH) at ANSL which has an area of 18 m x 46 m. Ion beam from LINAC will be transferred into the ion synchrotron by means of injection line. The synchrotron will be installed in the EEH (42 m x 49 m) and will occupy an area of 30 m x 30 m, which is equipped with two 50 tons cranes and which has special floor for heavy equipment installation and under-floor technical tunnels with the cross section of 2x2 m^2 for electrical communications. The walls for the synchrotron as well as for LINAC and other radioactive equipment will be constructed using existing more than thousand radiation safety concrete blocks in good condition.

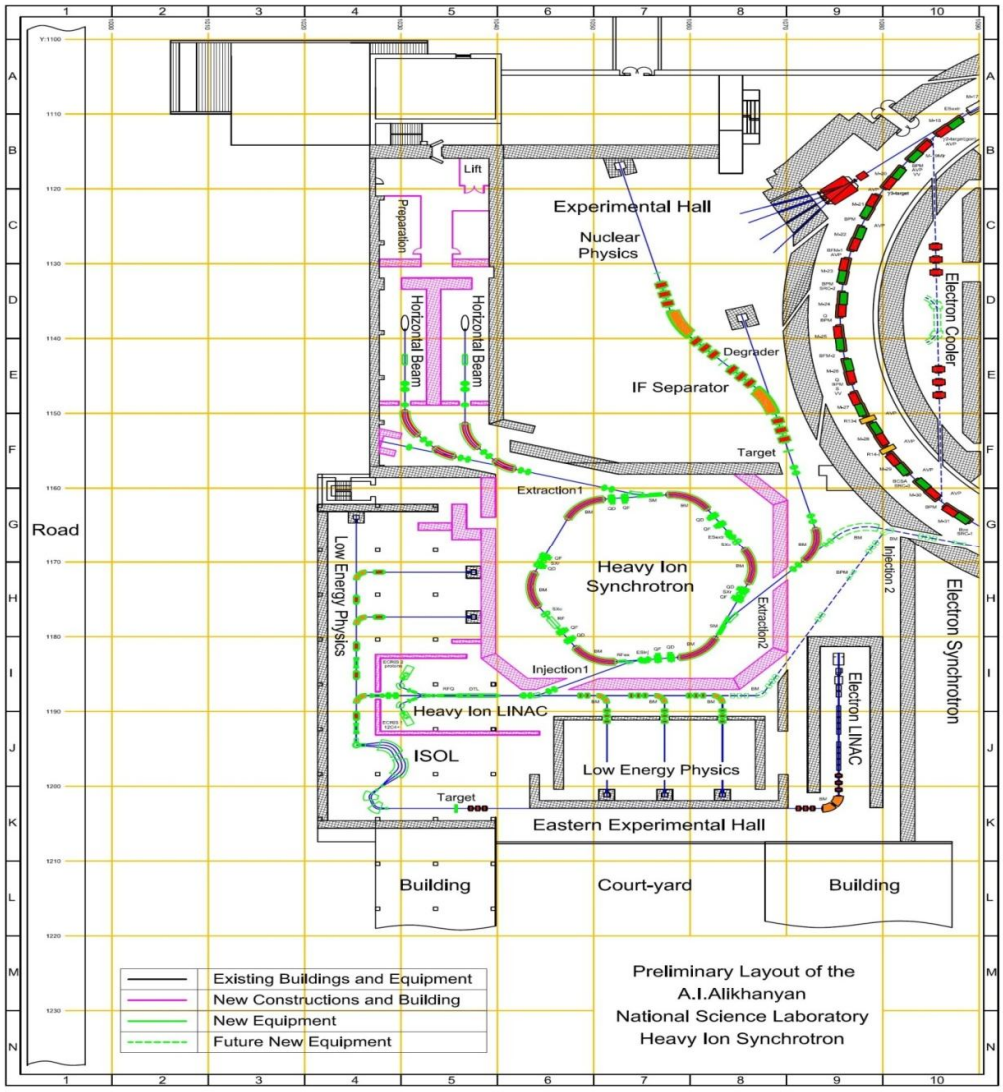

Fig. 3. ANSL facility

The extracted beam from synchrotron enters the treatment rooms by means of high energy extraction beam lines. Two rooms displaced in the existing small experimental hall are available for horizontal radiation treatment. The ion beam propagation plane level is the underground. The existing second and third floors of the small experimental hall (1000 m^2) will be modified and used as a patient flow area with a reception, examination offices and preparation rooms.

1.1. Capital Investment

A preliminary estimation of the required investment cost for ANSLAC ion therapy facility for non-profit organization (Transportation and VAT not included) in comparison with HIT facility are summarized in Table 2.

Table 2. Summary of the investment cost.

Main Subsystems	**HIT cost in 1000 Euros**	**ANSLAC cost in 1000 Euros**
Accelerator Complex	31 200	31 200
High Energy Beam Line	3 900	3 900
Horizontal Beam Line Vertical Beam Line	2 400	2 x 2 400
2 x Gantry	15 700	Will be used more simple device the cost of which will be close to the cost of horizontal beam line ~2 500
Medical Equipment	12 000	9 600
Laboratory Equipment and Furniture	3 300	2 500
Building	31 500	2 000
Preliminary Total Investment Cost	**100 000**	**56 500**

2. ANSLAC for Basic Nuclear Science

As was mentioned before**,** complementary to the carbon therapy program nuclear and applied physics research programs also will be implemented. The stable beams of protons, helium, carbon and oxygen nuclei with energies from 50 to 430 MeV/u from ANSLAC synchrotron will be transported to the main experimental hall on different experimental targets.

These experimental studies require the ***I***n-flight ***F***ragmentation technology (IF), the exact momentum and angular resolution of exotic nuclei and their mass identification. The construction of a high resolution magnetic spectrometer, equipped by precise timing detectors will be needed for investigation **of** the scattering of exotic nuclei on the stable nuclei.

The possibility of the production of exotic nuclei ^{8}He, ^{11}Li or ^{14}Be by the ion beams of ANSLAC will be investigated. Also, a program for nuclear physics experiments using the proton, helium, carbon or oxygen beams with energy 7 MeV/u straight directed from ANSLAC LINAC to the experimental equipments installed in the other experimental hall will be developed. The Fig. 3 shows the sketch of future ANSL facility.

Moreover, it is proposed to equip the ANSLAC LINAC by additional injection line allowing to inject and accelerate the stable and radioactive beams using Isotope Separation On-Line (ISOL)

technique and to extract them to experimental hall, where the target and detectors are located. The range of the atomic masses, energies and intensities should be investigated in details, in order to reach the atomic masses around A = 130 with total kinetic energy in order **of** 7 MeV/u with acceptable intensities.

The review of ANSLAC LINAC with its ion source based on Electron Cyclotron Resonance (ECR), allowing analyzing its applicability for the ion acceleration in the mass range above ^{16}O with acceptable intensity should be done.

3. The program of the radioactive beam investigations

The installation of the HIT facility in the premises of ANSL creates very attractive possibilities to make scientific and applied researches using the beams of the HIT synchrotron and of the ion LINAC as well as to increase the possibility of existing accelerator complex. The existing ANSL electron LINAC provides beam with energy range 20-75 MeV and intensity limited by 10 □A, so the beam power on the target is approximately 0.5 kW.

The possibility to have radioactive ion beams producted by electron driver first predicted by Yu. Ogahessian. ISOL technique using upgraded existing linear electron accelerator complementary with additional target/ion source and mass separator will be considered. The ***E***lectron ***D***river ***U***pgrade (EDU) will be coupled with the ISOL infrastructure like those elaborated at HRIBF and ISAC facilities.

The construction of ISOL facility will explore the fission of ^{238}U. Electron induced fission of the ^{238}U is based on the excitation of giant dipole resonance in the nuclei with characteristic energy range appreciatively 15-20 MeV and is fully competitive with hadrons beams fission capability per particle, having the energy range 50-200 MeV, allowing to have appreciatively $2x10^{11}$ fission/s.

Separation of ions by mass will be performed by mass-separator, which includes the focusing lenses and bending magnet, preceded by an ionization chamber.

The acceleration of radioactive nuclei will be realized in the LINAC of ANSLAC and further the ion beam will be transferred to the various targets for physical experiments.

The EDU will allow to produce the world competitive neutron-rich beams of fission fragments for research in nuclear structure, nuclear astrophysics, and applications. The upgrade of linear electron accelerator up to the parameters 30 kW and 50 MeV will provide 10^{13} fission/s on the uranium target. The yields of exotic nuclei for uranium target and for 10^{13} fission/s are presented below:

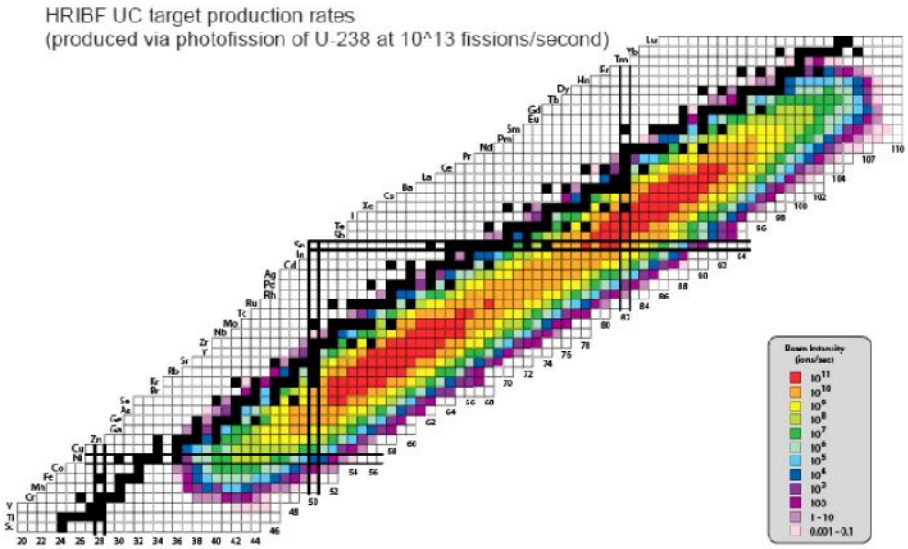

The possibility to use the electron synchrotron ARUS as storage ring for exotic nuclei (in far future program) will be investigated. This aspect will require maintenance and serving of all existing magnets and other components of the electron synchrotron in a good condition for upcoming several years.

3.1. The beam lines and corresponding physics directions

Three types of the beam lines will be available for basic science and applied research:

a) With stable ion beams of mass range A□16 and energy up to 400 MeV/u, the following physical investigations can be carried out:

- the properties of proton or neutron enriched nuclei;
- the properties of mirror nuclei;
- the knock-out and evaporation reactions;
- an isotope effect and isoscaling;
- the sub-threshold and near-threshold productions of mesons;
- the reactions of astrophysical interest.

b) The medium energy ion beams up to 7 MeV/u, stable or exotic beam supplied by ISOL extracted from the ion LINAC:

- The study of the nucleosynthesis reactions with unstable ion beams;
- The precise mass measurements for heavy and super-heavy nuclei using new experimental; timing technique under development in ANSL;
- α-, β- and γ-spectroscopy for structure study of neutron rich exotic nuclei in vicinity of single and double magic nuclei. Study of shell filling rules change toward the drip line, the modifications of pairing in the neutron rich nuclei, which produce deviations from systematic, shape coexistence phenomena and the associated shape-transitional behavior, search of prompt fission and the correlated neutron pair emission;
- The study of the mechanisms of fusion-fission of heavy and super heavy nuclei;
- The research of the structure of light exotic nuclei;
- The study, through Coulomb excitation, of the collective motion in complex neutron-rich nuclei. The key question is the influence of the neutron excess on collective resonance excitation modes, and on static deformations. Appearance of new collective modes, in particular of low-energy isovector vibration modes, that could increase the neutron capture cross sections, important for astrophysical r-processes.

The registration system includes precise timing detectors on base of *M*icro *C*hannels *P*lates (MCP) or equivalent other timing detectors, arrays of silicone strip detectors for particle identification and angular measurements as well as the γ- and neutron detection arrays working in coincidence.

c) The low energy, 40-60 keV radioactive beams, supplied by ISOL facility.

Study of the exotic neutron-rich isotopes (excitation energies, spins, magnetic moments, decay modes) of the daughter nucleus, formed after decay of parents, within energy range provided by □-decay. These beams may be also used for production of rare isotopes and this direction will be strongly enhanced after electron LINAC upgrade to the maximal current of approximately 600 □A.

4. Investigation of radiation damage effect of electronic components using in space

There are over 936 operating satellites in space, worth an estimated $200 billion to replace. They account for nearly $225 billion in revenue for the international telecommunication industry every year. These satellites are affected by events like cosmic rays, solar flares, energetic electrons.

Airline pilots and flight crews, as well as frequent fliers, receive increased doses of radiation from solar flares**.** Radiation effects can not only cause degradation, but can also cause failure of the electronic and electrical systems in space vehicles or satellites.

Satellites and spacecraft have complex microelectronic devices on board. If they fail, the consequences will be catastrophic. Cosmic radiation in space can damage sensitive electronics. Researchers have been looking into the influence of radiation on electronics.

The effects of ionizing particles on sensitive microelectronics is an important component of the design of systems as diverse as satellites and space probes, detectors for high energy physics experiments and even internet server farms.

Accelerators designed for nuclear physics are ideal for radiation effects studies. High energy accelerators are necessary to obtain enough range to penetrate a microchip or detector.

Synchrotron facilities are available for ***R***adiation ***E***ffects ***T***esting (RET) with wide range of ions. The techniques for doing these measurements and the advantages of using a synchrotron are already well known.

The research on the ion beams to test the suitability of various microchips for use in space should be carried out. Furthermore, fundamental research is being conducted which will help to develop radiation-resistant, lighter and more compact electronics to save room and weight. In the future, space systems will be able to dispense with the hitherto necessary shielding and backup electronics that are built-in for certain devices.

The "hardness" of an object to radiation is a major consideration in the design of satellites and space missions. The aerospace industry, NASA and the Department of Defense perform radiation effects studies first using sources (γ, α) and accelerators (e, n, p, heavy ions).

Storage chips for the European Space Agency (ESA), microprocessors (IBM) and other electronic components of satellite missions and astrophysical experiments (e.g. the AMS-Experiment or the Italian ALTEA-project) on board of the International Space Station (ISS) were successfully tested at the irradiation facility Cave A at GSI.

ANSLAC will be involved in this business having the ion beams with parameters presented in the Table 1.

The possibility to accelerate heavier ions in ANSLAC synchrotron for investigation of radiation damage effect of electronic components will also be considered.

1. ANSLAC facility realization timescale and priority

ANSLAC facility proposed to be realized with following main stages:

1. Preparation of existing infrastructures of ANSL for installation of the HIT type facility **1 year**
2. Installation of the HIT type accelerator complex for cancer therapy, including: **5 years**
   - ANSLAC ion sources and ion LINAC;
   - ANSLAC ion synchrotron with injection and extraction beam lines;
   - The horizontal and vertical beam lines to the treatment rooms.
3. R&D and construction of nuclear physics facility in the experimental hall including the stand for radioactive hardness control in the experimental hall **4 years**
4. R&D of the exotic nuclei beam facility, including: **3 years**
   - Upgrade of existing electron LINAC up to 30 kW and 50 MeV of electron energy.

- Electron beam line to the target/ion source system.
- Mass separator with ion injection beam line to ANSLAC LINAC with acceleration up to 7 MeV/u and higher energy.
- Investigation of the possibility for production and transportation of low energy exotic nuclei beams from ANSLAC LINAC to the different low energy nuclear physics experimental facilities.

5. Investigation of the possibility for acceleration of high mass stable ion beams in ANSLAC synchrotron **2 years**

Section I

Time – spatial control of characteristics of the channelled particles radiation with and without acoustic fields.

Investigation of the Channeling Radiation of 20 MeV Electrons in Quartz Single Crystal under the Hypersonic Fields

A.R. Mkrtchyan, A.H. Mkrtchyan, L.Sh. Grigoryan, E.M. Harutyunyan, V.R. Khocharyan, H.R. Muradyan

Institute of Applied Problems of Physics of NAS RA, Hr. Nersisyan str. 25, Yerevan, 0014, Armenia, malpic@sci.am

Experimental investigations of the channeling radiation (CR) were conducted on the 20 MeV electron beam of the LEA-50 linear electron accelerator of the Yerevan Physics Institute. The experimental setup based on new developed electron beam track was designed to detect channeling radiation in the forward direction. New remote controlled high precision goniometric device with 5 degrees of freedom, new high accuracy hypersonic generator with 100 W power output, and new hypersonic resonators where put signed quartz crystal for generator hyper frequency acoustic wave were developed. The sample of quartz single crystal was taken X-cut for the $(10\bar{1}1)$ plate and thickness of 1 mm. For the first time in air and vacuum channeling radiation of 20 MeV electrons from the quartz crystals detected. Rather complicated energy distributions of transition radiation (~1,3-2,5), PXR (5 KeV) range under the influence of acoustic waves, and axial channeling radiation in energy range from 1 KeV up to 30 KeV, and channeling radiation were obtained.

At an angle of channeling 5.75° increase the amplitude of the electric field intensity increasing dramatically and will not have the opportunity to increase the amplitude of the acoustic field. It was not observed and the further increase and process became nonlinear.

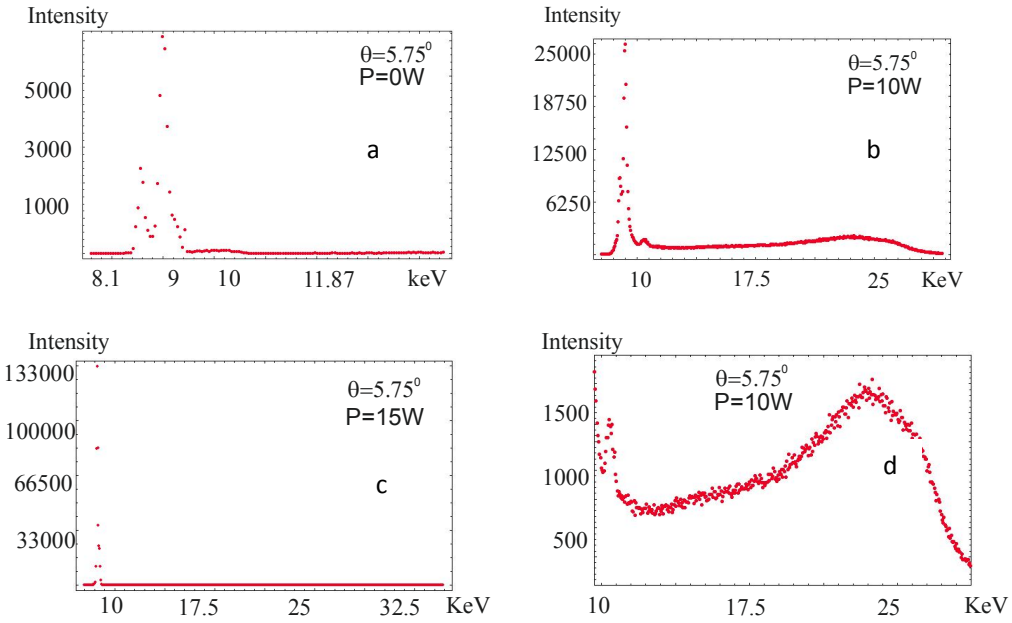

Channeling radiation of single crystal plate $(10\bar{1}1)$ X-cut quartz. Planar channeling degree is 5.75^0 horizontal and 12.5^0 vertical.

This is explained by the fact that the direction of acoustic waves inducted with electromagnetic waves coincides with lightest areas of the excitation of the crystal of quartz and therefore it becomes possible to obtain large amplitude waves, without prejudicing the edgy of acoustic waves.

On the emission spectrum are also observed two bands of radiation 11KeV and 17.5KeV. Theoretical analysis [1] finding the location of these bands in the energy spectrum corresponds to the coherent bremsstrahlung.

The influence of hypersonic vibrations was detected. Under the external field causes smart shifts, as well as the intensity and shapes variations of the CR for duplets 4,5 and 5,5 KeV yields, due to the hypersonic amplitude and frequency changes conducting non-linear effects were obtained. The increase of the hypersonic amplitude lead at first to the decrease, then to increase and finally to saturation of CR intensity for both lines.

Peaks shift of the channeling radiation of different transaction due to the frequency of ultrasound vibrations has been obtained.

References

1. A.R. Mkrtchyan, A.A. Saharian, V.V. Parazian, Modern Phys. Letters B, v.23, N 20 and 21 (2009) p. 2573-2584.

Planar positron channeling radiation generated in an acoustic superlattice

B. Azadegan[1], L. Sh. Grigoryan[2], W. Wagner[3],

1) Sabzevar Tarbiat Moallem University, POB 397, Sabzevar, Khorasan, Iran
2) Institute of Applied Problems of Physics of NAS RA, Hr. Nersisyan str. 25, Yerevan, 0014, Armenia
3) Helmholz-Zentrum Dresden-Rossendorf, POB 510119, 01314 Dresden, Germany,
w.wagner@hzdr.de

Planar positron channeling in an acoustic superlattice and stimulation of the emission of channeling radiation at resonance of the particle motion with the acoustic field excited in a $PbTiO_3$ single crystal is considered in the framework of classical mechanics and electrodynamics. Based on computed particle trajectories, spectral-angular distributions of channeling radiation influenced by resonant ultrasound have been simulated. The presented method explains the influence of ultrasonic waves on the intensity of channeling radiation in a rather simple and descriptive manner.

1. Introduction

Channeling radiation (CR), which has been explained as a self-contained source of X- and γ-rays in 1976 [1], is a well investigated phenomenon today (see, e.g., [2,3,4, 5,6,7]). At not too high energies (up to several tens of MeV) of the channeled light charged particles, CR emission has to be considered as a quantum process, whereas at highly relativistic energies classical mechanics and electrodynamics may be utilized for an adequate description of CR [8]. Since the decisive criterion is the number of bound states within the continuous transverse potential [9], which governs channeling, the situation is rather different for positrons and electrons at planar or axial channeling, respectively. Besides that, this number strongly depends upon the particle energy, atomic number and interatomic distances of the crystal as well [8, 10].

Furthermore, since channeling and associated CR emission is naturally controlled by the continuous potential of the considered crystallographic axis or plane of a single crystal, the idea to manipulate CR emission by means of dedicated modulation of the crystal lattice has been worked out already in the 1980s [11,12]. Very first model calculations predicted that the intensity of CR may be increased if the oscillatory motion of the channeled particles becomes resonant with ultrasonic waves (US) excited in the crystal [13,14]. It was suggested to apply piezoelectric single crystals in which US may be excited utilizing external electromagnetic RF-fields. Forthwith first measurements of electron CR on quartz, $LiNbO_3$ and CdS crystals were carried out at ultra-relativistic energies where the CR spectra show a smooth behaviour [15].

A consistent quantum theory of electron and positron CR at impact of US has been developed in a series of works published after year 2000 [16,17,18]. Based on it, systematic measurements of planar CR on quartz single crystals have been carried out at medium electron energies (14 – 32 MeV) as an important prerequisite for the envisaged experimental investigations [19,20]. Since the frequency of resonant US strongly depends upon the transition energy between bound channeling states, measurements where single CR lines are resolved were categorically necessary.

Eventually, the effect of US on planar electron CR could be verified experimentally for two different crystallographic planes of quartz [21,22,23]. It should be mentioned that, in agreement with preceding simulations, resonant enhancement of the CR intensity has been observed at

hypersound frequencies of about 12 GHz.

In the framework of quantum theory, the mechanism of CR stimulation by resonant US has been explained by the dispersive behaviour of the eigenstates of channeled particles in the continuous planar potential [24]. Within an acoustic superlattice of certain US wavelength, the longitudinal momentum of channeled particles, which occupy corresponding transverse states, is no more an integral of motion. Hence, conservation of total energy directly leads to a quantum uncertainty [24] which appears in an intermixture of dedicated channeling states due to a resonant increase of the dispersion of transverse energy. The induced modification of the occupation of bound states finally influences the CR intensity.

At particle energies, where the classical treatment of channeling is valid (see, e.g., [25]), a description of this resonance effect is still missing. This paper for the first time offers a descriptive classical explanation of the influence of resonant US on CR. Exemplarily and for simplicity we consider planar positron channeling in a polyatomic $PbTiO_3$ crystal. Since the piezoelectric constants of this material are much larger than those of quartz, generation of US by external electromagnetic fields should principally be more effective.

In what follows we briefly consider theoretical basics which have been applied for detailed computing of particle trajectories in an acoustic superlattice. Based on these data, spectral-angular distributions of CR have been calculated by means of classical electrodynamics. The results presented provide a simple picture how resonant US influence channeling and CR emission.

2. Theory

Let us consider a relativistic charged particle planar channeled in a piezoelectric single crystal, and assume that longitudinal US are excited in the crystal along the z– direction of channeling. In this case, the quasi-static, continuous and periodic transverse potential of the channeling plane, U(x), is modulated by another periodic function, Λ(z). Since, for a relativistic particle, z ≈ ct (c − velocity of light), the potential V(x,z) is time-dependent, and the usual procedure applied to calculate the continuous planar potential, namely averaging of the atomic potential in space (over y and z) and time (over thermal atomic vibrations), has to be modified. As shown in [26], V(x,z) may approximately be written as the product U(x) Λ(z) where

$$\Lambda(z) \cong 1 + 2 \sum_{m=1,2,..} (-1)^m J_m(mk_s a^*) \cos\left[m\left(k_s z + \varphi\right)\right] \tag{1}$$

does not yet depend on the crystal parameters (except, of course, the velocity of US in the crystal, us), Jm(z) denotes the Bessel function, ks = ωs/us is the wave number of US, a* = a sin(ωst) their amplitude and ωs the frequency.

The (undisturbed) periodic planar potential in the most common form reads

$$U(x) = \sum_n v_n \exp(ingx); (n = ...,-1,0,1,2,...) \tag{2}$$

Where ***g*** is the reciprocal lattice vector normal to the considered crystallographic plane, and the coefficients of this Fourier series are given by

$$v_n = \frac{2\pi a_0 Z_1 e^2}{V_c} \sum_j \exp[M_j(\vec{g})] \cdot \exp(-i\vec{g} \cdot \vec{r}_j) \sum_{i=1}^{4} a_i \exp[-\frac{1}{4}(\frac{b_i}{4\pi^2})(ng)^2] \qquad (3)$$

(a0, Z1, e and Vc are the Bohr radius, atomic number, electron charge and the volume of unit cell, respectively, rj is the radius vector to the lattice site of atom j in the unit cell, ai and bi are parameters defined in [27]). The Debye-Waller factor Mj (g) = g2<uj2>/2 takes the one-dimensional mean-squared thermal vibration amplitude <uj2> of atom j into account.

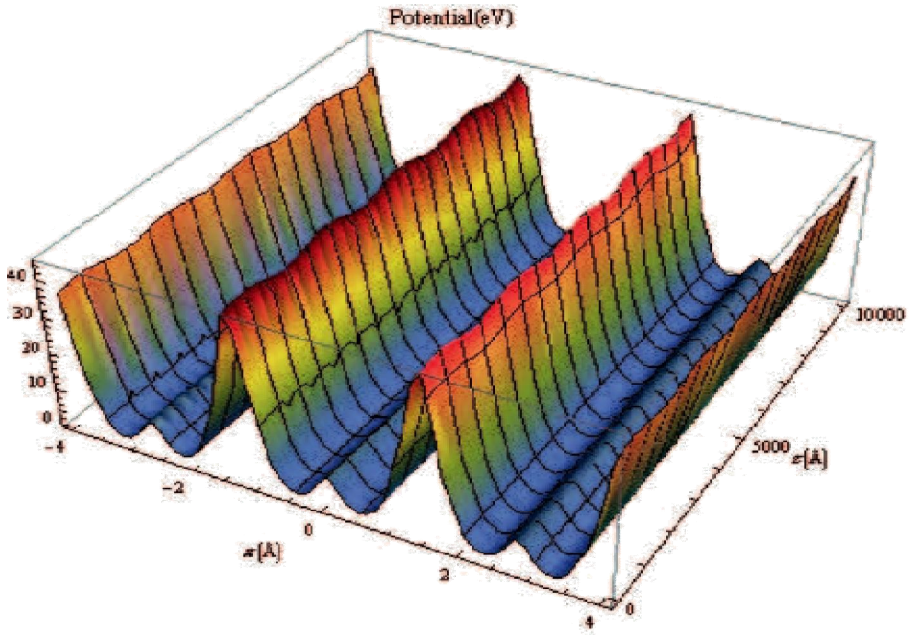

Fig. 1 The (110) planar potential of a $PbTiO_3$ single crystal modulated by ultrasound of $k_s = 1.282$ Å^{-1}.

The continuous potential, modulated by US, of the (110) plane of a PbTiO3 single crystal, calculated numerically for positron channeling, is shown in Fig. 1. Due to the perovskite structure of PbTiO3, the undisturbed (110) potential is by no means a harmonic one (as usually assumed for analytic calculations of positron channeling; see, e.g., [13]). Therefore, bound channeling states, which would result from a quantum calculation, are not equidistant. Accordingly, from a classical calculation one would expect a CR spectrum peaked at several frequencies. This situation partly resembles planar electron channeling where, as exploited in our former works [21,22,23], the frequency of US had to be resonant to some CR transition for observing the effect of intensity enhancement of CR.

The classical description of CR generation is based on the calculation of the trajectory of the channeled particle (here r(t) = x(t)+z(t); y(t) = 0) obtained by solving the equations of motion

$$\gamma m \ddot{x}(t) = -\frac{\partial V(x,z)}{\partial x}; \gamma m \ddot{z}(t) = -\frac{\partial V(x,z)}{\partial z} \qquad (4)$$

(γm – relativistic particle mass, γ – Lorentz factor) at given initial conditions, i.e., the coordinates of the point of incidence of the particle into the crystal and the projections of its momentum for an angle of incidence, Θ_0, with respect to the channeling plane

$$x(0) = x_0; z(0) = z_0; p_x(0) = p\sin(\Theta_0); p_z(0) = p\cos(\Theta_0). \quad (5)$$

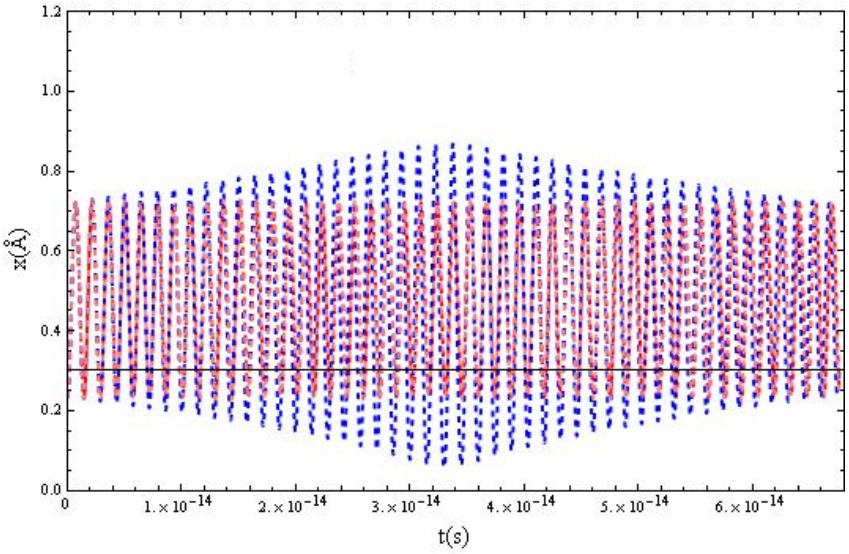

Fig. 2 Trajectories $x(t)$ of positrons channeled along the (110) plane of a $PbTiO_3$ crystal at impact of resonant and non-resonant ultrasonic waves (see text).

According to classical electrodynamics, the energy of CR radiated into a solid angle dΩ within a frequency interval (ω, ω+dω) is given by

$$\frac{d^2E}{d\omega d\Omega} = \frac{e^2}{4\pi^2 c}\left|\int_0^\tau \exp\left[i\left(\omega t - \vec{k}\cdot\vec{r}\right)\right]\frac{\vec{n}\times((\vec{n}-\vec{\beta})\times\dot{\vec{\beta}})}{(1-\vec{\beta}.\vec{n})^2}\,dt\right|^2 \quad (6)$$

where dβ/dt = dr(t)/c dt means the particle velocity, n defines the direction of photon emission, k = ωn/c denotes the wave vector of CR, and τ is the time-of-flight of the particle through the crystal [4].

3. Trajectory calculations

In what follows we exemplarily demonstrate the output of a trajectory calculation for positrons of energy 40 MeV channeled along the (110) plane of an ultrasonic superlattice created in a PbTiO3 single crystal. The equations of motion (4) have been solved numerically for the initial conditions (5): x0 = 0.235 Å, Θ0 = 0. The period of transverse oscillations of a channeled particle amounts to T = 1.408 × 10−15 s. As shown in Figs. 2 and 3, the influence of US with a wave number ks = 1.488 × 10−3 Å−1 appears as an increase of the amplitude of transverse oscillations, x(t), and transverse velocity, βx (t). Simultaneously, one observes a (coherent) decrease of the longitudinal velocity, βz (t) (see Fig. 4). This means that US, which are resonant to the oscillatory motion of the channeled particle [13,18], force a transfer of longitudinal momentum to transverse one. Trajectories and velocities not influenced by US are also shown in Figs. 2 – 4. They depict the results of corresponding calculations but for wave numbers different from the resonant one by ± 5 % (ks = 1.571 × 10−3 Å−1 and ks = 1.406 × 10−3 Å−1). This finding again underlines the

prediction of theory that the influence of US on CR emission is selective.

It is worth to remind here that the impact of resonant US in a quantum treatment of channeling appeared as a large increase of the dispersion of corresponding eigenvalues. Hence, the quantum uncertainty explored in Ref. [24] also reflects a resonant coupling of longitudinal and transverse momentum of the channeled particle. Since the effect is discrete, its verification for planar electron channeling [21,22,23] succeeded only for selected CR transitions at appropriate tuning of the US frequency.

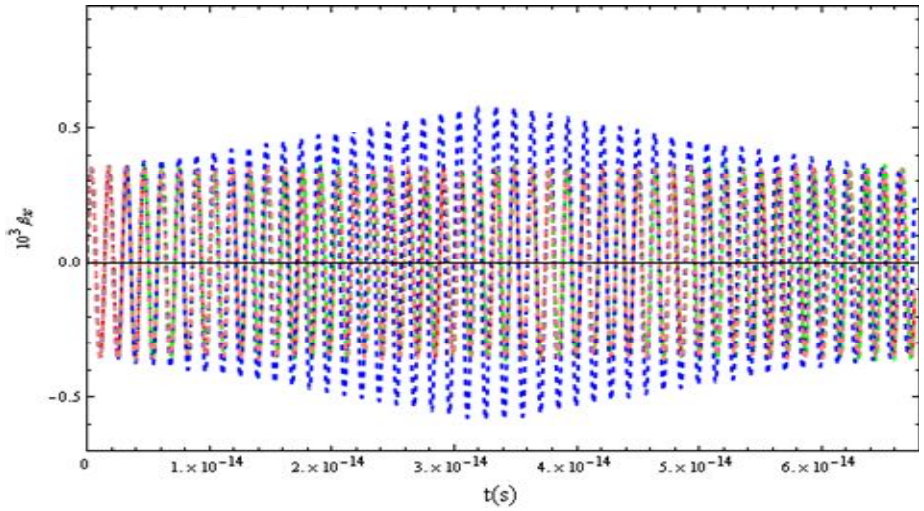

Fig. 3 Transverse velocity β_x (t) = dx/c dt of positrons channeled along the (110) plane of a $PbTiO_3$ crystal at impact of resonant and non-resonant ultrasonic waves (see text).

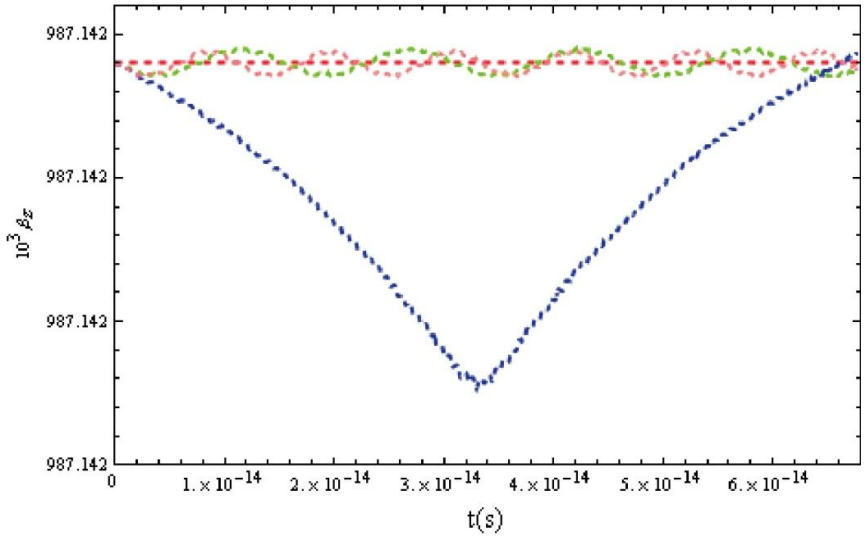

Fig. 4 Longitudinal velocity β_z (t) = dz/c dt of positrons channeled along the (110) plane of a $PbTiO_3$ crystal at impact of resonant and non-resonant ultrasonic waves (see text).

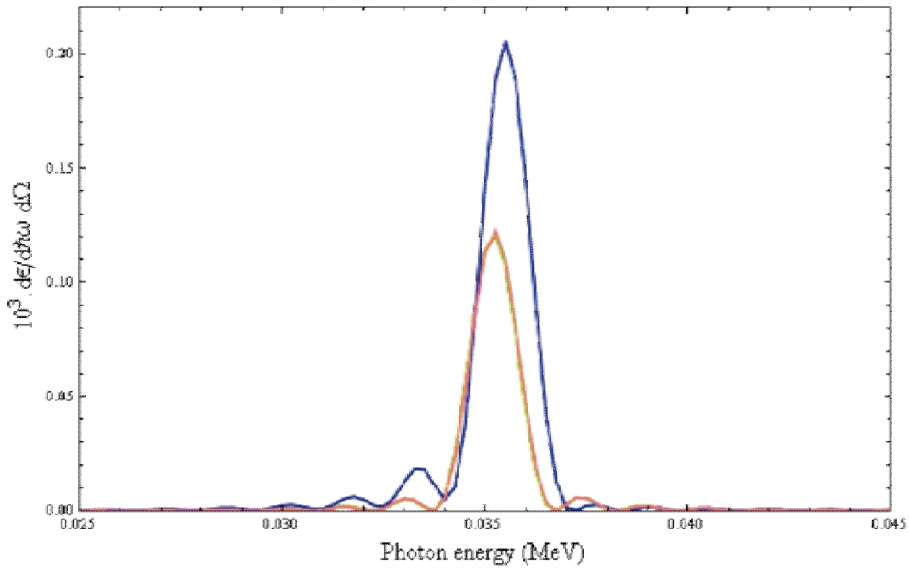

Fig. 5 Spectral-angular distributions of forward emitted CR for positrons of energy 40 MeV impinging with $\Theta_0 = 0$ at $x_0 = 0.235$ Å and channeled along the (110) plane of a 10 μm thick $PbTiO_3$ crystal at impact of resonant (larger amplitude) and non-resonant (smaller amplitude) ultrasonic waves.

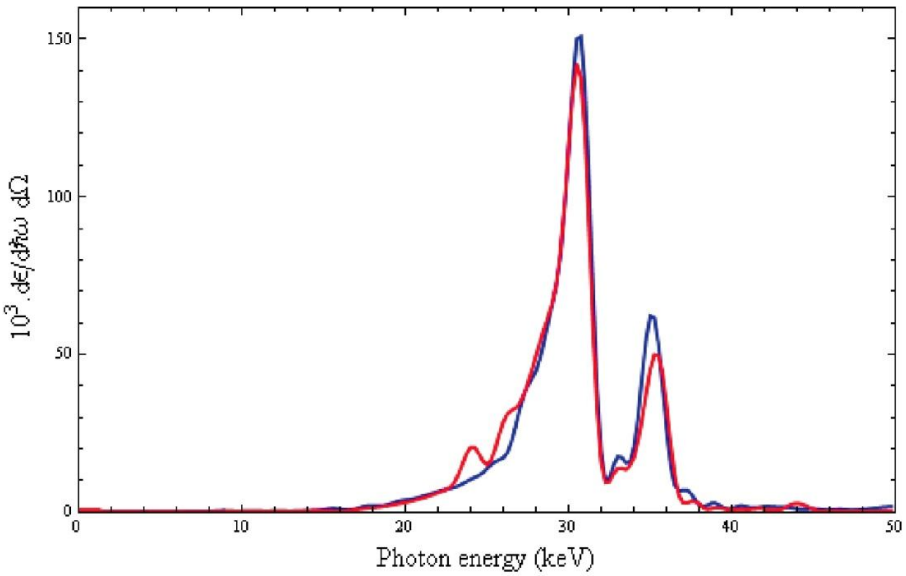

Fig. 6 Spectral-angular distributions of forward emitted CR for positrons of energy 40 MeV channeled along the (110) plane of a 10 μm thick $PbTiO_3$ crystal at impact of US with wave number $k_s = 1.488 \times 10^{-3}$ Å^{-1} (larger amplitude) compared to the CR spectrum without US (smaller amplitude).

4. Stimulation of CR emission by ultrasound

The radiation emitted by channeled positrons moving through the $PbTiO_3$ crystal on oscillating trajectories as found in Sect. 3 has been calculated according to (6). The corresponding spectral-angular distributions of forward emitted CR are shown in Fig. 5. At impact of US resonant with the oscillatory motion of channeled particles one observes an enhancement of the CR intensity (upper curve in Fig. 5) at a photon energy of $E_{CR} = 2\gamma^2 h/T$ where h is the Planck constant. Non-resonant US does, however, not influence CR emission.

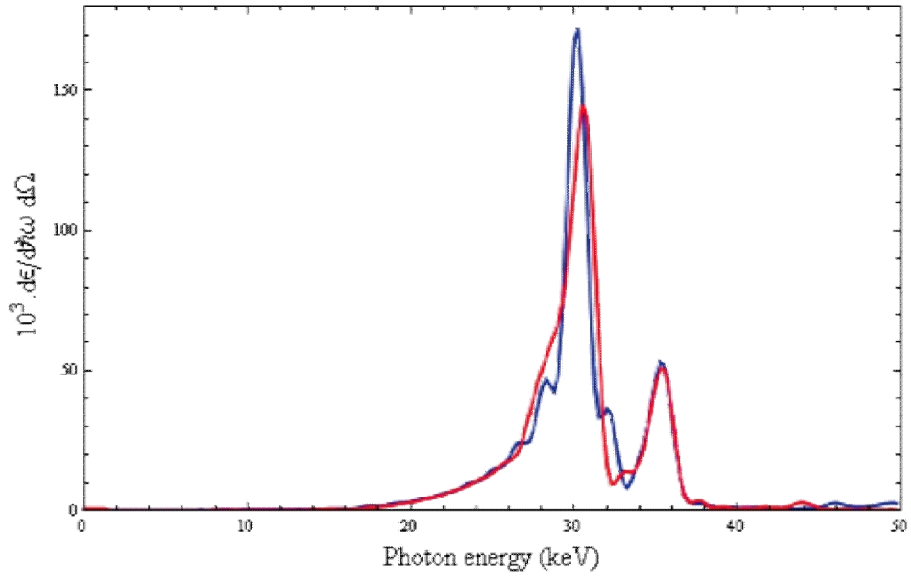

Fig. 7 Spectral-angular distributions of forward emitted CR for positrons of energy 40 MeV channelled along the (110) plane of a 10 μm thick $PbTiO_3$ crystal at impact of US with wave number $k_s = 1.282 \times 10^{-3}$ Å^{-1} (larger amplitude) compared to the CR spectrum without US (smaller amplitude).

Naturally, variation of the initial conditions results in varied trajectories. Therefore, averaging over relevant initial parameters is necessary to simulate the residual CR spectrum. For a parallel positron beam ($\Theta_0 = 0$) one would observe CR spectra as shown in Fig. 6, where the upper spectrum reveals the influence of US with wave number $k_s = 1.488 \times 10^{-3}$ Å^{-1}, and the lower one depicts CR emission without US. The spectra are characterised by two maxima (CR "lines"). From comparison with Fig. 5 one may conclude that the relative influence of US with given k_s on the CR intensity is larger for the smaller CR peak at about 35 keV. A second example calculated for $k_s = 1.282 \times 10^{-3}$ Å^{-1} is shown in Fig. 7. In this case, US mainly stimulate the intensity of the dominant first CR peak at about 30 keV.

5. Summary

This work presents first classical trajectory calculations for channeling in an ultrasonic superlattice. As may easily be realised, resonant ultrasound influences the transverse amplitude of the oscillatory motion as well as the transverse and longitudinal velocities of the channeled particle. Its longitudinal momentum is no more a conserved quantity. A resonant ultrasonic field changes the CR intensity as has been demonstrated by simulations of CR spectra for planar positron channeling in a $PbTiO_3$ single crystal. The possible magnitude of CR stimulation is, of course, subject to experimental investigations.

Due to the anharmonic continuous potential of the crystallographic (110) plane of $PbTiO_3$, features found for positron channeling resemble planar electron channeling. Up to now, stimulation of CR emission by ultrasonic waves has only been proved for electron channeling in piezoelectric quartz crystals. Suitable positron beams were not available. However, efforts to modify the positron beam line of the Beam Test Facility at INFN LNF Frascati, Italy, are reported in Ref. [28] recently. The verification of the observed effect of CR intensity enhancement by resonant ultrasonic waves on other crystals and/or beams of relativistic charged particles is, therefore, of principal interest.

References

1. Kumakhov M A, Phys. Lett. **57** (1976) 17.

2. Sàenz M A and Überall H, *Coherent Radiation Sources* (Heidelberg: Springer, 1985)
3. Kumakhov M A and Komarov F F, *Radiation from Charged Particles in Solids* (New York: AIP, 1989)
4. Kumakhov M A and Weddel R, *Radiation of Relativistic Light Particles during Interaction with Single Crystals* (Heidelberg: Spektrum, 1991)
5. Akhiezer A I and Shul'ga N F, *High-Energy Electrodynamics in Matter* Amsterdam: Gordon and Breach, 1996)
6. Rullhusen P, Artru X and Dhez P, *Novel Radiation Sources Using Relativistic Electrons* (Singapore: World Scientific, 1998)
7. Baier V N, Katkov V M and Strakhovenko V M, *Electromagnetic Processes at High Energy in Oriented Single Crystals* (Singapore: World Scientific, 1998)
8. Andersen J U, Andersen S K and Augustyniak W M, K. Dan. Vidensk. Selsk. Mat. Fys. Medd. **39** Nr. 10 (1977)
9. Lindhard J, Phys. Lett. **12** (1964) 126.
10. Chadderton L T, in: *Channeling* ed. Morgan D V (London: Wiley, 1973) p. 287.
11. Baryshevsky V G, Dubovskaya I Ya and Grubich A O, Phys. Lett. **A**77 (1980) 61.
12. Mkrtchyan A R, Gasparyan R H and Gabrielyan R G, Phys. Lett. **A**115 (1986) 410.
13. Mkrtchyan A R, Gasparyan R H, Gabrielyan R G and Mkrtchyan A G, Phys. Lett. **A**126 (1988) 528.
14. Dedkov G V, Phys. Status Solidi **B**184 (1994) 535.
15. Avakyan R O et al., Pis'ma Zh. Eksp. Teor. Fiz. **48** (1988) 577.
Avakyan R O et al., Nucl. Instrum. Methods **B**48 (1990) 266.
16. Grigoryan L Sh et al., Radiat. Eff. Defects Solids **152** (2000) 225;269. **153** (2000) 13;212; 289;307.
17. Grigoryan L Sh et al., Nucl. Instrum. Methods **B**173 (2001) 132;184.
18. Grigoryan L Sh et al., Nucl. Instrum. Methods **B**201 (2003) 25.
19. Wagner W, Azadegan B, Grigoryan L Sh and Pawelke J, EPL **78** (2007) 56004.
20. Azadegan B, Grigoryan L Sh, Pawelke J and Wagner W, J. Phys. **B**41 (2008) 325101.
21. Wagner W, Azadegan B, Büttig H, Pawelke J, Sobiella M and Grigoryan L Sh, in: *Proc. Int. Conf. "Channeling 2008"* (Erice, Italy) ed. Dabagov S B and Palumbo L (Singapore: World Scientific, 2010) p. 378.
22. Wagner W, Azadegan B, Büttig H, Mkrtchyan A R, Grigoryan L Sh and Pawelke J, in: *Proc. Int. Conf on Electrons, Positrons, Neutrons and X-Rays Scattering under External Influences* (Yerevan-Meghri, Armenia, 2009) ed. Mkrtchyan A R, Bushuev V A and Roshchupkin D V (Yerevan: NAS IAPP Press, 2010) p. 35.
23. Wagner W, Azadegan B, Büttig H, Mkrtchyan A R, Grigoryan L Sh and Pawelke J, Nuovo Cimento **C**34 N. 4 (2011) 133.
24. Mkrtchyan A R, Grigoryan L Sh, Mkrtchyan A H, Khachatryan H F, Wagner W and Azadegan B, in: *Proc. Int. Conf on Electrons, Positrons, Neutrons and X-Rays Scattering under External Influences* (Yerevan-Meghri, Armenia, 2009) ed. Mkrtchyan A R, Bushuev V A and Roshchupkin D V (Yerevan: NAS IAPP Press, 2010) p. 44.
25. Bogdanov O V, Korotchenko K B and Pivovarov Yu L, J. Phys. **B**41 (2008) 055004.
26. Grigoryan L Sh, Mkrtchyan A H, Khachatryan H F, Wagner W, Saharian A A and Baghdasaryan K S, Nucl. Instrum. Methods **B**212 (2003) 51.
27. Doyle P A and Turner P S, Acta Crystallogr. **A**24 (1968) 390.
28. Backe H, Krambrich D, Lauth W, Buonomo B, Dabagov, S B, Mazzitelli G, Quintieri J, Lundsgaard Hansen J, Uggerhøj U I, Azadegan B, Dizdar A and Wagner W, Nuovo Cimento **C**34 N. 4 (2011) 175.

Energy Band Structure and Bloch Wave Functions of Particles in the Crystal

Erine A. Babakhanyan

National Research Laboratory after A.I. Alikhanian (Yerevan Physics Institute), Armenia, 0036, Alikhanian Br. str. 2

Introduction. The orientation phenomena arising during transmission of charged particles in crystals are long ago being the object of interest of physicists. By means of channeling effect – the most known direction in physics of orientation phenomena, it is possible to study the thermal fluctuations and displacements of atoms in a lattice, the distribution of electron density in the interatomic space in crystals, as well as the possibility the usage of channeling for creation the efficient control systems for beams of high energy particles.

The channeling of light particles – electrons and positrons – is attractive, especially, in connection with an opportunity of using of the appeared during the channeling monochromatic hard radiation, which presents a practical interest.

Channeling effect has served as a base for revealing the new experimental methods for studying the solid state composition and structure.

Due to the unique possibilities to determine to a big accuracy the location of impurity atom and self-interstitials in crystalline lattice, to find the profiles of radiation defects and to classify them, to study the structural imperfection in the surface and near-surface layers of crystals and thin monocrystalline films, these methods find more and more wide application in various areas of science and engineering: nuclear physics, solid-state physics, semiconductor technology, microelectronics etc. [e.g. 1,2].

Energy band structure. The general case of a particle having arbitrary mass and charge and moving in the crystal is convenient for solving the task of finding the energy band structure and Bloch wave functions in a periodic potential of the crystallographic planes.

In earliest works concerning the computer modeling of passage of ions in monocrystals, the anomalous high transition of ions in comparison with an amorphous sample was received. The main point of this effect is observation of an exit dependence of particles on the incidence angle in case of their incidence by the small angle (θ) to a crystallographic plane or axis[2].

Many theoretical and experimental works, where it was investigated the channeling of various particles (p, e^+, e^-, π^+, π^- *etc.*), have followed thereupon.

While for protons, ions and other heavy particles of the certain energy range it is possible to apply the classical consideration, for e^+, and especially for e^-, the quantum description is necessary due to diffraction effects.

Quantum theory of channeling. The consequent quantum theory of channeling effect is developed in a series of works of Yu.M. Kagan and Yu.V. Kononets [3].

M.A. Kumahov's work [4] has stimulated the appearance of some works on study of the radiation arising in a mode of channeling [5].

New experiments in case of planar channeling of electrons in crystals concerning the radiation spectra investigation are carried out recently [6]. As well as new experiments with beams of relativistic electrons and positrons on the LNF Frascati (Italy) with energies 20÷855

[2] In this case the transverse energy is comparable with a potential well depth: $E_\perp \sim E\cdot\sin^2\theta \sim E\cdot\theta^2 \sim V$, and the transverse motion acquires the quantum character.

MeV are planned within the framework of TPU-LNF collaboration and for interpretation of the experimental data received in 2007 on the race-track microtron MAMI (Mainz, Germany) [7].

In the research of channeling effect of charged particles in crystals the big importance has a finding of the energy spectrum structure (zones and gaps) in the periodic potential formed by chains or planes of atoms of the crystalline solid-state lattice [8] (see Fig. 1).

The channeling of electrons differs from the channeling of heavy particles. Features of electron channeling are caused by influence of their wave properties and negative charge.

For light particles, in particular, for electrons, the quantum number characterizing the number of bound states in the potential of a crystalline lattice, is much less, than for positrons of the same energy, and much less, than for heavy particles.

In the one-dimensional potential (planar channeling) the transverse motion is described by Schrödinger's equation with some efficient one-dimensional periodic potential. The wave function of the passing through a crystal particle represents the superposition of corresponding Bloch functions, which properties define, practically, the whole spectrum of physical phenomena observed under channeling conditions.

Krönig-Penney potential. In simple cases the effective periodic potential is represented by a series of potential barriers of equal height. The particle states in such a potential are divided into two groups: the first one with energies less than the height of a barrier (so-called, below-barrier states), permits a simple consideration, for example, within the framework of the strong coupling approximation, and the above-barrier ones with energies in excess of a potential barrier height [9]. The last play the special role, for instance, in the anomalous deep penetration of electrons into the crystal under channeling conditions [10].

For revealing the basic conformities to natural laws of behavior of particles in periodic potential, and also from the point of view of a possibility of full analysis realization, the most acceptable is the model of the periodic potential formed by right-angle barriers of definite width and height. Such potential named as Krönig-Penney potential has allowed, in particular, to analyze the distinctions in channeling pictures of positively and negatively charged particles that turned out to be possible in case of studying a problem in the uniform scheme, considering the narrow wells for negatively and wide ones – for the positively charged particles that is equivalent to inversion of potential relative to the top of well.

The dispersion equation determines the energy of transverse motion as a function of the quasimomentum of the particle, which analysis leads to important conclusions about the properties of wave functions.

The study of wave functions in the center of Brillouin zone and their symmetry properties both in the absence and the presence of so-called "degeneracy", consists in disappearance of the forbidden band between certain neighboring energy bands and, consequently, in their merging [11] (see Fig. 2 and Fig. 3).

The phenomenon of violation of parity alternation in the wave functions in the above-barrier area in case of transition from one energy band to another is revealed, and is show that it is because the reflection coefficient from the hole or barrier of the isolation unit of a periodic crystal potential becomes zero.

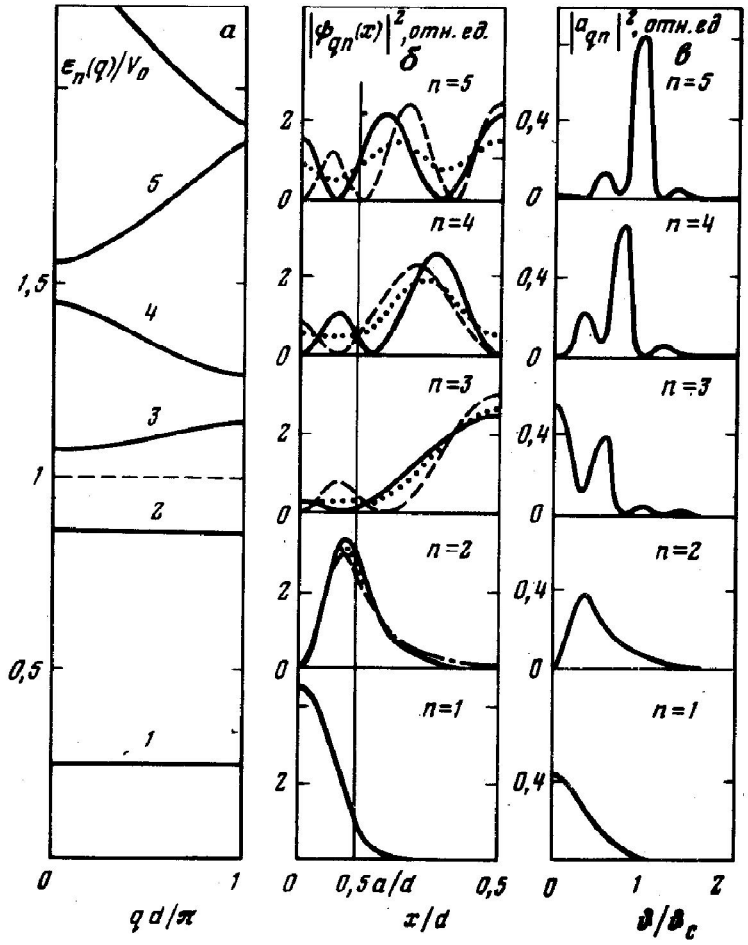

Fig.1. Energy band structure, the Bloch wave functions and populations of bands as a function of incidence angle θ, for electrons with energy 10 MeV.

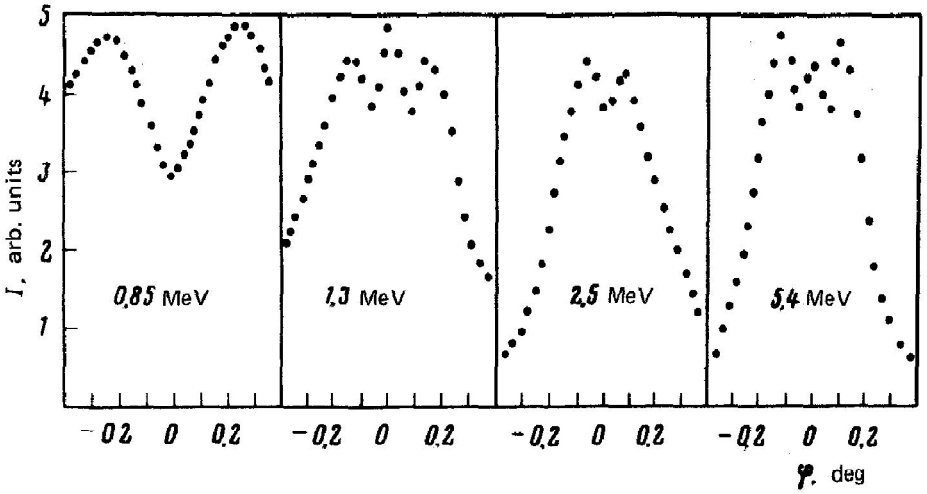

2 FIG. 1. Experimental angular distributions of electrons in the plane which is orthogonal to the plane {110} planes of silicon and which passes through the axis of the incident beam.

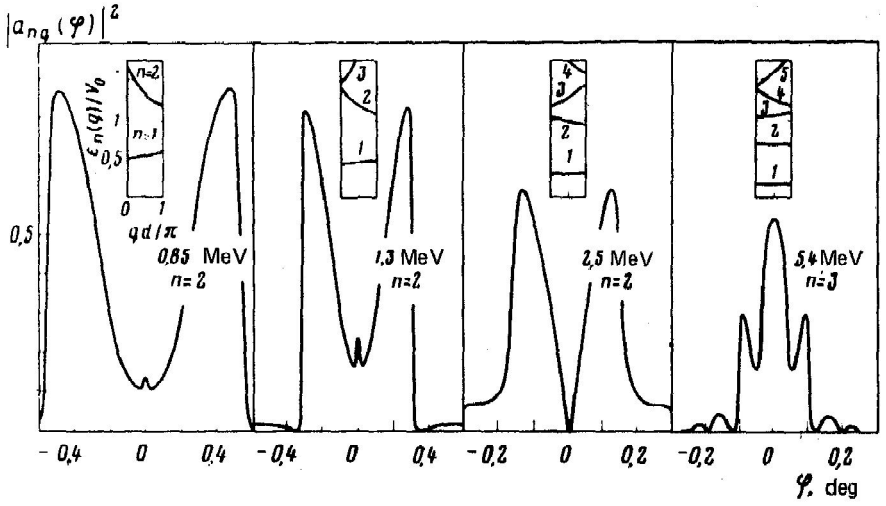

3 FIG. 2. Band structure of the transverse-motion energy levels and angular distributions for electrons in low-lying bands above the barrier according to the Kronig-Penney model, with the parameters given in the text proper.

The Schrödinger's equation has following form

$$\left[-\frac{\hbar^2}{2m}\frac{d^2}{dx^2}+V(x)\right]\psi(x,t)=E\psi(x,t)$$

The sizes of areas of "boundary" coherence, i.e. such areas of the quasimomentum, where the coherent influence of regular medium leads to the fact that the wave function differs from the plane wave.

The dependence of the number of levels and zones within the potential hole on the parameters of potential and particle is shown. The process of consequent lowering of the above-barrier energy zones in a hole with a smooth increase of particle energy (that is the same – with change of depth of the hole) is traced.

The widths of allowed and forbidden zones of whole spectrum (both the below-barrier and above-barrier ones) are investigated. It is established that in the above-barrier area they have an oscillatory character.

Thus, the dependence of channeling pattern of various particles on their energy, incidence angle, structure of distribution of wave functions along the crystal thickness is established [12, 13].

Conclusion

The knowledge of energy spectrum structure allows to find the Bloch state wave functions. During the interaction of the charged particles moving in crystal, the wave functions represent the superposition of Bloch functions. The population of every Bloch state is characterized by the Fourier-component squared.

The analytical results make a basis for the further studying the phenomena in a channeling mode of particles in crystals (the behavior of particles on the different depths of penetration into a crystal, angular distributions of particles, both inside a crystal, and on an exit of it etc.).

As have shown the works of scientists from Tomsk O.V. Bogdanov et al. [6], the account of the zone structure of energetic spectrum of channeled electrons results in qualitative change of angular distributions of X-ray radiation under the Bragg angles. Therefore it is interesting within the framework of our approach to study the radiation, as well as an output of the nuclear reactions appearing in case of interaction of charged particles moving in a crystal.

References

1. Hayrapetyan D.B., Dvoyan K.G., Ghazaryan E.M., Tchanchapanyan A.A. Electronic States of a Cylindrical Quantum Point with a Thin Crescent-shaped Cross-section in Case of Modified Pöschl-Teller Potential // Reports of NAS RA, Physics, 2008; 108(4): 320-330 (*in Russian*).
2. Backe H., Rueda A., Lauth W., Clawiter N., El-Ghazaly M., Kunz P., Weber T. (*Mainz U., Inst. Phys.*). Forward Diffracted Parametric X-radiation from a Silicon Single Crystal // Nucl. Instrum. Meth. 2005; B234: 138-147. (International Workshop on Relativistic Channeling and Related Coherent Phenomena, Frascati, Rome, Italy, 23-26 Mar 2004).
3. Kagan Yu. and Kononets Yu.V. Theory of Channeling // JETP, 1970; 58: 226; 1973; 64: 1042; 1974; 66: 1693 (*in Russian*).
4. Kumakhov M.A. On the Possibility of Existence of the Effect of Spontaneous Emission γ-quants by Relativistic Channeled Particles // DAN USSR, 1976; 230(5): 1077-1080 (*in Russian*).

5. Dabagov S.B. and Ognev L.I. Passage of MeV-energy Electrons through Monocrystals // Nucl. Instrum. Methods B, 1988; 30: 185-190.
6. Bogdanov O.V., Korotchenko K.B., Pivovarov Yu.L. Angular Distribution of Diffracted X-ray Radiation in Case of (111)-channeling of Electrons in Si: the Influence of Structure of Energetic Bands // JETP, 2007; 85(11): 684-688 (*in Russian*).
7. Backe H., Kunz P., Lauth W., Rueda A. Planar Channeling Experiments with Electrons at the 855 MeV Mainz Microtron MAMI // Nuclear Instruments & Methods in Physics Research B. 2008; 266 (17): 3835-3851.
8. Babakhanyan E.A., Kononets Yu.V. Energy Band Structure and Bloch Functions in the Planar Channeling Model with the Krönig-Penney Potential // Physica Status Solidi, 1980; 98b(1): 59-77.
9. Babakhanyan E.A., Hayrapetian G.A. On the Above-Barrier Reflection by the Planar Channeling of Electrons and Positrons in Crystals // Radiation Effects, 1986, Vol. 91, p. 287-291.
10. Kagan Yu., Babakhanyan E.A. and Kononets Yu.V. The Special Role of the Above-Barrier States in the Pattern of Channeling of Electrons in Crystals // JETP Lett., 1980; 31(12): 776-780 (*in Russian*).
11. Babakhanyan E.A., Vorob′ev S.A., Kononets Yu.V., Popov D.E. Energy Dependence of the Structure of the Angular Distributions of Electrons in Planar Channeling // JETP Letters, 1982; 35(5): 184-187 (*in Russian*).
12. Babakhanyan E.A. The Evolution of a Planar Channeling Picture of Electrons and Positrons with Thickness of Crystal // Proceedings of International Conference "Electrons, Positrons, Neutrons and X-rays Scattering under the External Influences". 2010, Yerevan–Meghri, Armenia, p. 56-61.
13. Babakhanyan E.A. The Depth Evolution of Density Distribution Structure for Planar Channeled Particles in Quantum Approach // Nuovo Cimento, 2011; 34(4): 119-124.

Section II

Time – spatial control of characteristics of X – ray and optical transition radiation with and without acoustic influences.

Creation of a New Generation of Coherent X-Ray Sources

A.R. Mkrtchyan, A.H. Mkrtchyan, V. R. Kocharyan, A.E. Movsisyan

Institute of Applied Problems of Physics of NAS RA, Hr. Nersisyan str. 25, Yerevan, 0014, Armenia,
malpic@sci.am

The effect of influence of external acoustic fields on X-ray transition radiation of relativistic electrons was first investigated theoretically [1] and experimentally [2]. These investigations showed that the acoustic field amplitude increase leads to an increase of the intensity of transition radiation.

In the present work details of experimental investigations of X-ray transition radiation from the periodical permittivity structure are discussed. It is shown the possibility of Creation of a new generation of coherent x-ray sources according the scheme presented in the Figure below.

This phenomenon is observed for electrons of 20 MeV energy. For the electrons source we used the LEA-50 linac of the Yerevan Physics Institute [2]. The beam parameters are: current of the electron beam is 0.1 mcA, the energy resolution is $\pm$30 KeV, the vertical aperture is 0.0005 angular radian, the horizontal aperture is 0.01 angular radian. As a sample of investigations amorphous quartz with different thickness was taken. The acoustic field in the sample was excited by a specially designed system of high Q resonators. The emitted transition radiation and electron beam passes trough vacuum tube. For separation of the produced transition radiation from electron beam, additionally X-cut quartz crystal was placed after the amorphous quartz sample. The crystal was placed in the specially designed MHz mount and has satisfied full pumping condition for transition radiation [3-4]. The separated transition radiation passes through vacuum tube and can be used as a coherent x-ray source.

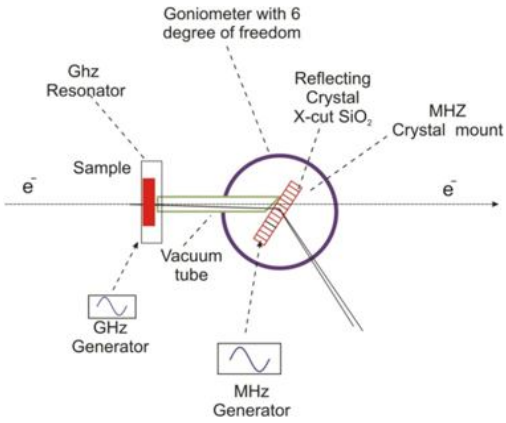

The detailed analysis of experimental data shows that the peak of intensity depends on amorphous quartz purity, frequency and amplitude of the excited hyper frequency acoustic fields. Results of investigation shows:

- The intensity of radiation may be varied by changing the value of hyper frequency electromagnetic field amplitude.
- The registered value of ratio N_γ/N_e is very large from expected and depends on target quality.
- The intensity of the radiation depends of $\Delta\omega_s$ ()i.e. boundary layers of plots by $\Delta\omega_s$.
- The analysis of numerous experiments results shows that the ratio value varies in the range > 1.
- For the targets of different summary thickness the intensity has no changes, i.e. only last layers have contributing in intensity.

According to the developed theory [1] the estimation of measured parameters has been in good agreement.Let us note also that as a source of monochromatic x-ray radiation it can be used PXR when the crystal is excited by acoustic field.

References

1. A.R. Mkrtchyan et al. Preprint ASA SSR, IAPP, Yerevan **1987**.
2. A.R. Mkrtchyan et al. Nanotechnologies in the area of physics, chemistry and biotechnology, Fifth ISTC SAC, Seminar (St. Petersburg, Russia, **2002**),p 202-204.
3. A.R. Mkrtchyan et al. Письма в ЖТФ. **-1983**. -Т.9, В.19. -С.1181-1184. [4] A. R. Mkrtchyan et al. Proceedings the 51st Workshop of the INFN, Channeling **2008**, October 25- November 1, Erice, Italy p.p. 306-308.

Modeling of a New Type Radiators for Generation of Transition and Cherenkov Radiations

A.S. Gevorkyan [1,2] **, H.G. Abajyan** [1]

[1] *Institute for Informatics and Automation Problems, NAS of Armenia, Yerevan, Armenia*
[2] *Joint Institute for Nuclear Research, LIT, Dubna, Russia*

Summary

We has investigated the problem of creation of dielectric constantsuperlatticein media type ofSiO_2under the influence of external electromagnetic fields. The media as an ensemble of $1D$ spatial spin glass of finite length is considered. The complex-classical Hamiltonian was a first used for investigationof statistical properties of spin system in external fields with taking into account relaxation effects. The distribution functions of different parameters of spin glass system are calculated from first principles of complex-classical mechanics. It is shown that behaviors of different distributions parameters are quite different even at weak external fields. Critical properties of media such catastrophes in Clausius-Mossotti equation depending on value of an external fields are studied. It is shown that the complex-classical approach excludes catastrophes, which allows organize continuous parallel computing on the whole region of values ofan external field including critical points. By way of calculation it is proved that under the influence of weak external fields' creation of dielectric constant superlattice is possible. The last circumstance is very important for finding new effective radiators of transition and Cherenkov radiations.

1 Introduction

The formation and governing of periodically modulated refractive index in medium is a most important problem of solid state physics and material science. First of all it is related to the possibility of developing compact UV or X-ray Free-Electron Lasers (FEL) based on emission of transition radiation (TR) [1].
Currently the following two problems are discussed intensely:

a. A gas-plasma medium with periodically varied ionization density [2-10],
b. A special periodical solid-state superlattice-like (SSL) structures composed of layers with different refraction indexes [11-19].

Note that TR is generated at passing of electron beam via neighboring layers of medium with different permittivities. The radiation power in this case is proportionalto amplitude of value $\left[\varepsilon_1^R(\omega)-\varepsilon_2^R(\omega)\right]^2$ [20],where ω a frequency of radiation is and $\varepsilon_{1,2}^R(\omega)=\mathrm{Re}\,\varepsilon_{1,2}(\omega)$ designates the real parts of permittivitiesofcorresponding layers.
In the present article a new microscopic approach has been developed for studying the properties of stationary dielectric constant in dielectric medium under the influence of external standing electromagnetic field.
Mathematically the problem is solved as follows. The dielectric medium in the external electromagnetic field is modeled as a $3D$ spin-glass system. Taking into account the fact that on the infinite plane (x,y)) the distribution of vector-spins are isotropic we use the Birgoffergodic hypothesis and reduce the initial $3D$ spin-glass problem on a two conditionally separated $1D$ problems. It allows investigating each of the problems separately. In the work we have constructed

all expressions which are necessary to allow for the contribution of orientation effects at calculation of stationary and frequency-depending dielectric constants. As was shown, in result of catastrophe of Clausius-Mossotti equation, in the region of short wave-length, the difference between permittivities of neighboring layers may be essentially large.
Last circumstance allows us in homogenous and the isotropic dielectrics of spin-glasses type, artificially to create a super-lattice from different permittivity's the parameters of which it is possible to control by external fields and use this structure for generation of extremely intensive transition radiation.

2 Formulation of the problem and basic formulas

It is well known that in isotropic media (as well as in the crystals with cubic symmetry) the dielectric constant ε_s is well described by the Clausius-Mossotti equation (see [21,22,23])

$$\frac{\varepsilon_s - 1}{\varepsilon_s + 2} = \frac{4\pi}{3}\sum_m N_m^0 \alpha_m^0, \qquad (1)$$

where N_m^0 is the concentration of particles (electrons, atoms, ions, molecules or dipoles) with given m types of polarizabilities and α_m^0 are the coefficients of polarizabilities, correspondingly. From this equation follows that the static dielectric constant ε_s depends on the polarizability properties of the particles as well as on their topological order. The homogeneity and isotropy of the medium are disturbed in external fields. Nevertheless, there is every reason to expect that formula (1) will be applicable after a minor generalization.
Taking into account the influence of the external electromagnetic fields, the equation for the dielectric constant formally may be written as:

$$\varepsilon_{st}^{(\nu)}(g) = \frac{1+2\Lambda(g)}{1-\Lambda(g)}, \qquad \Lambda_\nu(g) = \frac{4\pi}{3}\left[\sum_m N_m^0 \alpha_m^0 + \rho_\nu(g)\right]. \qquad (2)$$

In (2) the symbol $\varepsilon_{st}(g)$ designates the dielectric constant depending on the external field parameters $g = (\Omega, h_0)$, where Ω and h_0 correspond to the frequency and amplitude of the external field; in addition, if the medium can be represented respectively as a model of disordered spin system (spin glass), then $\rho_\nu(g)$ designates the coefficient of polarizability along axis $\nu = (x, y, z)$ which is connected to orientational effects of spins in an external field. Following from the general considerations, we can represent the medium as an ensemble of $1D$ spatial spin-chains (SSCs) of a certain length L_x (see Fig. 1). Note that the coefficient of polarizability $\rho_\nu(g)$ is the mean value of polarization of an ensemble per spin, which should be complex in general and equal to:

$$\rho_\nu(g) = \frac{\overline{p}_\nu(g)}{N_x}, \qquad \overline{p}_\nu(g) = \int p_\nu F_{L_x}(E, \mathbf{p}, g)\, dE d\mathbf{p}, \qquad \mathrm{Re}\, E \le 0, \qquad (3)$$

where N_x denotes the number of spins in the chain, $(E, \mathbf{p})$ are correspondingly the energy and the polarization of a spin-chain with the length L_x and $F_{L_x}(E, \mathbf{p}, g)$ is its distribution function defined for the ensemble (see definition (11)).
It is obvious that for some value of $\rho_\nu(g)$ the expression for $\Lambda_\nu(g)$ goes to zero, which means that a catastrophe occurs in the Clausius-Mossotti equation (2).
Now, our aim is the calculation of the polarizibility coefficient $\rho_\nu(g)$ with consideration of relaxation effects occurring in a system of spins under the influence of external field. Note that in

this case the coefficient $\rho_v(g)$ will have a complex value and, correspondingly, the problem of catastrophe will be solved in a natural way (for more details see section **3**).

We consider a classical ensemble of disordered $1D$ spatial spin-chains (SSC) with the length L_x, where for simplicity it is supposed that the interactions between spin-chains are absent. The specificity of the problem is such that statistical properties of the system interest us on very short time intervals δt at which the system cannot be thermally relaxed. Let us note that for the problem the following time correspondences take place $\tau << \delta t < \Omega^{-1} << \tau_T << 1$, where τ is the time of spin relaxation in an external field and τ_T is the time of thermal relaxation. In other words, we suppose that the spin-glass system is frozen and insusceptible to thermal evolution.

Mathematically, such type of compound can be described by the $1D$ Heisenberg spin-glass Hamiltonian [24,25,26]:

$$H(N_x) = -\sum_{i=0}^{N_x-1} J_{ii+1} \mathrm{S}_i \mathrm{S}_{i+1} - \sum_{i=0}^{N_x-1} \mathrm{h}_i \mathrm{S}_i, \qquad (4)$$

where S_i describes the i-th spin which is the unit length vector and has a random orientation, h_i is the external field which is orientated along the axis x:

$$h_i = h_0 \cos(k_x x_i), \qquad x_i = i \cdot d_0, \quad k_x = 2\pi / L_x. \qquad (5)$$

In addition, J_{ii+1} characterizes the random interaction constant between i and $i+1$ spins in (4). J_{ii+1} can have positive as well as negative values (see [24,26]).

For further investigations, Hamiltonian (4) is convenient to write in spherical coordinates (see Fig. 1):

$$H(N_x) = -\sum_{i=0}^{N_x-1} \{J_{ii+1}[\cos\psi_{i+1}\cos(\phi_i - \phi_{i+1}) + \tan\psi_i \sin\psi_{i+1}] + h_0 \cos(2\pi i / N_x)\tan\psi_i\}\cos\psi_i. \qquad (6)$$

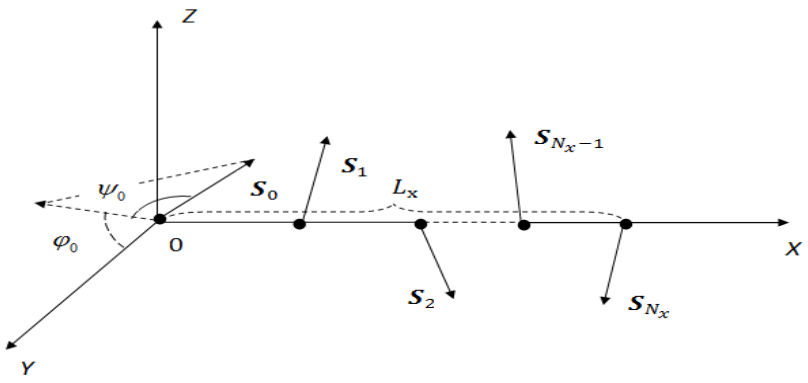

Fig. 1: A stable $1D$ spatial spin-chain with random interactions and length $L_x = d_0 N_x$, where N_x designates the number of spins in the chain. The spherical angles φ_0 and ψ_0 describe the spatial orientation of the $\mathbf{S}_0$ spin, the pair of angles (φ_i, ψ_i) defines the spatial orientation of the $\mathbf{S}_i$ spin.

Equations (6) for the stationary points of the Hamiltonian will play a central role in the consecutive calculations of the problem :

$$\frac{\partial H}{\partial \psi_i} = 0, \qquad \frac{\partial H}{\partial \phi_i} = 0, \qquad (7)$$

where $\Theta_i = (\psi_i, \varphi_i)$ are the angles of the i-th spin in the spherical coordinates, ψ_i is the polar and φ_i the azimuthal angle.

Using expression (4) and equations (7), it is easy to find the following system of trigonometric equations:

$$\sum_{\nu=i-1;\nu\neq i}^{i+1} J_{\nu i}[\sin\psi_\nu - \tan\psi_i \cos\psi_\nu \cos(\phi_i - \phi_\nu)] + h_i = 0,$$
$$\sum_{\nu=i-1;\nu\neq i}^{i+1} J_{\nu i}\cos\psi_\nu \sin(\phi_i - \phi_\nu) = 0, \qquad J_{\nu i} \equiv J_{i\nu}. \tag{8}$$

If the interaction constants between the i-th spin with its nearest-neighboring spins J_{i-1i}, J_{ii+1}, as well as the angles $(\psi_{i-1}, \varphi_{i-1})$, (ψ_i, φ_i), are known, it is possible to explicitly calculate the pair of angles $(\psi_{i+1}, \varphi_{i+1})$. Correspondingly, the i-th spin will be in the ground state if the followinginequality conditions are satisfied (Sylvester conditions) at the stationary point $\Theta_i^0 = (\psi_i^0, \varphi_i^0)$:

$$A_{\psi_i\psi_i}(\Theta_i^0) > 0, \qquad A_{\psi_i\psi_i}(\Theta_i^0) A_{\phi_i\phi_i}(\Theta_i^0) - A^2_{\psi_i\phi_i}(\Theta_i^0) > 0, \tag{9}$$

where $A_{\alpha_i\alpha_i}(\Theta_i^0) = \partial^2 H_0/\partial\alpha_i^2$, $A_{\alpha_i\beta_i}(\Theta_i^0) = A_{\beta_i\alpha_i}(\Theta_i^0) = \partial^2 H_0/\partial\alpha_i\partial\beta_i$, in addition:

$$A_{\psi_i\psi_i}(\Theta_i^0) = \left\{ \sum_{\nu=i-1;\nu\neq i}^{i+1} J_{\nu i}[\cos\psi_\nu \cos(\phi_\nu - \phi_i^0) + \tan\psi_i^0 \sin\psi_\nu] h_0 \cos(2\pi i / N_x) \tan\psi_i^0 \right\} \cos\psi_i^0$$
$$A_{\phi_i\phi_i}(\Theta_i^0) = \sum_{\nu=i-1;\nu\neq i}^{i+1} J_{\nu i}\cos\psi_\nu \cos(\phi_\nu - \phi_i^0)\cos\psi_i^0, \qquad A_{\psi_i\phi_i}(\Theta_i^0) = 0. \tag{10}$$

Using equations (8) and taking into account conditions (9)-(10) we can calculate a huge number of stable $1D$ SSCs, which will allow investigating the statistical properties of the $1D$ SSCs ensemble. It is supposed that the average polarization (magnetization) of the $1D$ SSCs ensemble (polarizability of $1D$ SSC) is equal to zero in the absence of an external field.

Now we can construct the joint distribution function of the energy and polarization of the $1D$ SCCs ensemble subject to the external influence. To this aim itis useful to divide the dimensionless real energy axis E into the region, $0 > E_0 > ... > E_n$ and thepolarization axis $\mathbf{p}$, into regions $0 > p_{0x} > ... > p_{nx}$, $0 > p_{0y} > ... > p_{ny}$ and $0 > p_{0z} > ... > p_{nz}$, where $n>>1$. The number of stable $1D$ SSC configurations with the length L_x within the energy range $[E - \delta E, E + \delta E]$, $\delta E << 1$, and correspondingly polarizations of range $[p_\eta - \delta p_\eta, p_\eta + \delta p_\eta]$, $|\delta p_\eta << 1|$, where $\nu = (x, y, z)$, will be denoted by $M_{L_x}(E, \mathbf{p}, g)$ while the full number of stable $1D$ SSC configurations by

$$M_{L_x}^{full} = \sum_{i,j,l,k=1}^{n} M_{L_x}\left(E_i, p_{j;x}, p_{l;y}, p_{k;z}\right).$$

Accordingly, the distributionfunction for the ensemble may be defined by the expressions:

$$F_{L_x}(E, \mathbf{p}, g) = M_{L_x}(E, \mathbf{p}, g) / M_{L_x}^{full}, \tag{11}$$

$$\lim_{n\to\infty}\sum_{i,j,l,k=1}^{n} F_{L_x}(E_i, p_{j;x}, p_{l;y}, p_{k;z}, g)\delta E_i \delta p_{j;x}\delta p_{l;y}\delta p_{k;z} = \int_{-\infty}^{0} F_{L_x}(E, \mathbf{p}, g)dEd\mathbf{p} = 1,$$

where the second one expresses the normalization condition of the distribution function to unity.

3 Spin glass with taking into account of relaxation effects in ensemble

Using the following notation:

$$\xi_{i+1} = \cos\psi_{i+1}, \qquad \eta_{i+1} = \sin(\phi_i - \phi_{i+1}), \tag{12}$$

we can solve exactely the recurrent system of equations (8):

$$\xi_{i+1}^2 = C_2^2 \big/ J_{ii+1}^2 \eta_{i+1}^2, \qquad \eta_{i+1}^2 = C_2^2\, A/B. \tag{13}$$

Also we find an additional conditionfor spin-spin interaction constant:

$$J_{ii+1}^2 \geq C_1^2 + C_2^2. \tag{13'}$$

Recall that (13') plays an important role at simulation. In previous warks [27], we have shown that even for a weak external fields there arise such values of polarization which lead to catastrophe in equation (2). In order to solve this issue, it is necessary to consider occurring in spin system relaxation effects.As authors have shown, this problem can be solved in the framework of the complex-classical trajectory method [27].The considered expansion can be written in the form of following system of recurrent equations:

$$Re\{\widetilde{\xi}_{i+1}^{\,2} - \widetilde{C}_2^2 \widetilde{J}_{ii+1}^{-2}\widetilde{\eta}_{i+1}^{-2}\} = 0,\ Im\{\widetilde{\xi}_{i+1}^{\,2} - \widetilde{C}_2^2 \widetilde{J}_{ii+1}^{-2}\widetilde{\eta}_{i+1}^{-2}\} = 0,\ Re\{\widetilde{\eta}_{i+1}^{\,2} - \widetilde{C}_2^2\, \widetilde{A}\widetilde{B}^{-1}\} = 0,$$
$$Im\{\eta_{i+1}^2 - \widetilde{C}_2^2\, \widetilde{A}\widetilde{B}^{-1}\} = 0,\ Im\{\widetilde{A}_{\widetilde{\psi}_{i+1}\widetilde{\psi}_{i+1}}(\widetilde{\Theta}_{i+1})\} = 0,\ Im\{\widetilde{A}_{\varphi_{i+1}\widetilde{\varphi}_{i+1}}(\widetilde{\Theta}_{i+1})\} = 0,$$
$$Im\{\tilde{J}_{ii+1}^2 - \tilde{C}_1^2 - \tilde{C}_2^2\} = 0. \tag{14}$$

The tildas over the symbols designate the analytic extension of the functions in the complex region: $\widetilde{\sigma} = \sigma^r + i\sigma^I$, where σ^r and σ^I are the real and imaginary parts of the function, correspondingly.The condition of local minimum energy for spins requires to satisfy the following inequalities:

$$Re\{\tilde{A}_{\tilde{\psi}_i\tilde{\psi}_i}(\tilde{\Theta}_i^0)\} > 0, \qquad Re\{\tilde{A}_{\tilde{\phi}_i\tilde{\phi}_i}(\tilde{\Theta}_i^0)\} > 0, \qquad Re\{\tilde{J}_{ii+1}^{\,2} - \tilde{C}_1^{\,2} - \tilde{C}_2^{\,2}\} \geq 0. \tag{15}$$

4 Numerical simulation of statistical properties of an ensemble

In this section we discuss the case when relaxation occurs by the above-mentioned two degrees of freedom.We assume that the ensemble consists of M spin-chains, each of them consists from $N_x = 25$ spins. For simulation of equations (14) with consideration of conditions (15) we use a parallel algorithm the scheme of which is represented in [9].For the spin glass problem an important issue is the calculation of the medium magnetization (throughout the text also called polarization). As was numerically shown, the distributions of both real and imaginary parts of polarizations are symmetric in the case when external fields are absent (see Fig. 2***a, b***).

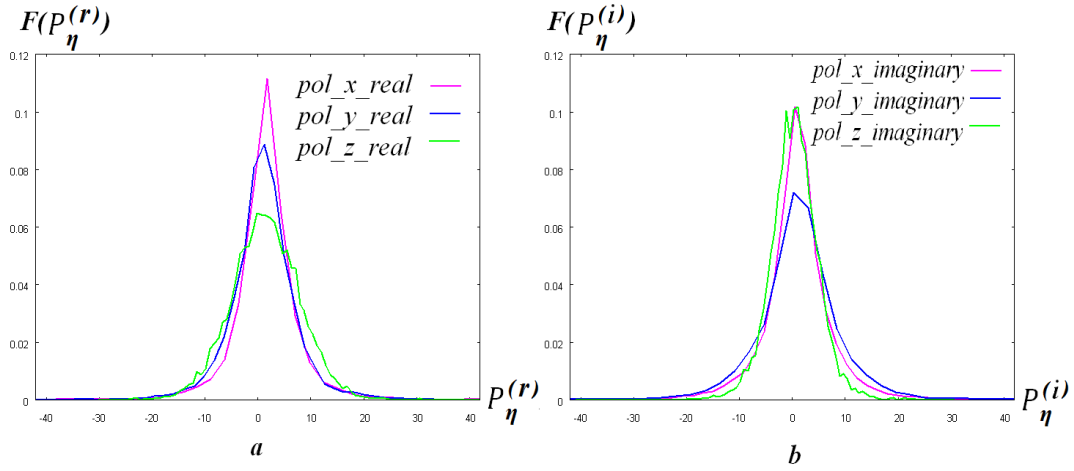

Fig. 2: **a**)Distributions of the real part of polarizations on the coordinates x, y, z, **b**)distributions of the imaginary part of polarizations on the coordinates x, y, z.

The considered case we have the following results for the mean values of $1D$ SSCs' polarizations $(\overline{p}_x^{(r)} = 0.14921, \overline{p}_y^{(r)} = -0.45993, \overline{p}_z^{(r)} = 1.0893)$ and for the imaginary part of polarization, correspondingly: $(\overline{p}_x^{(I)} = 0.29102, \overline{p}_y^{(I)} = -0.39594$ and $\overline{p}_z^{(I)} = 0.067269)$. Such values of polarizations are possible if the absolute values are greater than the number 25 on all coordinates (Fig. 2***a***). Recall that in the absence of external field the spin magnitudes are equal to unity and, correspondingly, the maximal absolute value of the $1D$ SSC polarization is less than 25. The latter means that both the internal and external degrees of freedom of the spin system are excited under relaxation in the external field.The most interesting and important questions about statistical systems concern their critical behaviors in external fields. In this sense, the behavior of spin-chains ensemble magnetization (the mean value of polarizability) in the external field is a very important parameter. We have investigated the behavior of the ensemble polarization depending on the external field. Using definition (3), we have calculated the mean values of polarizations $\overline{p}_v^{(o)}(\gamma)$ on all coordinates, where the index $(o = r, i)$ designates the real and imaginary parts.

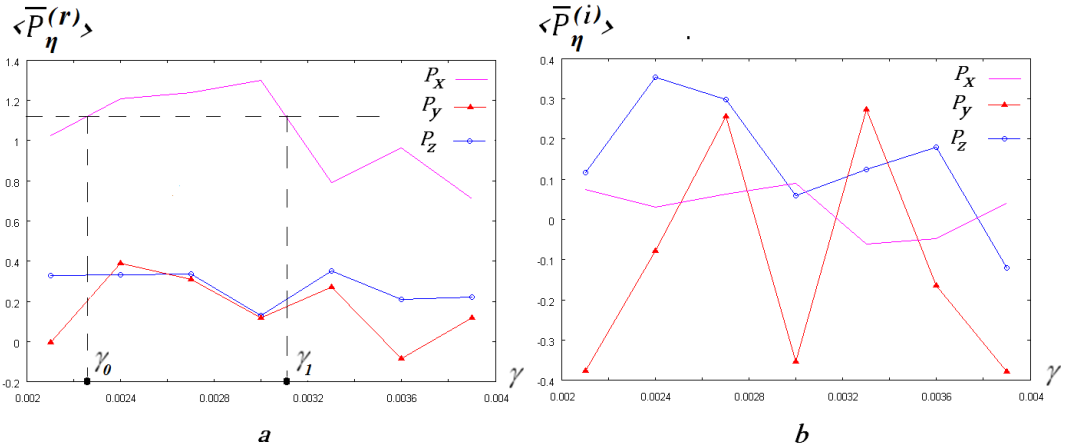

Fig.3: In the figure**a** curves of the real part of polarizations are shown on different coordinates (x, y, z) after full (it means the averaging by fractal structures too) averaging on the spin-chains ensemble. The usual Clausius-Mossotti equation (2) (without consideration of relaxation effects) has a catastrophe figure **a** for two values of external field (γ_0, γ_1). In the figure **b** curves of the imaginary part of polarizations are shown after full averaging by the spin-chains ensemble.

The numerical simulation has shown that the mean values of both the real and imaginary parts of the polarizations are strongly frustrated [27] depending on the parameter γ. This frustration does not disappear at grid convergence of computation region. Moreover, at each separation the self-similarity of structure is conserved which testifies to its fractal character. It is important to note that in the system critical phenomena may occur connected with catastrophes in the Clausius-Mossotti equation (2) (see Fig. 3***a***) when the real part of denominator in the equation tends to one. The analysis of a large class of spin glasses shows that catastrophes occur when the real part of polarizability coefficient connected with orientational effects varies between $\rho(\gamma)\propto 0.025\div 0.05$ and the contribution coming from relaxation effects is not considered in equation (2).These problems are solved by consideration of relaxation effects which lead to formation of the imaginary part in the polarizability coefficient which fully eliminates the divergence in equation (2) (see Fig. 3***b***).

Finally, we return to the definition of the main object of statistical physics, which is the partition function. As is well known, the partition function of a classical many-particle system is defined in the configuration space as follows [30]:

$$Z(\beta)=\int \exp\{-\beta H(\{r\})\}dr_1 dr_2 ..., \qquad \beta=\frac{1}{k_B T}, \tag{16}$$

where k_B is the Boltzmann constant and T is the thermodynamic temperature. If the number of spins or spin-chains in the system is large, the quantity (16) is a functional integral. Anyway, the number of integrals in expression (16) is very large as a rule and the main problem lies in their correct calculation. However, in representation (16) configurations of spin-chains which are not physically realizable do obviously contribute. Moreover, the weight of these configurations is not known in general and it is unclear how to define it. With this in mind and also taking into account the ergodicity of the spin glass in the above-mentioned sense, we can define the partition function in the space of the energy and polarization $(E,\mathbf{p})$ of superspin in the form [27]:

$$Z_*(\beta;N_x)=\langle\int \exp\{\beta H(E,\mathbf{p})\}F_{L_x}(E,\mathbf{p},g)dE\,d\mathbf{p}\rangle, \qquad \mathrm{Re}\,E\le 0, \tag{17}$$

where $F_{L_x}(E,\mathbf{p};g)$ is the distribution function of an ensemble, where $\mathbf{p}$ denotes polarization of 1 D SSC which is complex, $d\mathbf{p}=dp_x^{(r)}dp_y^{(r)}dp_z^{(r)}dp_x^{(i)}dp_y^{(i)}dp_z^{(i)}$. In addition, $H(E,\mathbf{p})$ designates Hamiltonian in a new space, and $(E,\mathbf{p})$ and $<...>$, correspondingly, designate the averaging by fractal structures like definition (17).

Thus, according to the new definition, the partition function is a complex function and its derivatives have regular behaviors respectively at the critical points.

5 Conclusions

In order to solve the problem of critical phenomena in spin glasses under external fields, we first examined the possibility of its description in the framework of complex Hamiltonian. We have studied a short-range interaction model of the spin glass which consists of 1D SSCs. We use the condition of stationarity point of the Hamiltonian on the nodes which allows find a system of recurrent equations (7) or (8) based on the fact that stable spin chains are essentially classical trajectories, where the role of time in the context of this problem is the sequence of nodes. These equations together with Sylvester conditions (9) allow step by step construction of stable spin-chains as classical trajectories. The generalization of classical trajectories on the complex classical trajectories leads to a system of equations (14) which satisfy inequalities (15). The solutions of

equations (14)- (15) for both angles and spin-spin coupling constants are complex since all parameters of the problem are complex. As a result, it helps to avoid the catastrophe in equation (2) and build up a reliable numerical algorithm for solving the spin glass problem taking into account relaxation effects. The developed approach allows us to generalize the Clausius-Mossotti equation and makes it suitable for qualitative and quantitative study of the dielectric constant's behavior of medium including the cases where critical phenomena occur in the medium.By the way of exact numerical simulation we showed that arising of a critical polarization in the spin glass medium under the influence of weak external fields is possible (see Fig. 3).
The last is a very important physical result which with the experimental result is
being agreed []. This phenomenon obviously can be used for creation of a new type of effective radiators for transition and Cherenkov radiations.

Finally, it is important to note that the presented approach allows us to construct a new more correct partition function (17), which is a complex function and its derivatives do not diverge at the critical points.

References

1. V. V. Apollonov, A. Artemyev, M. Feodorov, *et al.*,Optic Express **3**, 162 (1998).
2. K.R.Chen and J. M. Dawson,Phys.Rev. Lett. **68**, 29(1992).
3. R. N. Agarwal and V. K. Tripathi, IEEE Trans. PlasmaSci. **23**, 788 (1995).
4. K. Nakajima *et al.*, Nucl. Instrum. Methods A **375**,593 (1996).
5. V. A. Bazylev, T. J. Schep, and A. V. Tulupov, J. Phys.D **27**, 2466 (1994).
6. V. A. Bazylev *et al.*, Nucl. Instrum.Methods A **358**,433 (1995).
7. N. I. Karbushev, Nucl. Instrum. Methods A **358**, 437(1995).
8. M. V. Fedorov and E. A. Shapiro, Laser Phys. **5**, 735(1995).
9. A. I. Artemev, M. V. Fedorov, J. K. McIver, andE. A. Shapiro, IEEE J. Quantum Electron. **34**, 24(1998).
10. J. Zhang, Z. Dai, and Z. Ren, J. Phys. D **33**, 1798(2000).
11. M. A. Piestrup and P. F. Finman, IEEE J. QuantumElectron. **19**, 357 (1983).
12. M. B. Reid and M. A. Piestrup, IEEE J. QuantumElectron. **27**, 2440 (1991).
13. G. Bekefi, J. S.Wurtele, and I.H.Deutsch, Phys.Rev.A **34**, 1228 (1986).
14. A. E. Kaplan and S. Datta, Appl. Phys. Lett. **44**, 661(1984).
15. M. S. Dubovikov, Phys. Rev. A **50**, 2068 (1994).
16. C. S. Liu and V. K. Tripathi, IEEE Trans. Plasma Sci.**23**, 459 (1995).
17. M. A. Piestrup *et al.*, Phys. Rev. A **43**, 2387 (1991).
18. M. A. Piestrup *et al.*, Phys. Rev. A **43**, 3653 (1991).
19. A. E. Kaplan, C. T. Law, and P. L. Shkolnikov, Phys.Rev. E **52**, 6795 (1995).
20. V. L. Ginzburg and V. N. Tsytovich, Phys. Rept. **49**, 1(1979).
21. Ch. Kittel, Introduction to Solid State Physics. J. Wiley and sons. 1976.P.599.
22. D. J. Griffith, Introduction to Electrodynamics. Prentic Hall. 1989. P.192.
23. R. Becker, Electromagnetic Fields and Interactions. Dover Publications, 1982.
24. K. Binder and A. P. Young , Rev. Mod. Physics. 1986. V.58. PP.801-976.
25. M. Mézard , G. Parisi and M. A. Virasoro, Spin Glass Theory and Beyond. World Scientific. 1987. V.9.
26. A. P. Young (ed.), Spin Glasses and Random Fields. World Scientific. 1998.
27. A. S. Gevorkyan and H. G. Abajyan,Proc. of the 6th conference on Foundations of Physics and Probability, Växjö, Sweden. 2012. pp. 95-105.
28. A. G. Gevorkyan, H. G. Abajyan and E. A. Ayryan,LIT Scientific Report 2010-2011. 2011. pp. 171-175.

29. A. S. Gevorkyan, H. G. Abajyan and H. S. Sukiasyan, Journal of Modern Physics, vol. 2, no. 6, pp. 488-497, 2011.
30. G. Wannier,Statistical Physics, Dover Publications. 1987. P.532.
31. A. R. Mkrtchyan et al., in Nanotechnologies in the Area of Physics, Chemistry and Biotechnology, Fifth ISTC SAC Seminar, St. Petersburg, Russia, 2002, p. 02.

Optical Transition Radiation of Electrons with Energy 7.5 Mev in Fused Quartz in the Presence of the Acoustic Field

A.H. Mkrtchyan, A. A. Aslanian, A. K. Atanesyan, Z.G Amirkhanyan, V. R. Kocharyan A.E. Movsisyan

Institute of Applied Problems of Physics of NAS RA, Hr. Nersisyan str. 25, Yerevan, 0014, Armenia

In contemporary accelerator technology problem diagnosis beams is very relevant since it is necessary not only to measure the size and position of the beam, but also to control its profile and angular divergence. One of such method is based on the detection of the optical transition radiation relativistic electrons.

However, the optical transition radiation has small intensity. In this regard, the possibility of increasing the optical transition radiation in the presence of external influences on the spectral distribution of the OTR is considered[1-3].

In present paper experimentally and theoretically first studied and analyzed the optical transition radiation in the presence of an acoustic superlattice excited in amorphous quartz plate electromagnetic fields hypersonic frequency.

In this paper we theoretically investigated the spectral angular distribution of the optical transition radiation in the plate under the presence of standing longitudinal acoustic field.

Longitudinal hyper frequency electromagnetic oscillation induces a plate along the normal to the surface of a superlattice with a permittivity

$$\varepsilon(\omega, z) = \begin{cases} 1 & by\ z < l, z > 0 \\ \varepsilon_0(\omega) + \varepsilon_1(\omega, z) & by\ 0 \le z \le l \end{cases}$$

Where $\varepsilon_0(\omega)$- the average permittivity of the medium [4], $\varepsilon_1(\omega, z)$-dielectric constant occurs in the presence of acoustic oscillations.

$\varepsilon_1(\omega, z) = -\Delta\varepsilon \cos(k_0 z + \varphi_1),\ \Delta\varepsilon = \frac{\Delta n}{n_0}\ (\varepsilon_0(\omega) - 1)$

where ω- frequency radiation, k_0- wave number of ultrasound, n_0 - number of electrons per unit volume for fused quartz.

Numerically calculate the angular distribution of optical transition radiation of electrons with energy 7.5 MeV in the amorphous quartz in an ultrasonic superlattice [5, 6]. These results show that acoustic waves can control the parameters of the radiation and the results obtained with good accuracy coincides with the settlement and the quasi-classical approximation.

In particular it is shown that there are new resonance peaks in the spectral distribution and when the frequency and amplitude of the acoustic field, the resonance peaks increases and shifts. With increasing frequency the acoustic field position of the resonance peak of the OTR is shifted toward shorter wave i.e. spectral distribution is shifted from blue to infrared and the intensity of the OTR peaks increases as the amplitude of the acoustic field.

References

1. Rule D., Fiorito R. And Kimura W., Proceedings of the 7th Beam Instrum Workshop Argonne IL, AIP Conf. Proc., 390 (1997)
2. Ter-Mikaelian M., High-Energy Electromagnetic Processes in Condensed Media (Wiley/ Interscience, New York) 1972

3. Potylitsyn A. And Potylitsyn N., ArXiv:physics/ 0002034 (2008)
4. A.R. Mkrchyan, A.H. Mkrtchyan, V.R. Kocharyan, Z.G. Amirkhanyan, A.E. Movsisyan, A.A. Aslanyan and P.N. Zhukova. Optical transition radiation in fused quartz under external acoustic field.// II Nuovo Cimento 2011, Vol 34C, N 4.
5. A.R. Mkrchyan, A.H. Mkrtchyan, V. Kocharyan, Z. Amirkhanyan, A. Movsisyan, A. Aslanyan, A. Potyitsyn, A. Gogoliev and V, Bespalov. Experimental investigation of optical transition radiation in amorphous quartz.// II Nuovo Cimento 2011, Vol 34C, N 4, 2011
6. A.G. Mkrtchyan, A.A. Aslanyan, Z.G. Amirkhanyan, V.R. Kocharyan, A.E. Movsisyan. Optical Transition radiation of relativistic electrons in amorphous quartz.//Proceedings of National Academy of Sciences of Armenia 2010, p.45, N4. p.p. 278-280.

Transition radiation in presence of acoustic waves for an oblique incidence

A. R. Mkrtchyan, V. V. Parazian, A. A. Saharian

Institute of Applied Problems in Physics, 25 Nersessian Street, 0014 Yerevan, Armenia

Abstract Forward transition radiation is considered in an ultrasonic superlattice excited in a finite thickness plate under oblique incidence of relativistic electrons. The influence of acoustic waves on both the intensity and polarization of the radiation is investigated. In the quasi-classical approximation, a formula is provided derived for the spectral-angular distribution of the radiation intensity. It is shown that the acoustic waves generate new resonance peaks in the spectral and angular distributions. The heights and the location of the peaks can be controlled by tuning the parameters of the acoustic wave. The numerical examples are given for a plate of fused quartz.

1. Introduction

Transition radiation is produced when a uniformly moving charged particle crosses an interface between two media with different dielectric properties. Such radiation exhibits remarkable properties and at present it has found a number of important applications [1]-[5]. In particular, the transition radiation is widely used for particle identification, for the measurement of transverse size, divergence and energy of electron and proton beams (see, for instance, [6] and references therein). An enhancement for the transition radiation intensity may be achieved by using the interference between the radiations emitted by many interfaces in a multilayer structure. From the point of view of controlling the parameters of various radiation processes in a medium, it is of interest to investigate the influence of external fields, such as acoustic waves, temperature gradient etc., on the corresponding characteristics. The considerations diffraction radiation [7], parametric X-radiation [8], channeling radiation [9], bremsstrahlung of high-energy electrons [10], electron-positron pair creation by high-energy photons [11], have shown that the external fields can remarkably change the both spectral and angular characteristics of the processes. Recently there has been broad interest in compact crystalline undulators with periodically deformed crystallographic planes as an efficient source of high energy photons [12] (for a review see [13]).

In Refs. [14, 15] we have considered the X-ray and optical transition radiation from ultrarelativisitic electrons in an ultrasonic superlattice excited in fused quartz plate. The radiation from a charged particle for a semi-infinite laminated medium has been recently discussed in [16]. In these references the transition radiation is considered under normal incidence of a charged particle upon the interface of the plate. In the present paper we generalize the corresponding results for oblique incidence. The angle between the particle velocity and the normal to the interface is an additional parameter which can be used for the further control of angular-frequency distribution and the polarization of the radiation.

We have organized the paper as follows. In the next section we give the general expression for the spectral-angular distribution of the radiation intensity. Numerical examples for the radiation intensity in the case of a plate made of fused quartz are given in section 3. The main results are summarized in section 4.

2. Radiation intensity

Consider the transition radiation from a charged particle in a plate of thickness l with dielectric permittivity ε_0 which is immersed into a homogeneous medium with permittivity ε_1. We assume

that the z axis of the Cartesian coordinate system (x, y, z) is directed along the normal to the plate and the boundaries of the plate are located at $z = -l$ and $z = 0$. The trajectory of the particle with velocity $\vec{v}$ is in the (x, z) plane and forms with the z axis a given angle α. For the particle coordinates one has

$$x(t) = v(t - t_0)\sin\alpha,\ z(t) = -l + v(t - t_0)\cos\alpha \qquad (1)$$

Here we do not take multiple scattering effects into account (for the discussion of these effects see [1]). So, we can write $\vec{v} = (v\sin\alpha, 0, v\cos\alpha)$. In the presence of longitudinal ultrasonic vibrations, excited in the plate along the normal to its surface, the dielectric permittivity can be written in the form

$$\varepsilon(z) = \begin{cases} \varepsilon_0 + \Delta\varepsilon\cos(k_s z + \omega_s t + \phi), & -l \le z \le 0, \\ \varepsilon_1, & z < -l,\ z > 0 \end{cases} \qquad (2)$$

where ω_s, k_s are the cyclic frequency and the wave number of the ultrasound, and ϕ is the initial phase. In the discussion below we will assume that during the transit time of the particle the dielectric permittivity in the superlattice is not notably changed. For relativistic particles and for the plate thickness $l \le 1$ cm this condition is satisfied for $\nu_s << 10^{11}$ Hz.

For the radiation in the spectral range $\omega >> k_s c$ the presence of the small parameter $k_s c/\omega$ allows us to employ the quasi-classical approximation for the investigation of the radiation field in the forward direction. The latter may be evaluated in a way similar to that discussed in [1] for the case of normal incidence (see also [10]). Considering the radiation in the region $z > 0$, we denote by θ and φ the polar and azimuthal angles for the radiated photon with respect to the axis z For the corresponding wave vector one has

$$\vec{k} = \frac{\omega}{c}\sqrt{\varepsilon_1}(\sin\theta\cos\varphi, \sin\theta\sin\varphi, \cos\theta) \qquad (3)$$

Unlike to the case of the normal incidence, discussed in [7, 8], in the case of oblique incidence we have radiations with two different polarizations. For the first one the electric field is parallel to the observation plane (plane formed by the vectors $\vec{k}$ and $\vec{v}$) and for the second one the electric field is perpendicular to the observation plane. These two polarizations are referred as parallel and perpendicular polarizations, respectively.

First we consider the spectral-angular density of the total radiation intensity averaged over the phase of particle flight into the plate. In the angular region $\sin\theta < \sqrt{\varepsilon_0/\varepsilon_1}$, it is given by the expression

$$I(\omega, \varphi, z) = \frac{dI(\omega, \varphi, z)}{d\omega d\varphi dz} = \frac{e^2 \sin^3\theta\cos^2\alpha}{\pi^2 c\sqrt{\varepsilon_1}} \sum_{m=-\infty}^{+\infty} J_m^2\left(\frac{\omega\Delta\varepsilon/(2ck_s)}{\sqrt{\varepsilon_0 - \varepsilon_1\sin^2\theta}}\right)$$
$$\times\left[\frac{\vec{P}(\omega, \varphi, z)}{V(\omega, \varphi, z)} - \frac{\vec{Q}(\omega, \varphi, z)}{U_m(\omega, \varphi, z)}\frac{\cos^{1/2}\theta}{(\varepsilon_0/\varepsilon_1 - \sin^2\theta)^{1/4}}\right]^2 \qquad (4)$$
$$\times\sin^2\left[\frac{\omega l\sqrt{\varepsilon_1}}{2c\cos\alpha}U_m(\omega, \varphi, z)\right]$$

where e is the charge of the particle, $J_m(b)$ is the Bessel function, and

$$a = \frac{\omega^2 \Delta\varepsilon/(2ck_s)}{\sqrt{\varepsilon_0 - \varepsilon_1 \sin^\theta}}. \tag{5}$$

In (4) we have defined the functions

$$\begin{aligned} U_m(\theta,\varphi,\alpha) &= 1/\beta_1 - \sin\theta\cos\varphi\sin\alpha - \cos\alpha\sqrt{\varepsilon_0/\varepsilon_1 - \sin^2\theta} - \frac{mk_s c}{\omega\sqrt{\varepsilon_1}}, \\ V(\theta,\varphi,\alpha) &= 1/\beta_1 - \sin\theta\cos\varphi\sin\alpha - \cos\theta\cos\alpha \end{aligned} \tag{6}$$

with $\beta_1 = v\sqrt{\varepsilon_1}/c$ and

$$\begin{aligned} \vec{P}(\theta,\varphi,\alpha) &= (\sin\varphi, \cos\theta\tan\alpha - \cos\varphi, -\sin\varphi\tan\alpha), \\ \vec{Q}(\theta,\varphi,\alpha) &= \left(\sqrt{\varepsilon_1/\varepsilon_0}\sin\varphi, \cos\theta\tan\alpha - \sqrt{\varepsilon_1/\varepsilon_0}\cos\varphi, -\sin\varphi\tan\alpha\right), \end{aligned} \tag{7}$$

In general, the dielectric permittivities ε_0 and ε_1 are functions of ω. In what follows we assume that $\beta_1 < 1$. For the case of normal incidence, $\alpha = 0$ the general formula (4) coincides with the result previously derived in [8].

For the spectral-angular density of the radiation with the perpendicular polarization we have the following expression:

$$\begin{aligned} I_\perp(\omega,\theta,\varphi) = \frac{e^2\sin^2(2\alpha)}{4\pi^2 c}\frac{\left(1-\sqrt{\varepsilon_1/\varepsilon_0}\right)^2}{\sqrt{\varepsilon_0 - \varepsilon_1\sin^2\theta}}\sin^3\theta\cos\theta\sin^2\varphi \\ \times \sum_{m=-\infty}^{+\infty}\frac{J_m^2(a(\theta))}{U_m^2(\theta,\varphi)}\sin^2\left[\frac{\omega l\sqrt{\varepsilon_1}}{2c\cos\alpha}U_m(\theta,\varphi)\right]. \end{aligned} \tag{8}$$

The radiation intensity for the parallel polarization is found from the relation

$$I_\parallel(\omega,\theta,\varphi) = I(\omega,\theta,\varphi) - I_\perp(\omega,\theta,\varphi) \tag{9}$$

with the total intensity given by (4). In the case of normal incidence, the intensity for the perpendicular polarization vanishes, $I_\perp(\omega,\theta,\varphi) = 0$, and the radiation is polarized in the observation plane.

Various special cases of formulas (4) and (8) have been considered in the literature. In the case of the normal incidence we recover the results of Refs. [7] and [8] for the X-ray and optical transition radiations respectively. In the absence of the acoustic wave we have $\Delta\varepsilon = 0$ and in formulas (4) and (8) the $m = 0$ term contributes only. In this case we obtain the quasi-classical approximation for the radiation intensity in a finite thickness plate for oblique incidence. The corresponding exact expression for the radiation intensity in this problem is well known from the literature [11] (see also Refs. [1]-[6]). The features of the optical transition radiation in a finite thickness plate for an oblique incidence have been discussed in Refs. [12] on the base of Pafomov's formulas. For a transparent material in the over-threshold case and under the condition $l\omega/v >> 1$, the dominant contribution comes from the term in the exact formula with the resonant factor $\sin^2(y)/y^2$ with y given by the argument of the sin function in (4) with $m = 0$ Now, for simplicity

considering the case of the radiation into the vacuum, it can be seen that for a relativistic particle with $(1-v/c)<<1$ the radiation intensity near the Cherenkov peaks is well approximated by the formulas obtained from (4) and (8) in the limit $\Delta\varepsilon = 0$.

As it is seen from formulas (4) and (8), the radiation intensities for both polarizations have peaks the angular location of which is determined from the equation

$$U_m(\theta,\varphi,\alpha) = 0 \qquad (10)$$

with the function $U_m(\theta,\varphi,\alpha)$ defined in (6). In the approximation under consideration the location of the peaks does not depend on the amplitude of the acoustic oscillations. In the presence of acoustic waves we have a set of peaks specified by m. The angular location of the peak with $m=0$ coincides with that for the peak in the absence of acoustic waves. The angular distance between the peaks induced by the acoustic waves is of the order $(\omega_s/\omega)(c/v_s)$.

In order to present the condition (10) in a physically more transparent form, we introduce the wave vector $\vec{k}_0$ for the photon inside the plate (in the absence of the acoustic wave):

$$\vec{k}_0 = \frac{\omega}{c}\sqrt{\varepsilon_0}\left(\sin\theta_0\cos\varphi, \sin\theta_0\sin\varphi, \cos\theta_0\right) \qquad (11)$$

where $\sin\theta_0 = \sqrt{\varepsilon_1/\varepsilon_0}\sin\theta$ In terms of this vector, the condition for the peaks is written in the form

$$\vec{k}_{0m}\vec{v} = \omega, \vec{k}_{0m} \equiv \vec{k}_0 + m\vec{k}_s \qquad (12)$$

with $\vec{k}_s = (0,0,k_s)$ The latter is the condition for the Cherenkov radiation in the medium of the plate. Hence, we conclude that the peaks in the region $z>0$, determined by the condition (10), correspond to the Cherenkov radiation emitted inside the plate and refracted from the boundary. We can have a situation where the Cherenkov radiation emitted inside the plate is completely reflected from the boundary and in the exterior region we have no peaks. In this case the equation (10) has no solutions. There are also cases then the Cherenkov radiation is confined inside the plate in the absence of the acoustic excitations and the peaks defined by (10) appear as a result of the influence of the acoustic waves. The location of the peaks can be controlled by choosing the incidence angle α.

We denote by $\theta = \theta^{(m)}(\alpha,\varphi)$ the location of the peaks with respect to the polar angle θ for given values of α and φ. For the radiation intensity at the peaks we get the expression

$$I(\omega,\theta^{(m)},\varphi) = \frac{e^2\varepsilon_1 l^2\omega^2\sin^3\theta^{(m)}\cos\theta^{(m)}}{4\pi^2c^3\left(\varepsilon_0-\varepsilon_1\sin^2\theta^{(m)}\right)^{1/2}} \times \vec{Q}^2(\omega,\theta^{(m)},\varphi)J_m^2\left(\frac{\omega\Delta\varepsilon/(2ck_s)}{\sqrt{\varepsilon_0-\varepsilon_1\sin^2\theta^{(m)}}}\right). \qquad (13)$$

The relative contribution of the component with the perpendicular polarization is given by

$$\frac{I_\perp(\omega,\theta^{(m)},\varphi)}{I(\omega,\theta^{(m)},\varphi)} = \left(1-\sqrt{\varepsilon_1/\varepsilon_0}\right)^2\frac{\sin^2\varphi\sin^2\alpha}{\vec{Q}^2(\theta^{(m)},\varphi,\alpha)} \qquad (14)$$

In the absence of the ultrasonic vibrations the location of the peak is given by $\theta^{(0)}$. The ultrasound reduces the height of this peak by the factor $J_0^2\left(a\left(\theta^{(0)}\right)\right)$. In particular, for a given radiation frequency, the frequency or the amplitude of the ultrasound can be tuned to eliminate this peak.

3. Radiation in a plate of fused quartz

In this section we consider the optical transition radiation in a plate of fused quartz. For the velocity of longitudinal ultrasonic vibrations one has $v_s \approx 5.6\times10^5$ cm/s. For the dielectric permittivity of fused quartz we use the Sellmeier dispersion formula

$$\varepsilon_0 = 1+\sum_{i=1}^{3}\frac{a_i\lambda^2}{\lambda^2-l_i^2} \qquad (15)$$

with the parameters $a_1 0.6961663$, $a_2 = 0.4079426$, $a_3 = 0.8974794$, $l_1 = 0.0684043$, $l_2 = 0.1162414$, $l_3 = 9.896161$. In (34), λ is the wavelength of the radiation measured in micrometers. Formula (15) well describes the dispersion properties of fused quartz in the range $0.2\mu m \le \lambda \le 6.7\mu m$. In this spectral range fused quartz is very weakly absorbing.

In figures below we plot the spectral-angular density of the total radiation intensity in the forward direction, $I(\omega,\theta,\varphi)/\hbar$, for electrons with the energy 2 MeV and for the plate thickness $l = 1$ cm. For the oscillation relative amplitude we have taken the value $\Delta n/n = 0.05$, where n_0 is the number of electrons per unit volume for fused quartz.

In accordance with general features described above, the presence of the acoustic wave leads to the appearance of new peaks in both angular and spectral distributions of the radiation intensity. The height of the peaks can be tuned by choosing the parameters of the acoustic wave. In particular, the peak in the radiation intensity which is present in the absence of the acoustic wave is reduced by the factor $J_0^2(a)$. This peak can be completely removed by taking the parameters of the acoustic wave in such a way to have $a = j_{0,s}$, $s = 1,2,3,...$, where $z = j_{0,s}$ are the zeroes of the function $J_0(z)$.

In figure 1, for separate values of the angle α (numbers near the curves), we display the radiation intensity, defined by (4), as a function of the cyclic frequency for the fixed value of the polar angle $\theta = 1$ (left panel, here and below the angles are given in radians) and as a function θ for the fixed value of $\omega = 3.23\times10^{14}$ Hz (left panel). The graphs in figure 1 are plotted for the frequency of acoustic wave $\nu_s = 1.5\times10^6$ Hz and for the azimuthal angle $\varphi = 0.1$. In figure 2 we show the spectral distribution for the total intensity for different values of the acoustic wave frequency ν_s (numbers near the curves in units of 10^6 Hz). The graphs are plotted for $\theta = 1, \varphi = 0.1, \alpha = 0.1$.

4. Conclusion

In the present paper we have studied the influence of acoustic waves, excited in a plate, on the spectral and angular characteristics of the transition radiation for the oblique incidence of a charged particle. For the optical transition radiation, the presence of the small parameter λ/λ_0 with λ and λ_0 being the wavelengths for the radiation and acoustic wave, respectively, allows us to apply the quasi-classical approximation for the evaluation of the radiation intensity in the forward direction. The spectral-angular distribution is described by formula (4) for the total radiated energy and by (8)

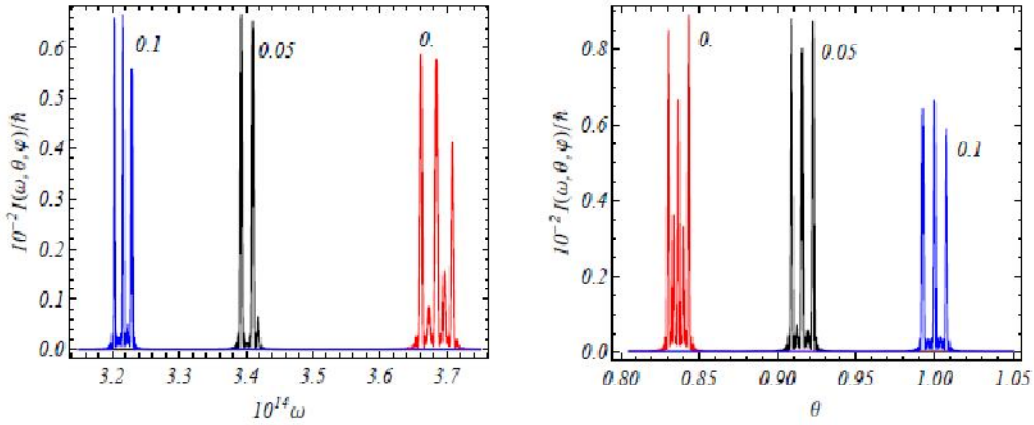

Figure 1. The spectral and angular distributions of the radiation intensity for different values of the incidence angle α (numbers near the curves). The values of the parameters are as follows: $\varphi = 0.1, \nu_s = 1.5\times10^6$ Hz. For the left panel $\theta = 1$ and for the right one $\omega = 3.23\times10^{14}$ Hz.

for the component with perpendicular polarization. The radiation intensities for both polarizations have strong peaks with the angular location determined from the condition (10). These peaks correspond to the Cherenkov radiation emitted inside the plate and refracted from the boundary. In the presence of acoustic waves we have a set of peaks with the angular separation of the order $(\omega_s/\omega)(c/v_s)$. The numerical examples for the optical transition radiation in a plate of fused quartz show that the acoustic waves allow controlling the both angular and spectral parameters of the radiation. In particular, new resonance peaks appear in the spectral-angular distribution of the radiation intensity.

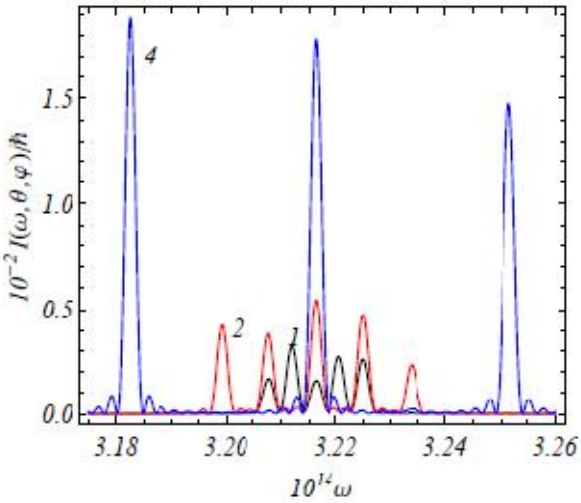

Figure 2. Spectral distribution of the total intensity for separate values of the acoustic wave frequency ν_s (numbers near the curves in units of 10^6 Hz).

Acknowledgment

The authors are grateful to Professors Babken Khachatryan and Levon Grigoryan for valuable discussions and suggestions. We acknowledge the Organizers of the Meghri11 Conference for a support.

References

1. Ter-Mikaelian M L 1972 High Energy Electromagnetic Processes in Condensed Media (New York: Wiley Interscience)

2. Gharibian G M and Yan S 1983 Rentgenovskoye Perekhodnoye Izluchenie (Yerevan: Izdatelstvo AN Arm. SSR)
3. Ginzburg V L and Tsytovich V N 1990 Transition Radiation and Transition Scattering (Bristol: Adam Hilger)
4. [4] Baier V N, Katkov V M and Strakhovenko V M 1998 Electromagnetic Processes at High Energies in Oriented Single Crystals (Singapore: World Scientific)
5. Rullhusen P, Artru X and Dhez P 1998 Novel Radiation Sources Using Relativistic Electrons (Singapore: World Scientific)
6. Potylitsin A P 2011 Electromagnetic Radiation of Electrons in Periodic Structures (Berlin: Springer)
7. Grigoryan L Sh, Mkrtchyan A H and Saharian A A 1998 Nucl. Instr. Meth. B 145 197
8. Mkrtchyan A R, Parazian V V and Saharian A A 2010 Mod. Phys. Lett. B 24 2693
9. Grigoryan L Sh, Mkrtchyan A R, Khachatryan H F, Arzumanyan S R and Wagner W 2010 J. Phys.: Conf. Series 236 012012
10. Khachatryan B V 2004 Doctor of Sciences Thesis (Yerevan)
11. Pafomov V E 1969 Proc. FIAN SSSR, Nuclear Physics and Particle Interaction with Matter 44 90 (Moscow: Nauka)
12. Ruzicka J and Mehes J 1986 Nucl. Instr. Meth. A 250 491; Hrmo A and Ruzicka J 2000 Nucl. Instrum. Meth. A 451 506

Radiation of the electron bunch moving in non-regular fields

Lekdar A. Gevorgian[(1)] and Valeri V. Vardanyan[(1)(2)(*)]

(1) Alikhanyan National Laboratory (YerPhI),Theory Department
(2) YSU, Faculty of Physics,(*) E-mail: vardanyanv@yerphi.am

The problem of spontaneous radiation of the electron bunch grazing into a charged metallic surface with randomly distributed needle shaped asperities is considered. Distances between two neighboring asperities have been described by gamma distribution. Being repealed by highly charged asperities the electrons of the bunch move along non-regular periodical trajectories in the planes parallel to the metallic surface. The spatial periods of the trajectories are random quantities which are described by the same gamma distribution. The radiation characteristics of the bunch have been obtained. It is shown that the angular distributions of the number of photons radiated from the bunch and from a single electron are the same but the frequency distribution of the bunch is being drastically changed at the hard frequency region. It is proposed to develop a new non-destructive method for investigation of the metal surface roughness. The frequency distribution of the number of photons radiated under the zero angle has been obtained. That allows to find the gain expression of the stimulated radiation.

1. Introduction

The radiation of the non-relativistic electron bunch moving parallel to the diffraction grating has been investigated in the experiment of Smith and Purcell [1]. Emitted wavelength dependence on the grating constant, bunch speed and the radiation angle is derived from the Huygens' Principle. As it is shown in [2] that dependence coincides with the oscillator radiation characteristic.

An anomalously high radiation intensity has been observed during the investigations of the transition radiation of the non-relativistic electron bunch grazing into a metal surface [3]. Later that anomaly has been proved in the experiment [4]. In the experiment [5] the authors have concluded that the anomaly is conditioned by the surface roughness. The right explanation of that phenomenon has been given in [6], where the radiation of the non-relativistic electron grazing into a rough metal surface has been presented as a mixture of the transition radiation and the undulator radiation conditioned by the random oscillations of the electron. In that work the random fields have been described by the Gaussian distribution. In the present work the case when the bunch electrons oscillate in the planes parallel to the metallic surface has been considered and gamma distribution has been chosen to describe the random roughness of the metal surface.

It's important for the applications to develop non-destructive methods for investigation of the metallic rough surfaces (see for example [7]). The solution of the considered in this work problem gives an opportunity to find out information about the metallic surface roughness using the bunch radiation characteristics.

2. Surface microundulator

One can assume that in our problem each electron in the bunch moves along a smooth curve like one represented on the fig. 1. On the figure by dots are represented needle shaped asperities of the metallic surface. Electrons move along z direction and oscillate along x direction. The distance between two asperities is l_k, which is also the spatial semiperiod of the electron motion.

Here we give the electron path by the following formula:

$$x = x_k \sin\frac{\pi}{l_k} z, \qquad (1)$$

where x_k is the amplitude of the trajectory.

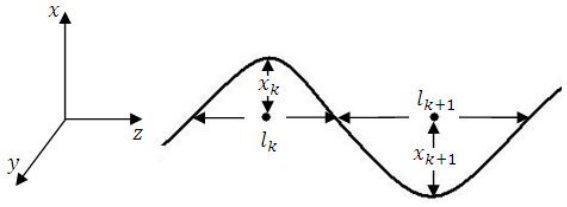

Fig. 1. The path of the electron

As it is already mentioned above the trajectory should be a smooth curve for which we require the derivatives of two sins at the embroidering point be equal to each other. From that requirement it is easy to find the condition:

$$\beta_\perp = \frac{x_k}{l_{k/2}} = const, \qquad (2)$$

which gives a relationship between amplitude and spatial semiperiod.

Here the following fact is very important. The bunch has a big number of electrons and at the given point of space and at the given moment of time we have photons radiated from the electrons which move along trajectories with different l_k. Generally speaking at the other moments of time the given electron may move along the trajectory with some other l_k but at that moment with his previous l_k will move some other electron. It's clear that for us it's not important from which electron the given photon has been emitted. From the mentioned feature it follows that we can assume that every electron moves along a trajectory with a constant l_k. This is the fact which makes possible to find out the bunch radiation characteristics.

As it is known the radiated field of the moving charge is given by the equation:

$$\vec{I} = \frac{1}{\beta c}\int_{-L/2}^{L/2}[\vec{n}\vec{v_t}]e^{i\omega t - i\vec{k}\vec{r}}dz, \qquad \beta = \frac{v}{c}. \qquad (3)$$

Here L is the length of the plate, $\vec{v_t}$ is the total velocity of the electron, v is the electron velocity component along the z axis, ω is the frequency of the radiated photon, $\vec{r}$ is a vector from the beginning of the coordinates to the electron location point, $\vec{k}$-wave vector and $\vec{n}$ is a unit vector pointing from the electron location point to the observation point. For the $\vec{n}$ one has the following:

$$\vec{n} = \hat{x}\sin\theta\cos\varphi + \hat{y}\sin\theta\sin\varphi + \hat{z}\cos\theta, \qquad (4)$$

where θ is the polar angle and φ is the azimuth angle. Calculating the $\vec{k}\vec{r} = k\vec{n}\vec{r} = \mathrm{k_x x} + \mathrm{k_z} z$ and substituting that together with (4) into (3) one will get:

$$\vec{I} = \frac{1}{\beta c}\int_{-\frac{L}{2}}^{\frac{L}{2}}[\vec{A} + \vec{B}\cos(\frac{\pi}{l_k}z)]e^{i(\omega\frac{z}{v} - \frac{\omega}{c}z\cos\theta)}e^{-i\frac{\omega}{c}\sin\theta\ \cos\varphi\ \frac{\beta_\perp}{2}l_k\sin\left(\frac{\pi}{l_k}z\right)}dz. \qquad (5)$$

Here the following designations have been introduced:

$$\vec{A} = v\sin\theta\,(\hat{x}\sin\varphi - \hat{y}\cos\varphi), \quad \vec{B} = \frac{\beta_\perp}{2}\pi v(\hat{y}\cos\theta - \hat{z}\sin\theta\sin\varphi).$$

Taking into account that in practice electrons oscillate with non large amplitudes the problem may be considered within a dipole approximation which means that in the radiation main contribution is made by the first harmonic. From the dipole approximation follows that the

oscillator parameter $q = \beta_\perp \gamma \ll 1$, where $\gamma = (1-\beta^2)^{-1/2}$ is the Lorentz factor, and the second exponent in (5) may be replaced by the first term of its Taylor expansion:

$$\vec{I} = \frac{1}{\beta c}\int_{-\frac{L}{2}}^{\frac{L}{2}}\left[\vec{A} + \frac{\vec{B}}{2}e^{i\frac{\pi}{l_k}z} + \frac{\vec{B}}{2}e^{-i\frac{\pi}{l_k}z}\right]e^{i\frac{\omega}{v}(1-\beta\cos\theta)z}\left(1 - \frac{\omega}{2c}\sin\theta\cos\varphi\frac{\beta_\perp}{2}l_k\, e^{i\frac{\pi}{l_k}z} + \frac{\omega}{2c}\sin\theta\cos\varphi\frac{\beta_\perp}{2}l_k\, e^{-i\frac{\pi}{l_k}z}\right)dz. \quad (6)$$

It is well known that the angular-frequency distribution of the number of radiated photons is given by the following:

$$\frac{d^2N}{d\omega do} = \frac{e^2\omega^2}{4\pi^2c^3}\frac{1}{\hbar\omega}\left|\overrightarrow{I_k}\right|^2 = \frac{\alpha\omega}{4\pi^2c^2}\left|\overrightarrow{I_k}\right|^2, \quad (7)$$

where $do = \sin\theta d\theta d\varphi$ is the solid angle, e is the electron charge, $\hbar$ is the Plank's constant and α is the fine structure constant.

Keeping in (6) just the terms described by the first harmonic and keeping the terms the exponents of which may become zero (the terms whose exponents may not become zero don't satisfy to the energy and momentum conservation laws), integrating the (6) and multiplying by the complex conjugate we will get

$$\left|\overrightarrow{I_k}\right|^2 = \overrightarrow{I_k}\overrightarrow{I_k}^* = \frac{1}{\beta^2c^2}\left[\frac{\omega^2\sin^4\theta\cos^2\varphi{\beta_\perp}^2v^2}{4c^2}{l_k}^2 - \frac{\omega\sin^2\theta\cos\theta\cos^2\varphi{\beta_\perp}^2\pi v^2}{2c}l_k + \frac{{\beta_\perp}^2\pi^2v^2}{4}(\cos^2\theta + \sin^2\theta\sin^2\varphi)\right]\frac{\sin^2\left(\frac{\omega}{v}\left(1-\beta\cos\theta-\frac{v}{\omega}\frac{\pi}{l_k}\right)\frac{L}{2}\right)}{\left(\frac{\omega}{v}\left(1-\beta\cos\theta-\frac{v}{\omega}\frac{\pi}{l_k}\right)\right)^2}. \quad (8)$$

Taking into account the fact that for big values of L the last multiplier of (8) becomes a δ-function one will get:

$$\frac{d^2N}{d\omega do} = \frac{\alpha L}{16\pi c^2}\omega{\beta_\perp}^2\left[\frac{\omega^2\sin^4\theta\cos^2\varphi}{2c^2}{l_k}^2 - \frac{\pi\omega\sin^2\theta\cos\theta\cos^2\varphi}{c}l_k + \frac{\pi^2}{2}(\cos^2\theta + \sin^2\theta\sin^2\varphi)\right]\delta\left(\frac{\omega}{v}\left(1-\beta\cos\theta-\frac{v}{\omega}\frac{\pi}{l_k}\right)\right). \quad (9)$$

The last formula is the angular-frequency distribution of the number of photons radiated from an electron moving along a sinusoidal trajectory with l_k spatial semiperiod. Although the number of electrons in the bunch is finite and, therefore l_k is a discreet quantity, with a sufficient accuracy l_k may be replaced with the l continuous quantity.

3. The angular distribution of the radiation from a single electron

One is able to find the angular distribution of the number of radiated photons from a single electron which moves along a trajectory with a spatial semiperiod l by taking into account that $do = sin\theta d\theta d\varphi = -dcos\theta d\varphi$ and by integrating (9) with respect to ω and φ. One can notice that as a result of integration ωl_k is being replaced with an expression which depends on θ. Taking into account that relativistic electrons radiate under the small angles ($\cos\theta \approx 1 - \theta^2/2$), for the angular distribution with respect to $\Theta = \theta\gamma$ one will get:

$$\frac{dN}{d\Theta} = \frac{\pi^3\alpha Lq^2}{4l}\Phi(\Theta), \qquad \Phi(\Theta) = \frac{1+\Theta^4}{(1+\Theta^2)^4}\Theta. \quad (10)$$

4. The frequency distribution of the radiation from a single electron

It is possible to find the frequency distribution of the number of radiated photons from a single electron which moves along a trajectory with a spatial semiperiod l by integrating (9) with respect to $\cos\theta$ and φ. After simple transformations introducing the following non-dimensional frequency:

$$X = \omega\langle l\rangle/\pi\beta c\gamma^2, \qquad (11)$$

where $\langle l\rangle$ is the mean value of the spatial semiperiods of the bunch electron trajectories (detailed information about the distribution of l is given in the next paragraph), for the frequency distribution one will get:

$$\frac{dN}{dX} = K[1 + (1 - tX)^2], \qquad K = \frac{\alpha L\pi^3 q^2}{32\langle l\rangle}, \qquad (12)$$

where $t = l/\langle l\rangle$. If the l of the electron is constant then $t = 1$ and (12) coincides with the first harmonic spectrum of the undulator radiation in the vacuum [8]. Because the argument of the delta function (9) is zero and the cosine function is limited one has X in the (0,2) interval. The (12) has a parabolic shape which in this case gets a minimum value at $X = 1$.

5. Gamma distribution

To obtain the bunch radiation characteristics one needs to choose a distribution function for the distances l between two neighboring asperities. Here the gamma distribution is chosen.

$$f(a,t) = \frac{a^a t^{a-1} e^{-at}}{\Gamma(a)}, \quad (13)$$

where a characterizes the degree of non-regularity (with smaller a the degree of non-regularity is getting bigger), $t = l/\langle l\rangle$, $\langle l\rangle$ is the mean value of the gamma distribution of l.

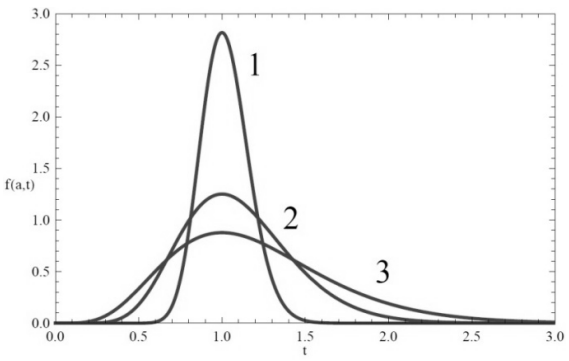

Fig. 2. Gamma distribution for different values of a: 1) a=50, 2) a=10, 3) a=5

Gamma distribution curves for different values of a are presented on the fig. 2. The radiation characteristics of the bunch are being obtained by averaging the corresponding characteristics of the single electron radiation.

It is known that the radiation line bandwidth is conditioned by the finiteness of the bunch motion and by its non-regularity as well as by the angular and energetic divergence of the bunch electrons. Usually the angular divergence is much smaller than the energetic divergence. For that case the radiation line bandwidth is determined by the following expression [9]:

$$\frac{\Delta\omega}{\omega} \approx \frac{2l}{L} + [2(\frac{\Delta\gamma}{\gamma} + \frac{\Delta l}{l})]^{1/2}.$$

It is considered the case when the radiation line bandwidth is caused by the random distribution of l.

6. The angular distribution of the bunch radiation

To obtain the angular distribution of the number of photons radiated from the bunch consisting of N_b electrons one needs to average the (10) by gamma distribution. Since the argument of the δ-function in (9) should become zero one has $t \le 2/X$. Averaging one will get:

$$\langle \frac{dN}{d\Theta} \rangle = N_b \frac{\pi^3 \alpha L q^2}{4\langle l \rangle} \int_0^{2/X} \frac{f(a,t)}{t} dt\, \Phi(\Theta). \quad (14)$$

From the comparison of (10) and (14) it is easy to see that the angular distribution of the bunch radiation does not differ from the angular distribution of the single electron radiation which moves along a trajectory with $2l$ spatial period. That distribution is depicted on the fig. 3. Let's notice that (10) has a maximum value at $\Theta \approx 0.5$ ($\theta \approx 1/2\gamma$).

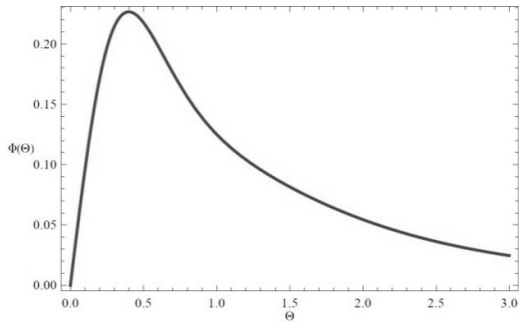

Fig. 3. Angular distribution of the number of radiated photons

7. The frequency distribution of the bunch radiation

By averaging (12) by gamma distribution for the frequency distribution of the number of radiated photons one will get:

$$\langle \frac{dN}{dX} \rangle = N_b \int_0^{2/X} K[1 + (1 - tX)^2] f(a,t)\, dt. \quad (15)$$

The (15) can be rewritten in the following analytic form:

$$\langle \frac{dN}{dX} \rangle = KN_b[2P(a, 2a/X) - 2XP(a+1, 2a/X) + X^2(1 + 1/a)P(a+2, 2a/X)], \quad (16)$$

where $P(a,X) = \int_0^X t^{a-1} e^{-t}/\Gamma(a) dt$ is the incomplete gamma function.

On the fig. 4 the numerical graphs are presented for the regular case and for the different values of a. As it is easy to see at the hard frequency region the spectrum drastically differs from the regular case.

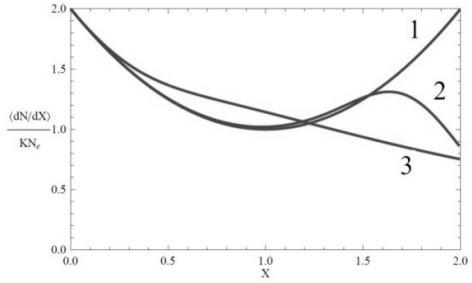

Fig. 4. Frequency distribution of the number of radiated photons: 1) the case of undulator radiation ($\mathbf{a} \to \infty$), 2) $\mathbf{a = 50}$, 3) $\mathbf{a = 2}$

8. The frequency distribution of the number of photons radiated under the zero angle

A topic of a special interest is the frequency distribution of the photon number radiated under the zero angle since it uniquely defines the gain calculation of the stimulated radiation.

Putting $\theta = 0$ in (9), using notation $t = l/\langle l \rangle$, multiplying (9) by the gamma distribution (13) and integrating over all possible values of t, for the frequency distribution of the number of photons radiated under the zero angle from the bunch one will get:

$$\langle \frac{dN}{dXd\Theta^2} \rangle = N_b \frac{\alpha L q^2 \pi^3}{8\langle l \rangle} F(a,X),\ F(a,X) = \frac{a^a 2^{a-1}}{\Gamma(a)} X^{-a} e^{-2a/X} \qquad (17)$$

The obtained results for different values of a are presented on the fig. 5.

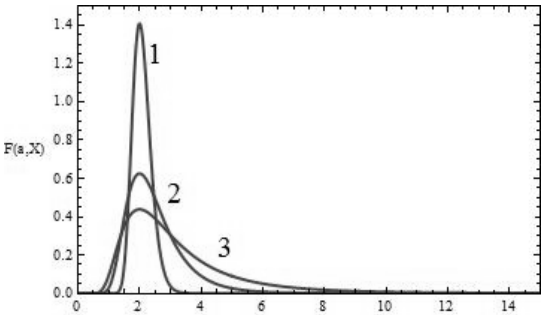

Fig. 5. Frequency distribution of the number of photons radiated under the zero angle: 1) a=50, 2) a=10, 3) a=5

9. Conclusion

And so the angular distribution of the bunch surface microundulator radiation coincides with the angular distribution of the single electron radiation. The frequency distribution is being drastically changed at the hard frequency region. It is proposed to develop a new non-destructive method for investigation of the metal surface roughness.

The frequency distribution of the number of photons radiated from the bunch under the zero angle has been obtained. That allows to find the gain expression of the stimulated radiation.

References

1. S.J. Smith, E.M. Purcell, Phys. Rev. 92, 1069 (1953)
2. L. Gevorgian, V. Vardanyan, Il Nuovo Cimento 34 C, N. 4, 311 (2011)
3. P. Von Blankenhagen, H. Boersch, D. Fritsche. H.G. Seifert, G. Sauerbrey, Physics Letters (Netherlands) 11, 296 (1964)
4. G.E. Jones. L.S. Cram, E.A. Arakawa, Phys. Rev. 147, 515 (1966)
5. F.R. Harutyunian, R.A. Hovhannissian, A.Kh. Mkhitarian, B.O. Rostomian, Physics Letters A 43, 107 (1973)
6. L.A. Gevorgian, N.A. Korkhmazian, Phys. stat. sol. (b) 105, 623 (1981)
7. J.L. Glover, C.T. Chantler, Martin D. de Jonge, Physics Letters A 373, 1177, (2009)
8. L.A. Gevorgyan, N.A. Korkhmazyan, Physics Letters A 74, 453 (1979)
9. L.A. Gevorgyan, N.A. Korkhmazyan, Sov. Phys. JETP 49, 622, (1979)

Section III

Time – spatial control of characteristics of the parametric X – Ray radiation (PXR) with and without acoustic influences.

On a New "Gram"

A.H. Mkrtchyan, V.R. Kocharyan

Institute of Applied Problems of Physics of NAS RA, Hr. Nersisyan str. 25, Yerevan, 0014, Armenia
vahan2@yandex.ru

The investigation of phenomenon of radiation of electromagnetic wave by relativistic electrons shows that dynamic maxima are formed.

The dynamic maxima for quartz single crystals were first observed by the author [1,2] on MAMI microtrone of Mainz University (Germany) for electron energy 255 MeV. In this work, it is reported about a new "gram" for crystal investigation with obvious advantages to the existing ones. In this work, the characteristic sections of dynamic maxima is renamed to Alpikograms in the author's honer.

Further the analogous investigatio on SiO_2 sample were made for electron energies of 180 MeV and 280 MeV.

The present work is devoted to the possibility of detailed investigation of crystal structure and determination of the universality of detection of location of both the light and heavy atoms. On the figure below it is shown the alpikogram of $LiNbO_3$. In the picture, the locations of the dynamic reflections (for the set of atomic planes $(3\bar{3}00)$ of lithium niobate with energies ~11 keV, ~16 keV, ~22 keV) and the characteristic radiation lines K_α-0.52 of oxygen and K_α-16.61, K_β-16.615 of the niobate are clearly seen.

Thus, by detecting the radiation of the scattered electrons and on the basis of Bragg condition, it is possible to construct the spatial structure of $LiNbO_3$. The suggested method enables to perform both the spectral and structural analyses analogous with Debyeagram, Lauegram, Fugigram both for light and heavy nuclei.

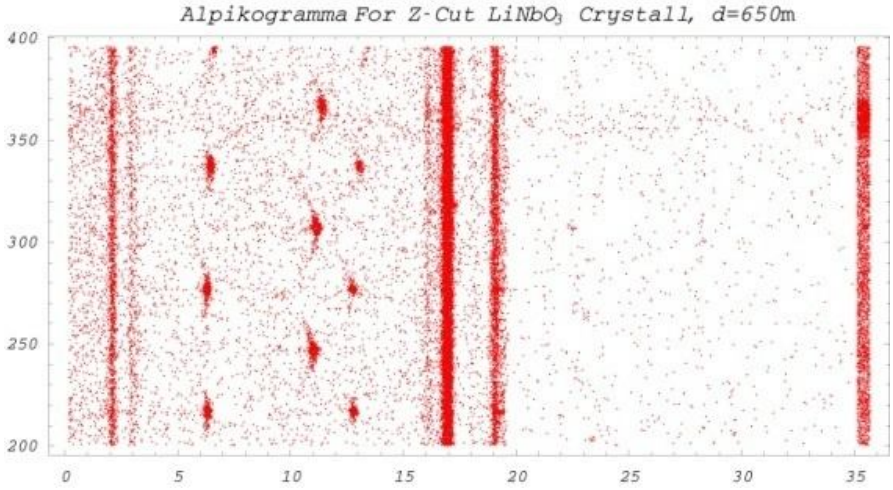

References

1. A.R.Mkrtchyan et al. Report January 1998-June **1999**, FZR-271, September 1999 ISSN 1437-322X, p-27
2. A.R. Mkrtchyan et al. V International Symposium Radiation from Relativistic Electrons in Periodic Structures, September, p.45, **2001**.

Section IV

Time-spatial control of characteristics of the coherent bremsstrahlung with and without acoustic influences.

Angular Distribution of Photons in Coherent Bremsstrahlung in Deformed Crystals

V. V. Parazian

Institute of Applied Problems in Physics, 25 Nersessian Str., 0014 Yerevan, Armenia

Abstract

We investigate the angular distribution of photons in the coherent bremsstrahlung process by high-energy electrons in a periodically deformed single crystal with a complex base. The formula for the corresponding differential cross-section is derived for an arbitrary deformation field. The case is considered in detail when the electron enters into the crystal at small angles with respect to a crystallographic axis. The results of the numerical calculations are presented for SiO2 single crystal and Moliere parameterization of the screened atomic potentials in the case of the deformation field generated by the acoustic wave of S -type.

1 Introduction

The investigation of high-energy electromagnetic processes in crystals is of interest not only from the viewpoint of underlying physics but also from the viewpoint of practical applications. From the point of view of controlling the parameters of various processes in a medium, it is of interest to investigate the influence of external fields, such as acoustic waves, temperature gradient etc., on the corresponding characteristics. The coherent bremsstrahlung of high-energy electrons moving in a crystal is one of the most effective methods to produce intense beams of highly polarized and monochromatic photons. Such radiation has a number of remarkable properties and at present it has found many important applications. This motivates the importance of investigations for various mechanisms of controlling the radiation parameters. In [1] we have discussed the influence of hypersonic waves excited in a crystal on the process of the bremsstrahlung of high energy electrons. To have an essential influence of the acoustic wave high-frequency hypersound is needed. Usually this type of waves is excited by high-frequency electromagnetic field through the piezoelectric effect in crystals with a complex base. In the paper [2], we have generalized the results of [1] for crystals with a complex base and for acoustic waves with an arbitrary profile. For the experimental detection of final particles in the process of coherent bremsstrahlung it is important to know their angular distribution. In the present paper the angular distribution of photons in the coherent bremsstrahlung in crystals is investigated in the presence of hypersonic wave. The numerical calculations are carried out for the quartz single crystal and for the electrons of energy 20 GeV.

2 Angular dependence of the cross-section

We consider the bremsstrahlung by high-energy electrons in a single crystal. The corresponding cross section can be obtained from the cross section for the bremsstrahlung on a single atom derived in [3]. The formulae [4] practically cannot be used for the investigation of bremsstrahlung in case of potentials of a complex form, for example in a crystal, as errors of approximations, admissible in the case of a single scattering center, can become inadmissible greater for many centers. By making use of the results derived in [3], the differential cross section for the bremsstrahlung on a single atom is presented in the form (the system of units $\hbar = c = 1$ is used)

$$\frac{d^5\sigma_{0b}}{d\omega dq_{\|}d\vec{q}_{\perp}dy}=\frac{e^2}{8\pi^4\varepsilon_1^2}\frac{q_{\perp}^2}{q_{\|}^2}\left[1+\frac{\omega^2}{2\varepsilon_1\varepsilon_2}-4y^2\,\frac{\delta}{q_{\|}}\left(1-\frac{\delta}{q_{\|}}\right)\right]\frac{|u(\vec{q})|^2}{\sqrt{1-y^2}}=|u(\vec{q})|^2\sigma_0(\vec{q},y),\quad(1)$$

where e is the electron charge, $\omega,\varepsilon_1,\varepsilon_2$ are the energies of photon, initial and final electrons respectively, $\delta=m_e^2\omega/(2\varepsilon_1\varepsilon_2)$, m_e is the mass of electron, $q_{\|}$ and $q_{\perp}$ are the components of the vector of momentum transfer $\vec{q}$, $\vec{q}=\vec{p}_1-\vec{p}_2-\vec{k}$ ($\vec{k},\vec{p}_1,\vec{p}_2$ are the momenta of photon, initial and final electrons respectively), parallel and perpendicular to the direction of the electron momentum, $u(\vec{q})$ is the Fourier transform of the atom potential. The variable y is expressed in terms of the angle θ_{γ} between the momenta $\vec{p}_1$ and $\vec{k}$ by the following relation:

$$\left(\frac{\varepsilon_1\theta_{\gamma}}{m_e}\right)^2=\frac{1}{\delta}\left(q_{\|}-\delta-\frac{q_{\perp}^2}{2\varepsilon_1}+\frac{q_{\perp}^2\delta}{m_e^2}\right)+y\,\frac{2q_{\perp}}{m_e}\left(\frac{q_{\|}}{\delta}-1-\frac{q_{\perp}^2}{2\varepsilon_1\delta}\right)^{\frac{1}{2}}.\qquad(2)$$

The regions of variables $q_{\|},q_{\perp},y$ in cross-section (1) are as follows [9]:

$$q_{\|}\geq\delta+\frac{q_{\perp}^2}{2\omega},-1\leq y\leq 1,q_{\perp}\geq 0.\qquad(3)$$

The differential cross-section for the bremsstrahlung in a crystal can be written in the form [2]

$$\sigma(\vec{q},y)\equiv\frac{d^5\sigma_{0b}}{d\omega dq_{\|}d\vec{q}_{\perp}dy}=\left|\sum_{n,j}u_{\vec{q}}^{(j)}e^{i\vec{q}\vec{r}_n^{(j)}}\right|^2\sigma_0(\vec{q},y),\qquad(4)$$

where $\vec{r}_n^{(j)}$ is the position of an atom in the crystal. In the discussion that follows, the collective index n enumerates the elementary cell and the subscript j enumerates the atoms in a given cell of a crystal. Here $\vec{q}$ is the momentum transferred to the crystal, $\vec{q}=\vec{p}_1-\vec{p}_2-\vec{k}$ and the differential cross-section in a crystal given by (4), differs from the cross-section on an isolated atom by the interference factor which is responsible for coherent effects arising due to the periodical arrangement of the atoms in the crystal.

After averaging on thermal fluctuations, the cross-section is written in the form (see, for instance [2] for the case of a crystal with a simple cell)

$$\sigma(\vec{q},y)=\left\{N\sum_j\left|u_{\vec{q}}^{(j)}\right|^2\left(1-e^{-q^2\overline{u_t^{(j)2}}}\right)+\left|\sum_{n,j}u_{\vec{q}}^{(j)}e^{i\vec{q}\vec{r}_{n0}^{(j)}}e^{-\frac{1}{2}q^2\overline{u_t^{(j)2}}}\right|^2\right\}\sigma_0(\vec{q},y),\qquad(5)$$

where N is the number of cells, $\vec{r}_{n0}^{(j)}$ determine the equilibrium positions of the atoms, $\overline{u_t^{(j)2}}$ is the temperature-dependent mean-squared amplitude of the thermal vibrations of the jth atom, $e^{-q^2\overline{u_t^{(j)2}}}$ is the corresponding Debye-Waller factor. In formula (5) the first term in figure braces does not depend on the direction of the vector k and determines the contribution of incoherent effects. The contribution of coherent effects is presented by the second term. By taking into account the formula (1) for the cross-section on a single atom, in the region $\varepsilon_1 q_{\perp}^2/\omega m_e^2<<1$ the corresponding part of the cross-section in a crystal can be presented in the form.

$$\sigma_c = \frac{e^2}{8\pi^4\varepsilon_1^2}\frac{q_\perp^2}{q_\parallel^2}\left[1+\frac{\omega^2}{2\varepsilon_1\varepsilon_2}-4y^2\,\frac{\delta}{q_\parallel}\left(1-\frac{\delta}{q_\parallel}\right)\right]\frac{1}{\sqrt{1-y^2}}\left|\sum_{n,j}u_{\vec{q}}^{(j)}e^{iq\vec{r}_{n0}^{(j)}}e^{-\frac{1}{2}q^2\overline{u_t^{(j)2}}}\right|^2. \quad (6)$$

When external influences are present (for example, in the form of acoustic waves) the positions of atoms in the crystal can be written as $\vec{r}_{n0}^{(j)} = \vec{r}_{ne}^{(j)} + \vec{u}_n^{(j)}$, where $\vec{r}_{ne}^{(j)}$ determines the equilibrium position of an atom in the situation without deformation, $\vec{u}_n^{(j)}$ is the displacement of the atom caused by the external influence. We consider deformations with the periodical structure:

$$\vec{u}_n^{(j)} = \vec{u}_0 f\left(\vec{k}_s\vec{r}_{ne}^{(j)}\right), \quad (7)$$

where $\vec{u}_0$ and $\vec{k}_s$ are the amplitude and wave vector corresponding to the deformation field, $f(x)$ is an arbitrary function with the period 2π, $\max f(x)=1$. In the discussion that follows, we assume that $f(x)\in C^\infty(R)$. Further following [5] and having made similar steps we receive the following formula for the differential cross section of coherent bremsstrahlung:

$$\frac{d^2\sigma_b^c}{d\omega dy} = \frac{e^2N}{\pi\varepsilon_1^2N_0\Delta}\sum_{m,\vec{g}}\frac{g_{m\perp}^2}{g_{m\parallel}^2}\left[1+\frac{\omega^2}{2\varepsilon_1\varepsilon_2}-4y^2\,\frac{\delta}{g_{m\parallel}}\left(1-\frac{\delta}{g_{m\parallel}}\right)\right]\frac{\left|F_m\left(\vec{g}_m\vec{u}_0\right)\right|^2\left|S\left(\vec{g}_m,\vec{g}\right)\right|^2}{\sqrt{1-y^2}}, \quad (8)$$

where N_0 is the number of atoms in the crystal $\vec{g}_m = \vec{g} - m\vec{k}_s$, $\vec{g}$ is the reciprocal lattice vector, $-m\vec{k}_s$ stands for the momentum transfer to the external field, $g_{m\parallel}$ and $g_{m\perp}$ are the components of the vector $\vec{g}_m$. The function $F_m(x)$ is defined by relation

$$F_m(x) = \frac{1}{2\upsilon}\int_{-\pi}^{\pi}e^{ixf(t)-imt}dt,\ S\left(\vec{g},\vec{g}_m\right) = \sum_j u_{\vec{g}}^{(j)}e^{i\vec{g}_m\vec{\rho}^{(j)}}e^{-\frac{1}{2}g^2\overline{u_t^{(j)2}}} \quad (9)$$

is the factor determined by the structure of the elementary cell. For a lattice with a complex cell the coordinates of the atoms are written as $\vec{r}_{ne}^{(j)} = \vec{R}_n + \vec{\rho}_j$, with $\vec{R}_n$ being the positions of the atoms for one of primitive lattices, and $\vec{\rho}_j$ are the equilibrium positions for other atoms inside n-th elementary cell with respect to $\vec{R}_n$. Now the relation between the variables y and θ_γ is written in the form:

$$y = \frac{m_e}{2g_{m\perp}}\frac{\left(\varepsilon_1\theta_\gamma/m_e\right)^2-(1/\delta)\left(g_{m\parallel}-\delta-g_{m\perp}^2/(2\varepsilon_1)+g_{m\perp}^2\delta/m_e^2\right)}{\left[g_{m\parallel}/\delta-1-g_{m\perp}^2/(2\varepsilon_1\delta)\right]^{\frac{1}{2}}}. \quad (10)$$

The regions of variables in cross-section (4) are

$$g_{m\parallel}\ge\delta+\frac{g_{m\perp}^2}{2\varepsilon_1},\ -1\le y\le 1,\ g_{m\perp}\ge 0. \quad (11)$$

For sinusoidal deformation field, $f(x)=\sin(z+\varphi_0)$ one has the Fourier-transform

$$F_m(x) = e^{im\varphi_0}J_m(x), \quad (12)$$

with the Bessel function $J_m(x)$.

The formula for the bremsstrahlung in an undeformed crystal is obtained from (8) taking $\vec{u}_0 = 0$. In this limit, the contribution of the term with $m = 0$ remains only with $F_0(0) = 1$. Now we see that formula (8) differs from the formula in an undeformed crystal by the replacement $\vec{g} \to \vec{g}_m$, and by the additional summation over m with the weights $|F_m(\vec{g}_m \vec{u}_0)|^2$. This corresponds to the presence of an additional one-dimensional superlattice with the period λ_s and the reciprocal lattice vector $m\vec{k}_s$, $m = 0, \pm 1, \pm 2, \ldots$. As the main contribution into the cross-section comes from the terms with $g_{m\|} \sim \delta$, the influence of the deformation field may be considerable if $|mk_s| \geq \delta$. Combining this with the previous estimates, we find the following condition: $u_0/\lambda_s \geq a/4\upsilon^2 l_c$. At high energies one has $a/l_c << 1$ and this condition can be consistent with the condition $u_0/\lambda_s << 1$.

In the presence of the deformation field the number of possibilities to satisfy the condition $g_{m\|} \geq \delta + g_{m\perp}^2/(2\varepsilon_1)$ in the summation of formula (8) increases due to the term $mk_{s\|}$ in the expression for $g_{m\|}$. This leads to the appearance of additional peaks in the angular distribution of the radiated photons. After the integration of (8) over *y*, due to these additional peaks, there can be an enhancement of the cross-section of the process [8].

3 Limiting cases and numerical results

Now, we consider the most interesting case when the electron enters into the crystal at small angle θ with respect to the crystallographic z-axis of the orthogonal lattice. The corresponding reciprocal lattice vector components are $g_i = 2\pi m_i/a_i$, $n_i = 0, \pm 1, \pm 2, \ldots$, where a_i, $i = 1, 2, 3$, are the lattice constants in the corresponding directions. For the longitudinal component we can write

$$g_{m\|} = g_{mz}\cos\theta + (g_{my}\cos\alpha + g_{mx}\sin\alpha)\sin\theta, \qquad (13)$$

where α is the angle between the projection of the vector $\vec{p}_1$ on the plane (x, y) and axis-y. For small angles the main contribution into the cross-section comes from the summands with $g_z = 0$. Having made the replacement of variable $y \to \varepsilon_1\theta_\gamma/m_e$ using the formula (10) from formula (8) one finds

$$\frac{d^2\sigma_b^c}{d\omega d(\varepsilon_1\theta_\gamma/m_e)} \approx \frac{e^2 N}{\pi\varepsilon_1^2 N_0 \Delta}\sum_{m,g_x,g_y}\frac{g_\perp^2}{g_{m\|}^2}\left[1 + \frac{\omega^2}{2\varepsilon_1\varepsilon_2} - 4y^2(\theta_\gamma)\frac{\delta}{g_{m\|}}\left(1 - \frac{\delta}{g_{m\|}}\right)\right] \times \frac{|F_m(\vec{g}_m\vec{u}_0)|^2 |S(\vec{g}_m, \vec{g})|^2}{\sqrt{1 - y^2(\theta_\gamma)}} \frac{\varepsilon_1\theta_\gamma/m_e}{(g_\perp/m_e)(g_{m\|}/\delta - 1 - g_\perp^2/(2\varepsilon_1\delta))^{\frac{1}{2}}}, \qquad (14)$$

where the notation $y^2(\theta_\gamma)$ is introduced in accordance with:

$$y^2(\theta_\gamma) = \frac{m_e^2}{4g_\perp^2}\frac{\left[(\varepsilon_1\theta_\gamma/m_e)^2 - (1/\delta)(g_{m\|} - \delta - g_\perp^2/(2\varepsilon_1) + g_\perp^2\delta/m_e^2)\right]^2}{g_{m\|}/\delta - 1 - g_{m\perp}^2/(2\varepsilon_1\delta)}. \qquad (15)$$

In (14) $g_\perp^2 = g_x^2 + g_y^2$, and the summation goes over the region $g_{m\|} \geq \delta + g_{m\perp}^2/(2\varepsilon_1)$, $0 \leq y^2(\theta_\gamma) \leq 1$ with

$$g_{m\|} \approx -mk_z + (g_{mx}\sin\alpha + g_{my}\cos\alpha)\theta . \qquad (16)$$

Note that in the argument of the functions F_m and S we have $\vec{g}_m \approx (g_x, g_y, 0)$.

We now assume that the electron enters into the crystal at small angle θ with respect to the crystallographic axis z and near the crystallographic plane (y,z) (the angle α is small). In this case with the change of δ, the sum over g_x and g_y will drop sets of terms which lead to the abrupt change of the corresponding cross-section. Two cases have to distinguish. Under the condition $\delta \sim 2\pi\theta/a_2$, in Eq. (14) for the longitudinal component, one has

$$g_{m\|} \approx -mk_{s\|} + \theta g_y \geq \delta + \frac{g_\perp^2}{2\varepsilon_1} . \qquad (17)$$

The formula (14) can be further simplified under the assumption $\vec{u}_0 \perp \vec{a}_1$ In this case, in the argument of the function F_m, one has $\vec{g}_m\vec{u}_0 \approx g_y u_{0y}$ and we obtain the formula

$$\frac{d^2\sigma_b^c}{d\omega d(\varepsilon_1\theta_\gamma/m_e)} \approx \frac{e^2N}{\pi^2\varepsilon_1^2N_0\Delta}\sum_{m,g_x,g_y}\frac{g_\perp^2}{g_{m\|}^2}\left[1+\frac{\omega^2}{2\varepsilon_1\varepsilon_2}-4y^2(\theta_\gamma)\frac{\delta}{g_{m\|}}\left(1-\frac{\delta}{g_{m\|}}\right)\right] \times\frac{\left|F_m(g_y u_{0y})\right|^2\left|S(\vec{g}_m,\vec{g})\right|^2}{\sqrt{1-y^2(\theta_\gamma)}}\frac{\varepsilon_1\theta_\gamma/m_e}{(g_\perp/m_e)\left[g_{m\|}/m_e-1-g_\perp^2/(2\varepsilon_1\delta)\right]^{\frac{1}{2}}} . \qquad (18)$$

In the second case, we assume that $\delta \sim 2\pi\theta\alpha/a_1$. Now the main contribution into the sum in Eq. (14) comes from terms with $g_y = 0$ and summations remain over m and n_1, $g_x = 2\pi n_1/a_1$. The formula for the cross-section takes the form

$$\frac{d^2\sigma_b^c}{d\omega d(\varepsilon_1\theta_\gamma/m_e)} \approx \frac{e^2N}{\pi^2\varepsilon_1^2N_0\Delta}\sum_{m,n_1}\frac{g_{m\perp}^2}{g_{m\|}^2}\left[1+\frac{\omega^2}{2\varepsilon_1\varepsilon_2}-4y^2(\theta_\gamma)\frac{\delta}{g_{m\|}}\left(1-\frac{\delta}{g_{m\|}}\right)\right] \times\frac{\left|F_m(\vec{g}_m\vec{u}_0)\right|^2\left|S(\vec{g}_m,\vec{g})\right|}{\sqrt{1-y^2(\theta_\gamma)}}\frac{\varepsilon_1\theta_\gamma/m_e}{(g_{m\perp}/m_e)\left[g_{m\|}/\delta-1-g_{m\perp}^2/(2\varepsilon_1\delta)\right]^{1/2}} , \qquad (19)$$

where

$$g_{m\|} \approx -mk_{s\|} + g_x\psi \ , \ \psi = \alpha\theta \ , \qquad (20)$$

and the summation goes over the values m and n_1 satisfying the condition $g_{m\|} \geq \delta + g_x^2/(2\varepsilon_1)$.

We have carried out numerical calculations for the coherent bremsstrahlung cross-section for various values of parameters in the case of SiO2 single crystal at zero temperature. To deal with an orthogonal lattice, we choose as an elementary cell the cell including 6 atoms of silicon and 12

atoms of oxygen (Shrauf elementary cell [6]). For this choice the y and z axes of the orthogonal coordinate system (x, y, z) coincide with the standard Y and Z -axes of the quartz crystal, whereas the angle between the axes x and X is equal to $\pi/6$. For the potentials of atoms we take Moliere parameterization with

$$u_{\vec{q}}^{(j)} = \sum_{i=1}^{3} \frac{4\pi Z_j e^2 \alpha_i}{q^2 + \left(\chi_i / R_j\right)^2}, \qquad (21)$$

where $\alpha_i = \{0.1, 0.55, 0.35\}$, $\chi_i = \{6.0, 1.2, 0.3\}$, R_j is the screening radius for the *j*-th atom in the elementary cell.

The calculations are carried out for the sinusoidal transversal acoustic wave of the S-type (the corresponding parameters can be found in Ref. [13]) for which the vector of the amplitude of the displacement is directed along X direction of quartz single crystal, $\vec{u}_0 = (u_0, 0, 0)0)$, and the velocity is $4.687 \cdot 10^5\ cm/\sec$ The vector determining the direction of the hyper sound propagation lies in the plane YZ and has the angle with the axis Z equal to 0:295 rad As the axis z we choose the axis Z of the quartz crystal. The corresponding function $F(x)$ is determined by formula (9). We have numerically evaluated the bremsstrahlung cross-section by making use of formulae (19) for values of parameters ε_1, ψ, u_0 taken from [2] when one has an enhancement of the cross-section.

Numerical calculation show, that in dependence of the values for parameters, the external excitation can either enhance or reduce the cross-section of the bremsstrahlung process. As an illustration of the enhancement in the cross-section integrated over the angle θ_γ on the left panel of Fig. 1 we have plotted the quantity $10^{-4}\left(m_e^2\omega/e^6\right)d\sigma_b^c/d\omega$, evaluated by using the formula from ref. [2], as a function of the ratio ω/ε_1 in the case of SiO2 mono crystal and Moliere parameterization of the screened atomic potential for $2\pi u_0/a_1 = 0$ (dashed curve), $2\pi u_0/a_1 = 0.82$ (full curve).

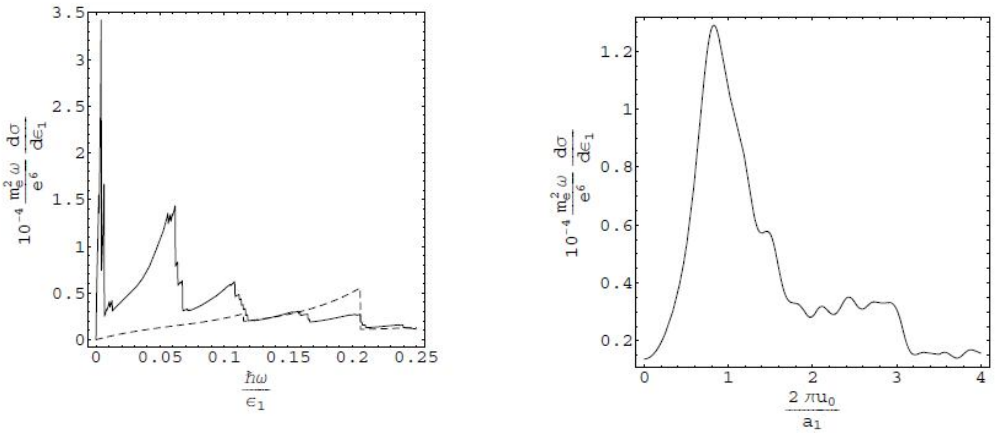

Figure 1: Coherent bremsstrahlung cross-section, $10^{-4}\left(m_e^2\omega/e^6\right)d\sigma_b^c/d\omega$ evaluated by the formula from ref. [2], as a function of ω/ε_1 for $2\pi u_0/a_1 = 0$ (dashed curve), $2\pi u_0/a_1 = 0.82$ (full curve), and as function of $2\pi u_0/a_1$ for the photon energy corresponding to $\omega/\varepsilon_1 = 0.055$. The values for the other parameters are as follows: $\psi = 0.00037$, $\varepsilon_1 = 20$ GeV, $\upsilon_s = 5 \cdot 10^9$ Hz.

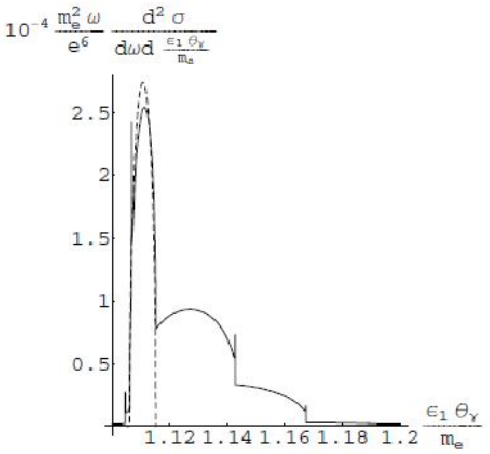

Figure 2: Coherent bremsstrahlung cross-section, $10^{-4}\left(m_e^2\omega/e^6\right)d^2\sigma_b^c/d\omega d\left(\varepsilon_1\theta_\gamma/m_e\right)$, evaluated by formula (19), as a function of $\varepsilon_1\theta_\gamma/m_e$ for $2\pi u_0/a_1 = 0$ (dashed curve), $2\pi u_0/a_1 = 0.82$ (full curve), $\psi = 0.00037$. The values for the other parameters are as follows: $\omega/\varepsilon_1 = 0.055$, $\varepsilon_1 = 20$ GeV, $\upsilon_s = 5\cdot 10^9$ Hz for the frequency of acoustic waves.

On the right panel the same quantity is plotted as a function of $2\pi u_0/a_1$ for the photon energy corresponding to $\omega/\varepsilon_1 = 0.055$. The values for the other parameters are taken as follows: $\psi = 0.00037$, $\varepsilon_1 = 20$ GeV, $\upsilon_s = 5\cdot 10^9$ Hz for the frequency of acoustic waves. For the amplitude of the deformation field corresponding to the numerical data of Fig. 1 the relative displacement of the neighboring atoms is of the order $10^{-3}\,\mathring{A}$, which is much smaller than the interatomic distance $(\sim 5\,\mathring{A})$. For these values of parameters, when one has an enhancement of the cross-section integrated over the angle θ_γ we have numerically analyzed the angular dependence of the bremsstrahlung cross-section by making use of formula (19). In Fig. 2 the quantity $10^{-4}\left(m_e^2\omega/e^2\right)d^2\sigma_b^c/d\omega d\left(\varepsilon_1\theta_\gamma/m_e\right)$ is depicted as a function of $\varepsilon_1\theta_\gamma/m_e$ in the case of SiO2 monocrystal for $u_0 = 0$ (dashed curve) and $2\pi u_0/a_1 = 0.82$ (full curve). The values for the other parameters are taken as follows: $\omega/\varepsilon_1 = 0.055$, $\varepsilon_1 = 20$ GeV, $\upsilon_s = 5\cdot 10^9$ Hz $\psi = 0.00037$.

As we see from the presented example, the presence of the deformation field leads to the appearance of additional peaks in the angular distribution of the emitted photon even for such ranges of values of an angle of photon momentum, where due to the requirement $-1 \le y \le 1$ the cross-section of process is zero when the deformation is absent. As we have already mentioned before, this is related to that in the presence of the deformation field the number of possibilities to satisfy the condition $g_{m\parallel} \ge \delta + g_{m\perp}^2/(2\varepsilon_1)$ in the summation in formula (8) increases due to the presence of the additional term $mk_{s\parallel}$ in the expression for $g_{m\parallel}$.

Acknowledgment

I am grateful to Aram Saharian for valuable discussions and suggestions.

References

1. A. A. Saharian, A. R. Mkrtchyan, V. V. Parazian, L. Sh. Grigoryan, Mod. Phys. Lett. **A19**, 99 (2004).
2. V. V. Parazian, J. Contemp. Phys. **41**, 221 (2006); A. R. Mkrtchyan, A. A. Saharian, V. V. Parazian, Mod. Phys. Lett.**B23**, 2573 (2009).
3. A. I. Akhiezer, V. F. Boldyshev, N. F. Shulga, J. Nucl. Phys. **22**, 1185 (1975).
4. H. Bethe, W. Heitler, Proc. Roy. Soc., **146**, 83 (1934); H. Bethe, L. Maximon, Phys. Rev., 93, 768 (1954); H. Davis, H. Bethe, L. Maximon, Phys. Rev., **93**, 788 (1954); H. Olsen, L. Maximon, H. Wergeland, Phys. Rev., **106**, 27 (1957); V. N. Baier, V. M. Katkov, V. S. Fadin, Radiation of relativistic electrons (Atomizdat, 1973) (in Russian).
5. V. V. Parazian, J. Phys.: Condens. Matter **21**, 185401 (2009).
6. J. S. Dana, E. S. Dana and C. Frondel, The System of Mineralogy. Vol. 3 Silica Minerals (John Wiley and Sons, 1962).
7. Acoustic Crystals, Edited by M. P. Shaskolskaya (Nauka, 1982) (in Russian).

Section V

Time – spatial control of characteristics X – Ray radiation by external influences.

Diffraction of Narrow X-Rays Bean in Weak Deformed Crystall

K.G. Trouni, G.R. Grigoryan

Institute of Applied Problems of Physics, Yerevan, Armenia

Huygens-Fresnel principle has been formulated for dynamic diffraction of x-ray radiation in a crystal with a weak field of deformation of a spatial lattice. Formulated principle allows to construct wave functions of the diffracted beams in a crystal lattice at any distance of r of a point source of initial radiation from a crystal.Features of interference absorption (Borrman effect) of x-ray wave packages in crystal are discussed for a weak field of displacement of a lattice.

Previosly in [1] the problem of dynamic diffraction of a narrow x-ray beam (spherically- wave approximation) in a crystal with a weak field of deformation was considered. Separate interest is represented by cases when the initial beam is formatted by a point source at some final distance from a crystal. In difference from a case of spherical wave approximation at which the initial beam contains all directions around of the exact Bragg direction of this reflection for the corresponding atomic planes of a lattice an incident beam of this kind raises a wave field essentially depending on distance a source- crystal. As a result of diffraction of such waves in a crystal two modes corresponding strongly and weakly absorbed wave fields [2] are raised in not deformed crystal. In case of a weak deformed crystal the curvature of trajectories of beams of two modes of a wave field can be neglected [3]. The curvature of trajectories of the diffracted x-ray waves is caused by a gradient of relative deformation of a lattice of a crystal. Criterion of such approach is a little changes of relative deformation within extinction length - characteristic length of dynamic diffraction of X-rays on a spatial lattice of a crystal. As a result of such assumption the trajectory of beams are such with that in not deformed crystal, i.e. rectilinear. Additional phase composed, caused by a deformation field, at such approach may be represented as an integral along a beam trajectory from the function of displacement describing local deviation from exact Bragg condition.

So, we will consider a case of symmetric Laue geometry with the crystal oriented near Bragg's condition in relation to a source of primary x-ray radiation with perpendicular to an entrance surface reflecting planes. According to Kirchof's integral formulation of a Huygens-Fresnel principle [4] quasiamplitudes ψ_0 и $\psi_h$of the crystal wave field are connected by functions by G_j (x, z) (j=0, h), defining influence of initial radiation $\psi_i(x', z')$in a point (x', z') of the planes of an entrance surface of a crystal (z=0) in the field in a point of observation P (x, z) in the registration plane:

$$\psi_j(x,z) = \int G_j(x-x', z-z')\psi_i(x', z')dx' \quad (1),$$

where integration is carried out on section of z' = 0 coinciding with an entrance surface of a crystal. The coordinate system (x, z) is chosen as follows: x axis is parallel to an entrance surface of a crystal, and the axis z is directed along an internal normal of this surface. Except this system the alternative system of coordinates by $(s_0, s_h)$with axes parallel to wave vectors $\overrightarrow{K_0}$ and $\overrightarrow{K_h}$ the diffracted waves in a lattice further will be also used. Transition from one system of coordinates to another will be defined by transformations:

$$z = (s_0 + s_h)\cos\theta_B$$

$$x = (s_0 - s_h)\sin\theta_B \text{ (θ _ Bragg's B-angle). (2)}$$

Let's consider diffraction of hard x-ray radiation on a spatial lattice of the crystal which field of displacement is described by square-law function of coordinates

$$\vec{h}\vec{u}(\vec{r}) = \propto s_0 s_h, \quad (3)$$

where $\vec{h}$ - a vector of a rreciprocal lattice for corresponding reflection.

Propagation of x-ray wave packages in a lattice is described by the wave equations following from Takagis equations.

For the reflected beam wit quasiamplitude ψ_h the equation looks as follows:

$$\frac{\partial^2 \psi_h}{\partial s_0 \partial s_h} - i \propto_h \frac{\partial \psi_h}{\partial s_0} + (\sigma\bar{\sigma} - i\alpha)\psi_h = 0, \quad (4)$$

here $\bar{\sigma} = \pi k c \chi_{\bar{h}}$, $\sigma = \pi k c \chi_h$, a $\propto_h = 2\pi k \frac{\partial \vec{h}\vec{u}(\vec{r})}{\partial s_n}$determines local shift from Bragg's condition, caused by lattice deformation, c- polarization factor equal 1 or $\cos 2\theta_B$ for two independent conditions of polarization of radiation, $\chi_h$and $\chi_{\bar{h}}$a Fouries-coefficients of polarizability of a crystal for direct ($\vec{h}$) and the backward $\vec{h}$diffraction vectors, respectively, $k = \frac{1}{\lambda}$wave number of radiation in vacuum.

In case of square-law functions (3) for displacement fields equation (4) by substitution

$$z = i\alpha s_0 s_h$$

leds to the known equation for confluent hyper geometric functions[6]

$$z\frac{\partial^2 \psi_h}{\partial z^2} + (1 - z)\frac{\partial \psi_h}{\partial z} - \left(1 - \frac{\sigma\bar{\sigma}}{i\alpha}\right)\psi_h = 0, \quad (5)$$

which solution is Kummer's function [5] ${}_1F_1(a, 1, z)$

$$\psi_h = {}_1F_1\left(1 - \frac{\sigma\bar{\sigma}}{i\alpha}, 1, z\right) = {}_1F_1\left(1 - \frac{\sigma\bar{\sigma}}{i\alpha}, 1, i\alpha s_0 s_h\right) \quad (6)$$

In case of small deformations, namely at

$$\left|\frac{\sigma\bar{\sigma}}{i\alpha}\right| \gg 1, \quad (7)$$

the solution (6) has asymptotic representation [6]

$$\psi_h \cong e^{i\alpha s_0 s_h} J_0(2\sqrt{(\sigma\bar{\sigma} - i\alpha)s_0 s_h}), \quad (8)$$

where $J_0(Y)$ Bessel's function of a zero order from complex argument Y. This solution differs from the relevant solution for perfect (not deformed, $\propto$ =0) crystal [7]by first phase factor in (8), and also, additional to parameter $\sigma\bar{\sigma}$ composed-iα in argument of function of Bessel. For amplitude of a transmitted wave ψ_0 from (8) taking into account the second of Takagi's equations [4]

$$-i\sigma\psi_0 = \frac{\partial \psi_h}{\partial s_h} - -i \propto_h \psi_h, \quad (9)$$

we have

$$-i\sigma\psi_0 \cong e^{i\alpha S_0 S_h}\sqrt{(\sigma\bar{\sigma}-i\alpha)\frac{S_0}{S_h}}J_1(2\sqrt{(\sigma\bar{\sigma}-i\alpha)s_0 s_h}), \qquad (10)$$

where $J_1(Y)$ Bessel's function of the first order.

By means of solutions (8), (10) point source functions are represented, since the last are solutions of the differential equation conjugate to the equation (5) with δ – function in the right part of the last and known as Green's functions of the corresponding problem.

Let monochromatic x-ray radiation falling on a crystal proceeds from the point source remote from the beginning of coordinates (x, y, z) on a vector $-\frac{\vec{k_0}}{k}\vec{r}$ so the wave field of an initial beam will be described by function

$$\frac{e^{-2\pi ikl}}{l}, \qquad (11)$$

where l -distance between a source and the current point on z=0 surface. In known parabolic approach because of a smallness of effective area around the beginning of coordinates ($x \ll l$) in the plane of observation (y=0) l it is possible to expand in a row round x=0 point, being limited to members square-law on x and substituting $l \cong r$ in a denominator (11) we will receive

$$\frac{e^{-2\pi ikl}}{l} \approx \frac{e^{-2\pi ikr\left(1+\frac{x^2}{2r^2}+\frac{x\sin\theta_B}{r}\right)}}{r} \quad . \qquad (12)$$

The linear member on x in an exhibitor (12) describes angular deviation corresponding components in a falling beam from Bragg's exact condition, the square-law member is caused by curvature of the wave front of an initial package. At $r \to \infty$ the last disappears that corresponds to transition to plane-wave approach, and at $r \to 0$ the square-law member appears prevailing that corresponds to approach of a spherical wave of Kato [8]. Thus approach (12) allows to formulate Huygens-Fresnel's principle in all interval $0 \le r < \infty$ source- crystal distances. Coming back to the integral formulation (1) with the account (8), (10) and (12) quasiamplitudes ψ_0 and ψ_h of the diffracted beams it is necessary to replace functions of influence of $G_h(x-x',z)$ with functions

$$G_h(x-x',z) = -\frac{i\sigma}{\cos\theta_B}e^{\frac{i\alpha}{4}\left(\left(\frac{z}{\cos\theta_B}\right)^2-\left(\frac{x-x'}{\sin\theta_B}\right)^2\right)}J_0\sqrt{(\sigma\bar{\sigma}-i\alpha)\left(\left(\frac{z}{\cos\theta_B}\right)^2-\left(\frac{x-x'}{\sin\theta_B}\right)^2\right)} \quad (13)$$

$$G_0(x-x',z) = e^{\frac{i\alpha}{4}\left(\left(\frac{z}{cos\,\theta_B}\right)^2-\left(\frac{x-x'}{sin\,\theta_B}\right)^2\right)}\sqrt{\frac{\frac{z}{cos\,\theta_B}+\frac{x-x'}{sin\,\theta_B}\left(1-\frac{i\alpha}{\sigma\bar{\sigma}}\right)}{\frac{z}{cos\,\theta_B}-\frac{x-x'}{sin\,\theta_B}}}J_1\sqrt{(\sigma\bar{\sigma}-i\alpha)\left(\left(\frac{z}{cos\,\theta_B}\right)^2-\left(\frac{x-x'}{sin\,\theta_B}\right)^2\right)}$$

References

1. К.Г. Труни, В. Р. Кочарян, Г. Р. Григорян. Изв. НАН. Армении, физика 47, 131 (2012)
2. A. Authier. Dynamical Theory of X-ray Diffraction, New York, Oxford University Press. (2001)

3. Л. А. Арутюнян, К. Г. Труни. Изв. НАН Армении, Физика, 5, 272, (1999)
4. S. Takagi. Acta Crystallogr., 15, 1311(1963)
5. П. В. Петрашень, Ф. Н. Чуховский. ЖЭТФ, 69,477 (1975)
6. Е. Янке, Ф. Эмде, Ф. Леш. Специальные функции. М. Наука (1968)
7. В. Л. Инденбом, Ф. Н. Чуховский. УФН, 107, 229 (1972)
8. L. V. Azaroff, R. Kaplow, N. Kato, R. J. Weiss, A. J. C. Wilson, R. A. Young X-ray Diffraction, New York, McGraw-Hill. (1974)

X-ray Localized Modes and High Resolution X-ray optics

Vladimir A. Belyakov

L.D.Landau Institute for Theoretical Physics, Moscow, Russia

Adstract: X-ray localized in crystal structures modes (being an analogue of known in photonic crystals optical edge [1,2] and defect [3] modes) are theoretically studied. As objects for X-ray localized modes observation may be regarded perfect crystals, naturally and by means of external fields modulated crystals, perfect multilayers and the same structure with plane defects. Studying of the problem performed in the framework of two-waves dynamical theory of X-ray diffraction. Dispersion equations for X-ray localized modes and expressions for the energy distribution in X-ray localized modes are found. In the limit of thick crystal layers analytic expressions for the mode life-times (frequency imaginary additions) are obtained. It is shown that in this limit the X-ray edge mode life-time growths as a third power of the crystal layer thickness [4]. In this limit the X-ray defect mode life-time growths exponentially with increase of the crystal layer thickness [6]. The influence of X-ray localized modes on the transmission and reflection spectra for perfect crystalline structure is studied. It is shown that the effect of anomalously strong absorption (amplification) reveals itself at the X-ray localized mode frequencies in absorbing (amplifying) crystals. In the case of the X-ray defect mode narrow transmission lines reveal themselves inside the frequency range of stop band. The options for experimental observation of the X-ray localized modes with the help of synchrotron radiation [4,6] are discussed. The perspectives of application of X-ray for studies of inelastic channels of X-ray interaction with crystalline structures and for ultra high X-ray monochromatization are pointed out.

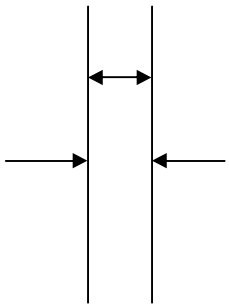

Fig.1a Schematic of the boundary problem for XEM

General equations: We shell study two types of localized modes: One mode localized in a perfect layer of periodic medium at wave length close to the edge of stop-band (so called Edge mode, see Fig.1a) and another one localized at defect layer in a perfect periodic medium at wave length inside of the stop-band (so called Defect mode, see Fig.1b). In the both cases it will be assumed the periodicity axes is perpendicular to the surfaces of periodic medium and to the defect layer (if it is available). Let us begin from the case of the Edge mode (EM) (see Fig.1a). At the beginning we have to solve the boundary problem for reflection and transmission of a monochromatized X-Ray beam incident normally at a perfect layer of periodic medium assuming that the X-Ray wave length is close to the structure period p. The solution of this problem (obtaining of the reflection and transmission coefficients) in the framework of two-waves dynamical theory of X-ray diffraction is well known (see, for example [5]), so we shall not present the corresponding procedure and shall use the final results.

If a plane wave is incident at the sample a Bloch wave [5] formally consisting of infinite number of plain waves is excited inside the sample. However only a few of these plain waves may be of large amplitude (order of one), the values of other amplitudes are negligibly small if space modulation of the sample dielectric constant is small. In our case of the two-waves approximation only two plane waves are of large amplitudes. So, the X-ray field in the sample may be presented by a superposition of only two plane waves of the form

$$E(z,t) = e^{-i\omega t}\,[A^{+}\exp(iK_{+}z) + A^{-}\exp(iK_{-}z)] \qquad (1)$$

where ω is the X-ray frequency and the wave vectors $K\pm$ satisfy to the condition

$$K_{+} - K_{-} = \tau, \qquad (2)$$

where τ is the reciprocal lattice vector of the periodic structure ($\tau = 2\pi/p$, where p is the structure period).
The wave vectors $K_{+}^{\pm}$ normalized by $\tau/2$ (i.e. $k_{+}^{\pm} = K_{+}^{\pm}/(\tau/2)$) and entering in two eigen waves in the sample determined by Eq.(1) are given by the following formula:

$$k_{+}^{\pm} = 1 \pm q = 1 \pm [\Delta\varepsilon^2 - \delta^2]^{1/2}/2, \qquad (3)$$

where $\Delta\varepsilon = \varepsilon - 1 - \delta$, ε is the X-ray photon energy normalized by ch/2p and δ is the amplitude of dielectric constant modulation.

The wave vectors $K_{-}^{\pm}$ are determined by the Eq.(2) and Eq.(3).

The ratio of amplitudes (A^{-}/A^{+}) in the eigen waves (1) is given by the expression

$$\xi^{\pm} = (A^{-}/A^{+})^{\pm} = \delta/(\Delta\varepsilon \pm [(\Delta\varepsilon)^2 - \delta^2]^{1/2}) \qquad (4)$$

The amplitudes of the two eigen waves $A_{\pm}^{+}$ and $A_{\pm}^{-}$ excited in the layer by the incident X-ray wave (with the amplitude equal to unity) are determined by the following equations

$$A_{+}^{+} + A_{-}^{+} = 1 \qquad (5)$$

$$\exp[i K_{-}^{+} L]\,\xi^{+} A_{+}^{+} + \exp[i K_{-}^{-} L]\,\xi^{-} A_{-}^{+} = 0$$

where L is the layer thickness.The explicit expressions for amplitude reflection R_a and transmission T_a coefficients if one introduces $Q = q\tau/2$. take the form:

$$R_a = -\delta\,(i\sin QL)/(2q\cos QL - i\delta\varepsilon\sin QL) \qquad (6)$$

$$T_a = 2q\exp[i\tau L/2]/(2q\cos QL - i\delta\varepsilon\sin QL).$$

The reflection $R = |R_a|^2$ and transmission $T = |T_a|^2$ coefficients versus the X-ray wave vector (energy) are presented at Fig.2 for typical values of the related parameters. At $Q = n\pi/L$, where n is an integer number, $R = 0$ and $T = 1$ for nonabsorbing medium.

The values of the eigen wave amplitudes $A_{\pm}^{+}$ and $A_{\pm}^{-}$ calculated according Eq.(5) are strongly oscillating functions of the incident X-ray energy (see Figs.2b presenting the calculation results for $L/p=250$). At the points of amplitudes $A_{\pm}^{\pm}$ maxima, close to the band edges, their values are much larger than the amplitude of incident at the layer X-ray wave.

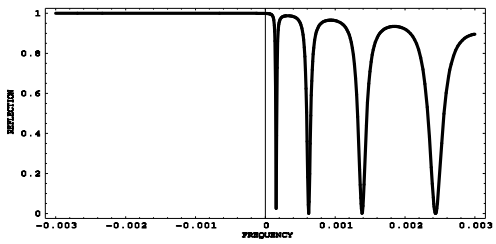

Fig.2a Reflection coefficient of eigen and incident X-ray waves at the specific energies

It happens that at the amplitude $A_{\pm}^{\pm}$ maxima points X-ray energies just coincide with the energies of zero reflection following from (6) for nonabsorbing periodic media (see Figs.2a; here and at all figures below at the frequency axes plotted $\nu=\delta[2(K-K_B)/(\delta K_B) -1]$, Brag wave vector $K_B =\tau/2$ and $\delta=0.05$.).

The mentioned relationship between the amplitudes shows that the X-ray energy density in the layer for these energies is much higher than the corresponding energy density of the incident wave outside the layer. So, one may to conclude that at the corresponding X-ray energies the incident X-ray wave excites some localized X-ray mode in the layer.

X-RAY EDGE MODES: In general, the performed above calculations of reflection R and transmission T coefficients as a function of the X-ray energy (according Eqs.(6)) give well known in the dynamical diffraction theory results [5] (Fig.2a). Namely, X-ray strong reflection inside the stop band and energy oscillations of T and R outside of the stop band edges with $0\le R\le 1$ and conserving of the relationship $T+R=1$ for all X-ray energies for nonabsorbing media. The corresponding calculations of the amplitudes of the excited in the layer eigen waves $A_{\pm}^{+}$ (Fig.2b) reveal a nontrivial energy dependencies of A_{+}^{+} and A_{-}^{+}. Namely, close to the stop band edges (outside of the stop band edges) their energy oscillations are accompanied by an essential enhancement of the amplitude values relative to the incident X-ray wave amplitude. The thicker is a layer the higher is the enhancement. As the Figs.2 show the positions of the eigen amplitude oscillations maxima (for a nonabsobing layer) just coincide with the positions of reflection coefficient minima for nonabsorbing layer at which $R=0$.

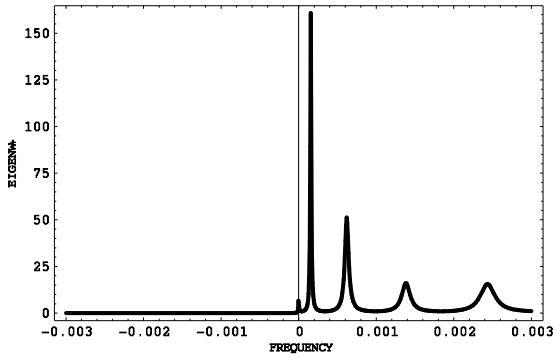

Fig.2b Eigen wave amplitude A_{+}^{+}

To find X-ray localized modes one has to solve the homogeneous system corresponding to the inhomogeous system (5), i.e. the Eqs.(5) with zero values of the right hand side. The condition of solvability of the obtained homogeneous system determines the discrete frequencies of these localized modes:

$$tg(q\tau L/2)= -2iq/\Delta\varepsilon \qquad (7)$$

In a general case the solution of Eq.(7) determining the XEM energies (frequencies) ε_{EM} may to be found only numerically. The XEM energies ε_{EM} occur to be complex quantities which may be presented as $\varepsilon_{EM} =\varepsilon^0_{EM}(1+i\Delta)$, where Δ in real situations is a small parameter. So, the localized modes are weakly decaying in time, i.e. they are quasistationary modes. Luckily, an analytic solution may be found for some limiting case, namely, for a sufficiently small Δ ensuring the condition $(QL)Imq<<1$. In this case the values of ε^0_{EM} real part are coinciding with the energies of zero values of reflection coefficient R for a nonabsorbing layer determined by the condition

$$(\tau Lq/2)=n\pi \quad \text{and} \quad \Delta=-½(\delta)(n\pi)^2/((\delta)L\tau/4)^3, \qquad (8)$$

where n is the edge mode number growing with departure of the X-ray energy from the stop band edge (with n=1 corresponding to the X-ray energy closest to the stop band edge).

In the found solution of the homogeneous system following from (5) the eigen solutions amplitude ratio is $A_-^+/ A_+^+ =-1$ and the X-ray field inside the layer is a superposition of two eigen waves of the form determined by Eq.(1) with the found amplitude ratio. The following from (1) explicit expression for the X-ray field inside the layer is given by the formula:

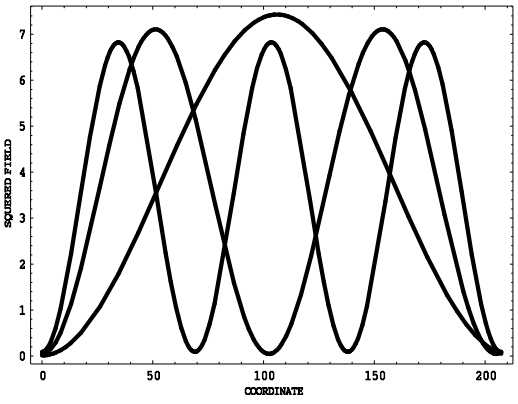

Fig.3 Envelope of XEM energy distribution

$$E(z,t) = \exp(-i\omega_n t) [2i\exp(i\tau z/2)\sin(Qz)-\exp(-i\tau z/2)(\xi^+\exp(iQz)+\xi^-\exp(-iQz))], \quad (9)$$

where ω_n is determined by the XEM energy ε_{EM}, and q (Q) is determined by Eq.(3).

The presented by (9) eigen solution of the boundary problem is a localized at the layer thickness L standing wave with a modulated along z amplitude. The number of modulation periods at the layer thickness L is coinciding with the XEM number n. The distributions of XEM density of energy following from Eq.(9) for the XEM numbers n = 1,2,3 are presented at Fig.3. The Fig.3 shows that in the XEM the distributions of XEM density of energy is localized inside the layer and the density of of energy experiences oscillations inside the layer with the number of the oscillations just equal to the XEM number n. The Fig.3 presents a total energy distribution in the layer (L/p=200, as the coordinate plotted z/p). However, as it is clear from the Eqs.(1,9), in each point of the layer the total energy density is presented by two X-ray plane waves propagating in the opposite directions, so one may calculate separately for any point in the layer the intensities of X-Ray waves propagating in the

opposite directions. In general, the coordinate distribution of the corresponding energy density of the X-Ray waves propagating in the opposite directions is similar to the one presented at Fig.3. However these distributions are of a special interest close to the layer surfaces. The Fig.4 (parameters are the same as at Fig.3) shows the density of energy coordinate distributions of the waves propagating inside and outside of the layer close to the layer surfaces.

One can see that at the layer surface the density of energy of the wave propagating inside the layer is strictly zero, but for the same point the density of energy of the wave propagating outside the layer is not zero, however small. It means that the XEM energy is leaking from the layer through its surfaces. From Eq.(9) follows the expression for the leaking wave amplitude at the layer surface

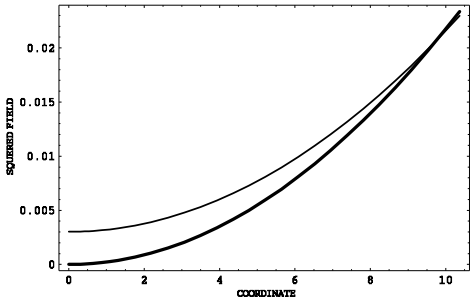

Fig.4 Energy flow (inward the sample bold line)

$$E_{out}=(\tau n\pi/(\delta L))/(\tau/2)^2 \approx np/(L\delta). \qquad (10)$$

The Eq.(10) shows that the energy leakage from XEM is inversely proportional to the squared layer thickness L and proportional to the squared number n of XEM. So, the most long living is the first XEM. If $L\delta/p \ll 1$ the leaking wave amplitude E_{out}, as the Eq.(10) shows, is small, (i.e. $E_{out} \ll 1$).

For a nonabsorbing layer (which is under consideration here) the only source of decay is the X-ray leakage through its surfaces, i.e. the decreasing of the XEM energy in unite time is simply equal to the X-ray energy flow via both layer surfaces. The leaking energy flow is $2c\,|E_{out}|^2$, where c is the speed of light, so one using (9,10) easily gets the following expression for the XEM life-time τ_m

$$\tau_m=\int|E(\omega_{EM},z,t)|^2dz/\{d[\int|E(\omega_{EM},z,t)|^2dz|]/dt\}\approx(5/16)(L/c)[1+(4/5)(L\delta/dn)^2], \qquad (11)$$

where the integration runs over the sample thickness. At the condition $(L\delta/pn) \gg 1$ the Eq. (11) reduces to

$$\tau_m \approx (1/4)(L/c)(L\delta/pn)^2. \qquad (12)$$

So, for sufficiently thick layers for growing their thickness L the XEM life-time τ_m growths as a third power of the thickness and is inversely proportional to the square of the XEM number n.

ABSORBING LAYERS: Let us examine now XEM in absorbing periodic media. The motivation of this study, in particular, is due to the anomalously strong absorption effect known in the photonics [2]. What will be the corresponding effect in the X-ray optics? Examine in more details the formulas of the preceding sections assuming for simplicity that the absorption in the layer is isotropic and constant in the layer. The absorption of X-ray results in appearance of imaginary part in the X-ray wave vector (It is equivalent to a complex dielectric constant of the layer). Define the ratio of the X-Ray wave vector imaginary part to its real part as γ, i.e. $k=k_0(1+i\gamma)$. Note, that at actual situations $\gamma<<1$. At Figs.5 (L/p=50; γ=0.001 (a),γ=0.005 (b)) the 1-R-T calculated versus the real part of the X-ray wave vector (frequency) are presented for several values of positive γ (positive γ corresponds to the X-ray absorption). Due to the assumed isotropy of the absorption the energy (wave vector) dependencies of the calculated characteristics are symmetric relative to the Bragg energy (the mid point of the stop band), it is why only the energy above the Bragg energy are presented at the figures. All mentioned quantities reveal energy beats close to the edge of the selective reflection band. The positions of corresponding maxima and minima are determined by the layer thickness L, δ and are slightly dependent on the value of γ.

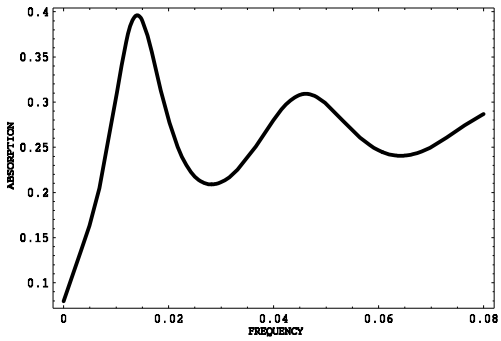

Fig.5a Total absorption versus frequency

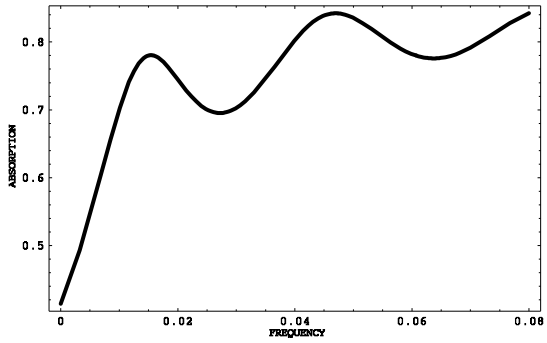

Fig.5b Total absorption versus frequency

In absorbing layers the sum of intensities of the reflected and transmitted beams is less than the intensity of the incident beam, i.e. R+T<1. The equality holds only for nonabsorbing layers, i.e. in this case R+T=1. As an example the positions of the beats minima of the reflection coefficient R (following from (6)) are seen at Fig.2a for nonabsorbing layer.

The most interesting situation corresponds to the case of a>>1(a= $\delta L\tau/4$) close to the edges of selective reflection band. The edges of selective reflection band K_e are connected to the Bragg wave vector KB by the following relation

$$K_e = K_B/(1\pm\delta)^{1/2} = \tau/2(1\pm\delta)^{1/2}. \qquad (13)$$

So, $\nu/(\delta-1)$ at the edges is $\nu_e = 2(1/(1\pm\delta)^{1/2}-1)/\delta \approx -(\pm 1)$.

For a small γ and LImQ<<1 the reflection and transmission coefficients following from Eq.(6) at the energies of reflection minima are reduced to the following expressions:

$$R=(a^3\gamma)^2/[(n\pi)^2+a^3\gamma]^2, \qquad T=(n\pi)^4/[(n\pi)^2+a^3\gamma]^2, \qquad (14)$$

$$R+T=1-2(n\pi)^2a^3\gamma]/[(n\pi)^2+a^3\gamma]^2.$$

It foolows from (14) that for each n maximal absorption, i.e. maximal 1-R-T, occurs for $(n\pi)^2 = a^3\gamma$. It means that the maximal absorption occurs for a special relationship between δ, γ and L and if this relationship, i.e. $(n\pi)^2 = a^3\gamma$, is fulfilled R=1/4, T=1/4 and 1-R-T=1/2. This result corresponds to a strong enhancement of the X-ray absorption for weakly absorbing layers because the assumed smallness of γ. The absorption enhancement may be observed by direct measuring of 1-R-T. However, from the experimental point of view, more favorable looks a measuring of the intensity of some inelastic process, for example, measuring of secondary particles produced by X-ray via inelastic processes.

X-RAY DEFECT MODES: Let us examine the X-ray defect mode (XDM), for certainty, at the defect structure (DMS) consisting from two perfect periodic layers with inserted between them an isotropic layer of thickness d (see Fig.1b). Similarly to the case of XEM the problem, is examined in the dynamic diffraction theory approximation [6] with conserving all main notations accepted for XEM for the X-ray propagation direction coinciding with the periodicity axes (normal incidence at the DMS, see Fig.1b). So, we just present here the main results related to the XDM (all details of the study may be found in the citations) as the following. The expressions for X-ray reflection and transmission coefficients for DMS as functions of the frequency of incident at the DMS X-ray are found. It happens that for the definite discrete X-Ray energies (frequencies) the amplitudes of the X-ray eigen waves in the DMS reach sharp maxima.The corresponding energies are just inside of the X-ray stop band (energies forbidden for X-ray propagation in the periodic layers) and coincide with the frequencies of localized in the DMS X-ray defect modes in a direct analogy with the optical defect modes [3]. The dispersion equation for the localization problem is found in the dynamic diffraction theory approximation [6] for the X-ray propagation direction coinciding with the periodicity axes. The dispersion equation for the XDM may, similarly to the optical case [3], be presented in the form:

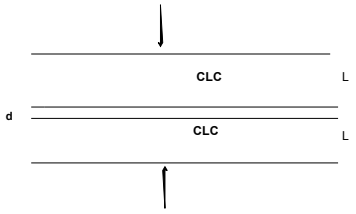

Fig.1b Schematic of the boundary problem forXEM

$$\{\exp(2ikd)\sin^2qL-\exp(-i\tau L)[(\tau q/\kappa^2)\cos qL+i((\tau/2\kappa)^2+(q/\kappa)^2-1)\sin qL]^2/\delta^2]\}=0, \qquad (15)$$

where k and q are the X-ray wave vector and diffraction addition to it, respectively.

The X-ray reflection and transmission coefficients for DMS may be expressed via reflection and transmission coefficients of an individual layer:

$$|T(d,L)|^2=|[T_eT_d\exp(ikd)]/[1-\exp(2ikd)\,R_dR_u]|^2,$$

$$|R(d,L)|^2=|\{R_e+R_uT_eT_u\exp(2ikd)/[1-\exp(2ikd)R_dR_u]\}|^2, \qquad (16)$$

where $R_e(T_e)$, $R_u(T_u)$ and $R_d(T_d)$ are the amplitude reflection (transmission) coefficients of the layer (see Fig.1a) for the X-ray incidence at the outer top layer surface, for the X-ray incidence at the inner top layer surface from the inserted defect layer and for the X-ray incidence at the inner bottom layer surface from the inserted defect layer, respectively.

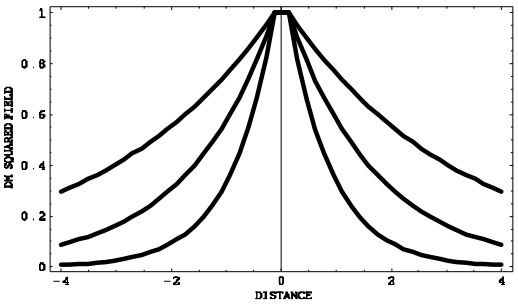

Fig.6 Envelope of XDM

The X-ray energy density in DMS for XDM is

presented at Fig.6 (From the top to bottom δ=0.05, 0.1, 0.2; d/p=0.5). Reflection (transmission) coefficients demonstrate minimum (maximum) in the stop band for X-ray propagating at the frequency of XDM (calculated reflection coefficients are presented at Fig.7(L/p=33, d/p=0.2) and Fig.8(L/p=33,d/p=0.5)).

The position of this minimum (maximum) inside the stop band energy distribution depends on d/p, the ratio of the defect layer thickness to the value of layer period.

For absorbing media X-ray experiences abnormally strong absorption at the XDM frequency. The XDM life-time is determined by solution of the dispersion equation (15) which in a general case has to be solved numerically and shows sharp increase of the life-time with increase of the periodic layers thicknesses. For thick periodic layers the XDM life-time may be found analytically. For the XDM frequency just at the stop band center the XDM life-time is presented by the formula

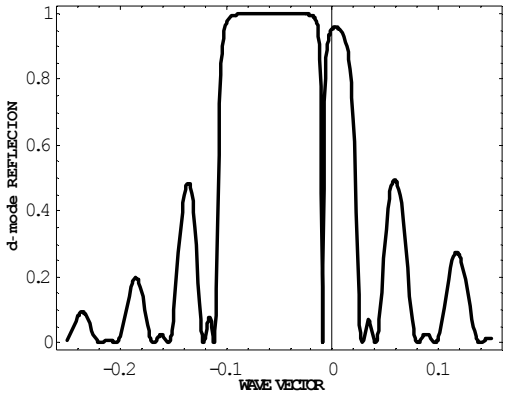

Fig.7 Reflection at DMS for d/p=0.2

$$\tau_D = [(3\pi(L/p)/(c\tau)]\exp[2\pi\delta L/p]. \qquad (17)$$

For the X-ray localized modes (the both EM and DM) phenomena related to these structures are of great interest because the perspectives to obtain a low threshold lasing in the X-ray wave length range [4,6].

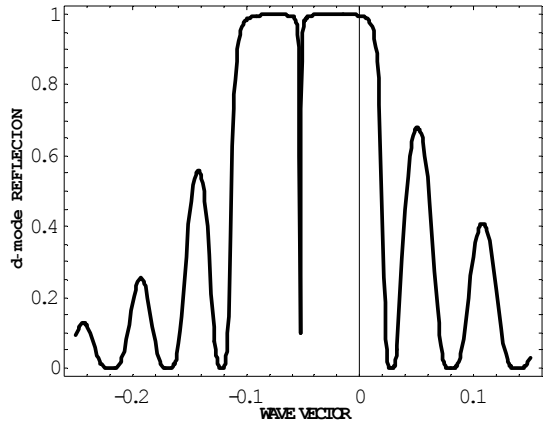

Fig.8 Reflection at DMS for d/p=0.5

Conclusion: There are several approaches to observe and investigate the localized X-ray modes (XEM and XDM). The simplest ones, in technical aspect, are connected with measuring of the MDS reflection and transmission spectra to observe minima in reflection and maxima in transmission (see Fig.7-8) and with measuring of the absorption enhancement at the XEM and

XDM frequencies. This kind of measurements demands a high X-Ray monochromatization [6] (order of 1 meV at the X-Ray energy order of 10 keV). For the lower X-ray energy the demands for X-ray monochromatization are much softer. So, modern synchrotron radiation (SR) sources look as an appropriate tool for such kind of studies. Another approach is connected with the time-domain measurements. The XEM and XDM life-tims are much longer than the flight-time of X-ray quantum through the distance corresponding to the DMS thickness (order of 1 picosec). It is why the time-delay technique is applicable to the studies of localized X-Ray modes. And here again the modern SR sources look as an appropriate tool for the time-delayed measurements because of their temporal structure of the X-Ray emission.

The presented here study demonstrate that the X-ray localizations in DMS are more efficient than in the case of XEM [6] and that the existing experimental techniques are applicable for the experimental investigations of the problem.

The work is supported by the RFBR grants № 11-02-90419-Ucr_f_a and 12-02-01016_a.

References

1. V. I.Kopp, Z.-Q. Zhang, and A. Z.Genack, Prog. Quant. Electron. **27(6)**, 369 (2003).
2. V.A. Belyakov and S.V.Semenov, JETP, **109**, 687 (2009).
3. V.A. Belyakov and S.V.Semenov, JETP, **112**, 694 (2011).
4. V.A. Belyakov and N.Kaputkina, Proceedings of the XIVth international workshop "Nanophysics and Nanoelectronics", NIzhnii Novgorod, 2010, V.2. p.327.
5. V.A. Belyakov, (1992). *Diffraction Optics of Complex Structured Periodic Media*, Springer Verlag, New York.
6. V.A. Belyakov, Proceedings of the XVIth international workshop "Nanophysics and Nanoelectronics", NIzhnii Novgorod, 2012, V.2. p.542.

Estimation of the Parameters of the Diffracted Monochromatic X-Ray Beams in External Influences

K.T. Hayrapetyan[1], S.N. Noreyan[1], V.V. Margaryan[1]

[1] *"X-Ray Pungs Laboratory", Armenia, Yerevan, Vagharshyan 19*
E-mail:x-ray.web.am,

The submitted work is devoted to studying of dependence of angular width of fully pumped monochromatic X-ray radiation upon the radiation source-- a single crystal (the investigated sample) distance and dependence of absolute value of intensity of monochromatic X-ray radiation upon the thickness of a single-crystal under external influences (fully pumped condition) in Laue geometry.

As it is known, the angular width of a fully pumped X-ray beam [1], under external influences, depends upon the thickness of a single-crystal (t) [2], and the radiation source – the sample distance [3]. For a fixed the radiation source - the single crystal distance with the single crystal thickness increase the angular width of the full pumped X-ray beam linearly increases.

From the mentioned above follows that with the thickness increase of the single crystal the angular area of the fully pumped beam increases and therefore the integrated intensity of the reflected beam increases.

On the other hand, the single-crystal thickness increase leads to the increase in the integrated intensity absorbed by the single crystal. It is natural to assume, that under the described conditions, by the thickness change of the investigated single crystal, it is possible to find that optimal thickness, at which the absolute value of the fully pumped X-ray beam, will be maximal.

So, we assume that a spherical X-ray beam with a homogeneous distribution of intensity is falling on the crystal, which angular width is $\Delta\theta$. In this case the integrated intensity of the incident beam can be expressed as: $I_0 = k\Delta\theta$, where k- angular density of the intensity of the beam for any direction within the angular aperture $\Delta\theta$. We denote the angular width of the fully pumped beam by $\Delta\varphi$. It is expressed as follows:

$$\Delta\varphi = \frac{t\frac{\Delta d}{d_0}tg^2(\theta)+\frac{t}{R}}{L_0\frac{\Delta d}{d_0}\sin(\theta)+1},$$

Where $t-$ the thickness of a crystal, R - radius of curvature of atomic planes, θ - Bragg angle, L_0 - distance between the source and a sample, d_0 - interplane distance, and Δd - measure of the average change of the interplane distance in unit distance. Then, the integrated intensity of the full pumped beam equals to

$$I = k\,\Delta\varphi\, e^{-(\mu t)} = k\frac{t\frac{\Delta d}{d_0}tg^2(\theta)+\frac{t}{R}}{L_0\frac{\Delta d}{d_0}\sin(\theta)+1}e^{-(\mu t)}$$

where μ - coefficient of linear absorption. The last expression takes its maximum value when $\mu t = 1$. Experimental setup is shown in Figure 1.

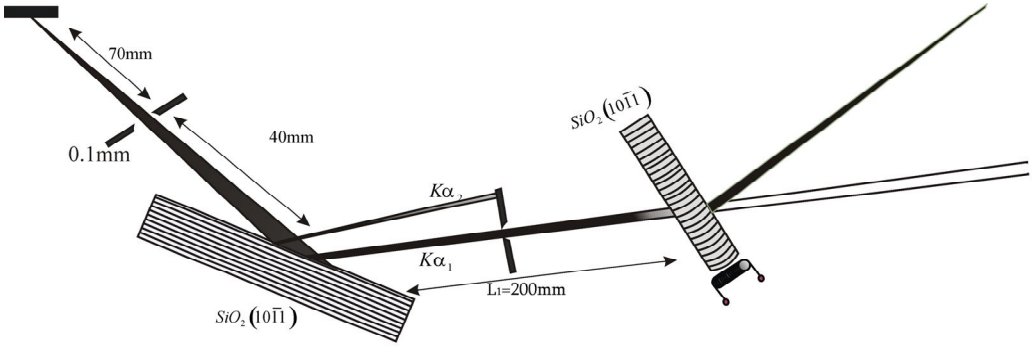

Fig. 1. The experimental setup

For the study of the dependence of the absolute value of the integrated intensity of the fully pumped X-ray beam upon the thickness of the crystal is chosen a plane-parallel plate of X-cut quartz crystal. The study was carried out for the reflecting atomic planes (10-11) of the chosen single crystal. By varying the thickness of the sample from 3.5 mm to 0.15mm in 100 μm steps, for each thickness the dependence of the absolute value of the integrated intensity of fully pumped X-rays beam upon the value of the temperature gradient is obtained. A detailed analysis of the results of the experimental studies shows that the absolute value of the integrated intensity of the fully pumped X-ray beam reaches its maximum under the condition: μt = 1. On Fig. 2 the dependence of the absolute value of the integrated intensity of the fully pumped X-ray beam upon μt expression is presented.

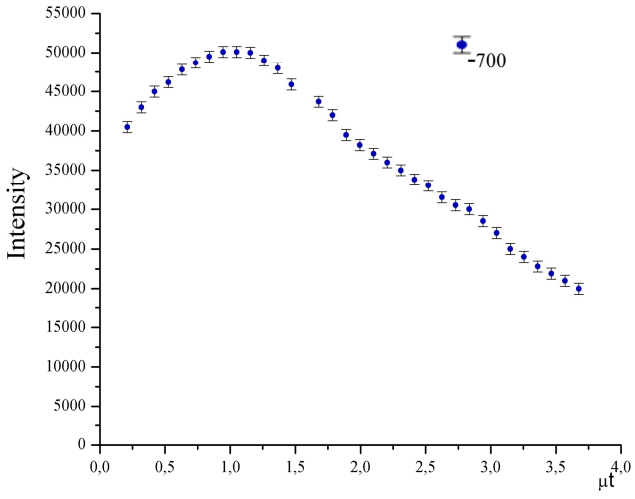

Fig. 2. The dependence of the absolute value of the integrated intensity of the fully pumped X-ray beam upon μt expression.

To prove the obtained experimental results, the Takagi equation is solved and the calculations are made. The shift function of the deformation field formed under the influence of the temperature gradient can be written in the form:

$$U_x = \frac{t^2 - (t-2z)^2}{8R}$$

As seen, it depends only upon the z coordinate. For the analysis of the angular width of the fully pumped X-ray beams at fixed distances (L_1, L_2), calculations for the intensity of the reflected beam as a function of the angle of reflection were made. In fig.3, the results of the calculations of the intensity of the fully pumped X-ray beam, depending on the angle of reflection for reflecting atomic planes (10-11) of the quartz single crystal with thickness t = 0.61mm, respectively located at distances L1 = 20 cm and L2 = 120 cm from the X-ray source are presented. In fig. 4 the results of the same calculations for the quartz single crystal with thickness t = 1.43mm are presented. In the presented curves it is clearly expressed the relationship of the angular widths of the fully pumped X-ray beams to the thickness of the sample and the distance between the X-ray source and the sample. As it can be seen, with the increase in the distance

between the source and crystal, the angular width of the fully pumped X-ray beam reduces, which well agrees with experimental results.

The theoretical calculations for estimating the value of the integrated intensity of the pumped X-ray beam at the condition of the fully pumping are made.

In fig. 5 the results of calculations of the dependence of the integrated intensity of the pumped X-ray beam upon the thickness for the reflecting atomic planes (10-11) of the quartz single crystal at the condition of fully pumping are presented. As seen in fig. 5, the maximum intensity of the reflected beam is obtained at $\mu t \approx 1$ which confirms the experimental results. The results of studies allow us estimate the parameters (integrated intensity, angular divergence, energy dispersion) of monochromatic X-ray beams, conditioned by an experiment geometry and parameters used in the single crystals.

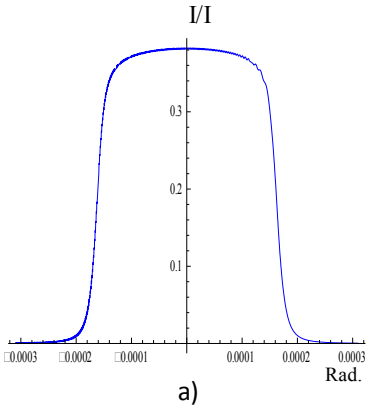

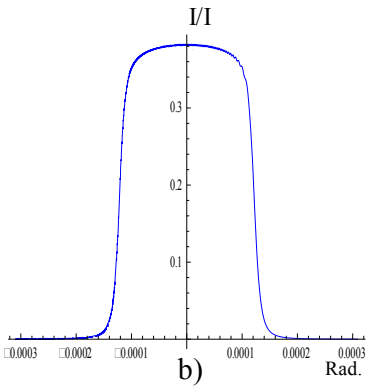

Fig.3. Curves of the angular distribution of the relative intensity of the reflected beam for the crystal thickness t = 1.43mm, for the source-sample distances L1 = 20cm (a) and L2 = 120 cm (b)

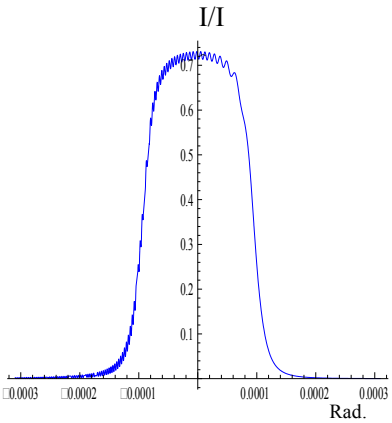

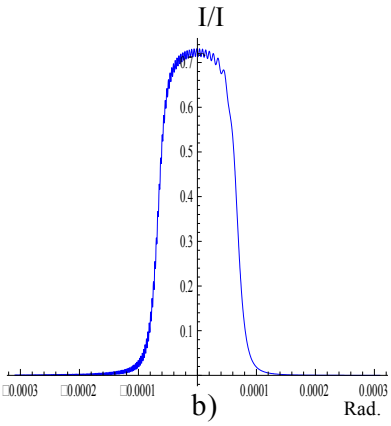

Fig.4. Curves of the angular distribution of the relative intensity of the reflected beam for the crystal thickness t = 0.61mm, for the source-sample distances L1 = 20cm (a) and L2 = 120 cm (b)

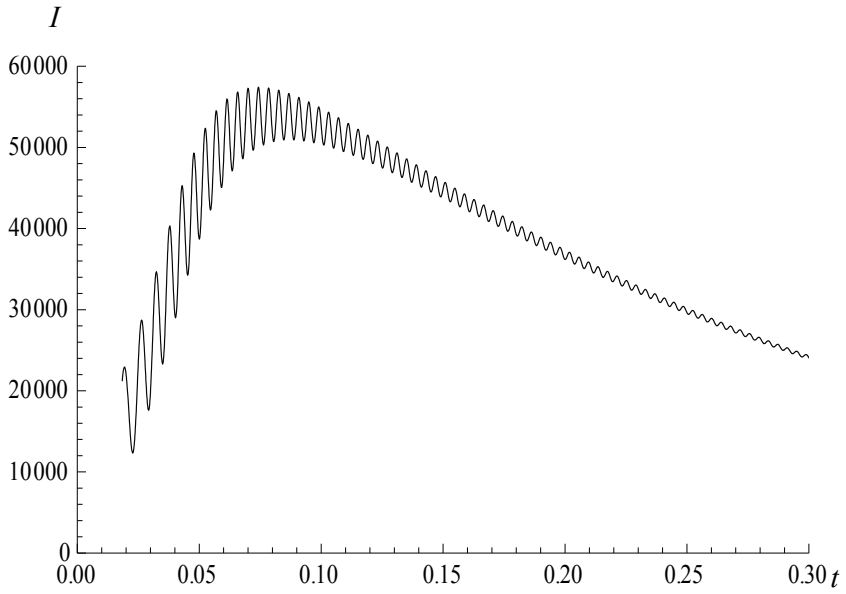

Fig. 5. The dependence of the integrated intensity of fully pumped X-rays upon the crystal thickness

References

1. Мкртчян А. Р., Навасардян М. А., Мирзоян В. К.. Полная переброска рентгеновского излучения, дифра-гированного монокристаллом от направления прохождения в направление отражения под действием температурного градинета. //Письма в ЖТФ, 1982, Т.8, В.11, С.677-680.
2. S.N. Noreyan, V.K. Mirzoyan, V.R. Kocharyan. Dependence of Full Pumped Angular Width of X-ray from Thickness of Single Crystal in The Presence of Temperature Gradient. Journal of Contemporary Physics, 2004, v.39, N2, s.124-130
3. V.V. Margaryan, K.T. Hayrapetyan, S.N. Noreyan, The Peculiarities of Angular Width of Diffracted X-Rays at The Presence of Temperature Gradient, Acta Cryst. 2009. A65, s214

X-Ray Diffraction Research of Frozen Lyotropic Liquid Crystals

H.G.Badalyan, A.H.Hovsepyan, Kh.M.Ghazaryan

Yerevan State University,1 Alex Manoogyan str. Yerevan, 0025, Armenia

The experimental results in this paper were obtained by the methods of optical-polarization microscope and the simultaneous X-Ray diffractions at large and small angles. The polarization microscope method makes possible obtaining information about the over-molecular structure and the orientation of colloidal formations. This method was used to investigate the over-molecular structural changes of liquid crystals, when the sample was cooled under 0˚ C. The lyotropic liquid crystal domain size changes due to their cooling were investigated by the polarization microscope method, taking into account that it exhibits the structural-relaxation processes which were going on in inhomogeneous solutions. To investigate the inter-system structural changes the X-Ray diffraction devices, URS-2, DRON-3M, having the special cameras, RKSO, RKOP, KRON, NOV and RKD, were used, which made possible to carry out simultaneous diffraction at large and small angles (Fig. 4).

The cameras, RKSO, RKOP and KRON are for obtaining images on flat films, but they were adjusted for detecting reflexes at the 100-150 mm sample-film distances, at small angles.

The X-Ray investigation experimental device sketch is presented in Fig. 1.

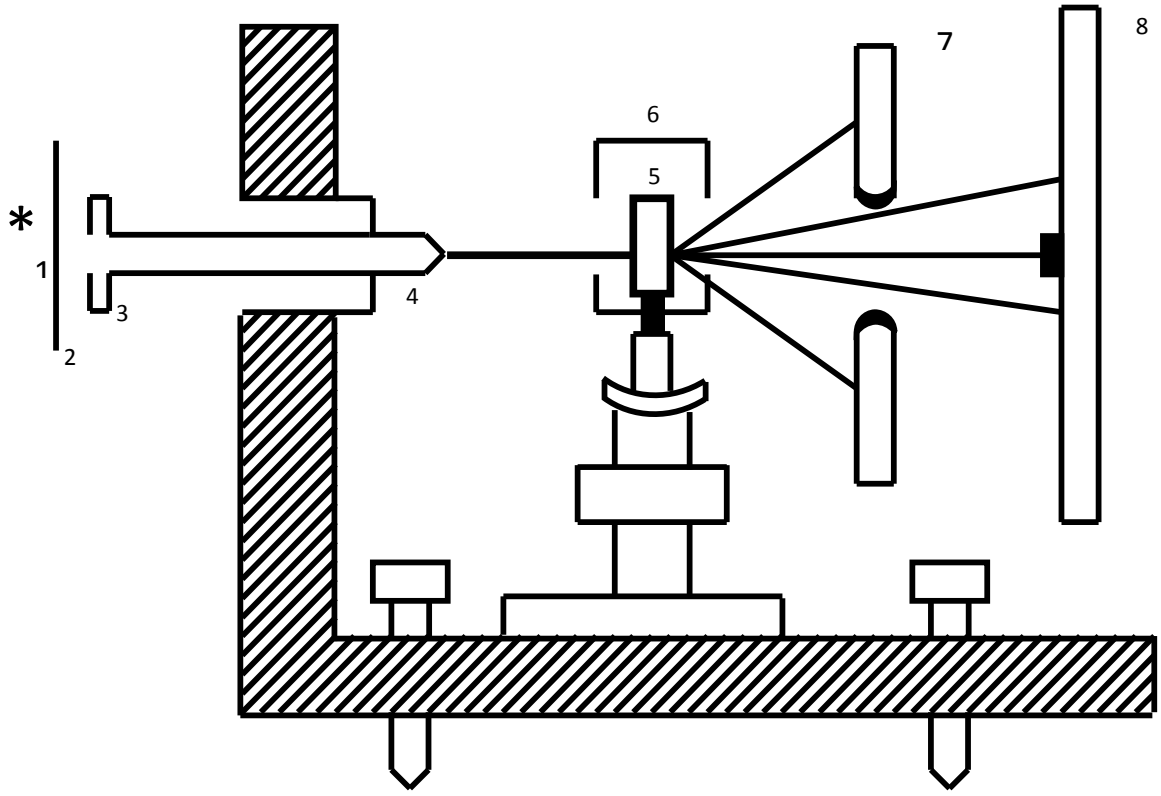

Fig. 1. The sketch of the X-Ray camera.1. The light source. 2. The filter. 3. The diaphragm. 4. The collimator. 5. The sample. 6. The crio-camera. 7-8. Photo taking boxes with films.

We poured the 20% Pentadecil-Water system liquid crystal sample into the special thin wall capillary of 1 mm diameter, then we hermetically closed the both ends. To be sure the system in the vitro is liquid crystalline (micelilar) we watched it through an optical microscope (Fig. 12).

A sandwich sample was prepared for the optical-polarization microscope. It had been done sandwiching the crystalline system with a corresponding concentration of the amphyphilc matter between two closing glass sheets. It was seen through the optical microscope that the amphyphilc matter molecules formed regular micelles (in the Pentadecil-Sulphanat-Sodium-Water system) at room temperature (Fig. 4).

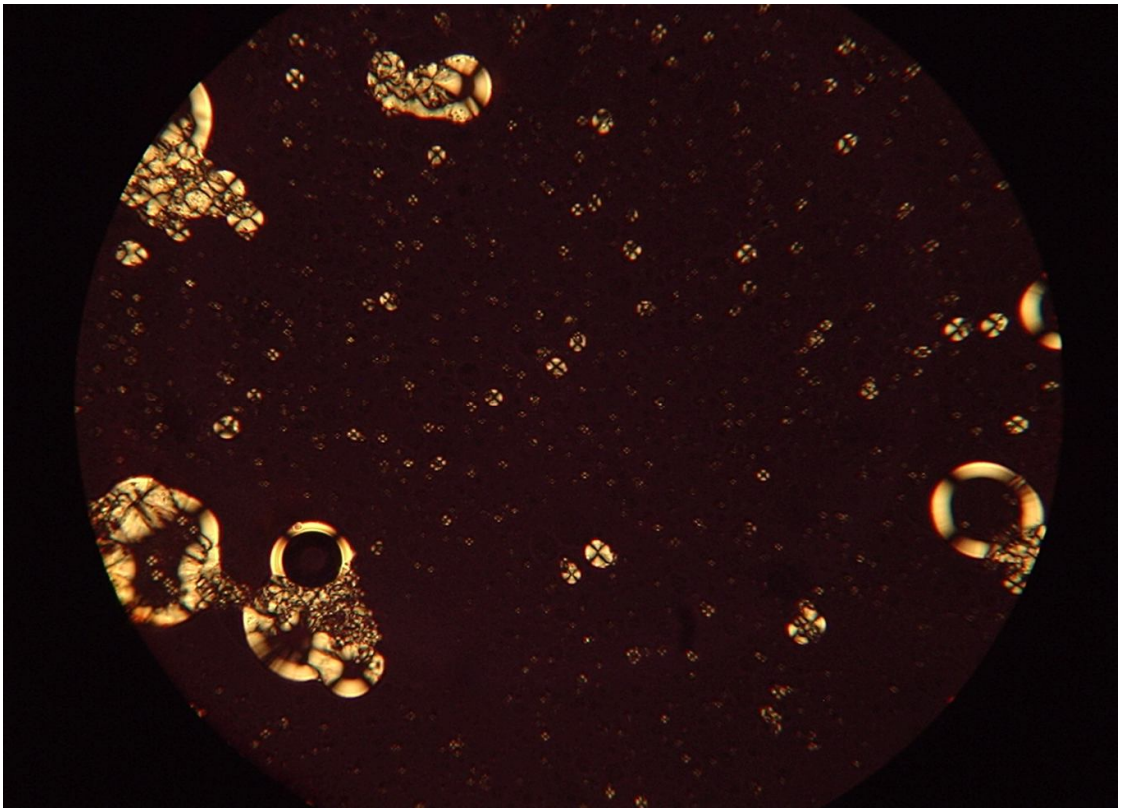

Fig. 4. The over-molecular structure of the Pentadecil-Water-Liquid crystalline system, at the temperature of 300 K.

The same sample was quickly cooled by liquid Nitrogen and then it was watched through the optical microscope. In this case, the certain parts of the micelle image were clearly seen to be distorted, and the transition from the confocal structure to the fan (rhipidium) structure (Fig. 5).

Then, we let the sample get melted and warmed till the room temperature, without removing it from the microscope view. In this case the obtained image was not restored and it had some remnant distortion (Fig 6).

Then, having been convinced that there were liquid crystalline systems with the same over-molecular structure in both cases, we put the sample into the X-Ray camera and – through the X-Ray diffraction at room temperature – got the X-Ray pattern of the liquid sample, after which we defined the system identity period through the device, ИЗА-2, measuring the reflex distances, which was, for the given case: d_0=30 $\mathring{A}$:

Then the sample was quickly cooled by the liquid nitrogen in the crio-camera and the cooled sample structural changes were studied through the X-Ray diffraction and optical polarization microscope methods.

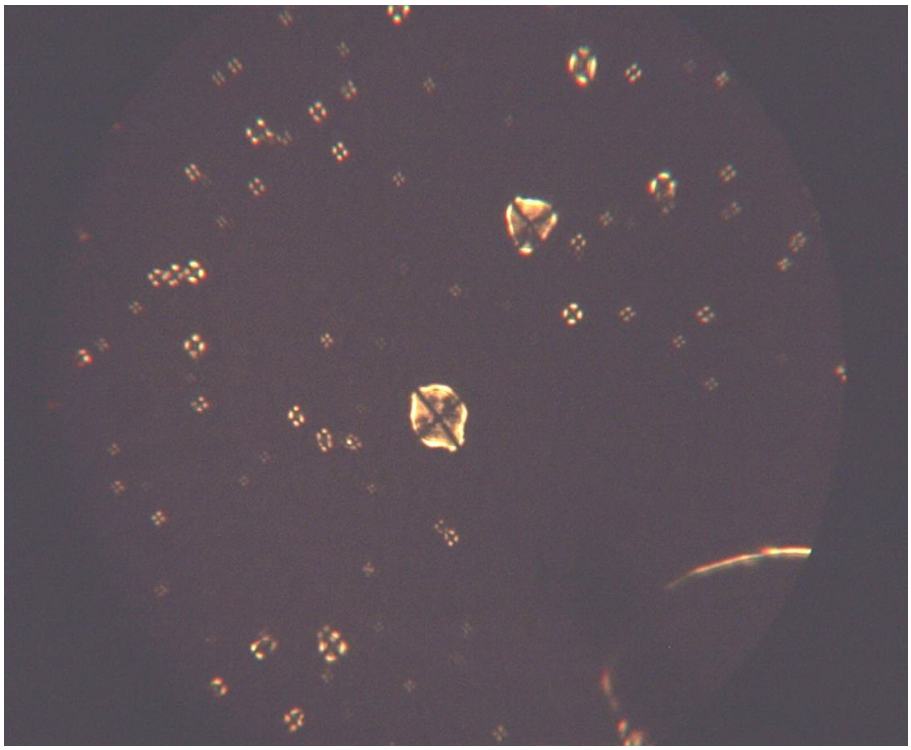

Fig. 5. The over-molecular structure of the Pentadecil-Water-Liquid crystalline system after cooling.

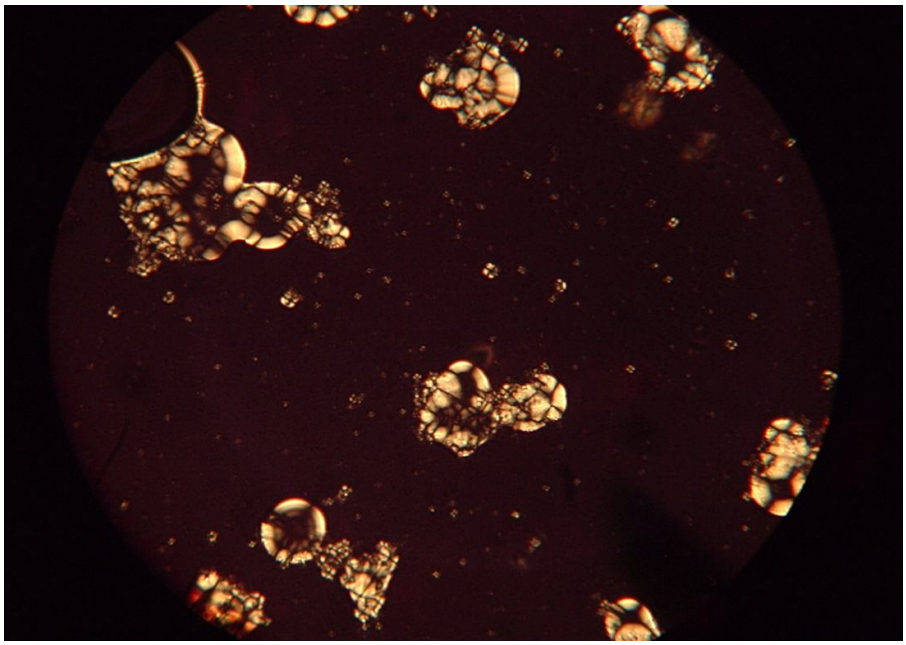

Fig. 6. The over-molecular structure of the Pentadecil-Water-Liquid crystalline system after melting the sample.

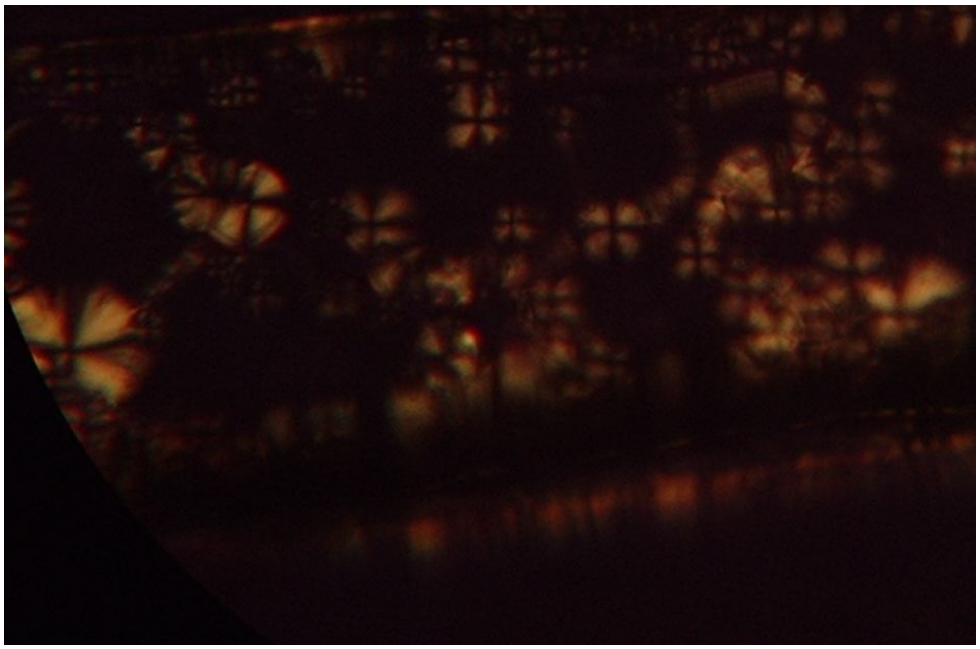

Fig. 7. The image of the liquid crystalline system in the capillary before cooling obtained through the optical- polarization microscope.

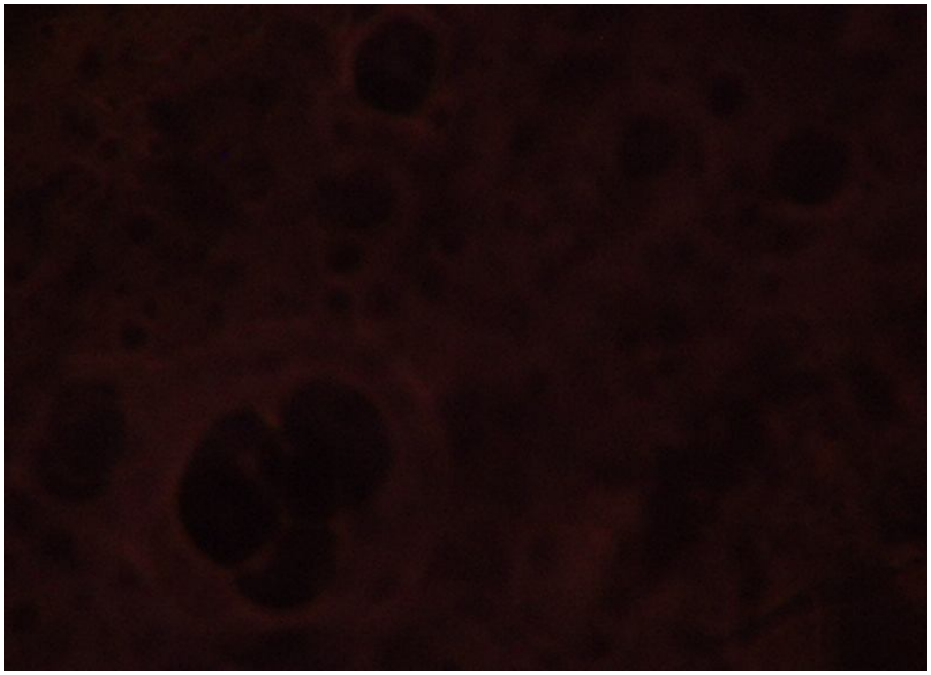

Fig. 8. The image of the liquid crystalline system in the capillary before cooling obtained through the optical- polarization microscope after melting and heating it again.

The image of the obtained micelles was essentially different from that of obtained at the room temperature. We put the cooled sample in the X-Ray camera where a temperature under 0^0 C was provided through a special mini-refrigerator, working by the Peltie battery. After a three hour exposition, developing it on an X-Ray film, we got that there were three fan (rhipidium) type blackened regions with a larger period (d=44,6 $\mathring{A}$) instead of the former two rings, and these evidenced that there also were systems with periodically increasing (up to d=119 $\mathring{A}$) arrangement

that held their former structure at separate places. This was the evidence of the fan (rhipidium) structure existence.

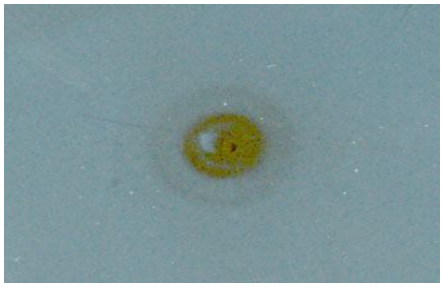

Fig. 9. The X-Ray image of the liquid crystalline system after cooling.

Switching the refrigerator off, we left the sample get melted, simultaneously watching the X-Ray diffraction from that sample. In this case, the sample structure was fan (rhipidium) type at small angles, and it was a diffuse ring at large angles.

The first fact proves that the system fan (rhipidium) structure holds for a long time (more than three hours) simultaneously forming water ice like associates (d=8.29 $\mathring{A}$). Thus, the system exhibits certain "memory" in respect to its former cooling.

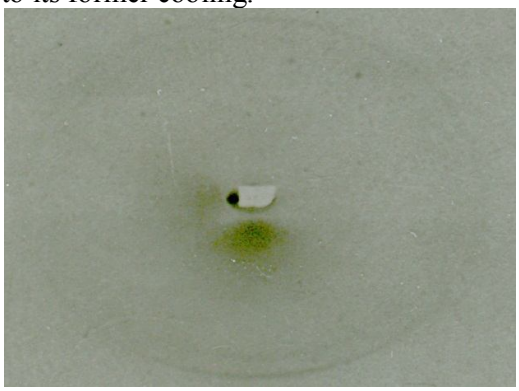

Fig. 10. The X-Ray image of the liquid crystalline system after melting.

Taking the experimental data, one can assert that both the liatropic system over-molecular and inter-system structures change. They are restored after melting the sample only partially, exhibiting certain memory. Certain transition from the confocal structure into the fan (rhipidium) structure is present there.

References

1. M.J.Sammon and J.A.N. Zazadzinsk: and M.R.Kuzma «Electron- Microscope Observation of the Smectic-Nematic Transition in a Lyotropic Liquid Cristal» CAL REVIEW LETTERS,1986, Dec.1
2. J.James and Jane F.Heathcock Unilever Research, Isleworth«Electron and Optical Microsopy Study of the Lamellar Mesophase Region of the water /Sodium Octanote/ Decanole Ternary system»J.Chem.soc., Faraday Trans 1, 1981, 77, 28

3. H.G. Badalyan.Kh..M.Ghazary, M.A.Stepanyan, M.Kh..Minasyants, A.A.Shaginjan Electrolit influence on molecular structure of lyotropic liquid crystals. News AS of Armenia, Physicist, v.38 n2 pp 130-133 2003.
4. L.A.Minasbekyan, . H.G. Badalyan, P.H.Vardevanyan. Hermodynamic Profile of Interaction of Porphyrines with Nucleic Acids Brilliant Light in Life and Material Sciences pp213-219 , 2006 October 1.

Six-Beam Diffraction in Two-Block Interferometer (Gap Fringes)

Ruben Ts. Gabrielyan

Yerevan State University

The X-Ray interferometer method has special significance in the X-Ray topography methods, because of its huge sensitivity (up to $\Delta d/d = 10^{-8}$) in respect to distortions of the crystal lattice periods. The possibility of getting a Muar picture by the interferometer is evidence of its high sensitivity. On the other hand, the presence of the Muar is resulted by the insufficient perfection of the interferometer blocks structures. These imperfections can arise either during the growth of the crystal, or in the interferometer manufacturing process.

The most effective X-Ray interferometer pattern of all is the solid monolith interferometer based on Laue reflection and consisting of three plate blocks on the common stand [1, 2]. Also the two-block interferometer, i.e. the interferometer having a two-block solid monolith system with a non-diffracting band (narrow gap) has been in wide use [3-5]. The interference pattern obtained from the two-block interferometer was called 'displacement stripes' (Gap Fringes.)

In all works devoted to displacement stripes (gap fringes) only the two-wave scattering has been considered. On the other hand, it is known that multi-wave scattering is richer and more informative than the two-wave one.

The multi-wave diffraction is rather sensitive method for detecting the crystal defects due to the complicated character of the field established in the crystal. This, in its turn, is due to the fact that the interference coefficient of absorption is significantly decreased in the multi-wave regions in many cases, and the crystal becomes transparent for X-Rays, because the wave field amplitude distribution inside the crystal in the two-wave case has sinusoidal character. And the distribution obtained in multi-wave diffraction (when the local waves give interference) can have much narrower maxima just like the amplitude distribution pattern in an optical wave transmitted the diffraction grating with sufficiently great number of gaps. This means that fields can arise, which completely get round the atoms and at same time the thermal oscillations influence is excluded, and this causes a zero absorption coefficient [6, 7].

This is the most wonderful property of the multi-wave diffraction and it makes possible to carry out topographical investigations (including the interferometric ones) having topographic patterns with high contrast.

Investigations by multi-wave diffraction have one more advantage over the two-wave ones, viz. one can obtain the defect patterns from a few planes, and consequently, the defect type can be stated with high accuracy.

We obtained and investigated an interference pattern from the two-block interferometer on the silicon monocrystal with six-wave scattering of the configuration, $\left(2\bar{2}0, 2\bar{4}2, 0\bar{4}4, \bar{2}\bar{2}4, 20\bar{2}\right)$. The choice of the configuration was not random, for it is known that the interference coefficient of absorption of one of the modes of this configuration vanishes [6-9]. Therefore there are very many both theoretical and experimental works devoted to investigation of this configuration. For the experiment, a two-block system on the common stand was prepared from a silicon crystal that had been almost without a dislocation. The blocks had been cut out in such a way that the horizontal plane was the scattering plane for one of the strong reflection of the type, (220). The output of the crystal into the multi-wave scattering position could be carried out by simple rotation round the axis perpendicular to the first reflecting plane (Reninger's method). If the intersection line of the

strongly reflecting planes, (220), is perpendicular to the primary beam (at the initial position), then the rotation angle φ is defined as follows:

$$\cos\varphi = \frac{tg\theta}{tg\frac{\alpha}{2}}$$

where α is the angle between the reflecting planes, (220), and θ is Bragg's angle. In our case φ was 71^0. For the alignment of the interferometer it is more convenient to make cutting of the blocks in such a way that the larger surface of the interferometer was vertical. In this case the larger surface of the interferometer forms an angle 19^0 with the crystallographic plane, (111); Fig. 1 a.

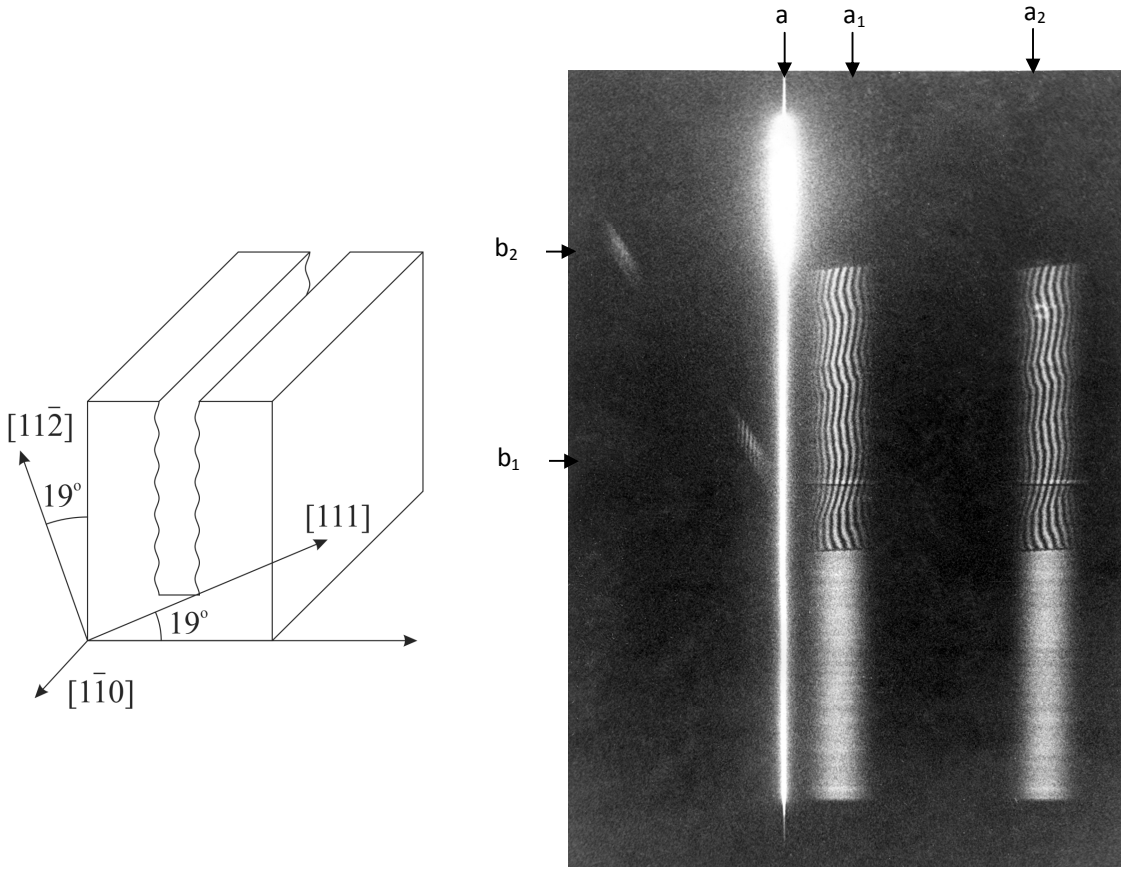

Fig. 1. A two-block interferometer for obtaining six-wave gap fingers (a). The interference pattern from the two-block interferometer (b).

The thickness of each block was 6.5 mm, the gap width was 0.4 mm and the radiation was $MoK\alpha$.

The patterns were obtained through the Japan topographic camera A-3, Regaku Denki. In fig. 1b the racks of the following reflexes are presented:

a is the track of the incident beam; (short waves);

a_1 is the reflex $\left(2\bar{2}0\right)$ in the incident direction;

a_2 is the reflex $\left(2\bar{2}0\right)$ in the reflection direction;

b_1 is the reflex $\left(\bar{2}02\right)$ in the incident direction;

b_2 is the reflex $\left(\bar{2}02\right)$ in the reflection direction;

In the X-Ray picture the displacement stripes (bands) of strong reflexes $\left(\bar{2}02\right)$ and $\left(2\bar{2}0\right)$ are clearly seen. Due to weakness of the intensity the reflexes, $\left(\bar{2}\bar{2}4\right)$, $\left(2\bar{4}2\right)$, and $\left(0\bar{4}4\right)$ are not seen.

The measurements showed that the displacement stripe periods of the reflexes b_1 and b_2 are 2.5 times smaller than those for the two-wave case and that they are vertical, too. This is due to the geometry of the experiment, as the reflexes a_1, a_2 and b_1, b_2 aroused in the result of the reflection from the equivalent atomic planes of the type, (220). Passing from the two-wave region to the multi-wave one, no special (new) curvatures of splitting of the interference lines (or displacement stripes) are observed in the reflexes a_1 and a_2, which could have been aroused due to multi-wave interaction and which are observed in the multi-wave pendulum stripes [10]. It never means that the pendulum stripes are more sensitive than the displacement stripes. To detect fine multi-wave effects the used crystal and the chosen configuration as well as the radiation type are more important. It is known that the multi-wave regions obtained on the silicon monocrystal – especially with molybdenum radiation – are so narrow that they are hardly distinguishable from the two-wave background. To apply the multi-wave scattering for interferometric and topographic investigations it is necessary to strengthen the resolving of the method, i.e. to use collimated beams having less angular divergence compared with the multi-wave diffraction region sizes. Moreover, in this case it is necessary to provide the parallelism of the beam not only in the horizontal plane, but also in the vertical one. On the other hand, it is seen from Fig. 1 b that there are clearly observed enhance and aufhellung effects in the multi-wave regions of the reflexes a_1 and a_2, even without any special vertical collimation, which are rarely observed in usual conditions for the silicon monocrystal.

Concluding, it is to be noted that the present work aimed at combining the two sensitive methods, viz. the multi-wave scattering and X-Ray interferometric, and doing this, the interference pattern for the six-wave (non-complanar) diffraction is obtained for the first time. The obtained interference pattern was compared with that obtained through the two-wave scattering.

References

1. U. Bonse, M. Hart, Zschr. Phys., v. 188, p. 154, 1965.
2. J. Chikawa, Appl. Phys. Letters, v. 7, p. 193, 1965.
3. A. Authier, A. Milne, M. Sauvage, Phys. Stat. Sol. 26, 469, 1968.
4. U. Bonse, M. Hart, Phys. Stat. Sol., 33, 351, 1969.
5. V. Haroutyunyan, P. Bezirganyan Phys. Stat. Sol., 99, 329, 1987.
6. T. Joko, A. Fukuhara, J. Phys. Soc. Jap. V. 22, №2, 597, 1967.
7. T. Huang, M. Tillinger, B. Post, Z. Naturforsch. Bd. 28 ^{a}, №5, 600, 1973.
8. P. Bezirganyan, R. Gabrielyan, V. Kohn, A. Toneyan, Phys. Stat. Sol., 85, 349, 1984.
9. V. Kohn, A. Toneyan, Acta Crystall., A42, N.6, 426, 1986.
10. Козмик В. Д. Кшевецкая М. Л.,Кшевецкий С. А., Михайлюк И. П., Остапович М. В., Кристаллография, т.21, вып.1, 38, 1976.

Investigation of Crystal Surfaces by Gap Fringes

Ruben Ts. Gabrielyan

Yerevan State University

As it is known, those methods of the X-Ray diagnosis are super-sensitive, which are based on the interference of the diffracted beams. In this connection, the X-Ray interferometric having the sensitivity, $\Delta d / d$, up to 10^{-8} for observation of crystal lattice period distortions has aroused great interest.

It is also known that for obtaining the interference patterns it is necessary to superpose two or more coherent wave beams, the phase difference of which varies sufficiently slowly from point to point in the field of their superposition. In the X-Ray wavelength region, superposition of two or more beams can be carried out through three- and more-block interferometers. It is easy to get convinced that in the general case, it is impossible to superpose the waves diffracted in the two-block crystal systems. Nevertheless, if the crystals of the two-block system are sufficiently close to each other, the waves diffracted in the first block are superposed on the entrance surface of the second block (Fig. 1). Then an interference pattern is obtained behind the system and the system turns into a two-block interferometer. The two-block interferometer was used first in [1-4].

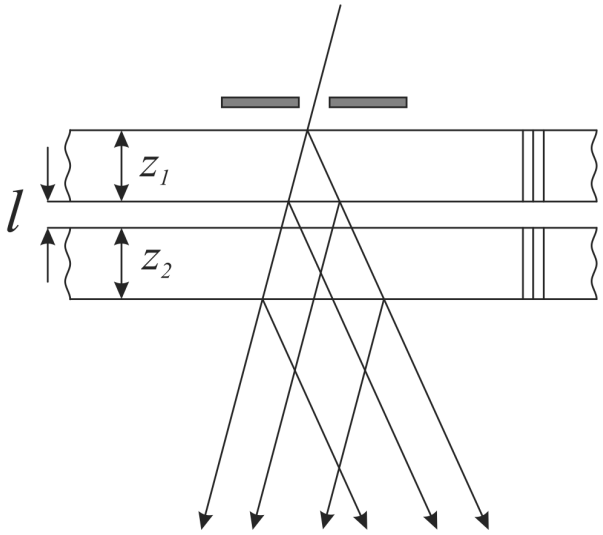

Fig. 1. The sketch of the two-block interferometer and the paths of the rays in it.

In the case, if the blocks are sufficiently thick, the diffracted waves having an anomalously large absorption coefficient are almost completely absorbed both in the first and second block. The anomalously weak absorbing waves aroused in the first block are superposed on each other on the surface of the second block, and if this second block is thick enough (if it is absorbing) here, too, the aroused anomalously strongly absorbing waves are almost completely absorbed. Thus, only the interference pattern aroused by the anomalously weak absorbed wave interference is observed behind such two-block system.

In [1-4], the interference patterns aroused in two-block interferometers are investigated theoretically and experimentally. As the centres of the superposing beams are displaced on the

entrance surface of the second crystal the interference lines (stripes) aroused in such interferometer were called gap fringes (displacement stripes.)

In [5, 6], the problem of diffraction of the incident wave on the two-block interferometer with a wedge like gap is solved.

The aim of the present work is to obtain the gap fringes in the two-block interferometers and show their high sensitivity to the structural distortions (especially to those on the surface) of the crystalline lattice on a certain example.

The two-block interferometers (samples) for this experiment were made from an almost perfect silicon monocrystal. The distance between the blocks were 0.6 mm, the thickness of each block was 6.5 mm. After machining the samples were chemically polished. The experiment was carried out with the Japan topographic camera A-3. The anomalously transmitted beams (reflexes 220) of MoK_{α} radiation were detected by the photographic method. We investigated the obtained interference pattern from the two-block interferometer and observed that the gap fringes were almost periodically curved (Fig. 2b). In [7], such curvatures were explained by the effective disorientation of the blocks, which could be aroused in the crystal growth processing or in making process of the interferometer. Consequently, there a necessity of checking the actual cause of these curvatures was aroused. Looking for the answer of this problem, we noticed that in the gap cutting process (by a special circular saw) some regular (periodic) rough edges from top to bottom were aroused between the interferometers, on the crystals' inside surfaces. It is seen in Fig. 2b that the interference pattern (gap fringes) has regular (periodic) curvatures as well, and they are from the top to the bottom, too. It is hard to imagine, from the physical point of view, that these coincidences are accidental and are not connected. Detailed investigation of this phenomenon showed that it is due to just the very roughness and especially the deformations of the inside surfaces of the blocks of the two-block interferometer which arouse in the making process. The roughness of the inside surfaces of the interferometer were not removed in the etching process (the gap was very narrow, and the etcher could penetrate with difficulty), and was that had led to the curvatures of the gap fringes. To be assured in this we made a special device (on a thin lengthy steel plate) and mechanically machined the inside surfaces of the interferometer blocks completely removing their roughness away, and then we etched them again. The new obtained interference pattern (Fig. 2c) had almost straight gap fringes.

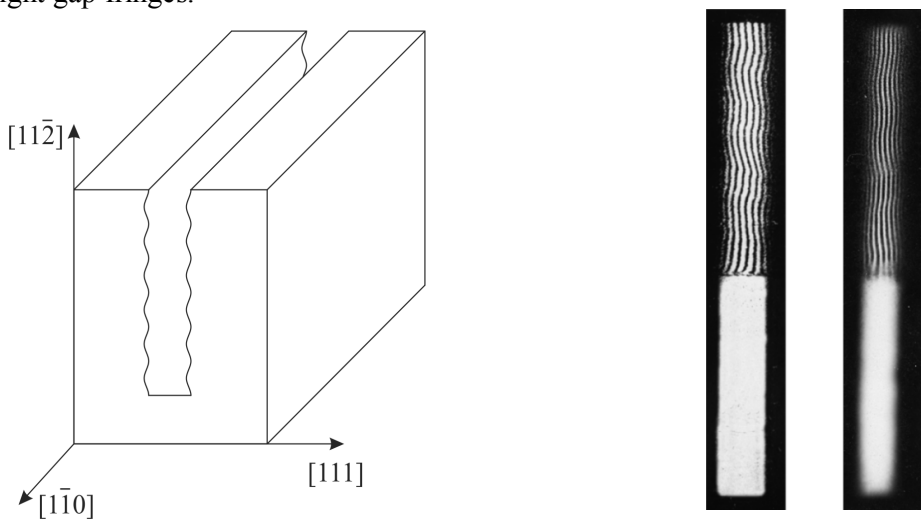

Fig. 2. The general appearance of the two-block interferometer (a). The gap fringes from the two-block interferometer. Before polishing the inside surfaces (b). After Polishing (c).

The fact that the curvatures are not removed away completely means that though the inside surfaces of the interferometer blocks became smooth after machining (polishing), nevertheless, the tensions aroused in sawing process remained and the sample etching did not completely remove this defected near surface layer. This result is very important, as it shows in a certain example that there is a possibility of investigating the near surface layers of a monocrystal with a more sensitive method, i.e. by the interferometer method.

Indeed, the distance among the neighboring gap fringes (stripes) is defined by the following formula:

$$\sigma_{n,n+1} = \left[\frac{n+1}{\sqrt{l^2 + (n+1)^2 \Delta_0^2}} - \frac{n}{\sqrt{l^2 + n^2 \Delta_0^2}} \right] tg\theta_0 (z_1 + z_2) \Delta_0 \qquad (1)$$

Where z_1 and z_2 are the thicknesses of the first and second blocks, respectively;

n - is the number of the gap fringe;

l - is the gap width (the distance between the interferometer blocks;

λ - is the wavelength;

Δ_0 - extinction length;

θ - Bragg's angle.

As it is seen from formula (1), the distance, σ between the gap fringes depends both on the distance between the interferometer blocks and the total thickness of the crystal blocks of the interferometer, $z_1 + z_2$.

On the other hand, the roughness of the inside surfaces of the interferometer leads both to changes of the distance between the blocks and the total thickness of the blocks from top to bottom. As it is seen from formula (1), the gap fringe period decreases if the gap width increases, which is expressed well in Fig 2b. Our experiments showed that the change of the total thickness of the blocks due to the roughness does not lead to essential change of the gap fringes distances.

Consequently, we come to the following conclusions:

1. Measuring the amplitudes of the gap fringes oscillations, we can define the heights of the roughness knobs of the crystal surface.
2. Measuring the periods of the gap fringes oscillations, we can define the repetition frequency of the roughness knobs of the crystal surface.
3. Finally, and the most important, through the gap fringes (displacement stripes) one can investigate the defected structure of the near surface layer of monocrystals.

Further theoretical investigation will make possible to carry out quantitative investigation of the surface imperfectness of crystals through the gap fringes.

References

1. Authier A., Milne A. D., Sauvage M., Phys. Stat. Sol. 26, 469, 1968.
2. Bonse U., Hart M., Phys. Stat. Sol. 33, 351, 1969.
3. Hart M., Milne A. D., Acta Cryst., A26, 223, 1970.
4. Baker J. F. C., Hart M., Helliar J., Z. Naturforsch., 28a, 553, 1973.
5. Bezirganyan P. H., Haroutyunyan V. S., Phys. Stat. Sol.(a) 99, 37, 1987.
6. Haroutyunyan V. S., Bezirganyan P. H., Phys. Stat. Sol.(a) 99, 329, 1987.
7. Габриелян Р. Ц., Мшецян А. Л., Тонеян А. Г., Межвуз. сб. науч. трудов. Физика,-1987, вип. 8-9, с. 121-125.

Section VI

Control of Characteristics of Plasma by Acoustic Fields

Amplitude-Frequency Characteristics of Nitrogen Acoustoplasma in the Visible Spectral Range

Aleksan S. Abrahamyan, Karen V. Akobyan, Sergey V. Kagramanyan, Eduard G. Kakosyan, Kristine G. Sahakyan, Ruben Yu. Chilingaryan, Suren A. Chilingaryan

Institute of Applied Problems of Physics NAS of RA

In this paper is considered the first (wavelength range 0.55-0.7μm) and the second (wavelength range 0.34-0.44μm) positive systems of the molecular nitrogen for transitions with vibrational quantum numbers from $\Delta v=-1$ to $\Delta v=-4$ [1]. Dc discharge and acoustoplasma discharge modes are compared.

If supply discharge tube by modulated current, which contains constant and variable components, the variable component reduces to generation of acoustic waves in a tube. These acoustic waves interact with the plasma, through which flows modulated current, consequently plasma transforms to the new state, which has been called acoustoplasma. Parameters of acoustoplasma can considerably differ from plasma parameters without acoustic interaction (unperterbed plasma).

In Fig.1 shown block diagram of the experimental setup.

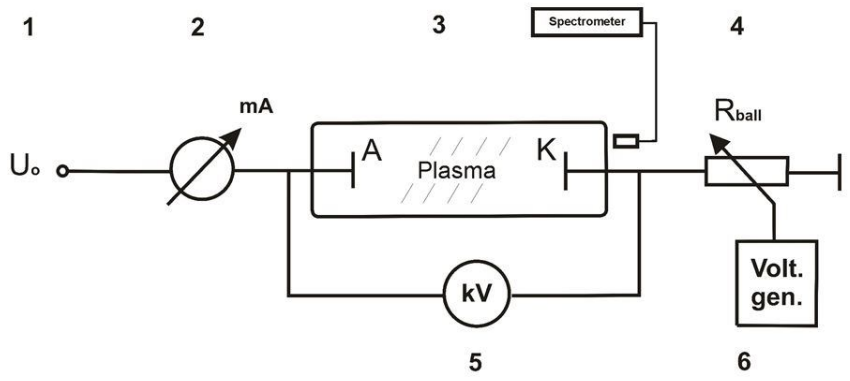

Fig.1 Block diagram of the experimental setup. 1. Source of high-voltage regulated DC voltage, 2.Milliampermetr, 3-Discharge tube 4. Ballast resistor, 5. Kilovoltmeter, 6. Driving generator.

Source of DC voltage **1** is connected to an anode of the discharge tube **3**. By variable ballast **4**, which is connected to the cathode of tube, modulated discharge current flowing through the tube. As a variable ballast resistance was used high-voltage electron tube. Schema of the lamp as a current generator provides the possibility to obtain a sinusoidally modulated current at the cathode of tube with constant and variable components. Sound generator **6** provides the necessary frequency and amplitude for modulation current. Nonlinearity of parameters of the discharge tube leads to fact that the current at the anode can be nonsinusoidal. The magnitude of discharge current was measured by milliampermetr **2**. Kilovoltmeter **5** shows the voltage applied to the anode-cathode of

discharge tube. Signals from milliamperemeter **2** and kilovoltmeter **5** fed to digital indicator and dual-beam oscilloscope.

We used discharge tube with a water-cooled system, the inner diameter is 5 mm, the length of the discharge gap - 250 mm. The discharge current contains a constant and a variable components (modulated current). The frequency of sinusoidal modulation is 0,1 – 30 kHz. The gas pressure in the tube varied from 0,1 to 100 Torr .

The radiation from the discharge was measured by the OCEAN OPTICS PC2000 spectrometer. The waveforms of voltage and current on the discharge, their amplitudes, average values and other characteristics of the discharge simultaneously were measured.

As a spectral line intensity has been selected energy characteristic (the area bounded by the spectral line, i.e. maximum intensity of the line multiplied by its width at half).

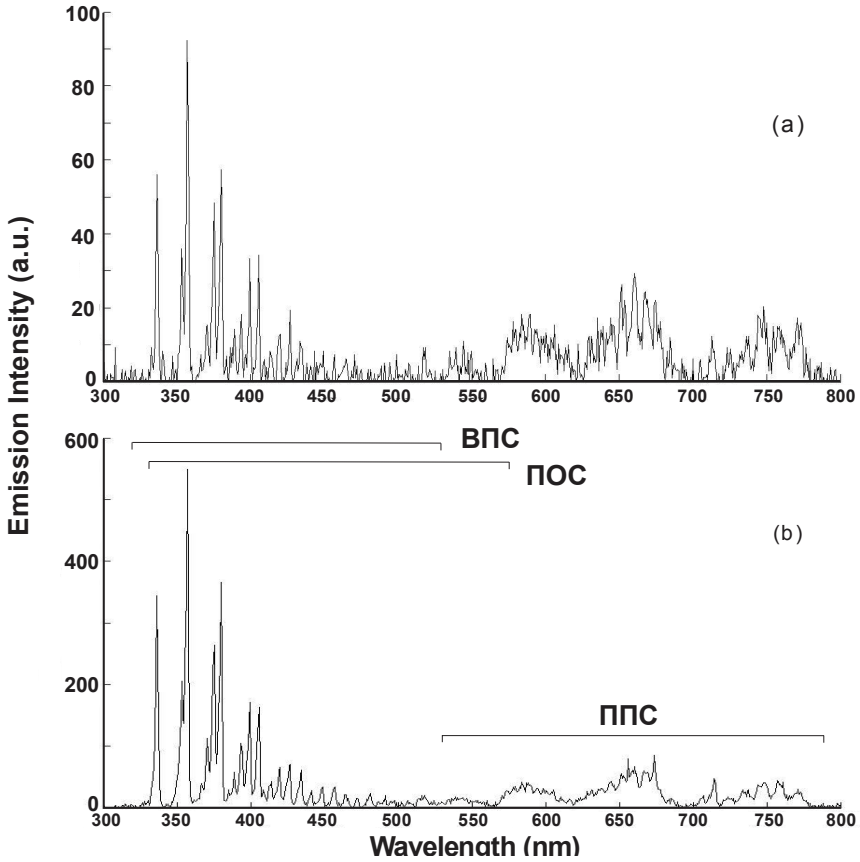

Fig.2 Emission spectra of molecular nitrogen plasma obtained along the discharge tube at the gas pressure Po=10 Torr. a) direct current Io=7mA, b) acoustoplasma discharge <I>=7mA, I~=22mA, f=25kHz.

Fig 2 shows that in case of transition from dc discharge to acoustoplasma discharge mode significant (up to 6 times) increase of spectral line intensity has been experimentally obtained (for the same power supply).

In fig.3 shown the identification of spectral lines of the second positive system of nitrogen.

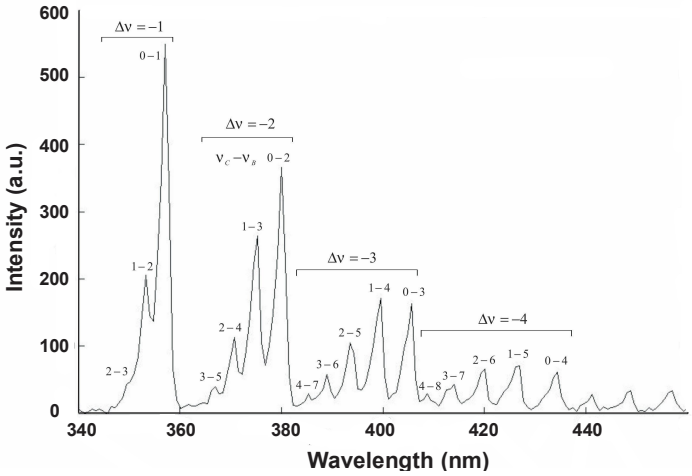

Fig.3 Identification of the spectral lines of the second positive system of N_2
In acoustoplasma discharge, frequency of current modulation f = 25kHz, the pressure in the discharge module P_0=10Torr.

Here Δν - transitions with the variational numbers. For example, Δν = -1 corresponding to the transitions between the vibrational quantum numbers 0-1, 1-2, 2-3.

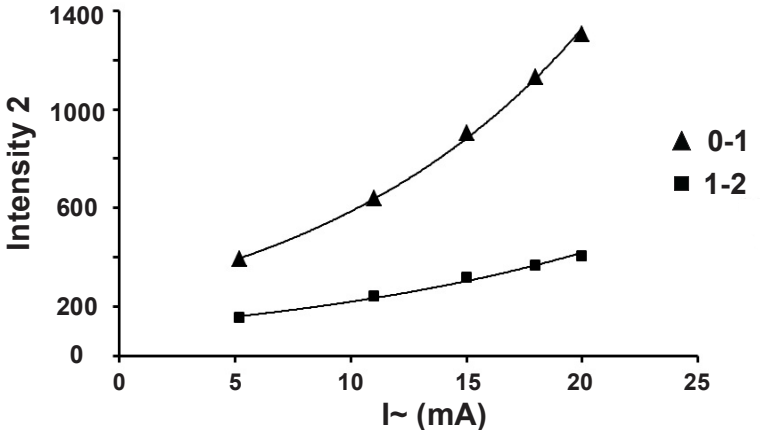

Fig.4. The intensity of spectral lines λ_{0-1} = 357,69nm and λ_{1-2} = 353,67 nm, the amplitude of the variable component of the discharge current f = 30kHz, <I> = 6,2mA, <U> = 2,9kV, P_0 = 10torr.

In fig.4 shown dependence of the spectral lines of the second positive system of nitrogen for the transitions (0-1) and (1-2) on the amplitude of the variable component of the discharge current at a constanat value of the constant copmonents.

From fig. 4 shows, that when the variable component of the current increases from 5 to 20mA, for line with λ_{0-1} = 357,69nm, the intensity increases from 260 to 1400 (in relative units), i.e. more than 5 times. At the same time for a line with λ_{1-2} = 353,67 nm, the intensity increases from 180 to 300, i.e. 1,7 times. This shows the impact of selectivity acoustic regime to differ lines, with different vibrational quantum numbers.

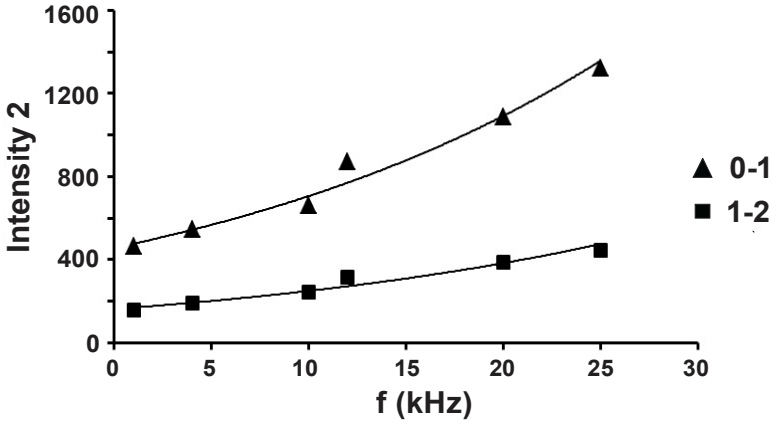

Figure 5. The dependence of the spectral of spectral lines of nitrogen λ_{0-1} = 357,69nm and λ_{1-2} = 353,67 nm, on the modulation frequency of the discharge current. <I> = 6,2mA, <U> = 2,9kV, P_0 = 10Torr.

Figure 5 shows that with increasing frequency (in the range 0-30 kHz), the intensity increases as well.

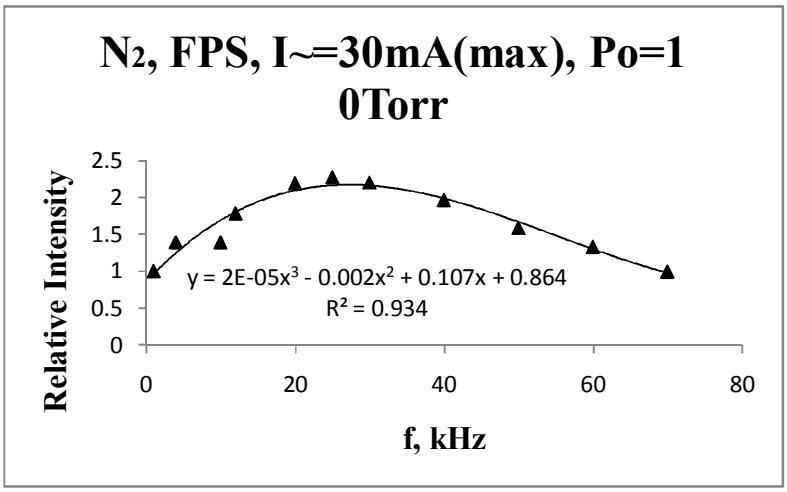

Fig.6. The dependence of the frequency modulation of integrated intensity of the FPS

Figure 6 shows the depndence of the frequency modulation of the integrated intensity the (in 0,55-0,7 μm) for the first positive system (FPS) of nitrogen. Results are normalized to the intensity at a modulation frequency of 1 kHz. From fig. 6 seen that, the increase in the integrated intensity has a clear resonance in the 20 – 35 kHz, which appears the first spiral mode (up to these frequences, there were only the longitudinal acoustic modes). In fig. 6 also shows the approximation of experimental results by third – degree polynomial.

Figure 7 shows the dependence of the integrated intensity of the first positive system of nitrogen (in the wavelength range 0,555-0,7 μm) of the gas pressure in the discharge tube. Results are normalized to the intensity at a pressure of 2 Torr .

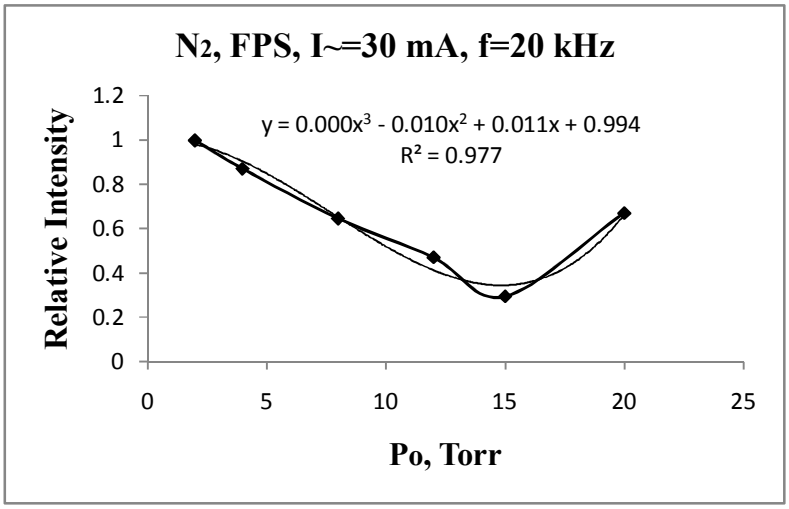

Fig.7.The dependence of the integrated intensity of the FPS of the gas pressure in the discharge tube.

From fig.7 shows that the minimum intensity have to pressure of 15 Torr, after which the intensity begins to grows again. This is due to the different states acoustoplasma at pressure below and above 15 Torr, and with increasing energyinvest with increasing pressure.

Thus, the discharge acoustoplasma mode lets you change the intensity of individual spectral lines.

References

1. Pearse R. W. B. and Gaydon A. G, 1976 The Identification of Molecular Spectra 4th edn (London: Chapman and Hall).
2 S.A. Chilingaryan, Investigation of the jumps and instabilities in acoustoplasma by external acoustic fields, Abstracts of Ph.D. diss.m IAPP NAS RA, Yerevan 2011, 32 pages. (In Russian).

Accounting of the Energyinvest in Acoustoplasma

Sahakyan K. G.

Institute of Applied Problems of Physics of NAS of RA

To solve inverse problems, it's necessary to take into account many causal relationships, that affect the physical process. Therefore, we must have a sufficiently large base of experimental data. In non correct posed inverse problem small perturbations of observed data may lead to solutions of arbitrarily large perturbations. Therefore, in measurements is required a high accuracy [1].

Usually, current is being measured only at one point of the circuits, assuming, that it is the current flows across the branch of the discharge tube. However, in acoustoplasma discharge currents, which measured from the anode and cathode sides of the tube, may be different, due to the unsteadiness during the modulation period. This will rise errors in the measurement of some parameters of the discharge.

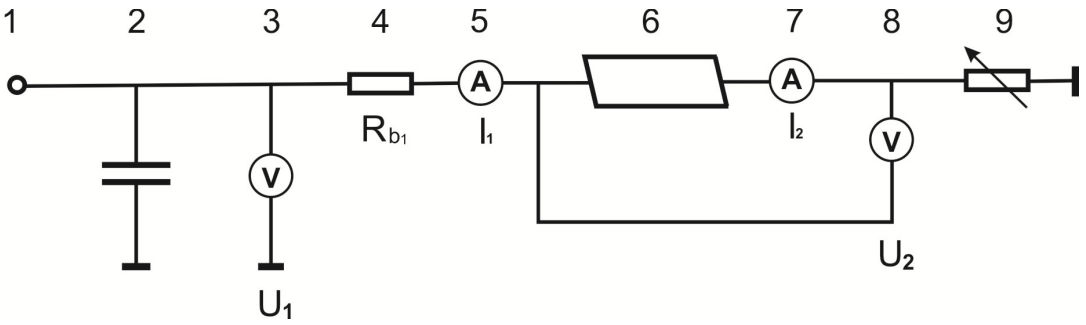

Fig.1. Circuit of experiments

In below is proposed a method of increasing of the mesaurment accuracy of energyinvest in acoustoplasma. Figure 1 shows the experimental setup. Voltmeter 3 measures the high voltage U_1, which is formed by the power supply 1 on a capacitor filter 2. Protective ballast resistance 4 limits the maximum current in the scheme. Ammeter 5 shows the current I_1, which flows into the anode of the discharge tube 6. Ammeter 7 shows the value of current I_2, I_1which flows from the cathode of the discharge tube 6. Voltmeter 8 shows the voltage U_2 at the anode-cathode-distance of the discharge tube. Variable resistance 9 defines the current, which flows from the cathode of the discharge tube. Variable resistance 9 is assembled on a high-voltage electron lamp according to the scheme, which allows to obtain a sinusoidal current on the cathode of the 6 tube. A high-capacity capacitor of 2 filter provides the closure of the alternating current component in a sequential circuit over the entire range of modulation frequencies of 9 resistance.

When we measuring dynamic parameters in acoustoplasma, due to the nonlinearity of the resistance of the discharge and possible changes in the concentration of charged particles, the current I_1 and the voltage U_2 are not sinusoidal, in spite of I_2 current is sinusoidal. Moreover, the average currents $\langle I_1 \rangle$ and $\langle I_2 \rangle$ are equal, but the instantaneous values of these currents differ from each other.

In figure 2 ostsillogram currents I_1 (Ian), I_2 (Icat) and U_2 (Utub) for different modulation frequencies of the discharge current are demonstrated. Figure 2 shows that for frequencies above 1kHz current I_2 is different from sinusoidal. This is associated with abrupt changes in the parameters of the tube during each modulation period. In [2] it has shown, that these changes are phase transitions in acoustoplasma.

f (kHz)	**0.5**	**1**	**1.5**	**2**	**2.5**	**3**	**3.5**
U_{tub} kV) **I_{an} (mA)**	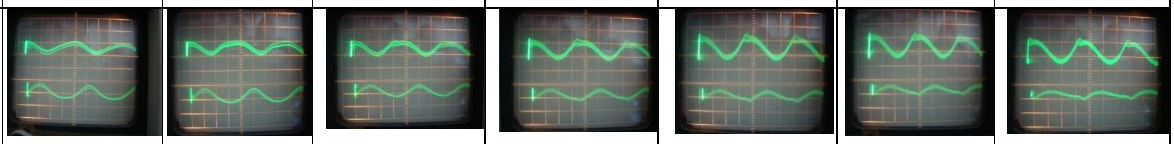						
U_{tub} kV) **I_{cat} mA)**	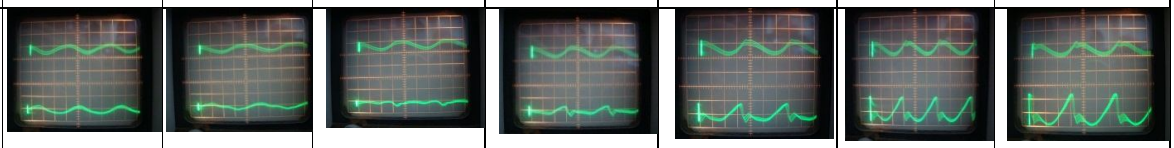						

Fig.2

It must be reiterated, that the difference in the curves obtained I_1 and I_2 can be explained either by changes in the concentration of charged particles in a plasma discharge, or different velocity of motion of the electrons at the anode and cathode.

Usually, the energyinvest into the discharge tube measured [3] as

$$\mathbf{W_{tub}= U_2I_1.} \qquad \mathbf{(1)}$$

In our case energyinvest is determined by the following procedure: the voltage on the 4 ballast resistance is $\mathbf{U_{Rb1}=I_1R_{b1}}$. The voltage on the 9 nonlinear resistor is $\mathbf{U_{R9}=U_1-U_{Rb1}-U_2}$. Instantaneous power, which consumed from the 1 source, is $\mathbf{W_1=U_1I_1}$, instantaneous power allocated on the ballast resistance $\mathbf{R_{b1}}$ is $\mathbf{W_{Rb1}= R_{b1}\ I_1^2}$, instantaneous power allocated on the 9 controlled nonlinear resistor is $\mathbf{W_9=U_{R9}\ I_2}$. Then, the power, released in a discharge tube, is $\mathbf{W_{tub}=W_1-W_{Rb1}-W_9}$. Or in general form

$$\mathbf{W_{tub}= U_1I_1-R_{b1}\ I_1^2-I_2U_1+I_1I_2R_{b1}+U_2I_2.} \qquad \mathbf{(2)}$$

Figure 3 shows the comparision of the instantaneous (dynamic) values of energyinvest, defined by (1) and (2) expressions for modulation frequency 3 kHz.

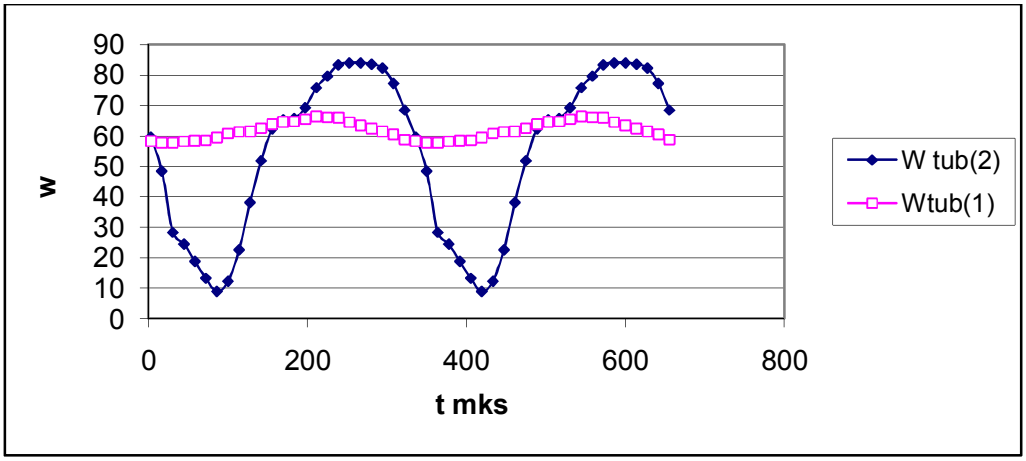

Fig.3

As we can see in figure 3, the power on the tube, which is calculated from (1), remains practically constant ($Wtub_1$, on fig.3). When the dynamic power on the tube is calculated from (2), i.e. take into account the difference of currents at anode and cathode, curve also is shown at fig.3. Have to note that average values for both curves are equal, the difference between the mean values of power, counted by the formulas (1) and (2) is 0,1%. Thus, in experiments with acoustoplasma to obtain accurate values of the dynamic parameters of the discharge current it must be measured simultaneously from the anode of the discharge tube and from the cathode side, because during the period of the modulation the charge changes that has accumulated in the tube, and there is a virtual source voltage.

References

1. A.N. Tikhonov, V.Y. Arsenin. Methods for solving incorrectly tasks. Moscow: Nauka, 1986. 287p (rus.)
2. A.S.Abrahamyan, S.A.Chilingaryan, K.V.Hakobyan, A.S.Mikayelyan, Phase Transitions And Catastrophes In Acoustoplasma, Int. Seminar on Plasma Physics, 13 - 15 February 2011, Ouargla, Algeria, Proccedings, pp. 90-94.
3. A.R. Mkrtchyan, A.S. Abrahamyan, K.P. Haroyan, T.J. Bezhanyan, R.B. Kostanyan, K.S. Mkrtchyan., Control of the parameters of the gas discharge CO_2 laser with acoustoplasmic interaction. Rus. Conf. of Low-temperature. FNTP 2004, Petrozavodsk, Russia, June 28-30, 2004., Proc. V.1, pp. 127 – 131 (rus).

Accounting RCL Parameters of Acoustoplasma Discharge

Aleksan S. Abrahamyan, Suren A. Chilingaryan, Kristine G. Sahakyan

Institute of Applied Problems of Physics NAS of RA

By modulation of discharge current in a discharge tube acoustic field is produced. Discharge tube serves as an acoustic resonator for these acoustic oscillations. At the resonance frequency standing wave regime is realized and amplitude of acoustic oscillations rapidly increases. These acoustic waves interact with plasma which leads to plasma transform to the new state, which has been called acoustoplasma [1].

We use the method of electro-acoustic analogy which has been developed for analyzing the acoustic system [2]. In terms of this method acoustic pressure p considered as an analog of voltage, vibrational speed V – analog of the current density, volume rate of oscillations $U_a = VS$ (where S - cross section of acoustic line) – analog of the current. For a tube with the length l acoustic mass and resistance are $m_a = m/S^2 = \rho l/S$, $r_a = r_M/S^2$ respectively. For the volume **V** acoustic flexibility is $c_a = c_M S^2 = \mathbf{V}/\gamma p_{a.c.}$

Let us consider analogue of the acoustic and electric systems for narrow tube (Fig. 1a) with the length $L << \lambda$ and cross section $S = \pi r^2$, thermal conductivity coefficient of tube wall is β. Equivalent electrical circuit of the discharge tube is shown in Fig. 3.1b. For this scheme input acoustic impedance is $z_{вх} = r_M + i\omega m$, $r_M = 8\pi\mu l\beta\alpha$, $m = 4\pi\rho l r^2/3$, $1 \le \beta \le 2$, $\alpha = 1$ when $fr^2 < \mu\pi\rho$, where r_M - acoustic analog of active resistance, m - acoustic analog of induction, ρ - density of medium, μ - dynamic viscosity.

In electric analog of an acoustic system corresponding to the gas discharge tube it is necessary to add capacitor C, and change the resistance r_M, i.e. plasma in discharge tube is considered as an element with acoustic flexibility.

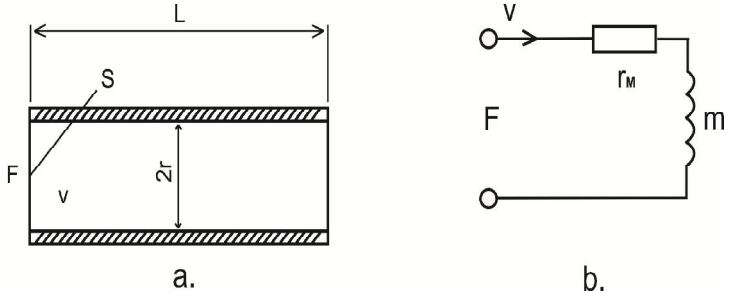

Fig.1. An analogue of the acoustic and electric system. a) narrow tube with a length $L << \lambda$, b) electrical analogue of tube with acoustic waves.

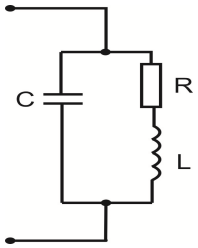

Fig.2. The equivalent electric circuit of a discharge tube with acoustoplasma.

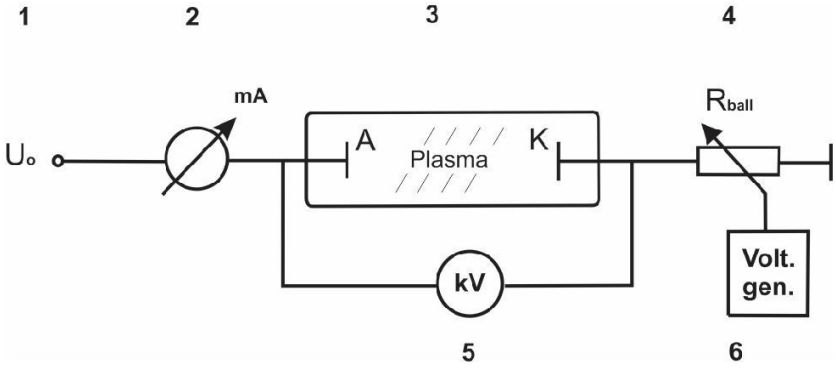

Fig.3. The experimental setup. 1- high-voltage regulated DC source, 2- milliamperemeter, 3- discharge tube, 4- ballast resistance, 5- kilovoltmeter, 6- sound generator.

In [3] noted that for power supply circuit of a discharge tube (shown in Fig.3) resonance characteristic of acoustoplasma discharge similar to phase characteristic of parallel oscillatory circuit. Moreover, quasi resonant frequency of such an oscillatory circuit is considerably higher than frequency of the first longitudinal acoustic resonance of the discharge tube. For experimental conditions described in [3] the first longitudinal acoustic resonance frequency was of the order of 0,4 kHz, and quasi resonant frequency – 3-4 kHz. In our case the first longitudinal mode is about 0,8 kHz and resonance frequency - 3 kHz.

In Fig.2 shown the electrical analog of an acoustic system of a discharge tube which is in acoustoplasma regime.

Thus, the discharge tube which is in acoustoplasma regime can be described as a parallel oscillatory circuit - two-terminal network with active and reactive components [3,4]. The complex impendence of two-terminal network has the form

$$Z = \frac{(R + i\omega L)\dfrac{1}{i\omega C}}{R + i\omega L + \dfrac{1}{i\omega C}} \qquad (1)$$

From (1) for the real $r(\omega)$ and imaginary $x(\omega)$ parts of complex impedance we obtain

$$r(\omega) = \frac{R}{(1-\omega^2 LC)^2 + (R\omega C)^2} \qquad (2)$$

$$x(\omega) = \frac{\omega L(1-\omega^2 LC) - R^2\omega C}{(1-\omega^2 LC)^2 + (R\omega C)^2} \qquad (3)$$

where R - ohmic resistance of the discharge, i - imaginary unit, ω - modulation frequency of the discharge current, L- inductance of the discharge, C- discharge capacity.

In case of direct current real part of complex resistance is $r(\omega) = R$. This value of resistance can be obtained from the experimental dc current-voltage characteristic (Fig.4).

Thus, during a period of modulation R, C and L quantities depend on the magnitude of discharge current, which itself depends on time. Consequently, R, C and L depend on current and on time. In the special case, when capacitance and inductance are independent of $I(t)$, the expression (2) takes the form:

$$r(\omega) = \frac{R\left(I(t)\right)}{\left(1-\omega^2 LC\right)^2 + \left(\omega R\left(I(t)\right)C\right)^2} \qquad (4)$$

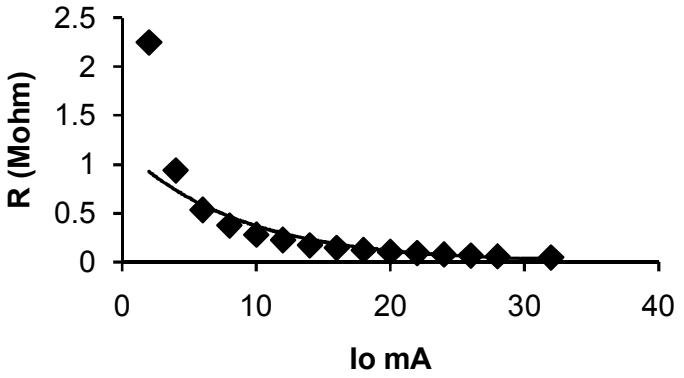

Fig.4. The dependence of ohmic resistance of dischage on the magnitude of dc, gas pressure in tube Po=25 Torr. Points – experimental values, solid line – theoretical approximation $R = 1{,}17\exp(-0{,}114 I_0)$.

As follows from Fig.4 the ohmic resistance of discharge is well approximated by an exponential dependence of the form: $R\left(I(t)\right) = A\exp\left(-\beta I(t)\right)$, and (4) finally can be written as follows

$$r(\omega) = \frac{A\exp\left(-\beta I(t)\right)}{\left(1-\omega^2 LC\right)^2 + \left(\omega CA\exp\left(-\beta I(t)\right)\right)^2} \qquad (5)$$

where A and β are constants determined from experiment for the certain acoustoplasma state, $I(t)$ - instantaneous value of total discharge current (measured on the anode side). The last expression (5) is shown in Fig.5.

Thus, if during a period of modulation $L = const$, $C = const$ and $R(I)$ represents dependence of ohmic resistance on discharge current only we can find out form of the resonance circuit characteristics which are shown in Fig.5 and Fig.6. According to our estimates equivalent capacitance and inductance of discharge are of the order of $C = 30\,pF$ and $L = 10^2\,Hn$ respectively. Discharge resistance R varied from $R_{\min} = 0{,}1\,MOм$ (curve 1) to $R_{\max} = 0{,}5\,MOм$ (curve 3), resistance at the average current is $0{,}22\,MOм$ (curve 2).

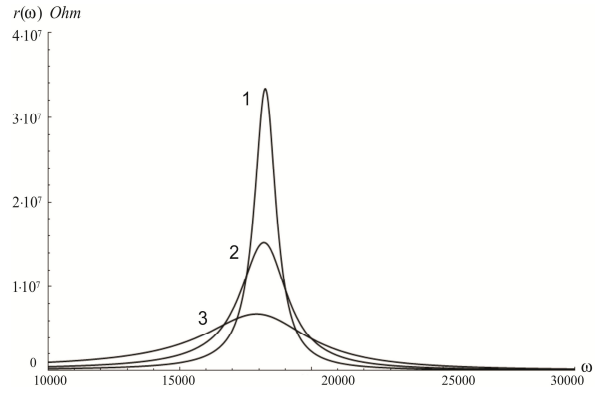

Fig.5. Frequency dependence of real part of the complex impendance of discharge tube shown in Fig.2

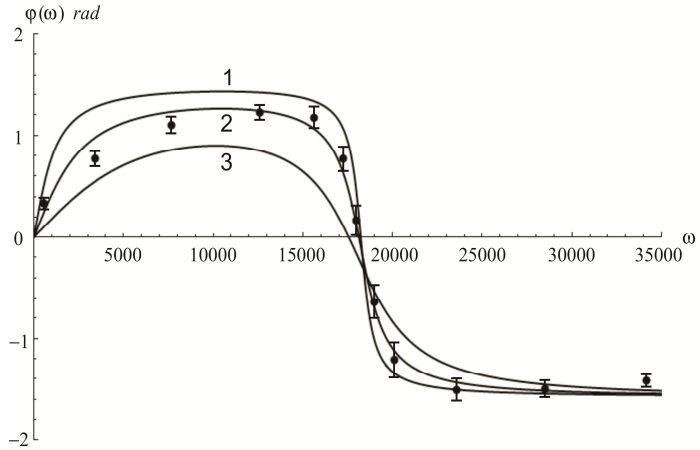

Fig.6. Frequency dependence of phase shift between voltage and discharge current (for the circuit shown in Fig.2)

From Fig.5 it follows that real part of complex impendance in acoustoplasma dischrage has a distinct resonance frequency (near the 2,8 kHz). By modulation of discharge current at a resonance frequency due-to modulation of $R(I)$ occurs modulation (during a period of modulation) of tuned-circuit Q-factor and real part of complex impendance of discharge tube (for curves 1, 2, 3 - tuned-circuit Q-factor are 18, 9 and 3,6 respectively).

Phase shift between discharge current and voltage given by

$$\varphi(\omega) = ArcTan\left[\frac{x(\omega)}{r(\omega)}\right] \qquad (6)$$

In Fig.6 shown both the theoretical curves (obtained from (6) for different values of $R(I)$ - solid lines) and experimantally measured points of phase shift between voltage (at the and of

discharge tube) and discharge current (measured from anode side). Exprimental values of phase shift are taken from [3]. The coincidence of the experimentally measured phase shift (between discharge voltage and current) with calculated values confirmed correctness of the constructed discharge tube model.

From Fig.6 one can conclude that during the period of modulation of discharge current small modulation of resonance frequency has occurred (during the period of modulation in our case resonance frequency changed approximately 110 Hz, i.e. 1,5-3% of the central resonance frequency).

Thus, by solving the inverse problem new result on the modulation of acoustoplasma parameters was obtained.

References

1. Мкртчян А.Р., Багдасарян А.С., Абраамян А.С., Костанян Р.Б. Мкртчян А.Г. Управление параметрамаи низкотемпературной газоразрядной плазмы акустическими колебаниями. Доклад на вручении премии имени А.М. Прохорова, 2009, 99с.
2. В.К. Иофе, В.Г. Корольков, М.А. Сапожков. Справочник по акустике. М.: Связь, 1979, 312с.
3. А.С. Абраамян, Т.Ж. Бежанян. Зависимость резонансных свойств газового разряда от схемы включения. Proceedings of the Conference on, LP-2007, с 225-228.
4. Г.И. Атабеков. Основы теории цепей. Учебник для вузов. М., Энергия, 1969, 424 с.

Defined Charge Distribution by Discharge Current Modulation in Acoustoplasma

Aleksan S. Abrahamyan, Kristine G. Sahakyan, Ruben Yu. Chilingaryan

Institute of Applied Problems of Physics NAS of RA

Two currents, one, which flows into the anode of the discharge tube ($\mathbf{I_{an}}$) , the other, which flows from the cathode discharge tube ($\mathbf{I_{cat}}$) was measured. During the period of discharge current modulation the difference between instantaneous value of discharge current ($\mathbf{I_{an}}$-$\mathbf{I_{cat}}$) forms a charge change in the discharge tube (excluding current diffusion to the walls of the tube). The characteristic of acoustoplasma is differ from the usual characteristics of a varicond (capacitor with variable capacitance). The dependences of the instantaneous voltage (at the ends of the discharge tube), charge, ohmic resistance and complex impedance of the discharge tube on time were also presented.

In Fig.1 is shown block circuit of the reasearch on the changes of charge in the discharge tube with plasma [1].

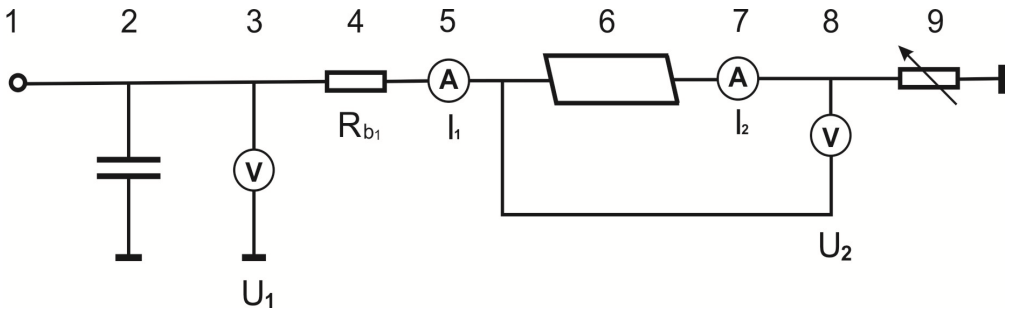

Fig.1

Voltmeter **3** measured the high voltage $\mathbf{U_1}$, which is formed by the source **1** on a filter capacitor **2**. Ballast **4** is protective and limits the maximum current in the circuit. Ammeter **5** shows the current, which flows into the anode of the discharge tube **6** ($\mathbf{I_1}$, or $\mathbf{I_{an}}$). Ammeter **7** shows the current value $\mathbf{I_2}$ ($\mathbf{I_{cat}}$), which follows from the cathode of the discharge tube **6**. Voltmeter **8** shows the voltage $\mathbf{U_2}$ at the ends of discharge tube ($\mathbf{U_{tub}}$) i.e. voltage between anode and cathode of the tube. Variable resistance **9** defines a current, which flows from the discharge tube cathode. Variable resistor **9** is assembled on a high-voltage electron tube according to the scheme, which allows to obtain a sinusoidal current on the cathode of the tube **6**. A high-capacity capacitor **2** allow a short circuit for the alternating current component in a entire range of modulation frequencies of resistance **9**. As the discharge tube has used CO2 laser LG-23 tube [2] with mixture of CO2: N2: He = 1: 1: 8, the pressure - 8 Torr. The modulation frequency of the discharge current - 3.5 kHz. Under the measuring the dynamic parameters in acoustoplasma, the non-linearity of the discharge resistance and possible changes in the concentration of charged particles, current and voltage may not be sinusoidal, although the input signal to control the variable resistor is sinusoidal and the current and voltage when running on an equivalent ohmic resistance tube also are sinusoidal. The average values of currents $\langle \mathbf{I_1} \rangle$ and $\langle \mathbf{I_2} \rangle$ are equal, but the instantaneous values of these currents differ from each other.

The experiment measured two currents, one – $\mathbf{I_{an}}$ **(I1),** which flows into the anode of the discharge tube, the other – $\mathbf{I_{cat}}$ **(I2)**,, which follows from the cathode discharge tube. The difference between the instantaneous values $\mathbf{(I_{an}-I_{cat})}$ forms a charge change in the discharge tube during the period of discharge current modulation. It does not take into account the diffusion current on the tube wall and the fact that the $\mathbf{I_{cat}}$ can also changed because of acceleration of electrons in the plasma and variation of electrons velocity in the cathode region. A more accurate result can be obtained only from the view of the above comments, but this is beyond the scope of this work.

Fig.2 shows the dependence of the charge in a discharge tube from the instantaneous value of the variable components of voltage at the ends of the discharge tube.

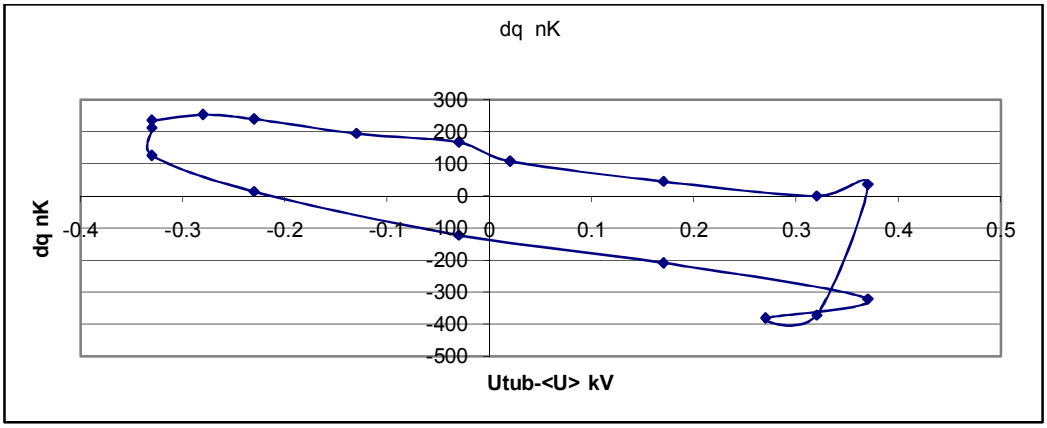

Fig.2. Coulomb-voltage characteristics of the acoustoplasma discharge

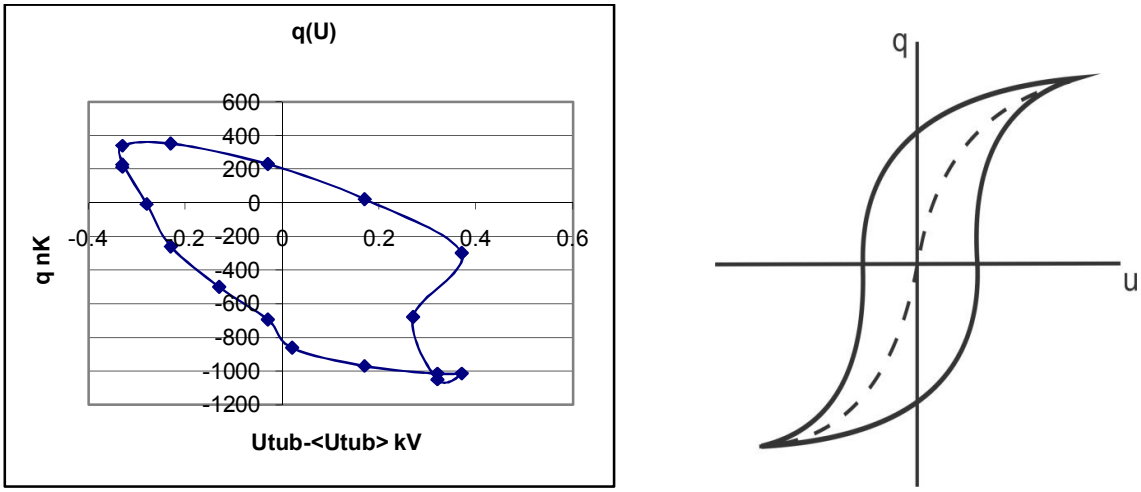

a b

Figure 3. Coulomb-voltage characteristic a - acoustoplasma discharge, b - variconds

From Figure 3, it follows that the characteristic features of acoustoplasma is differ from the usual variconds (capacitor with variable capacitance) [3]. First, a conventional variconds characterization comes from the 1st to the 3rd quadrant, - we have, from the 2nd to 4th. That is, an electrical hysteresis- the field of electric induction of variconds behind on the electrical tension (or

voltage), in acoustoplasma, the field of electric induction intensity change is ahead voltage. Second, if the usual variconds can describe a cusp catastrophe, there is a jump in the maximum stress shows that to describe the changes you want to jump and crash of a higher order (dovetail or butterfly).

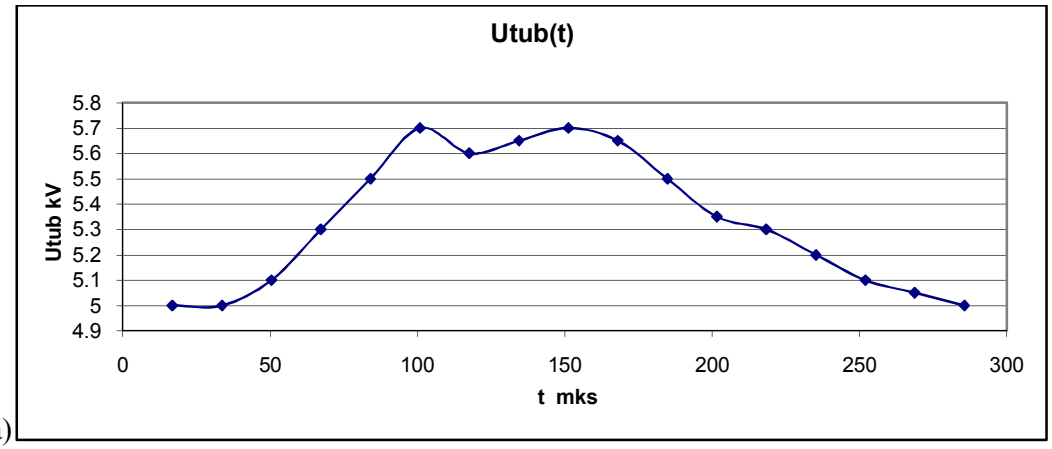

a)

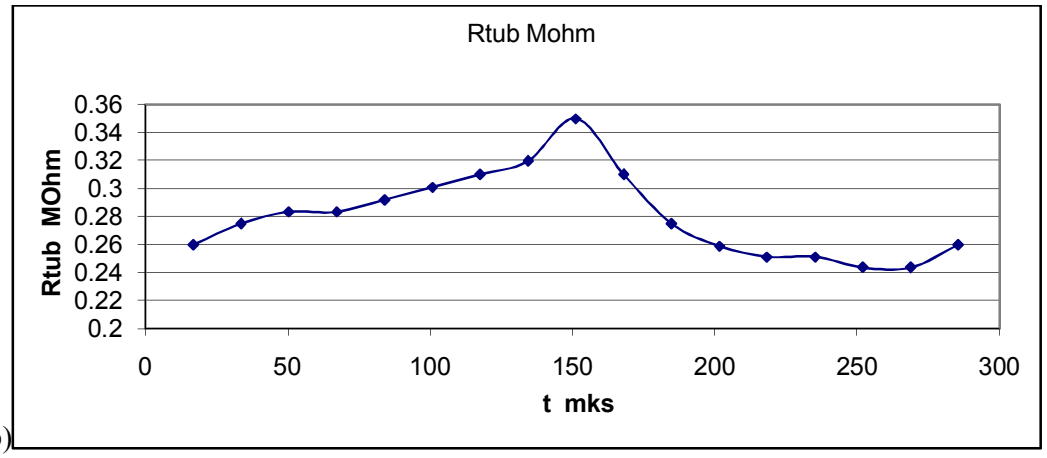

b)

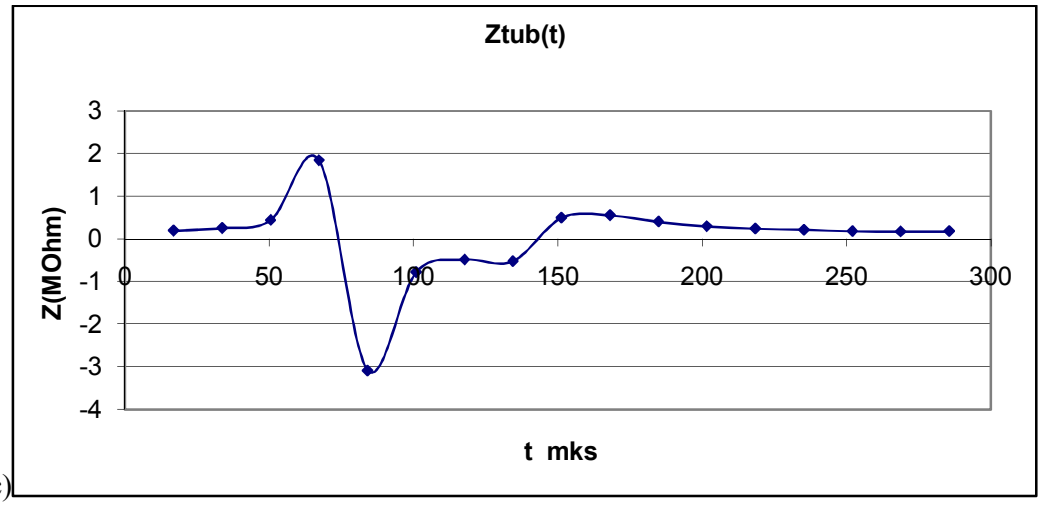

c)

Fig.4

Figure 4 shows the dependence of the time instantaneous voltage at the ends of the discharge tube (4a), ohmic (4b) and complex resistance of the discharge (4c), during one period of modulation.

In this paper is shown that Coulomb-voltage characteristic of acoustoplasma is differ from the Coulomb-voltage characteristic of usual variconds. The electrical hysteresis- the field of the electric induction is ahead of voltage.

References

1. K.G.Sahakyan. Accounting of the energyinvest in acoustoplasma, in this book.
2. Laser LG-23, manual.
3. L.A.Bessonov. Theoretical basis of electrotechnic. Moskow: Vyschaya shkola, 1967, 775p (rus).

Section VII

Technologies of New Basic Elements of X-Ray Optics

High-Resolution X-ray diffractometer based on Acoustic Monochromator

V.R. Kocharyan, A.H. Mkrtchyan

Institute of Applied Problems of Physics of NAS RA, Hr. Nersisyan str. 25, Yerevan, 0014, Armenia, Vahan2@yandex.ru

Creating of a new, more sensitive and versatile methods for research in various fields of science and technology, such as the definition of real structures of perfect crystals and nano systems, imaging of biological objects, the elements of micro and nano electronics, etc., is an urgent task. One of the essential factors of solving this problem is the alternative monochromatic, without harmonics, X-rays sources with controllable in space and time parameters, such as the angular divergence and intensity. One such method is the order of the radiation diffractometry angstrom wavelength deformed under external influences. In recent years in the scientific literature many papers published in this direction. In particular theoretical and experimental work carried out in the field of beams of X-ray energy in space and time under the influence of external fields should be noted [1-6]. These studies showed that the presence of external acoustic fields or temperature gradient can dramatically change the cross section for scattering in a given sample and thus can be the lever controlling the parameters of the diffracted X-rays in space and time. In its turn, this phenomenon opens new possibilities to produce beams with the specified parameters, thus the wide application of X-ray diffraction in science and technology.

The aim of this work - to show the advantages of monochromatic x-ray beam obtained by acousticmonochromator (AM) (Fig. 1) in relation to X-ray beam obtained by Bragg monochromator and illustrated by a sample made of powder Al_2O_3.

In order to demonstrate the benefits of the AM here are some results of experiments carried out on DRON-3M. At a distance of 20cm from the AM is a quartz crystal x - slice thickness of 0.9 mm and were taken by the schemes rocking curves (n,-n) and (n, n) in the Laue geometry. AM is located at a distance from the source of 20cm and is in complete transfer. To eliminate the variance in the scheme (n,-n) were chosen quartz crystal representing the family of atomic planes $(10\bar{1}1)$ in Fig. 2a. For comparison, rocking curves were taken with the same conditions with the difference that instead of the AM was used monochromator by Bragg.

It is obvious from figure 2 that the AM have some advantages in particular: they received more X-ray beams of monochromatic, about 2 times more intense than the beams obtained by Bragg monochromator, have no background, the intensity distribution is uniform and symmetrical as indicated by the absence of absorption.

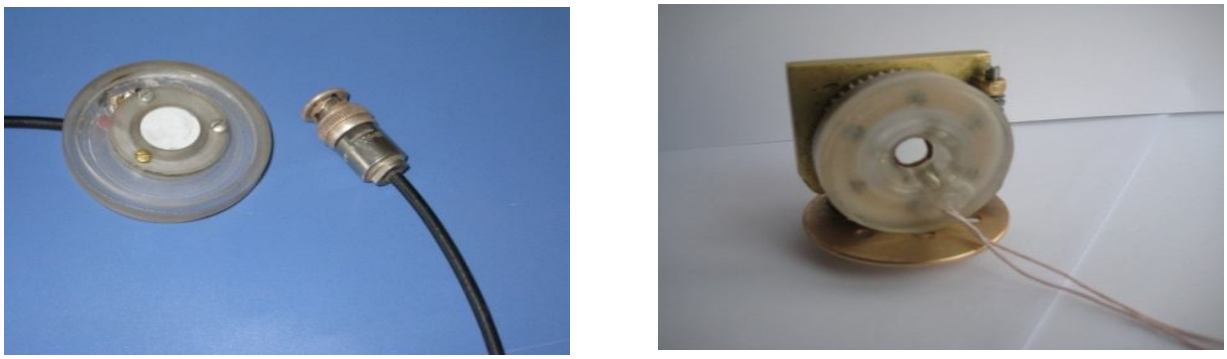

Fig. 1. Acoustomonohromator and its holder.

AM are used for X-ray and synchrotron beams which are controlled in space and time and are controllable parameters. AM gives the ability to control:

- degree of monochromic $\cdot \frac{\Delta\lambda}{\lambda} \approx 10^{-3} \div 10^{-5}$
- angular divergence $\Delta\theta \approx 2'' \div 3'$
- focal length $(-\infty, +\infty)$

With respect to the Bragg monochromator AM has the following advantages:

- integrated intensity is about 2 times more
- energy flux density is about 10 times more

In the base of DRON-3M diffract meters one can receive automatic diffract meters for structural studies at high speed and high accuracy using both AM and made our recording unit connected to the computer of the diffractometer. Automated recording unit and the AM have a great resistance to change ambient temperature, the intensity of X-rays falling on it and have stable performance over time. Fig. 3 shows the diffractogram pattern obtained for a few minutes of Al_2O_3 powder on the diffract meter described at the above.

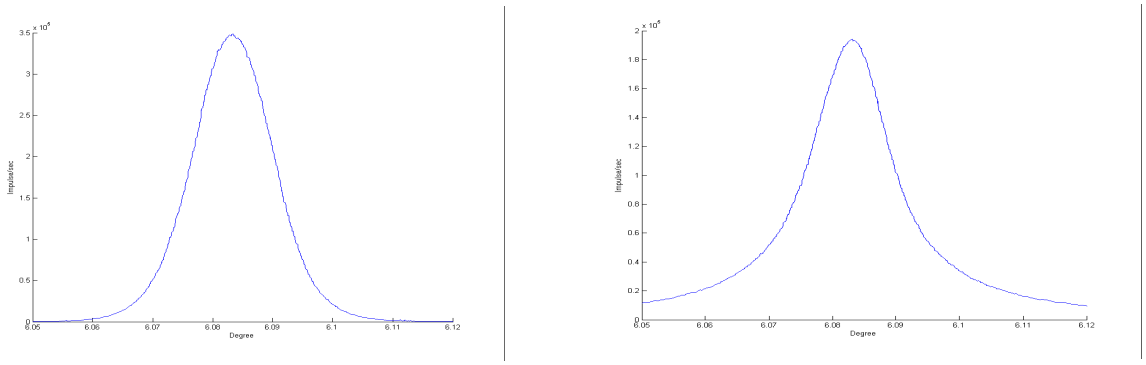

Fig. 2. Rocking curves of a quartz crystal, obtained from a family of reflecting atomic planes $(10\bar{1}1)$ scheme (n,-n) when the incident monochromatic beam was obtained a) AM b) Bragg monochromator.

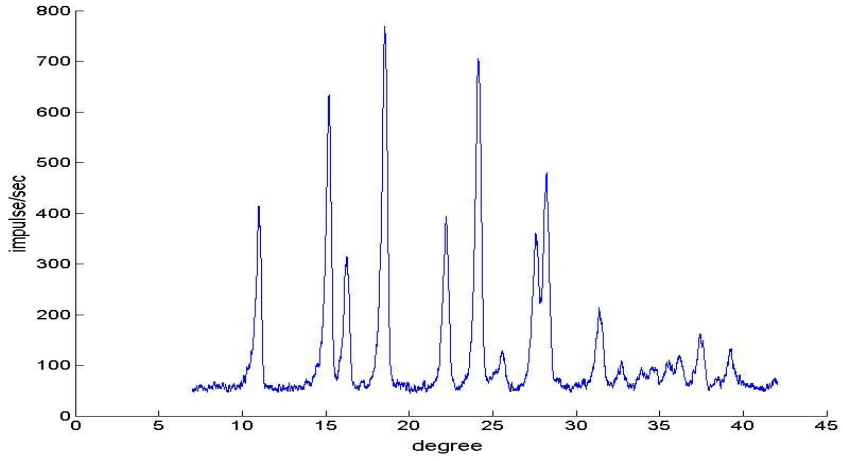

Figure 3. Diffraction pattern from a sample of the powder Al_2O_3 which is derived from basic research in the IPPF NAS using AM for X-ray beam.

References

1. A.R. Mkrtchyan, Navasardyan M.A., Mirzoyan, V.K. //Technical Physics Letters, 1982, vol.8, B.11,p.677-680.
2. A.R. Mkrtchyan, Navasardyan M.A., R. Gabrielian, and so on. //Technical Physics Letters, 1983, v.9, B.11, p.1181.
3. R.G. Gabrielyan, H.A. Aslanyan //Phys. Stat. sol.(b), 1984, V123, p.K97-K99.
4. A.R. Mkrtchyan, Navasardyan M.A., Mirzoyan, V.K. //Journal of Contemporary Physics (Armenian Academy of Sciences) 1986, v.21, B 6, p.340-344.
5. A.R. Mkrtchyan, V.K. Mirzoyan, , S.N. Noreyan //Journal of Contemporary Physics (Armenian Academy of Sciences) 1990. T.25. B.1. p.47-51.
6. V. R. Kocharyan, R. Sh. Aleksanyan and K. G. Truni. //Journal of Contemporary Physics (Armenian Academy of Sciences) V. 45, N. 4, 190-194, 2010.

Section VIII

Related Problems of Acoustophysics and Solid State Physics

Influence of Acoustic Fields on Main Parameters of Resonance Systems

A.R. Mkrtchyan, A.H. Mkrtchyan, A.S. Baghdasaryan, A.K. Atanesyan, V.V.Nalbandyan, T.G. Dovlatyan, V.N. Agabekyan, H.R. Muradyan, E.A. Mkrtchyan, S.A. Mirakyan, H. Hovhannesyan

Institute of Applied Problems of Physics of NAS RA, Hr. Nersisyan str. 25, Yerevan, 0014, Armenia

Experimental studies have been carried through for revealing of acoustic fields influence on the capsules filled with different liquids. Series of resonance capsules with different geometrical configurations have been developed and made, which, while being filled with the corresponding liquids, obtain definite resonance characteristic. Special systems for generation and modulation of acoustic fields have been also developed and made. In the experimental works, periodical structures with definite parameters were created in a liquid medium under the influence of an external electromagnetic field, which conducted the resonance interaction with acoustic fields. The experiments were carried through at the Institute of Applied Problems of NAS RA (IAPP NAS RA).

The obtained experimental data confirm the results of the previous experimental works carried out in the realm of NSTC [1], where the accumulative and re-vibration properties of natural and artificial water reservoirs have been revealed. The amplitude-frequency characteristic of the developed resonance capsules have been registered at the absence and presence of acoustic fields of different frequencies.

Being the first time, the effect of double-resonance has been observed under the influence of an external electromagnetic field and acoustic field. The different changes of values of the relative dielectric and magnetic transparency coefficient of investigated media have been revealed.

References

1. Мкртчян А.Р., Асланян А.А., Кочарян Л.А., Мкртчян А.Г., Котанджян Х.В., Багдасарян Э.Г., Арутюнян Г.Р., Барсегян Н.А., Озера и водозаполненные полости как чувствительные антенны и ‘‘запоминающие’’ устройства акустических колебаний инфразвуковых частот, Сборник докладов международного симпозиума, с. 86-93, Москва, 1997.

Acceleration of Ions in Liquid Medium in the Presence of External Acoustic Field

A.R. Mkrtchyan, A.H. Mkrtchyan, A.S. Baghdasaryan, A.K. Atanesyan, V.V. Nalbandyan, T.G. Dovlatyan, V.N. Agabekyan, H.R. Muradyan, E.A. Mkrtychan, S.A. Mirakyan, A.A. Aslanyan

Institute of Applied Problems of Physics of NAS RA, Hr. Nersisyan str. 25, Yerevan, 0014, Armenia

The possibility of resonance acceleration of ions and radicals in a liquid medium has been experimentally studied. The experimental installation has been developed on the basis of resonance capsules and equipment created at the Institute of Applied Problems of NAS of RA (IAPP NAS RA), which were also used in work [1]. New systems of linear acceleration have been developed with the corresponding systems of phase dislocation. The experiments have been carried through at the laboratories of IAPP NAS RA.

The acceleration of radicals H_2^+ and O_2^- in liquid media, which have different chemical compositions and polarization levels with a definite periodicity conditioned by external electromagnetic fields, has been experimentally studied.

Analogous spectra depending upon the polarization levels of media have been registered. Being the first time, a multiple acceleration of radicals in liquid periodical media has been observed under the influence of an external acoustic field.

References

1. A.R. Mkrtchyan, A.H. Mkrtchyan, A.S. Baghdasaryan, A.K. Atanesyan, V.V.Nalbandyan, T.G. Dovlatyan, V.N. Agabekyan, H.R. Muradyan, E.A. Mkrtchyan, S.A. Mirakyan, H.Hovhannesyan, Influence of acoustic fields on main parameters of resonance systems. International Conference on Electron, Positron, Neutron and X – Ray Scattering under External Influences, Yerevan-Meghri, 2011**,** Book of Abstracts, p. 61.

Need for high-resolution Study of the FFLO Superconductivity by Means of the Highly Sensitive Technique Based on the SFCO Test-Method: that is urgent for demonstration of the "singlet"-to-"triplet" spin-flip of Cooper pairs, crucial for true identification of the real nature of superconductivity

(project proposal on the basic superconductivity)

Samvel G. Gevorgyan

[1] *Superconductivity & Scientific Instrumentation Center, Yerevan State University, Yerevan, 0025, Armenia*

[2] *Institute for Physical Researches, National Academy of Sciences, Ashtarak-2, 0203, Armenia*

Abstract:

The problem of electron "pairing" above Meissner expel appeared when HTSC materials were discovered. And almost commonly is admitted now, that there is need to consider 2 physical processes for HTSC – electron pairing and long-range phase coherence among pairs (Cooper-pair condensation) – separately & independently of each other. So, superconductivity in HTSC material requires both the electron pairing and the Cooper-pair condensation (phase coherence among pairs). Otherwise, it is admitted now, that in HTSC material electrons become paired above Meissner expel (above T_0, starting from T_c) and start forming the SC-condensate only at T_0, while in a LTSC (conventional) materials the pairing & the Cooper-pair condensation take place simultaneously ($T_0=T_c$) – due to relatively large pair size it is assumed that their wavefunctions are overlapping in a LTSC).

Since discovery of HTSCs, however, a lot of basic empirical data is appeared, and importance to some old results (passed unnoticed in due time) is attached, and newly interpreted (all discussed in details below), indicating some global similarity between the HTSC and LTSC materials in connection with the physical principles of the electron "pairing" and establishment of the phase coherence among superconductive pairs. Therefore, doubts arose in our mind related with the present understanding of this problem. The gathered new data enables to believe that there are no essential differences between the HTSC & LTSC materials regarding the said 2 processes. Apparently, electron pairing and Cooper-pair condensation are separate and independent even in a LTSC material. Differences are in temperature scales. For the LTSC material these 2 processes run in a narrow temperature range (~30mK), while in HTSC the temperature scale is much longer (for YBaCuO material, it is even broader than 3K). Possibly, that is the main reason why separation of the T_c from the T_0 in a LTSC material was so problematic so far. The problem is still open also due to lack of methods for "non-perturbing" sensitive study of the SC-phase transition in clean (and so, tiny) objects with too small signals – especially at very beginnings of the phase transition, where even a SQUID technique is powerless to "notice" such small changes in a normal-state "skin"-depth.

Summarizing the gathered latest data, we came to the conclusion that now becomes important and urgent many-sided investigation of the Fulde-Ferrell-Larkin-Ovchinnikov superconductivity (**FFLO**-state) by more sensitive methods. Materials, in which theorists advise to study this phenomenon (but, with much higher resolution compared to earlier tests) are heavy-fermion superconductors (for example, $CeCoIn_5$), which have a layered electronic structure. This anisotropy hinders orbital motion of the electrons for magnetic fields aligned parallel to the conducting planes. Besides, the large spin susceptibility favors paramagnetic limitation. And so, these materials satisfy the delicate balance of properties needed to detect and study the FFLO superconductivity at temperatures below the 350mK. The unique **SFCO** (**s**ingle-layer **f**lat-**c**oil-**o**scillator) method, with its many capabilities, we suggest to use as a key instrument for precision study of the super-

conductive phenomenon, and the pair formation in the FFLO state. Such a study may enable unambiguous demonstration of the "singlet"-to-"triplet" conversion (spin-flip) of the pairs, and also separation of the ideal conducting ($R = 0$) and superconducting (ideal diamagnetic – $B = 0$) states, which are important not only for true interpretation of the real nature of the superconductive phenomenon, but also for correct understanding of microscopic mechanisms of the electron "pairing" (physical principles for establishment of the long-range phase coherence among the superconductive pairs).

1. Introduction:

The problem of electron pairing above Meissner expel raised after 1986 only, when high-temperature superconductive (**HTSC**) materials were discovered by *Bednorz* and *Muller* **[1]**. And majority of scientists is admitted presently **[2]**, that for truth there is need to consider 2 physical processes for *HTSC* material – the electron pairing, and the onset of the phase coherence – separately and independently of one another. So, superconductivity in *HTSC* material requires both the electron pairing and the Cooper-pair condensation. The later is also known as an onset of the long-range phase coherence among the pairs **[2]**.

In other words, it is admitted now **[2]**, that in a *HTSC* material electrons become paired above the Meissner expel (above the T_0, starting from the T_c) and start forming the superconductive condensate only at the T_0, while in low-temperature (*conventional*) *SC*-material (**LTSC**) it is assumed, that the pairing process and the onset of the phase coherence take place simultaneously (at the same temperature; T_0=T_c): due to relatively large pair size it is assumed that their wavefunctions are overlapping in *LTSC* material.

Shortly after the discovery of *HTSC*, however, a "*paramagnetic*" (**PM**) precursor to the superconductivity was detected by us in *LTSC* tin (**Sn**) **[3]** (see Fig.1). Weakly expressed this crucial effect (*in a central press it was first reported later*, *in* **[4]**) and indirectly related to it another fine effect **[5]** (Fig.2) – a thermal (*caloric*) peculiarity, seen on heat capacity vs. temperature curves before the well-known specific heat's "*jump*" – provide serious arguments to have a contrary opinion regarding the low-temperature *SC* materials. Although such a key effect (*first*, *also detected in LTSC tin*) appeared on *Corak*'s curves a half century ago **[5]**, but, to our surprise, it passed unnoticed so far – before our group noticed it, and could explain it in a paper **[6]** (*in a central press it was reported later* **[7]**). Below, we discuss the reasons why these two fine effects should have the same physical origin. To explain such global similarity of electromagnetic and thermal effects in *SC* materials (regardless it is *HTSC or LTSC* material) we used an advanced idea, which admits existence of two types of the Cooper pairs, both in *HTSC* & *LTSC* – "*singlet*" and "*triplet*". According to our understanding now, they show entirely different, non-traditional temperature behavior upon cooling of the superconductive material. For the *YBaCuO* composition *HTSC* material, the respective curves taken from the said papers **[6-7]** are shown in the Fig.3). Thus, we suppose that these, and some other data discussed below (included our results), enable to believe that there are no essential differences between HTSC and LTSC materials regarding the said two processes. Apparently, electron pairing and the Cooper-pair condensation (phase coherence) are separate and independent even in LTSC material. Difference is in a temperature scale. In LTSC materials these processes run in a narrow temperature range (~30mK – Fig.1), while in HTSC the temperature scale is much longer. For example, for the YBaCuO composition HTSC material the scale of PM effect (which indicates the scale of event selection for the above two physical processes) estimated by Gantmakher is ~1K [8] – see Fig.4, while much more precise and sensitive experiments by our group evidence, that it is even broader 3K [4] – Fig.5.

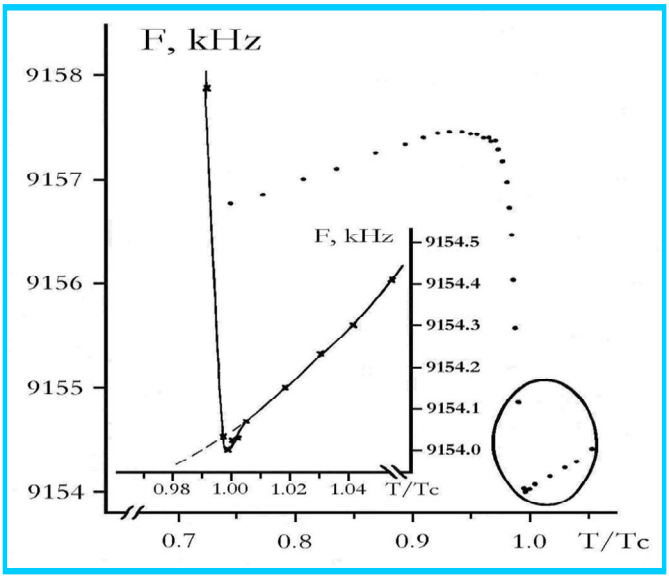

Fig.1. "Paramagnetic" effect detected upon transition to the SC-state of identical tin grains of ~ 5μm in dia. [3-4], registered by the solenoid-coil based less sensitive technique. Inset: enlarged view of the effect. Broken line is device temperature dependence.

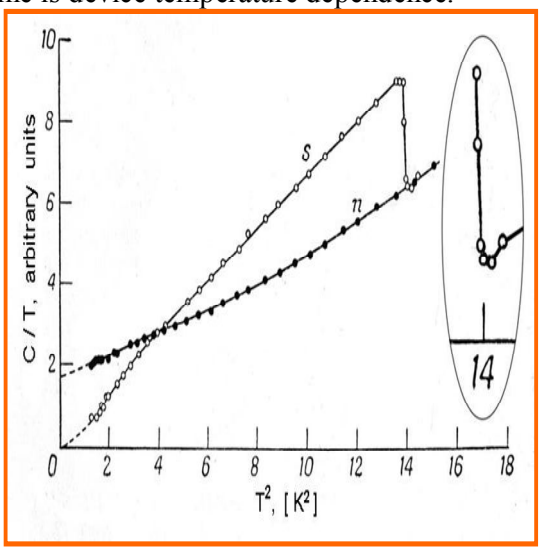

Fig.2. Heat capacity *vs.* temperature curves detected in tin by *Corak* **[5]**. **Inset:** enlarged view of a fine effect seen before the specific-heat's "*jump*". Symbol "***s***" corresponds to the *SC*-state, while "***n***" – normal (*superconductivity is suppressed by magnetic field*).

Possibly, this is the main reason why separation of the temperature Tc from the temperature T0 in LTSC material was so problematic so far. The problem is still open also due to lack of the methods for "non-perturbing" sensitive study of the SC-phase transition in clean (so, tiny) objects with too small signals – especially at very beginnings of the SC phase transition, where even a sensitive SQUID technique is incapable to "notice" such small changes in a normal-state "skin"-depth.

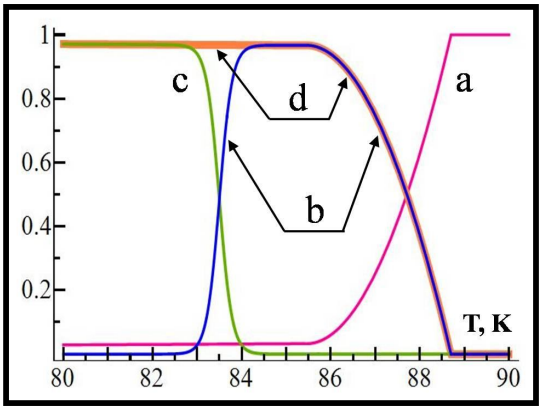

Fig.3. Temperature dependances of the normal conducting electrons (**a**), the "triplet" (**b**) and "singlet" (**c**) Cooper pairs, as well as the all pairs (**d**) **[6-7]**.

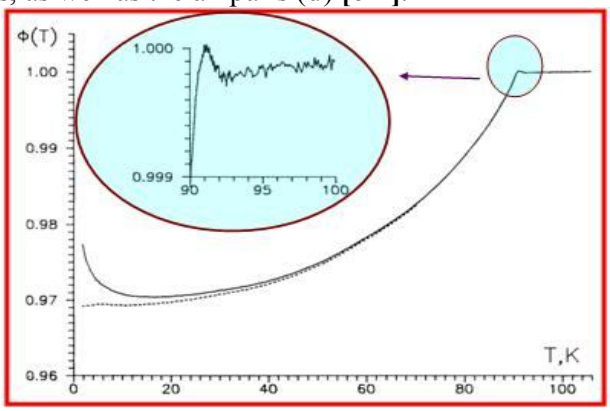

Fig.4. Superconductive phase transition of the ultra-fine YBaCuO powder with an average grain's size 2r=1920Å [8]. Inset: enlarged view of the "paramagnetic" (PM) effect.

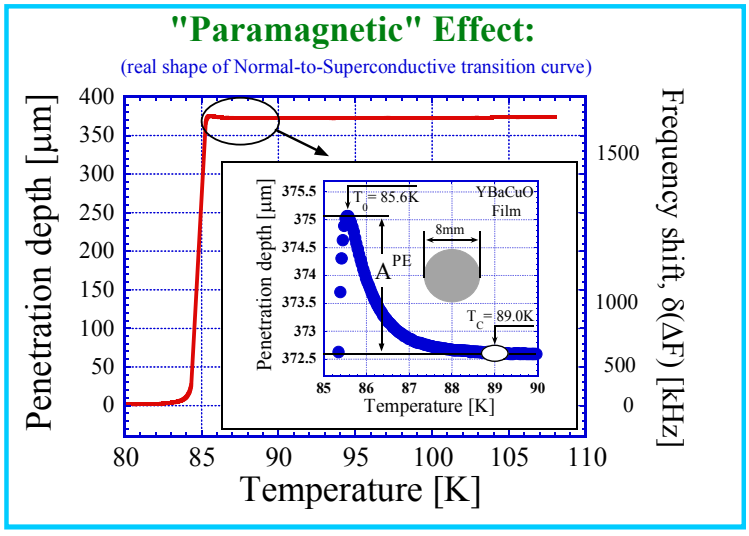

Fig.5. **N/S** transition of the *YBaCuO* disk-film **[4]**. **Inset**: enlarged view of the "*paramagnetic*" effect (**PE**) at the beginnings of *SC*-phase transition, which precedes the *Meissner* expel. A^{PE} is the effect's height.

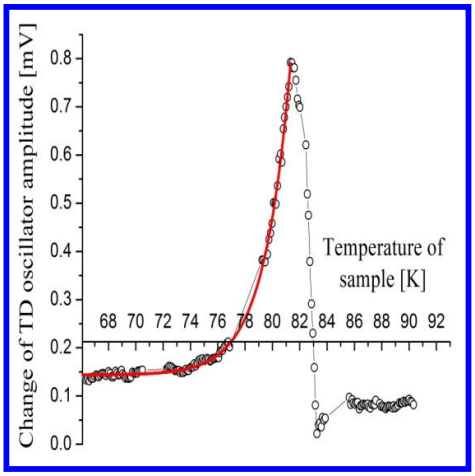

Fig.6. Indirect detection of a *caloric* effect in *YBaCuO* **[9]** by the new imaging method **[10-11]**, based on a sensitive *SFCO* technique **[13-16]**. Circles are measured data, while the solid line – exponential fit of the exponential data.

In this regard, it was so much urgent searches for the said *caloric* effect in high-T_c superconductive material. It is not so easy, however, to measure heat capacity (*moreover*, *its little changes at very starts of the phase transition*) in so small volume clean *HTSC* objects (*such as film-structures*, *single crystals*). We tried to do that, and could indirectly detect this fine effect also in a *YBaCuO* composition *HTSC* material **[9]** (Fig.6) – by the step-by-step creation, many-sided perfection and use of a radically new principle of operation imaging technique **[10-11]** (schematics see in Fig.7) based on combination of a well-focused laser scanning microscopy **[12]** and the **s**ingle-layer **f**lat-**c**oil-**o**scillator (**SFCO**) based highly sensitive new measurement technique, introduced by our group in Armenia **[13-14]**, and strongly improved in a last decade – due to wide international cooperation

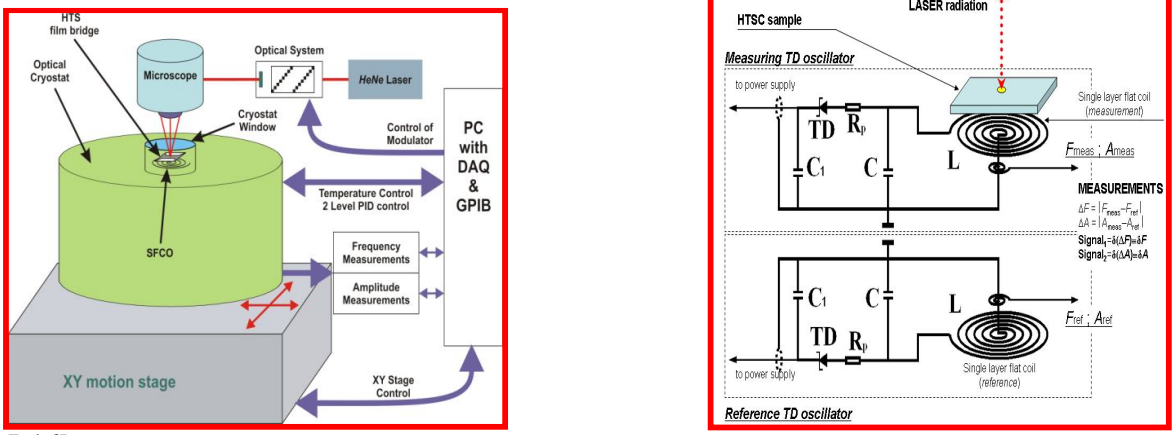

[15-16].

Fig.7. Schematics of a **c**ryogenic **l**aser **s**canning **m**icroscope (**CLSM** – left) **[10-11]**, based on a focused (Φ_{beam}~1.5μm) laser scanning microscopy **[12]** and a **s**ingle-layer **f**lat pick-up **c**oil-based tunnel diode **o**scillator (**SFCO**-technique – right) **[13-16]**.

As is known, superconductor is a double ideal material, since it becomes *ideal conductor* & gets properties of the *ideal diamagnetic* below some temperature. The latter behaves also as an *ideal conductor* – reverse is not true. But, must superconductor obtain such properties at the same moment (*temperature*)? And why transitions of a different nature (*1-st is assumed to be connected with*

electron-pairing, *followed by zeroing of the pair momentum*, *the 2-nd*, *with pair condensation – due to collection of enough "singlet" pairs – arguments see in* **[17]**) should occur at the same moment? And also, are there other different-nature effects, which occur at the same moment in a Nature? Such questions acquired meaning since the said "*paramagnetic*" effect was detected in μm-size tin grains **[4]** (T_c~3.7K – Fig.1), indicating the real physical onset of the Meissner expel. It precedes the diamagnetic ejection, and corrects the shape of the normal-to-superconductive (***N/S***) transition curve. The origin of above questions relates also with a "*preceding*" effect, opened in a percolating *YBaCuO* (in ceramics **[1]** and films **[18]** with granular structure of a material). As per it, the *resistive*-transition ends before the start of Meissner expel. It was seen by *Morris* too, in a *BiCaSrCuO* crystal **[19]**, but doesn't attract an attention of the author – perhaps, due to lack of assurance in accordance among temperature-scales of conducted tests, performed in different set-ups. Questions were deepened when the "*diamagnetic activity*" was revealed in *LaSrCuO* film by *Iguchi* **[20]** – at temperatures much higher the transition temperature of a material, established by the onset of the Meissner expel. A *super*-sensitive scanning-SQUID microscope is used for those tests. Such a flux activity is interpreted by the author as the effect *precursor* to Meissner state.

There are other *Meissner*-state precursor effects too. Let's stop also on the study conducted by *Tonica Valla* **[21]**. It shows that a "*pseudo-gap*" in the energy level of high-T_c *SC* materials' electronic spectrum is the result of electrons being bound into the Cooper pairs above the transition temperature to the *SC*-state, but unable to *super*-conduct, because pairs move incoherently. As to *LTSC* materials (*which act much closer to the Absolute Zero*), it was already said that, admittedly, superconductivity in these materials occur as soon as electron-pairs are formed. "In the case of high-T_c superconductors, however, electrons, though paired, "*do not 'see' each other* above some temperature," *Valla* says in **[21]**, "so they can't establish the phase coherence, with all the pairs behaving as a '*collective*'". Discussed above experimental data indicate, however, that such is the case for all types of superconductive materials.

Origin of a "*pseudo-gap*", along with the mechanism for forming the pairs necessary for superconductivity, has been among the biggest mysteries scientists have been trying to understand about high-T_c superconductors since their discovery. The material studied by *Valla* was the first high-T_c superconductor discovered (*LaBaCuO*). In spite of the fact that it at the ratio 1(Ba)**:**8(Cu) is not a superconductor, it has a similar energy signature – *including energy gap in its electronic spectrum* ("*pseudo-gap*") – as the other *HTSC* materials in their *SC*-states. *Valla*'s group interprets this finding as an evidence that pairs are formed first (as "*preformed pairs*") and phase coherence occurs later, at some lower temperature (*transition temperature* – in our symbols, at T_0), when thermal fluctuations of the phase are suppressed enough to cause superconductivity. *Valla*'s research shows "that a "*pseudo-gap*" is caused by the same interactions that are responsible for superconductivity – interactions that bind 2 electrons into a Cooper pair". "In high-T_c *SC* material, however, this pairing is only the first step," he says in **[21]**. "The phase transition is delayed, possibly – and ironically – because the pairing might be too strong. Figuratively speaking, a strong pairing produces "*small*" pairs with strongly fluctuating phases. Only by cooling the material to much lower temperatures do the phase fluctuations become suppressed. At that point, the phase becomes locked so the pairs can act coherently – and the system becomes a superconductor".

NO indication, however, on any microscopic physical mechanism for establishment of the phase coherence among superconductive pairs in *Valla*'s works, as well as in papers of other scientists. While, as a hint to the possible mechanism for absence (*at higher temperatures*) and presence (*later*, *at cooling*) of the phase coherence among pairs might be discussed existence of 2 types of Cooper pairs in a *SC* material (regardless it is high-T_c or low-T_c superconductor) – "singlet" & "triplet", with different angular momentum **[17]**. They have fully different temperature behavior upon cooling of a material (qualitatively illustrated by the Fig.3, for the *YBaCuO* **[6-7]**). Such an approach may result in the *ideal conductivity* (it starts with the pair formation, from the T_c – and

acts for both types of pairs). That is because pairs are quasiparticles with a Zero momentum, and so, with an infinitely large *de Broglie* wavelength, due to which they can move in a material without scattering, "*ignoring*" defects & impurities of the crystalline structure. At a later cooling of a material, starting from the T_0, such a reasonable approach may also result in the *superconductivity* (*ideal diamagnetism*, Meissner state) – but, for only the "singlet" pairs.

And finally, quite recently a research team from the Ruhr-University (Bochum), Christian-Albrechts-University (Kiel) and Santa Barbara (headed by Profs. *Kurt Westerholt*, *Hartmut Zabel* and *Konstantin Efetov*) could make an experimental sensation: their studies on the "*pairing*" behavior of electrons have proven experimentally the triplet superconductivity for first time **[22]**. In other words, they could detect empirically existence of the Cooper pairs, with parallel spin direction. In more details (see **[23]**), the said internationally integrated team has studied Josephson junctions with the barriers prepared from the Heusler compound Cu_2MnAl. In the ***as***-prepared state the Cu_2MnAl layers are nonferromagnetic, and the critical Josephson current density $\boldsymbol{j_c}$ decreases exponentially with the thickness of the Heusler layers $\boldsymbol{d_F}$. On annealing the junctions at 240°C the Heusler layers develop ferromagnetic order and they could observe a dependence $\boldsymbol{j_c(d_F)}$ with $\boldsymbol{j_c}$ strongly enhanced and weakly thickness dependent in the thickness range $7.0 < \boldsymbol{d_F} < 10.6$ nm. The research team interprets this feature as an indication of a triplet component in the *SC* pairing function, generated by the specific magnetization profile inside thin Cu_2MnAl layers.

Analyzing all above data (*and some other results*, *more or less related*) we came to the conclusion that many-sided study of the *Fulde-Ferrell-Larkin-Ovchinnikov* superconductivity (FFLO-state **[24-25]**) by the sensitive method stands important and urgent at the moment. Theorists advise that heavy-fermion *SC* materials are most of promising candidates for observing of the FFLO state. And therefore, we suggest studying this unique *SC* phenomenon in a $CeCoIn_5$, by involving new methods (*enabling much higher resolution*, *compared to Agosta's group earlier tests* **[26-27]**). This material has a layered electronic structure. Such anisotropy resists orbital motion of electrons for fields applied near parallel to the conducting ***ab***-planes of the material. Besides, the large spin susceptibility favors paramagnetic limitation. And so, this material fulfills the delicate balance of the properties needed to reveal, detect and study FFLO superconductivity at temperatures below 350mK. The unique *SFCO*-technique **[15-16]** (*with its unprecedented capabilities*, *enabling to reveal fine physical effects both at N/S phase transition* **[4, 28]** *and in established SC state* **[10, 29]**) will serve as the main instrument for precision study the superconductivity and Cooper pair formation in a FFLO state. This study may enable unambiguous demonstration of the "singlet"-to-"triplet" (*and back*) spin-flip of the Cooper pairs, and also separation of the *ideal conducting* ($R = 0$) and the *superconducting* (*ideal diamagnetic* – $B = 0$) states, which all are important not only for true interpretation of the real nature of the superconductive phenomenon, but also may bring to the correct understanding of the physical mechanisms of the electron "*pairing*" (*microscopic mechanisms for the establishment of the long-range phase coherence among superconductive pairs*).

2. Fulde-Ferrell-Larkin-Ovchinnikov Superconductivity in $CeCoIn_5$:

Superconductivity (**SC**) is a macroscopic quantum phenomenon discovered in 1911 by *Kamerlingh Onnes* **[30]** where electrons of opposite spin and momentum condense into pairs – according to the original explanation by *Bardeen*, *Cooper* & *Schrieffer* (**BCS**) in 1957 **[31]**. Enough large magnetic fields destroy superconductivity by coupling to the orbital motion of the electrons. This critical field (*orbital limit*) separates the uniform **S**uperconducting state from the **N**ormal metallic state. The magnetic field can, however, couple predominantly to the spins of electrons. The superconductor is then in a *paramagnetic limit*. It was shown in 1964 by ***F**ulde* & ***F**errell* **[24]** and independently, ***L**arkin* & *Ovchinnikov* **[25]**, that this superconductive state would be basically different from the *conventional BCS* case. In this new state, magnetic field tries to polarize opposite

spins of *SC*-pairs. In response, the superconducting order parameter develops nodes in a real space, leading to the alternating regions of *SC*-layers and spin-polarized magnetic walls. This FFLO state manifests itself as a "wedge" in the field-temperature (**B-T**) phase diagram at very low temperatures, below the critical field. The exact shape of B-T diagram and the FFLO "wedge" area as well depend on many microscopic parameters, such as the Fermi surface geometry, dimensionality of the host crystal, impurities, and ratio of orbital-to-paramagnetic effects **[24-25, 27]**.

As was said above, the material in which Agosta's group first observed the FFLO state in 2003 is the $CeCoIn_5$. It has a critical temperature of 2.3K, and the layered electronic structure, which hinders orbital motion of the electrons for magnetic fields aligned parallel to its conducting planes. And, it is among the most of suitable candidates for the detection and investigation of the FFLO superconductivity.

Three techniques were used to perform the heat capacity, magnetization and penetration depth studies of the FFLO state in mentioned initial works in 2003 **[26-27]**. The heat capacity measurements were performed in a rotatable calorimeter **[32]**. This thermodynamic method provides unambiguous evidence for the phase transitions in materials. The second technique used was a tunnel diode (**TD**) oscillator **[33]**. Such a technique with a solenoid shaped coil allows the experimentalist to make contactless measurements on down to *mm*-sized samples that are placed inside the coil of the self resonant tank circuit. Changes in materials properties alter the *TD*-oscillator resonance frequency, which in the superconducting state is directly proportional to the penetration depth of the magnetic field. The third was the torque measurement method using a cantilever that carries the sample and acts as one plate of a capacitor. The measured signal is a voltage proportional to the torque, which, in turn, is directly proportional to the magnetization of the specimen. This method enabled to detect changes to better than 1 ppm.

Fig.8 shows the measured in 2003 heat capacity vs. the field for field orientation parallel to planes. The blue curve taken at 425mK shows a jump at the critical field of 11.1T. The red curve taken at 250mK clearly displays a 2-nd transition at 10.5T, just below the critical field of 11.3T **[34-35]**. This (*additional*) thermodynamic transition is only present for temperatures below 350mK, and within ±10° of the plane parallel orientation. The lower of 2 transitions is the theoretically predicted uniform superconducting–to–non-uniform superconducting (FFLO) state transition. At angles higher than 10° the orbital effect starts to dominate the paramagnetic one and the FFLO *SC*'ty cannot be established. Thus, Agosta's measurements in 2003 were the first thermodynamic evidences of the non-uniform FFLO state **[26]**.

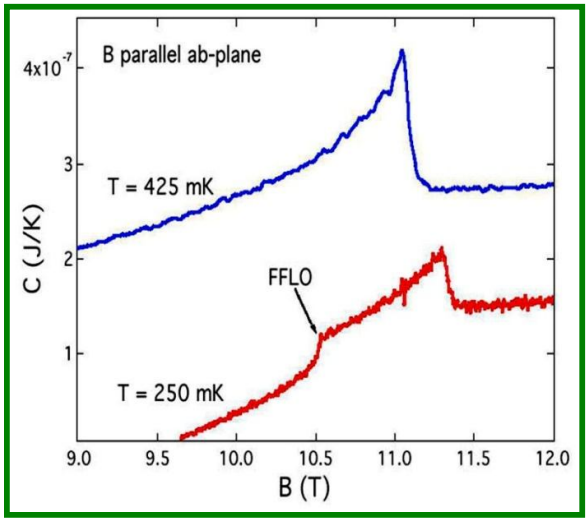

Fig.8. Heat capacity showing the additional *FFLO* phase transition below the critical field at 250 mK (see arrow) **[26-27]**.

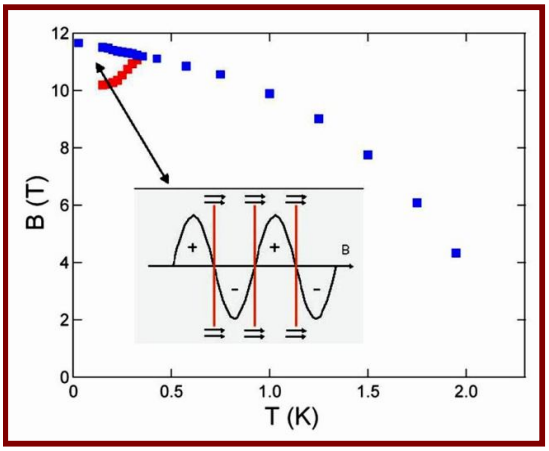

Fig.9. Critical field (blue) and *FFLO* transition line (red). Inset shows schematically nonuniform *FFLO* order parameter with magnetic walls. Hysteresis in the heat capacity measurements and the kink and jump nature of transitions in the *TD*-oscillator data confirm that the lower field transition is second order and the higher transition is first order **[23-24]**.

Fig.9 shows the constructed by Agosta in 2003 B-T phase diagram as obtained from the above heat capacity measurements for the plane parallel orientation. Blue squares denote the critical field, separating the normal metallic state from superconducting one. The "wedge" at low temperatures & high magnetic fields is the FFLO phase, with the red squares separating uniform from non-uniform superconductivity.

Fig.10 shows 2003 year Agosta's *TD*-oscillator tests vs. the applied field at 60mK. The red curve is taken with the field oriented parallel to conducting planes. The jump at 11.7T is the normal state phase transition, while the additional kink at 9.5T witnesses the FFLO transition **[26-27]**. The blue curve displays data taken at 15° & only the critical field at 9.8T is seen, behavior identical to that observed in 2003 year heat capacity tests (Fig.8). The kink in the *TD*-oscillator data matches appearance of the 2-nd phase transition seen in heat capacity in both angle and temperature. This provides evidence, that FFLO transition can be seen also in penetration depth studies – by use of *TD*-oscillator, even with a less sensitive solenoid pick-up coil. But, while studying *SC*-phenomenon in *YBaCuO* composition *HTSC* during the last 10 years we could convince scientists **[4, 9-11, 13-17, 29]**, that for plate-like objects (*films*, *crystals*) our flat-coil based *TD*-oscillator (*SFCO* method) shows by 3-4 orders of a value higher resolution, compared to its solenoid-coil based analog. This permits to believe, that ~1mm in dia. *SFCO* technique may satisfy technical conditions needed for much more sensitive detection and investigation of the FFLO state.

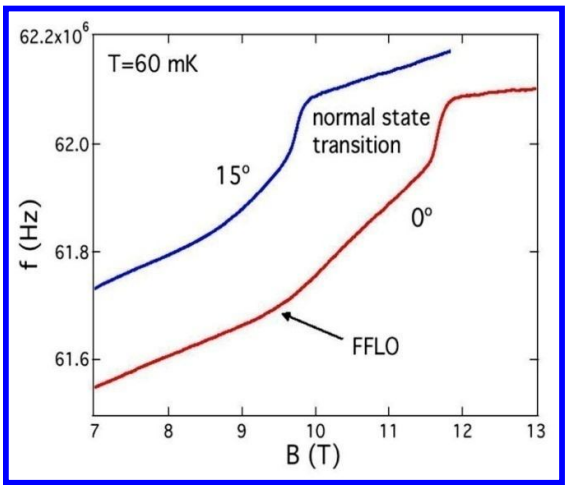

Fig.10. Penetration depth showing a kink (arrow) in the plane parallel orientation & identified as the FFLO signature [26-27].

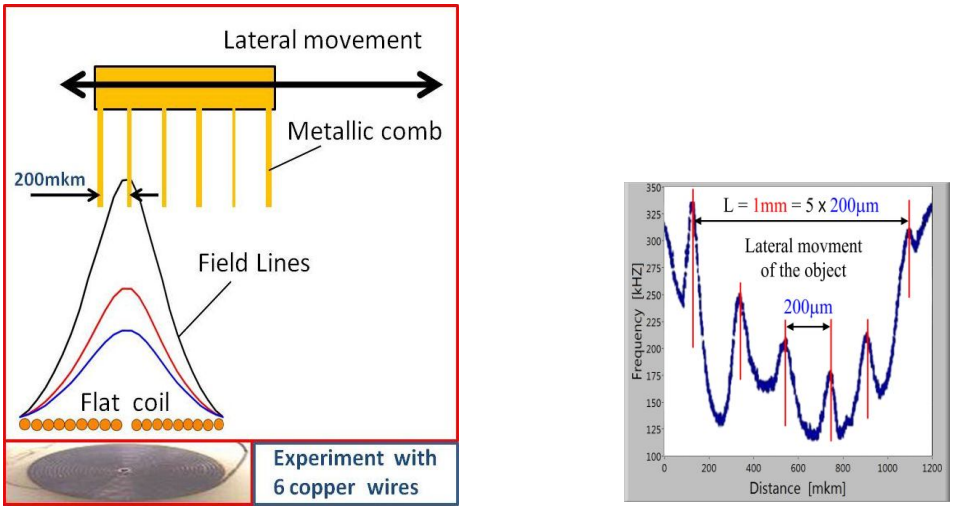

a) b)

Fig.11. Dependence of the *SFCO* technique's *TD* oscillator frequency shift *δ(ΔF)[kHz]* (**b**) on the lateral position of the ***1D*** grid-shaped metallic object (**a**) relative to the "*probe-formative*" flat coil face **[39]**.

3. High-resolution study of the Fulde-Ferrell-Larkin-Ovchinnikov superconductivity by means of the SFCO-*technique*:

Flat-coil-oscillator technique and its advantages

A single-layer flat-coil-oscillator (**SFCO**) test-method **[15-16]** is a good tool for doing ***MHz***-range measurements on thin, plate-like *HTSC* materials with small signals (see Fig.7 right). It enables to "*notice*" weakly expressed fine peculiarities of the superconductive phase transition in such objects. Due to flat shape of the coil, even few Cooper pairs, created in a flat *HTSC* material, lead to the strong deformation of a radio-frequency (**RF**) field configuration near the coil face at the Meissner expel. Similarly, even a little increase of a depth of skin layer of the material in normal state (*due to a little fall in its conductivity caused by a leave of electrons from Fermi surface at pairs' creation*) may also lead to the distortion of the field configuration around the coil, noticeable by this method. Just such key features (*the latter is even beyond the reach of the SQUID technique*) and high stability of the tunnel diode oscillator enabled to reach a *record*-high relative resolution in this method, and detect fine physical effects. Among the advantages of the method is its ability to reveal small amounts of energy-release ($\sim 10^{-9} W$) in a material caused by the movement of flux vortices created in *HTSC* material **[28-29]**. The method also allows detecting of *record*-small relative changes in *SC*-penetration depth, $\Delta\lambda/\lambda \sim 10^{-6}$ (abs. changes $\Delta\lambda \sim$1-3Å) **[4, 17]**. Such abilities of this technique (as a λ-test method) is important since in terms of the amount & variety of data obtained from tests, λ is the most suitable detecting parameter **[36-37]**. Use of a flat shape coil in a low power (*backward*) *TD*-oscillator enabled to improve the resolution of tests in flat *HTSC* objects by 3–4 orders of a value **[15-16]**. That is so as replacement of the solenoid coil by the flat one made testing coil's filling factor maximal possible (~1) for flat objects, while its value for the solenoid coil is about 10^{-4}–10^{-3}. Both, the frequency and the amplitude are used as testing parameters in this method. The measuring effects are determined both by distortion of the testing *RF* field configuration near the coil face (*which we are going to use for the checking whether or not established the ideal diamagnetic state*, *with* $B = 0$) and by absorption of its power by the sample (*due to various external or internal factors*), which we are going to use (*alongside with the direct 4-probe measurements*) for the checking whether or not established the *ideal conducting* state, with $R = 0$).

These finally lead to the changes of the measuring *tunnel diode* oscillator frequency or/and amplitude, respectively.

Our research shows also, that flat coil based *TD*-oscillator can be activated also with its internal capacitance **[38]** (*without an external capacitance C in its resonant circuit* – see Fig.7 right). That is the result of relatively high value of internal capacitances of the single-layer flat coils, compared to their parasitic capacitances with respect to the surrounding radio-technical environment. This opens exotic areas for the flat-coil oscillator application. Namely, a "*needle-like*" testing magnetic field of such a flat coil **[39]** (see Fig.11a), used as a pick-up in such a stable *TD*-oscillator, enables a novel method (*new approach*) for surface probing **[38-40]**, based on replacement of short-range, solid-state probes of the acting microscopes (*such as needles or cantilevers of tunneling* **[41-42]** *and atomic-force* **[43]** *microscopes*, *probes of the near-field microscopes*, etc.) by the long-range action non-solid-state ones. Such an unusual probe shows strong dependence of a detected signal on the size of the spatial-gap between the probe and the surface of the object **[40]** – crucial for the probe microscopy (**PM**) **[44]**. This opens an opportunity for designing of "*magnetic-field*" probes, with a *RF* power applied to the sample lying in the range of 1nW to 5μW. The gap between such a "*probe-formative*" flat coil and the object under test can be larger than 100μm **[40]**, compared with the 1nm gap of the acting probe microscopes **[44]**. Such a *SFCO*-probe could "*notice*" and distinguish details of the relief of the normal-metallic object – with 5-10μm spatial-resolution – even in a relatively large diameter ($2R_{coil}$~14mm) flat-coil probe **[39]** (see Fig.11). In order to demonstrate that we performed an experiment with one-dimensional (**1D**) metallic grid made of 6 copper wires (Fig.11a): each wire was 20-30μm in dia. and was positioned with an average interval of about 200μm between the wires. Copper wires distort the coil *RF*-field configuration when they move relative to the coil face (*or*, *when the coil moves relative to the grid*), leading to changes of the oscillator frequency or/and amplitude. The effects are maximum when each wire reaches to the coil center. Figure 11b illustrates the detected dependence of the oscillator frequency shift, $\delta(\Delta F)$, vs. the lateral position of the metallic-comb relative to the flat-coil face (*relative to the "magnetic-field" probe*). Average distance between the detected 6 vertical neighboring peaks on the curve in Fig.11b is ~200μm – just in agreement with the experimental setup in Fig.11a. That is why, we believe, that our *SFCO*-probe may distinguish (*both by amplitude and by frequency of the TD-oscillator*) details of the relief of the node structure in a real space (*consisting of the alternating regions of the superconducting layers and the spin-polarized magnetic walls*). For that aim, one needs to work out and create the *SFCO* method-based advanced "*magnetic-field*" probe, with a lithographically made single-layer flat coil of about 1mm (*or less*) in diameter **[45]** – *as an effective needle-type unique probing instrument with better than* 100nm *predicted lateral resolution*. Such a radically new probe will have considerably large work-distances (*more than* 100μm) between the probe and surface of the object, which may permit a "visual" control of the local area at the probing of the object, and, if needed, application of test perturbations (*for example*, *exposition to the laser radiation*).

Summarizing all the said above, let's once again note: we think, that at the moment becomes important and urgent many-sided, sensitive investigation of the ***F**ulde-**F**errell-**L**arkin-**O**vchinnikov* superconductivity (**FFLO**-state). The material in which theorists suggest to study this phenomenon is the heavy-fermion superconductor $CeCoIn_5$. The problem was investigated earlier by *Agosta*'s group **[26-27]**, but with much less resolution compared to what we suggest to do now. This material satisfies the delicate balance of properties needed to detect and study the FFLO superconductivity at temperatures below the 350mK. The unique *SFCO*-method (*with its unprecedented capabilities*) we suggest to use as the main scientific instrument for the precision study of the superconductivity and pair formation in the FFLO state. Such a study (*to be carried out approximately by the scenarios implemented in original experiments of Agosta's group* **[26-27]**) may enable unambiguous demonstration of the "singlet"-to-"triplet" spin-flip of the Cooper pairs, and also separation of the *ideal conducting* ($R = 0$) and *superconducting* (*ideal diamagnetic* – $B = 0$) states, which both are

important not only for true interpretation of the real nature of the superconductive phenomenon (*in a whole*), but also for correct understanding of microscopic mechanisms of the electron "*pairing*" (*physical mechanisms for the establishment of the long-range phase coherence among the superconductive pairs*).

At this, the distortion of a testing *RF* field configuration near the coil face (*taken by the frequency increase of the testing SFCO technique*) might be used for the checking whether the *ideal diamagnetic* state (with $B = 0$) is established or not? While, amount of the absorption of a testing *TD*-oscillator power by the sample under test (*taken by the amplitude increase of the measuring SFCO technique*) we advise to use to check whether the *ideal conducting* state (with $R = 0$) is established or not? Alongside with this, the establishment of the *ideal conducting* state one may check also by the improved *AC 4-probe* measurement technique.

Besides, both by the amplitude and the frequency of the 1mm in dia. flat-coil *TD*-oscillator probe (*to be worked out and created specially for these experiments in future*) one may try to detect and image details of the relief of the node structure, generated in a real space on the surface of the sample in the FFLO state (*consisting of the alternating regions of the SC layers & the spin-polarized magnetic walls*).

References

1. Bednorz J.G. and Muller K.A. *Possible high T_c superconductivity in the Ba-La-Cu-O system* // **Z. Phyzik**, **B 64**, pp.189-193, **1986**.
2. Mourachkine A. "***Room Temperature Superconductivity***", Chapter 4: Principles of Superconductivity (Cambridge Intern. Science Publishing, Cambridge, **2004**) – arXiv:***cond-mat/0409240***
3. Gevorgyan S.G., ***PhD Thesis***, Institute for Physical Research, NAS, Ashtarak-2, Armenia, **1989**.
4. Gevorgyan S.G., Kiss T., Ohyama T., Inoue M., Movsisyan A.A., Shirinyan H.G., Gevorgyan V.S., Matsushita T., & Takeo M. *New Paramagnetic Peculiarity of the Superconductive Transition Detected by a Highly Sensitive OFC magnetometer* // ***Superconductor Science & Technology***, **14**, No.12, pp.1009-1013, **2001**.
5. Corak W.S., Satterthwaite C.B. *Atomic Heats of Normal & Superconducting Tin between 1.2 & 4.5K* // ***Phys. Rev.***, **102**(3) pp.662-666, **1956** (see also: *"Superconductivity"*, E.A. Lynton, *Methuen & Co.*, London, 1969).
6. Kurghinyan B.K., Gevorgyan S.G., Ohanyan V.R. *Weakly expressed peculiarities of specific heat of superconductive materials and their relation to paramagnetic effect, detected by SFCO method* // ***Proceedings of the Yerevan State University*** (Natural Sciences), *Physics*, No.**3**, pp.82-90, May-June **2008** – in Armenian.
7. Gevorgyan Samvel G., Kurghinyan Bilor K., *On the thermal peculiarity of the SC transition, precursor to specific heat's 'jump':* its relation to the '*paramagnetic'* effect, precursor to *Meissner* ejection – both revealed in *HTSC* material by the *super*-high sensitive *SFCO* method – **arXiv:1109.0462** [cond-mat.supr-con], **2011**.
8. Gantmakher V.F., Golovko N.I., Naumenko I.G., Neminsky A.M., Petinova A.V. *Temperature dependence of the magnetic field penetration depth in $YBa_2Cu_3O_{7-\delta}$ measured on ultra fine powder* // ***Physica C:*** *"Superconductivity and its Applications"*, **171**, pp. 223-230, **1990**.
9. Gevorgyan S., Karapetyan G., Shirinyan H., Muradyan S., Gevorgyan G., Kurghinyan B., Gevorgyan V., Polyanskii A. *Study of fine Peculiarities of Heat Capacity in $YBa_2Cu_3O_y$ Films by Means of the Laser-coupled Flat-coil Oscillator* // ***Proc. of the Yerevan State University***, Physical and Mathematical Sciences, №**1**(224), pp.49-54, **2011**.

10. Gevorgyan S., Shirinyan H., Manukyan A., Sharoyan E., Takeo M., Polyanskii A., Sarkisyan A., and Matsushita T. *Flat Coil-based TD Oscillator Enabling to Detect Real Shape of Superconductive Transition Curve & Capable of Imaging Properties of HTSC Films with High Spatial-resolution* // ***Nuclear Instruments and Methods in Physics Research A*** (NIM-A), **520**, No.1-3, pp.314-319, **2004**.

11. Gevorgyan S.G., Shirinyan H.G., Karapetyan G.H., Gevorgyan G.S., Polyanskii A.A. *Imaging of the grain structure of thin HTS film by a single-layer flat-coil-oscillator test-method* (*SFCO*-technique) // ***Proc. of the Yerevan State University***, Physical and Mathematical Sciences, No.**2**, pp.50-54, May-August **2009**.

12. Zhuravel A.P., Sivakov A.G., Turutanov O.G., Omelyanchouk A.N., Anlage S.M., Lukashenko A., Ustinov A.V., Abraimov D. *Laser scanning microscopy of HTS films and devices* (Review Article) // ***Low Temp. Physics***, **32**, No.6, pp.592-607, **2006**.

13. Gevorgyan S.G., Movsisyan A.A., Movsesyan G.D., Shindyan V.A., Shirinyan H.G. *On the Possibility of Creation of Radically New Type Detectors of Particles & Radiation Based on High-T_c SC's* // ***Mod. Phys. Lett.*** **B**, vol.**11**, №25, pp.1123-1131, **1997**.

14. Gevorgyan S.G., Movsesyan G.D., Movsisyan A.A., Tatoyan V.T. & Shirinyan H. *Modeling of Tunnel Diode Oscillators and Their Use for Some Low Temperature Investigations* // ***Review of Scientific Instruments***, vol.**69**, No.6, pp.2550-2560, **1998**.

15. Gevorgyan S.G., Kiss T., Movsisyan A.A., Shirinyan H., Hanayama Y., Katsube H., Ohyama T., Takeo M., Matsushita T., and Funaki K. *Highly Sensitive Open-Flat Coil Magnetometer for the $\lambda(H,T)$ Measurements in Plate-Like High-T_c Cuprates* // ***Review of Scientific Instruments***, **71**, No.3, pp.1488-1494, **2000**.

16. Gevorgyan S., Kiss T., Ohyama T., Movsisyan A., Shirinyan H., Gevorgyan V., Matsushita T, Takeo M, Funaki K. *Calibration of the Open-Flat Coil-based TD Oscillator Technique (OFC magnetometer) for Quantitative Extraction of Physical Characteristics of Supercond. State* // ***Physica C***, **366**, No.1, pp.6-12, **2001**.

17. Gevorgyan S.G. ***J. of Contemporary Physics*** (National Acad. of Sci. of Armenia), Allerton Press, Inc., **38**(1) pp.41-53, and **38**(2) pp.45-50, **2003** – http://mentor.lanl.gov/ftp/***cond-mat***/papers/0501/***0501416***.pdf.

18. Avagyan AA., Akopyan R.B., Vartanyan V.O., Gevorgyan S.G., Pilosyan S.Kh., *The Cathodic Evaporation of Bismuth-containing High-Tc Superconducting Films with T_c>77K and Characteristic Features of Their Physical Properties* // ***Superconductivity:*** *Physics*, *Chemistry*, *Technique* (**SPCT**), **3**(1), pp.89-92, **1990**.

19. Morris P.A., Bonner W.A., Bagley B.G., Hull G.W., Stoffel N., Greene L., Meagher B., Giroud M. *Growth of high-T_c superconducting $Bi_4(Ca,Sr)_6Cu_4O_{16+x}$ crystals* // ***Appl. Phys. Lett.***, **53**(3), pp.249-251, **1988**.

20. Iguchi I., Yamaguchi T., Sugimoto A. *Diamagnetic activity above T_c as a precursor to superconductivity in $La_{2-x}Sr_xCuO_4$ films* // ***Nature***, **412**, p.420-423, **2001**.

21. Tonica Valla. *One Mystery of High-T_c Superconductivity Resolved* // ***Science*****:** *Physics* (*PHYSorg.com*), November 16, **2006** – *www.physorg.com/news82915060.html*.

22. Sprungmann D., Westerholt K., Zabel H., Weides M., and Kohlstedt H. *"Electron 'pairing': Triplet superconductivity proven experientially for first time"* // ***Science*****:** *Physics* (*PHYSorg.com*), December 1, **2010** – http://www.physorg.com/news/2010-12-electron-pairing-triplet-superconductivity-proven.html].

23. Sprungmann D., Westerholt K., Zabel H., Weides M., and Kohlstedt H. Evidence for triplet superconductivity in Josephson junctions with barriers of the ferromagnetic Heusler alloy Cu_2MnAl // ***Phys. Rev. B***, **82**, 060505(R), **2010** – DOI:10.1103/PhysRevB.82.060505.

24. Fulde P. and Ferrell R.A. // ***Phys. Rev.***, **135**, p.A550, **1964**.

25. Larkin A.I., Ovchinnikov Y.N. // ***Zh. Eksp. Teor. Fiz.***, **47**, p.1136, **1964** [***Sov. Phys. JETP***, **20**, 762, **1965**].
26. Radovan H.A., Tozer S.W., Murphy T.P., Hannahs S.T., Palm E.C., Hall D., Fortune N.A., Martin C., and Agosta C.C. *Fulde-Ferrell-Larkin-Ovchinnikov Superconductivity in $CeCoIn_5$* // *NHMFL Reports*, **10**(3), **2003** – www.magnet.fsu.edu.
27. Martin C., Agosta C.C., Tozer S.W., Radovan H.A., Palm E.C., Murphy T.P., Sarrao J.L. *Evidence for the FFLO state in $CeCoIn_5$ from penetration depth measurements* // **arXiv:cond-mat/0309125**(v2) 20 Apr **2004**.
28. Gevorgyan S.G., Kiss T., Shirinyan H.G., Movsisyan A.A., Ohyama T., Inoue M., Matsushita T., Takeo M. *The Possibility of Detection of Small Absorption in HTS Thin Films by Means of the Highly Sensitive OFC Magnetometer* // ***Physica* C:** "*Superconductivity and its Applications*", **363**, No.2, pp.113-118, **2001**.
29. Gevorgyan S.G., Kiss T, Inoue M, Movsisyan A.A, Shirinyan H.G, Harayama T., Matsushita T., Nishizaki T., Kobayashi N., Takeo M. *Peculiarities of the Magnetic Phase Diagram in Small-size Untwinned $YBa_2Cu_3O_y$ Crystal Constructed by Highly Sensitive OFC–magnetometer* // ***Physica* C**, **378-381**(P1), pp.531-536, **2002**.
30. Kamerlingh Onnes Heike, *The Superconductivity of Mercury* // ***Leiden Communications***, **122b**, p.124, **1911**.
31. Bardeen J, Cooper L.N., Schrieffer J.R. *Theory of Superconductivity*, ***Phys. Rev.***, **108**, pp.1175-1201, **1957**.
32. Hannahs S.T. and Fortune N.A. // ***Physica B***, **329-333**, p.1586, **2003**.
33. Coffey T., Bayindir Z., DeCarolis J.F., Bennett M., Esper G., and Agosta C.C. *Measuring radio frequency properties of materials in pulsed magnetic fields with a tunnel diode oscillator* // ***Review of Scientific Instruments***, **71**, No.12, pp.4600-4606, **2000**.
34. Fortune N.A. // ***Bull. Am. Phys. Soc.***, **48**, p.1027, **2003**.
35. H.A. Radovan, Fortune N.A., Murphy T.P., Hannahs S.T., Palm E.C., Tozer S.W., Hall D. *Electron-spin domains (communication arising): Magnetic enhancement of superconductivity* // ***Nature***, **427**, Issue 6977, pp. 802, **2004**.
36. Bonn D., and Hardy W. "*Phys. Prop. of HTS's V*", Ed. by Ginsberg, World Sci., Singapore, pp.9–97, **1996**.
37. Gulian A., Zharkov G., "*Nonequil. Electrons & Phonons in Supercond.*", Kluwer/Acad./Plenum, NY, **1999**.
38. Muradyan S.T., Gevorgyan S.G. *Investigation of TD-oscillators activated on the internal capacitance of their coils* // ***J. of Contemporary Physics*** (NAS of Armenia), Allerton Press, Inc., **43**, No.2, pp.97-100, **2008**.
39. Gevorgyan S.G., Muradyan S.T., Kurghinyan B.K., Qerobyan M.I. *Needle-like Properties of the Probing RF Field of "Magnetic-field" Probes based on the Single-layer Flat Coils* // ***Proc. of the Yerevan State University***, Physical and Mathematical Sciences, №**3**(226), pp.47-51, **2011**.
40. Gevorgyan S.G., and Azaryan M.G. *Flat Coil Nano-scale Resolution Probes for Nondestructive Study of Objects in Microelectronics* // **Proc**. of the 5-th International **Conference** on "Semiconductor Micro- & Nano-Electronics", Aghveran, **Armenia**, Sept. 16-18, pp.70-73, **2005**.
41. Binning G. and Rohrer H., "*Scanning Tunneling Microscope*," **U.S. Patent 4,343,993** Aug.10, 1982. Field: Sep.12, **1980**.
42. G. Binning et al., ***Appl. Phys. Lett.***, **40**, p.178, **1982**.
43. Binning R., Quate C., et al., Phys. Rev. Lett., **56**, p.930, **1986**.
44. Bikov V.A., "*Topical review on Probe Microscopes*" Russian Doctoral Degree Dissertation, Moscow, **2000** – in Russian.
45. Spiral Chip Inductors (U.S. Microwaves production – *www.usmicrowaves.com*).

To the optical properties of uniaxial crystals with a closed surface of the wave vectors at small values of one of the component of the dielectric tensor

H.S. Ericyan*, Zh.B. Khachatryan*, A.A. Papoyan, H.M. Arakelyan***.

**Yerevan state university, **Armenia state agricultural university*

The geometric analyze of transformations of the closed surfaces of wave vectors (SWV) for uniaxial media to open surfaces, which take place for values of frequencies when the one of the component of the dielectric tensor (ε_{ij}) changes a sign. Briefly some examples for optical singularities near the above mentioned frequencies is listed.

1.Introduction

It numbers of works (see, for example, [1-6]) the optical properties of the medium with the no closed SWV as in case of the traditional optics (see, for example, [7, 8]) but opened. The SWV is open, if a one component of the dielectric tensor is positive and another one is negative. Fresnel ellipsoid is also turning into an open surface. The opened character of the SWV leads to a series features of the optical properties.

In the present work the transformation on the closed SWV to the opened one at the decreasing of a one component of the dielectric tensor to zero and the changing of its sign. Some features of optical properties near the values of the frequencies when the change of a sign the dielectric tensor component takes place are specified.

2. Dispersion equation. The geometrical transformation of the closed SWV to the opened one.

The dispersion equation for the optically uniaxial medium with the dielectric tensor components, when $\varepsilon_{zz} = \varepsilon_{\|}$ and $\varepsilon_{xx} = \varepsilon_{yy} = \varepsilon_{\perp}$ has the form of:

$$\left(k_0^2 - \frac{\omega^2}{c^2}\varepsilon_{\perp} \right) \cdot \left(\frac{k_{ex}^2 + k_{ey}^2}{\varepsilon_{\|}} + \frac{k_{ez}^2}{\varepsilon_{\perp}} - \frac{\omega^2}{c^2} \right) = 0, \qquad (1)$$

where k_0 is the wave vector module for the ordinary wave, and the quantities k_{ex}, k_{ey}, k_{ez} are the projections of the wave vector for the extraordinary wave corresponding to x, y, z axes, correspondingly. The quantities $\varepsilon_{\|}$, $\varepsilon_{\perp}$ are the components of the tensor ε_{ij} corresponding to directions parallel and perpendicular to the optical axe.

Below, for simplicity, we shall consider the situation when $k_{ey} = 0$.

In Fig. 1 the examples of the SWV are presented for more and more small values of $\varepsilon_{\perp}$ at a given value of $\varepsilon_{\|}>0$. There is a uniaxial media with $0 < \varepsilon_{\perp} \quad \varepsilon_{\|}$ (Fig.1a). When the component $\varepsilon_{\perp}$ decreases then the radius of the spare becomes smaller and the major semi-axis of the ellipsoid does not change. In accordance to Fig.1b the ellipsoid is distended.

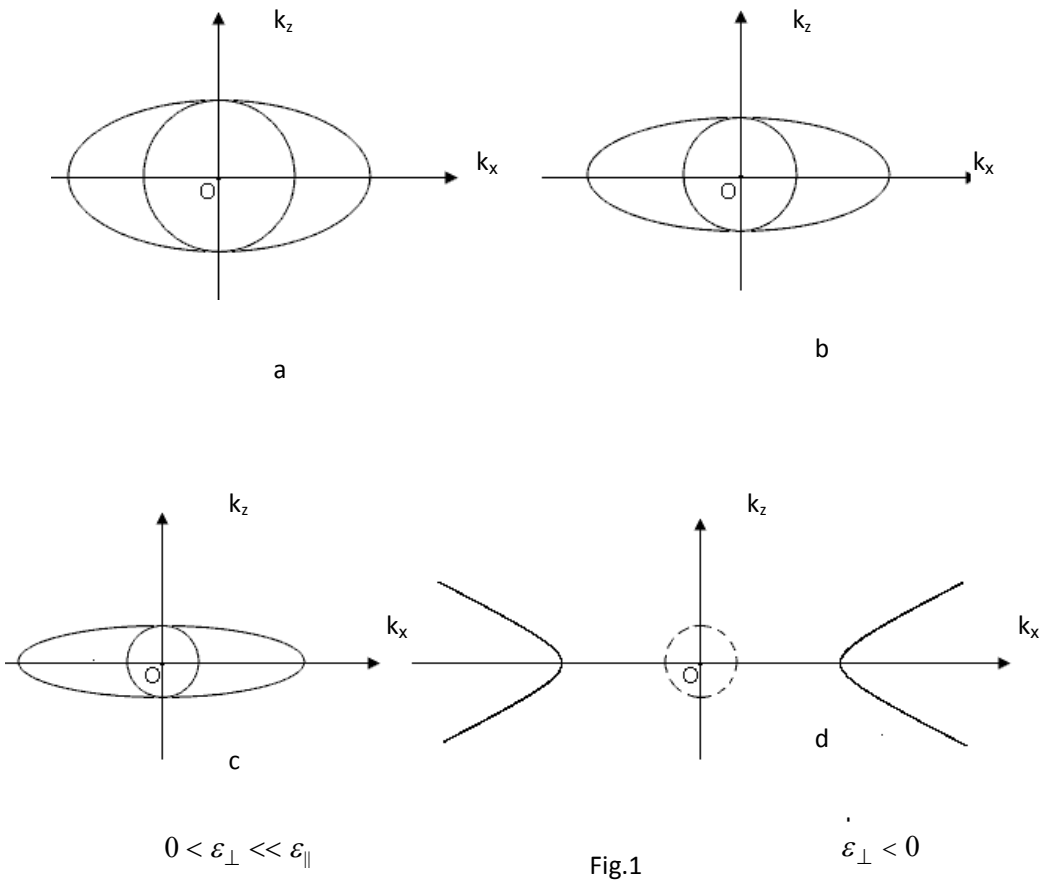

Fig.1

For the more small values of $\varepsilon_{\perp}$ compeering with $\varepsilon_{\perp}$ the ellipsoid becomes more distending. A further decrease of $\varepsilon_{\perp}$ does it negative and the ellipsoid transforms to hyperboloid with the distance between the vertexes equals to the big diameter of the ellipsoid. (Fig.1d). The sphere is absent (there is no ordinary wave). The further decrease of $\varepsilon_{\perp}$ leads to the increase of an aperture of the hyperboloid branches, when the vortexes remain unchanged.

If initially $\varepsilon_{\perp} > \varepsilon_{\|}$, then the decrease of $\varepsilon_{\perp}$ leads to an isotropic media ($\varepsilon_{\perp} = \varepsilon_{\|}$). The further decrease of $\varepsilon_{\perp}$ gives the result presented in Fig. 1 and the transformation SWV continues in accordance to Fig.1.

In Fig. 2 the examples of SWV forms are shown, which correspond to smaller values of $\varepsilon_{\|}$ at the given value of the component $\varepsilon_{\perp} > 0$. The decrease of component $\varepsilon_{\|}$ results to a more and more distended ellipsoid. The radius of the sphere remains constant.

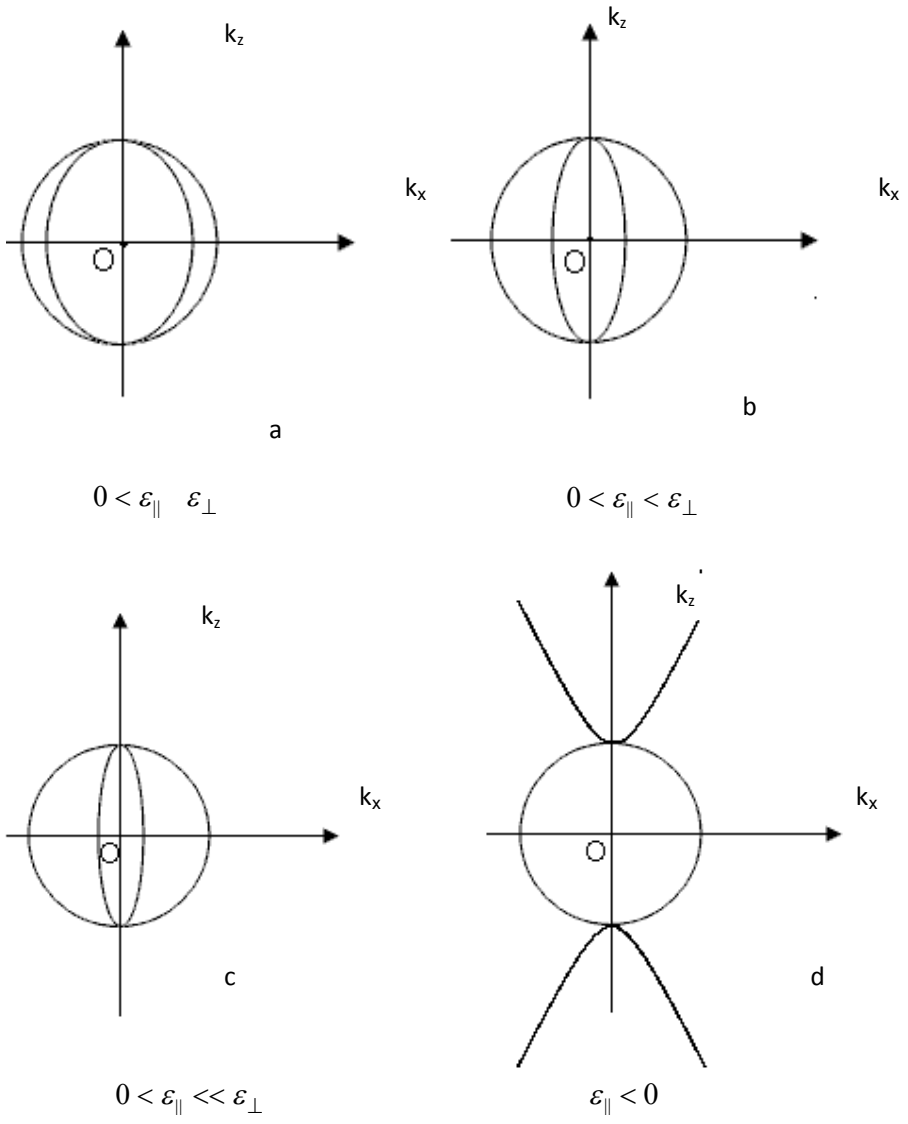

Fig.2

The sing change of the component $\varepsilon_{||}$ converts a distended ellipsoid to a hyperboloid with a distance of the vertexes equals to the big and unchanged diameter of an ellipse. A further decrease of component $\varepsilon_{||}$ increases an aperture of the hyperboloid branches. If an ellipsoid is initially located out of the sphere then for a gradual decrease of $\varepsilon_{||}$ the media becomes isotropic ($\varepsilon_{||} = \varepsilon_{\perp}$). A further decrease of component $\varepsilon_{||}$ leads to the result presented in 2a and the transformation SWV continues in accordance to Fig.2.

3. Some features of optical properties

Below, we will limit by indicating of some features of a media near the frequency corresponding to a change of a sign of dielectric permittivity components, based on a connection

between the shape of SWV and optical properties. We consider the reflection and transmission at a border perpendicular to a media optical axe.

a) For a frequency value near to the sign change of the component $\varepsilon_{\perp}$ the ordinary wave is excided by the falling wave for more and more small values of an incident angle. For large values of the incident angle a total reflection takes place.

b) Closing to $\varepsilon_{\perp}$ sign change region the refracted beam of extraordinary rays at the incident beam diverging from a point source becomes more and more parallel, but with a more and more small values of a transmission coefficient for any ray which undergoes refraction:: boundary acts as a lens. For that case the beam of refracting waves (not rays) strongly diverge.

c) For a frequency value near to the sign change of the component $\varepsilon_{\parallel}$ extraordinary refracting wave is excided at more and more small values of an incident angle. For large values of the incident angle the total reflection of wave polarized in the main cross section of crystal takes place.

d) Like to the case of small $\varepsilon_{\perp}$, for a small values of $\varepsilon_{\parallel}$ the large-angles between the wave vector and the Poynting vector are also carried out. For a small near to zero rejection of an incident angle at of from zero the refracted rays with the border normal draw the angle near to are close to $\pi / 2$.

In this paper, we did not take into account the imaginary parts of the dielectric permittivity components.

We thank Academician NAS of Armenian Republic R Mkrtchyan for interest and discussion.

References

1. H. S.Eritsyan. Kristallografiya, vol.33, pp.461-464, (1978).
2. H. S. Eritsyan. Optics of Gyrotropic Media and Cholesteric Liquid Crystals [in Russian], izd. Hayastan, Yerevan, 1988.
3. H. S. Eritsyan, H. M. Arakelyan. Optics of uniaxial crystals with open surfaces of wave vectors. "Light stoping" cone. J. Contemp. Phys. (Armenian Ac. Sci.), vol.38, no.5, pp.300-308, (2003).
4. H. S. Eritsyan, A. A. Papoyan, H. M. Arakelyan. Interaction of electromagnetic waves with inhomogeneous media having negative electromagnetic parameters. J. Contemp. Phys. (Armenian Ac. Sci.), vol.40, no.5, pp.346-354, (2005).
5. H. S. Eritsyan, A. A. Papoyan, H. M. Arakelyan. Media with non-classical forms of the surfaces of wave vectors of classical optics. J. Contemp. Phys. (Armenian Ac. Sci.), vol.43, no.4, pp.252-260, (2008).
6. H. M. Arakelyan. Interaction of light with the medium with an unusual form of the surfaces of wave vectors (Ph.D. dissertation).- Yerevan, Yerevan State University, 2010.
7. F. I. Feodorov. Optics of anisotropic media [in Russian], Minsk, izd AS BSSR , 1958.
8. L.D. Landau and E.M. Lifshitz. Electrodynamics of continuous media [in Russian], Nauka, Moscow, 1982.

The Effect of the Transport Current on The Superconducting Transition of the Bismuth HTS Ceramics

S.K. Nikoghosyan*[1,2], V.V. Harutyunyan[1], E.A. Mughnetsyan[2], E.G. Zargaryan[2], A.G. Sargsyan[2]

[1] A.I Alikhanyan National Research Laboratory, Yerevan, Republic of Armenia[2] International Scientific - Educational Centre of the National Academy of Sciences of the Republic of Armenia, nick@mail.yerphi.am

The effect of the transport current (I) on the superconducting transition (SC) of Bismuth High Temperature superconducting (HTS) ceramics of the $Bi_2Pb_2Sb_{2.5}Sr_2Ca_2Cu_3O_x$ (sample 1) and $Bi_{1.7}Pb_{0.3}Sr_{0.3}Ca_{0.2}$ $Cu_{3.5}$ O_x (sample 2) compositions in the presence of the uncompensated geomagnetic field of the Earth has been studied by means of measuring the temperature dependence of the direct current (DC) resistivity (ρ). It has been established that the SC transitions of these samples are stepwise.

It has been found out that for the temperatures lower than 85K in both of the samples at low values of I (much lower than its critical current I_c) SC transitions are relatively narrow while at high values of I their broadening and the shift toward lower temperatures take place. For the temperature fixed near 80K with the increase of the I initially quickly rise of the ρ has been observed with the tendency to saturation at high transport current. It has been established also that depending on I the trend of increase in ρ the steeper, the lower is the temperature of the sample. Furthermore, the threshold value Is at which the initial growth of ρ is observed, reduces with the increasing of temperature. It has been revealed that the effect of I on the change of the electrical properties is manifested considerably stronger for sample 1 both in superconducting and normal conditions.

The obtained results are interpreted within the structural features of the investigated samples.

Introduction

The superconducting (SC) transition in the HTS ceramics strongly depends on its structural composition, the magnitude and the direction of the applied magnetic field, the mode of its synthesis and also on its bulk density and the granule size [1-11]. The investigations of SC transition in HTS are often carried out measuring the current-voltage V-I characteristics (CVC) under direct current (DC) electric field by the well-known four-probe technique. Since the discovery of HTS similar measurements have been performed out for a number of metal-oxide compounds. It should be noted that the studies have been carried out on ceramic, single crystal and thin-film materials [12-24]. Numerous experiments have shown that, as a rule, in the case of metal-oxide ceramics near the SC transition, the behavior of CVC are described by the $V \sim (I-I_c)^n$ power law, where $n(H,T) > 1$ depends on the external magnetic field H and the temperature T of the sample. With the increase of both the temperature and the magnetic field the parameter n decreases approaching to the ohmic value $n \cong 1$ at $T_c(H)$. Such behavior of the C-V characteristics was tried to be explained in the framework of the Josephson medium, when HTS represented as a set of superconducting granules connected by weak (Josephson) links. Studies have been carried out at both in the presence and absence of the external magnetic field [12-14]. The results of analysis of these studies were revealed that the temperature of superconducting transition in the case of zero transport current is higher than that of with currents $T_c(I) < T_c(0)$, as well as the width of

superconducting transition is respectively narrower [4-6, 14-21]. The nature of SC transitions strongly depends on the structural composition of the HTS [1-11,15]. It was found out that at temperature lower than T_c, both the low transport currents and the weak magnetic field result in same changes of the resistivity [6, 20]. The Berezinskii- Kosterlitz-Thouless transition observed often at the same temperature is described by the hopping index in the power-law dependence of the CVC ranged from 3 to 1. However, sometimes the HTS exhibits power-law dependence, but no change in the index is observed [20, 21]. On the other hand, besides the theoretical significance, the investigations on changes in resistivity at low values of transport currents have important practical applications for development of detectors for weak magnetic fields. That's why the unambiguous research in this field is an urgent task. The aim of the present work is to study the effect of low transport currents on the superconducting transition of the bismuth ceramics in the presence of the Earth's geomagnetic field.

2. Experimental methods

Investigations were curried out on bismuth HTS ceramic samples with the following compositions: $Bi_2Pb_2Sb_{2.5}Sr_2Ca_2Cu_3O_x$ (sample 1) and $Bi_{1.7}Pb_{0..3}Sr_{0.3}Ca_{0.2}Cu_{3.5}O_x$ (sample 2). The technique of the synthesis of the samples had been described in the work [7]. The samples were rectangular with various dimensions about $8\times2\times1$ mm^3. The above mentioned investigations were curried out by means of measuring the current-voltage characteristics with the help of the four-probe method using direct transport current I. For this purpose on the surface of the samples four silver contacts of 0.5 mm^2 area were applied. They were arranged along the axis of the broad faces and were parallel to the long edges of the sample. The distance between the contacts was 1-2 mm. To obtain reliable ohmic contacts, as well as to create structural changes, the samples were slowly (3-4 degrees/min) heated in the air to the temperatures 600ºC (sample 1) and 820º C (sample 2) and were kept at these temperatures respectively for 30 and 15 minutes, then were left to cool off together with the furnace to room temperature. It should be also noted, that after carrying out of series necessary measurements, sample 1 was subjected to an additional 20-minute heat treatment (30+20 min) at the temperature 600ºC. During CVC measurements the transport current I flowed through the outmost two contacts and the voltage drop V of the sample was recorded by means of two central contacts. The applied transport (hardware) current I was varied within 25 μA to 105 mA, while the corresponding current density J flowing through its cross-section, was changed in the range of 0.000568 to 3 A/cm^2. When measuring, the sample is attached to the foil turbonit holder by copper contacts clip. The holder together with the sample is in foam plastic casing, which in its turn is tightly inserted into a massive copper pipe. All this system is immersed in liquid nitrogen or its vapors. The required temperature of the sample is set by means of maintaining the appropriate level of liquid nitrogen in the vessel. The temperature stability was achieved with the accuracy of 0,1K. The sample temperature was measured using the resistance of copper wire with the diameter of 30 μm. The measurements were carried out at temperatures ranging from 77K to 300K in the heating mode. The temperature rate was 1degree/min up to 130K and 3 degrees/min at high temperatures. The transport current was applied to the sample from a stabilized source after establishing the required temperature in the presence of the uncompensated magnetic field of the Earth. At some fixed temperatures near 80K, V-I characteristics were obtained for the studied samples, as well as superconducting transitions were identified in conditions of low densities its transport current (less than the critical superconducting current density Jc). The measurements of the current-voltage characteristics (CVC) for the samples were carried out both at room and liquid nitrogen temperatures. The resistivity was determined by $\rho = V\cdot S/(l\cdot I)$ low, where V is the voltage drop on the potential contacts, l – the distance between them, S – the cross-section of the sample, I – the

transport current passing through its cross-section area. Curve ρ (T) is drown for each fixed stabile value I. The voltage V and the current I were measured by the mikrovoltnanoampermeter R-321 and digital Versatile Voltmeter V7-21. The measurement errors for ρ did not exceed 5%.

3. The experimental results and their discussions

Fig.1 shows the superconducting transition for the sample 1. It's obvious that after the heating of the sample 1 for 30 minutes at temperature 600ºC, two distinctly visible SC transitions appear near 115K and 105K. However, the 20-minute additional heat-treatment of sample 1 at temperature 600ºC, causes a shift of these transitions in the temperature range lower than 90K (Fig. 2). We think that the observed steps (Fig. 1) on the curve ρ (T) may be due to the low-temperature (2201, $Bi_2Sr_2Cu_2O_x$, T_c<20K) and high-temperature phases (2212, $Bi_2Sr_2CaCu_2O_x$, T_c<90K; 2223, $Bi_2Sr_2Ca_2Cu_2Ox$, T_c=100-115 K) in the sample [1,4,6,8]. Nevertheless, the phase 2201 is strongly sensitive to various treatments, fills the intergranular layers and in the normal state has semiconducting properties manifested as a decrease of ρ with the increase of the temperature above 130K (Fig.1).

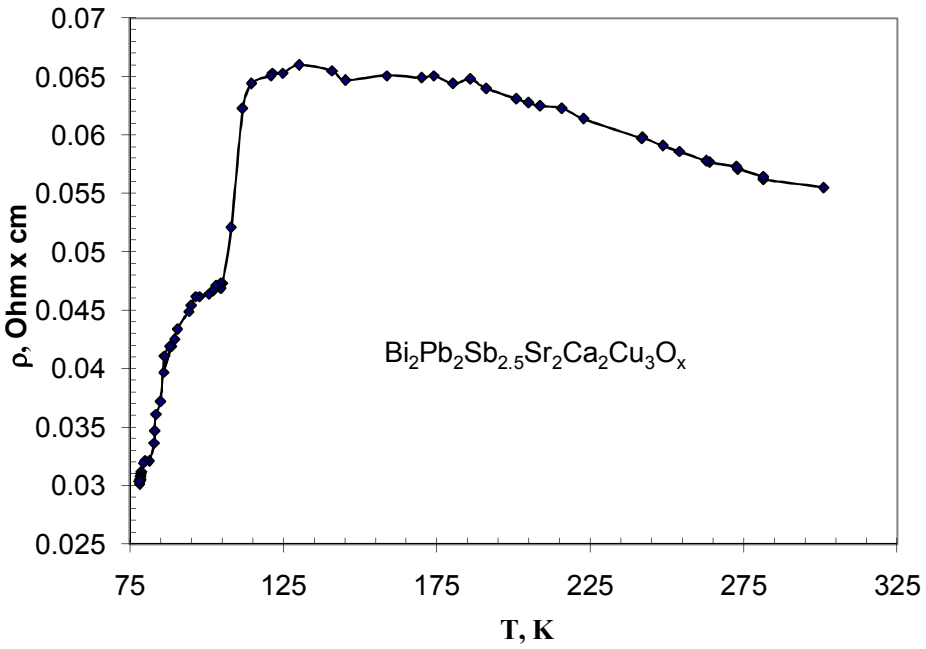

Fig. 1.The temperature dependence of the resistivity of the sample Bi2Pb2Sb2.5Sr2Ca2Cu3Ox after the annealing at temperature 600 ºC for 30 minutes at I=1mA.

In Fig 2 and 3 the superconducting transitions for the samples 1 and 2 are shown for different values of the transport current. It's obvious that the superconducting transitions for both of the samples retain the step form, which according to the well-known literature data is conditioned by their multiphase. Whereas after the heat-treatment or applying impurity additions in them the volume fraction of these phases [1-10] changes. After the additional (30+20 min.) heating of sample 1 at 600ºC, at temperatures above Tc the semiconducting behavior of conductivity disappears and appears the metallic one. Together with this the superconducting transitions are shifted and modified depending on the temperature of the samples and the value of the transport current (Fig. 2 and 3). At the same time for both samples both common and distinguishing characteristics of

behavior of superconducting transitions are observed. Thus, for these samples in the low-temperature transition region ρ(T) (lower than 90K) appears an arm weakly depended on the temperature, which reacts to the change of the transport current differently. However, if in the case of sample 1 the magnitude of ρ depends strongly on the transport current, while such dependence is not observed for the sample 2. The experimental dependence of ρ versus transport current in the sample 1 for fixed temperatures is shown in Fig. 4. The dependences of ρ and $T_c^{0.5}$ versus transport current density for both of the samples are shown in Fig.5 and Fig.6. It's obvious from Fig.4 that the resistivity with the increase of I initially quickly grows and tends to saturation at high transport current. Therefore, the transport current dependence of ρ is of a threshold nature. With the increase of the sample temperature the threshold value of I_s is shifted toward lower values of I. These results are attributed to the so-called weak (Josephson) links which under the influence of the transport current are destroyed leading to the increase of sample's resistivity ρ [21]. This is very similar to the phenomenon of magnetoresistance stipulated by growth of the resistivity under applied magnetic fields. This is another evidence in favor of the assertion, that the weak magnetic fields and low transport currents lead to similar effects [1,20]. Thus, it's shown that the transport current 2.5 mA and the magnetic field 1Oe lead to the same change in the resistance of the single crystal Bi2Sr2CaCu2Ox [20]. Therefore, the higher the sample temperature, the greater the concentration of the weak links to be destroyed. Hence, the increase of ρ occurs at much lower values of Is. It should be noted that for sample 1 with the increase of I or J at low fixed temperatures the initial rapid rise

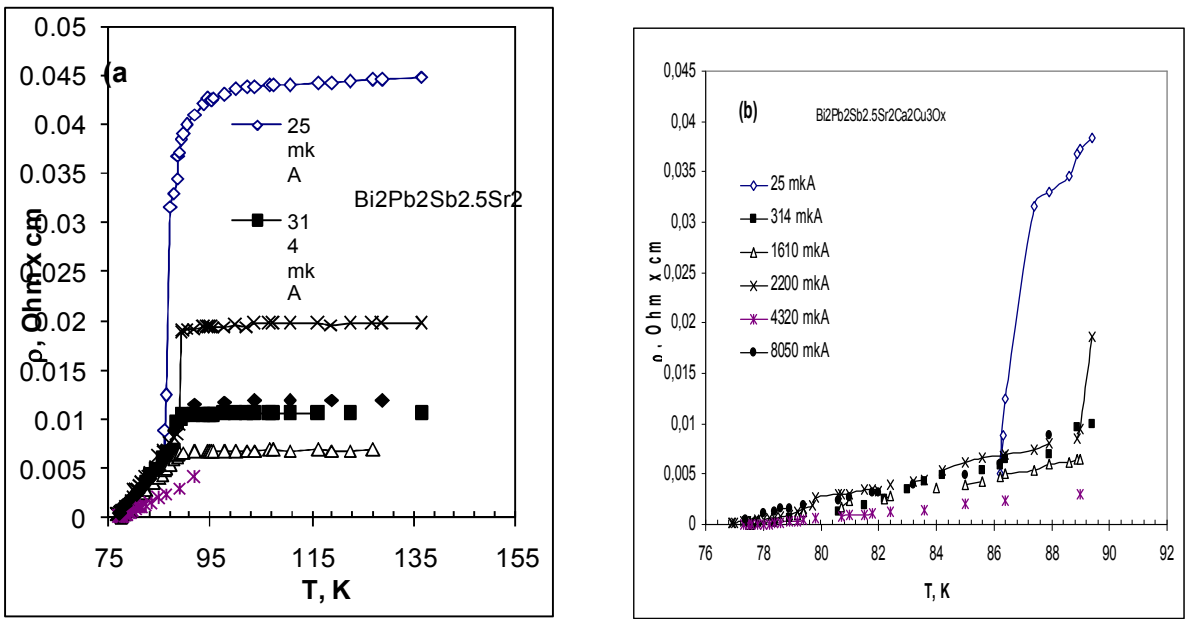

Fig.2. The temperature dependence of the electrical resistivity of the sample $Bi_2Pb_2Sb_{2.5}Sr_2Ca_2Cu_3O_x$ after the additional annealing (30+20 min.) at temperature 600ºC for different values of I. (a) Pattern in the wide range of temperatures, (b) The low-temperature arms of superconducting transitions.

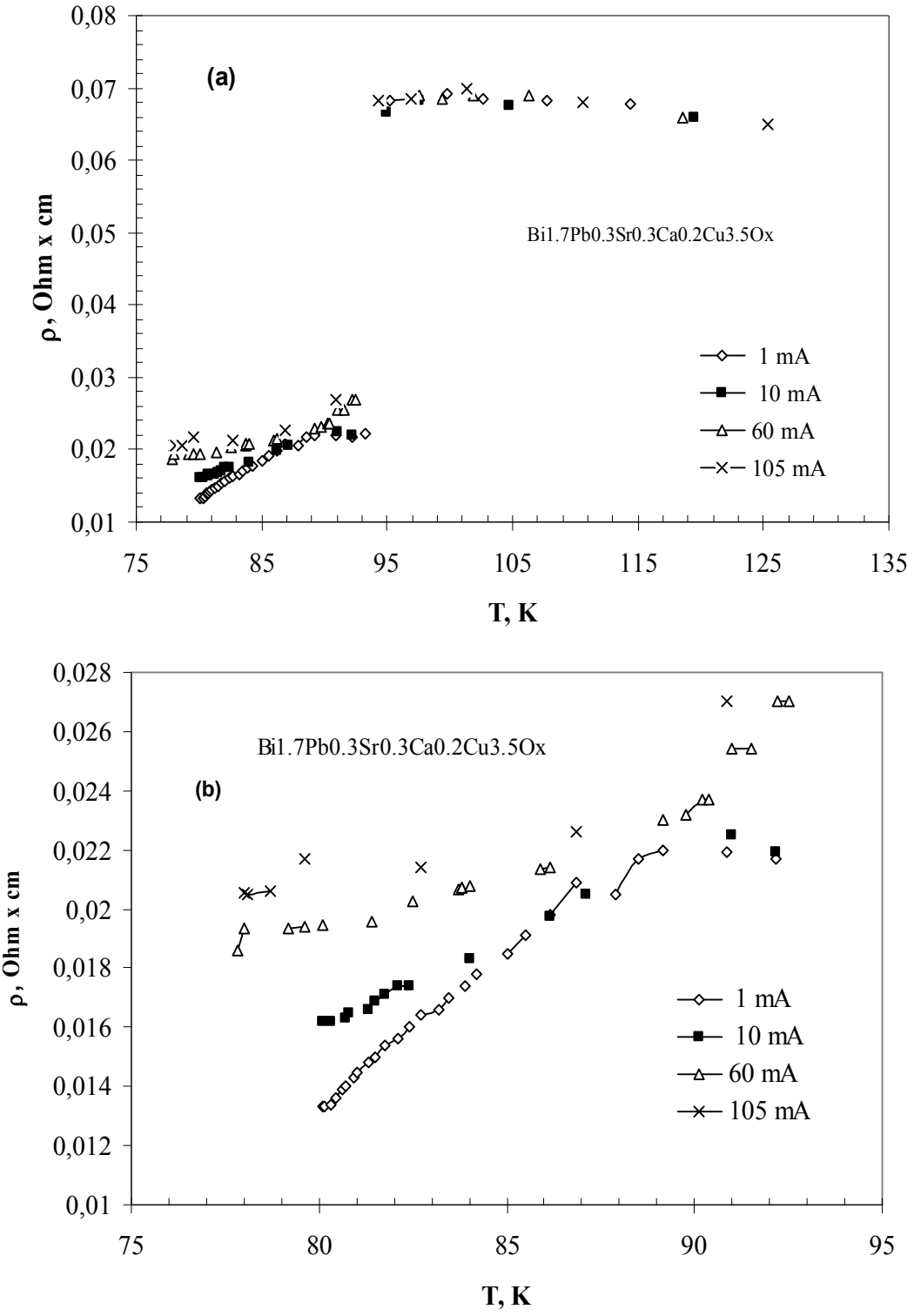

Fig.3. The temperature dependence of the electrical resistivity for sample 2 with Bi1.7Pb0.3Sr0.3Ca0.2Cu3.5Ox composition after the annealing at 820ºC for 15 minutes at different values of the transport current I. (a) View of the curves in the wide range of temperatures; (b) The low-temperature arms of the superconducting transitions.

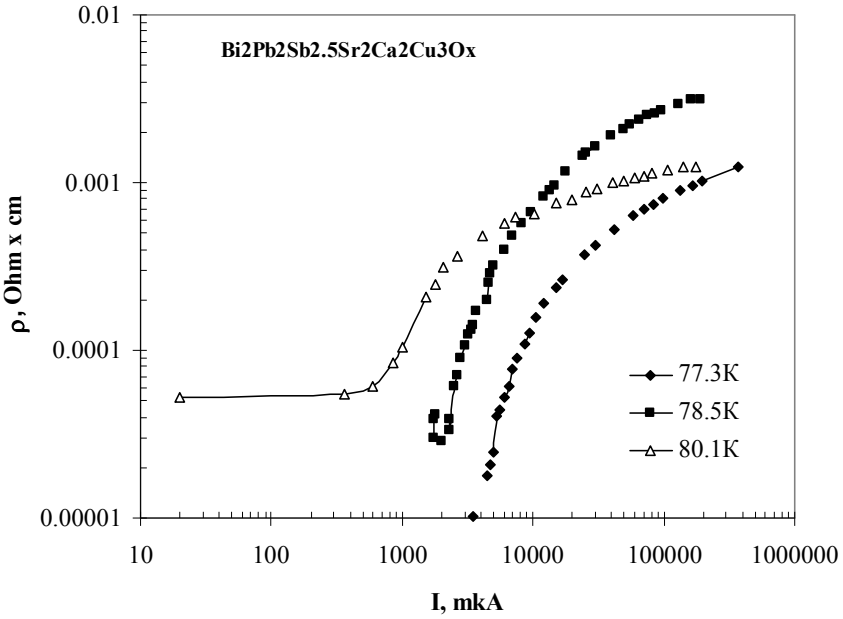

Fig.4.The dependence of resistivity of the sample Bi2Pb2Sb2.5Sr2Ca2Cu3Ox on I after its additional annealing (30+20 min.) at 600ºC for different fixed temperature of the sample.

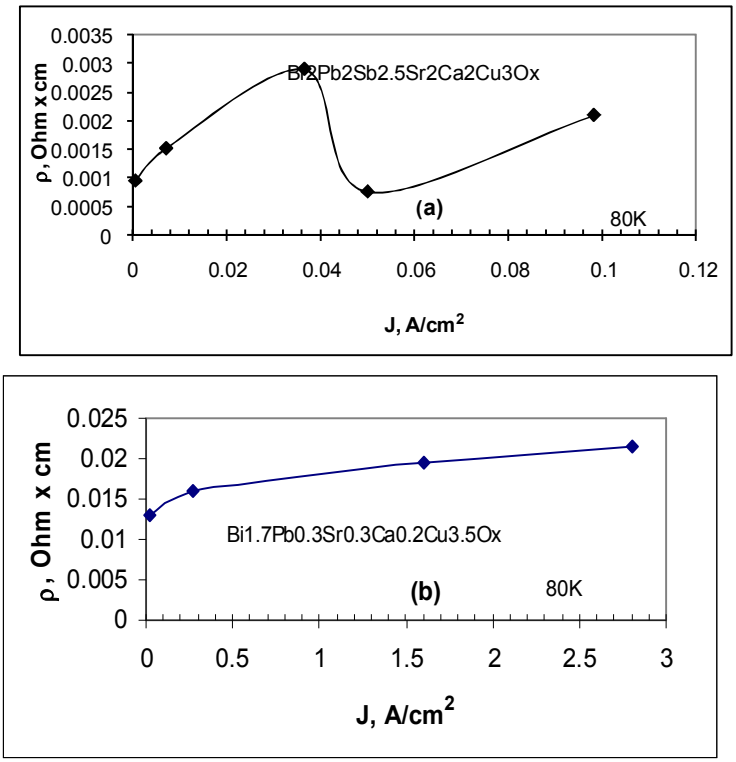

Fig. 5 The dependence of the electrical resistivity of Bi2Pb2Sb2.5Sr2Ca2Cu3Ox (a) and Bi1.7Pb0..3Sr0.3Ca0.2Cu3.5Ox (b) compositions on the transport current density J at 80K.

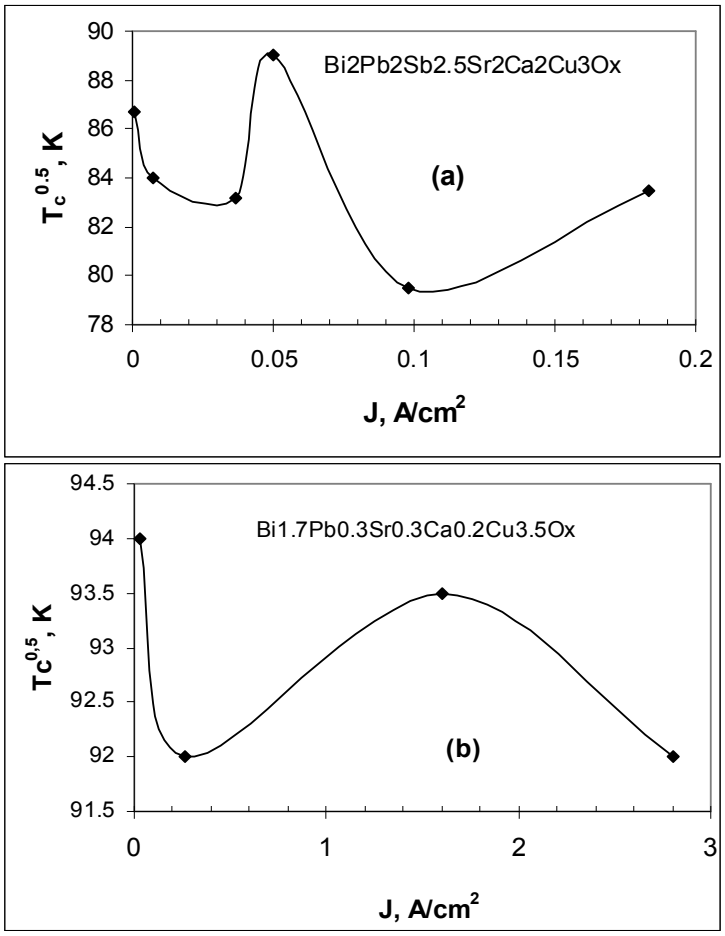

Fig.6. The dependence of the critical temperature (defined by the mid point of the electrical resistivity) on the transport current density for the samples of Bi2Pb2Sb2.5Sr2Ca2Cu3Ox (a) and Bi1.7Pb0.3Sr0.3Ca0.2Cu3.5Ox (b).

in ρ is followed by its relatively slow increase for larger values of current (Figs. 4 and 5). It's interesting that in the bismuth samples there is some range of magnetic fields where the effect of negative magnetoresistance is observed [23, 24]. However it's shown that this effect is absent in denser samples [23]. We should note that for sample 2 the density of which is also more (3.2 g/cm3) than that of sample 1 (2.1g/cm3), the effect of decrease in its resistance was not observed by us either (Fig. 5, b). It should also be noted that both the onset of superconductor transition $T_c^{0.5}$ defined by the mid point of ρ and value of the resistivity ρ at this level vary nonmonotonically depending on the transport current density of sample 1 as well as the inverse correlation between $T_c^{0.5}$ and ρ is observed in this case. In other words the larger value of $T_c^{0.5}$ corresponds to the smaller value of ρ.Whereas such a correlation for sample 2 is noticeable only at very low values of J. This comparison shows that for both samples the behavior of dependence $T_c^{0.5}$ against J is qualitatively similar, but for the sample 1 the regions of their increase and decrease are shifted towards the lower values of J with respect to the ample 2. It is evident from CVC measurements that the behavior of these characteristics depends on the temperature. Thus, for instance, for sample

1 at room temperature V depends on I almost linearly, whereas at 77.3K this dependence has an exponential form with the exponent of n >3 (Fig,7). In the case of sample 2 relationships between V and I is clearly marked linear and dissipative respectively at room temperature and liquid nitrogen temperature (Fig.8).

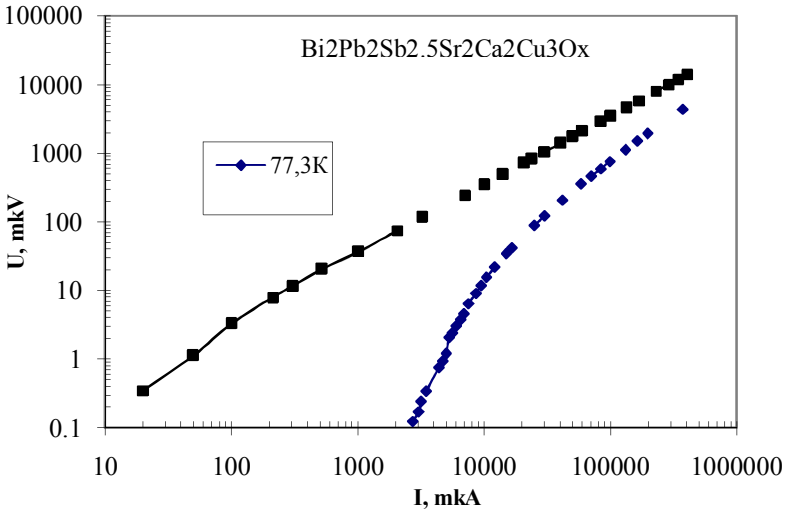

Fig.7. The current –voltage characteristics of the Bi2Pb2Sb2.5Sr2Ca2Cu3Ox sample at 77.3K and 291.5K after its additional annealing (30+20 min) at 600º C.

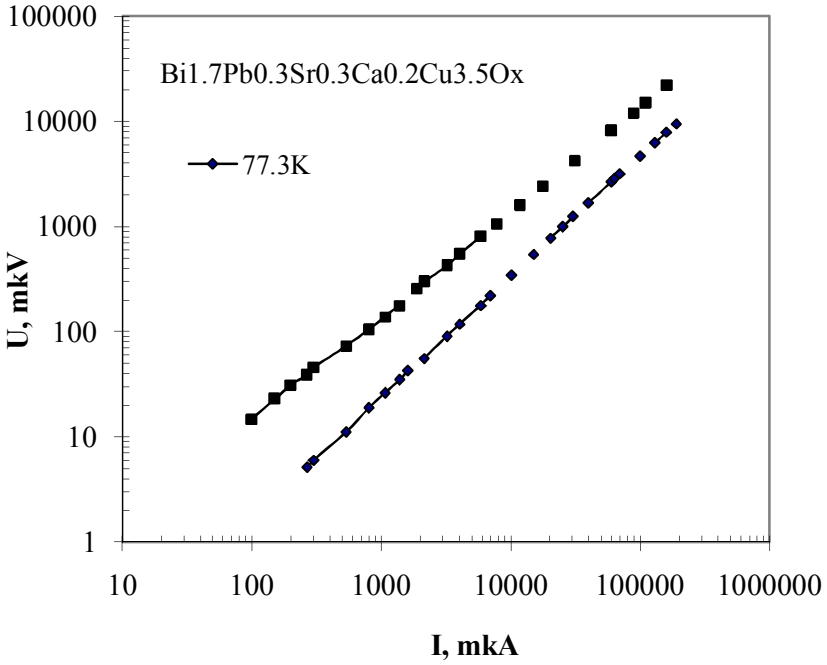

Fig.8. The current-voltage characteristics of the Bi1.7Pb0.3Sr0.3Ca0.2Cu3.5Ox sample at 77.3K and 298.6K obtained after its annealing at 820ºC for 15 minutes.

The comparison shows that the resistivity of sample 1 with the increase of the transport current rises much more rapidly at 77.3K than resistivity does in the case of sample 2. Thus, if in sample 2 with

increasing of I by order of three the resistivity increases less than for three time, then in sample 1 similar rise of I causes gain in ρ for 200 times (Fig.9). Such a distinction is apparently caused by the great inhomogeneity of the sample resulted from occurrence of the semiconducting phase 2201 as well as that of the high resistance phase of Ca2PbO4, Ca2CuO3, [1-8]. Much wider superconducting transitions of sample 1 as well as the observed nonmonotonic dependences of

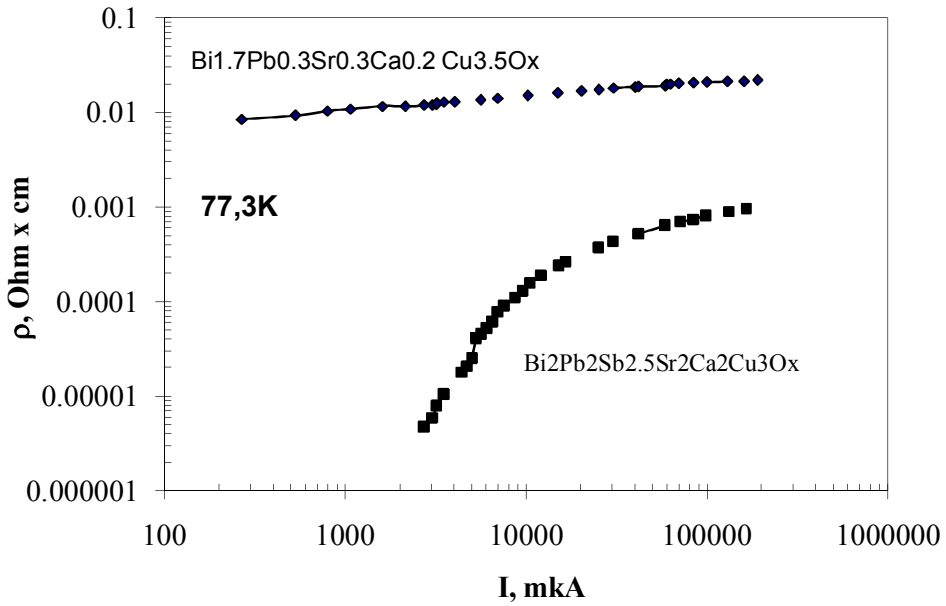

Fig.9. The dependence of the electrical resistivity on transport current I for the Bi2Pb2Sb2.5Sr2Ca2Cu3Ox and Bi1.7Pb0.3Sr0.3Ca0.2Cu3.5Ox samples obtained at 77.3K.

the critical temperature $T_c^{0.5}$ and ρ versus transport current density point to the inhomogeneity due to the occurrence of the semiconducting phase 2201 as well as the phases with high-resistance Ca2PbO4 and Ca2CuO3, [1-8]. Much wider SC transitions of sample1 testifies to this as well as the observed non-monotonic character of the behavior of the critical temperature $T_c^{0.5}$ and ρ of the transport current density J. However, it has been found out that at annealing temperatures higher than 820˚C the presence of the phase Ca2PbO4 is becoming unlikely [2] due to which much narrower superconducting transition is likely possible in sample 2 (Fig.1-3). Whereas enhancement of the annealing time after the high-temperature annealing at 600˚C on the one hand tends to decrease the 2201 phase and on the other hand to increase the volume fraction of the 2212 phase [1, 2, 8] in connection with the change in ratio of the Sr/Ca component content [2,7]. It should be noted that in this case the dependence of T_c upon the heat treatment conditions, impurity content of samples and their Sr/Ca ratio is non-monotonic.

It's noteworthy that the sharp increase in electrical resistivity depending on transport current for the HTS films and ceramics samples has been observed by other authors before as well. They relate such behavior to the decoupling of the superconducting cooper pairs [12,13,20,21].

Conclusion

The resistive superconducting transitions in bismuth samples with the Bi2Pb2Sb2.5Sr2Ca2Cu3Ox (sample 1) and Bi1.7Pb0.3Sr0.3Ca0.2Cu3.5Ox (sample 2) compositions are detected by current –voltage characteristics measurements and the influence of

low transport current on the nature of variation of these transitions has been studied too. The results obtained from investigations are as follows:

1. With the increase of the transport current density in both of the samples the low-temperature arm originated on the superconducting transition shifts towards the low temperatures. At the same time the electrical resistivity beginning with some threshold value of the transport current Is with the increase of I at first rises rapidly and is susceptible to saturation at higher values. It has been found out that the value of Is strongly depends on temperature and with its increase shifts towards the low values. The observed enhancement of the electrical resistivity is due to the destruction of weak links under the influence of the transport current.
2. In both of the samples the critical temperature of the superconducting transition for the mid point and the values of their electrical resistivity depending on I varies in non-monotonic manner. It was found out that the parameters of sample 1 are more sensitive to the change of the transport current in comparison with sample 2.
3. The observed experimental distinctions in the behavior of the superconducting transitions parameters of the studied samples depending on the transport current are attributed to their structural peculiarities (impurity-defect composition and their distribution, the granule size, the bulk density).

Similar investigations of the samples with different component compositions and bulk densities as well as heat treated under different conditions should be carried out in order to clarify the complete behavior of superconducting parameters depending on transport current.

For the final clarification of the nature of the superconducting parameters behavior of the transport current, similar investigations of the samples with different compositions should be carried out subjected to the heat treatment in different modes.

References

1. P. G. Vasilev, M. Mikhov, D. Kovacheva, K. Petrov, Superconducting and electrical properties of rapidly synthesized samples of $Bi_{1.6}Pb_{0.4}Sr_2Ca_2Cu_{3+y}O_{10+x}$, Superconductivity: Physics, chemistry, technique (SPCT), vol.3, issue. 6, part 1 (1990) pp. 1075-1082.
2. I. F. Kononyuk, V.V. Vashchuk, L. W. Maknach, Yu.G. Zonow, The ifluence of the heat-treatment conditions on the phase composition and electrical resistivity of superconducting ceramics $Bi_{2-x}Pb_xSr_2Ca_2Cu_3O_y$ ($0.2 \leq x \leq 0.4$), (SPCT), vol.3, issue 2 (1990), pp. 298-307.
3. P. B. Abramyan, A.A. Avagyan, S.G. Gevorgyan et al., The Synthesis and Study of the Samples with the Composition of $Bi_{1.7}Pb_{0.3}Sr_2Ca_2Cu_3O_y$, vol. 3, Issue 4 (1990), pp. 6980-707.
4. Yu. A. Tomashpolskii, A.K. Kochetov, N.V. Sadovskaya et al., The Phase Composition and the Microstructural Model of HTSC Ceramics Bi-Pb-Sr-Ca-Cu-O T_c = 101K, SPCT, vol. 3, Issue 4 (1990), pp. 708-712.
5. V.V. Shatalov, V.D. Kosinkin, V. A. Kuznetcova et al., The Influence of the Replacement of Copper on Molybdenum to the Phase Composition in the System Bi(Pb)-Sr-Ca-Cu-O, SPCT, vol. 4. Issue 7 (1991), pp. 1363-1367.
6. I.G. Vasileva, B.V. Reddy, N.N. Boldireva, I.N. Kuropyatnik, A.I. Romanenko, V.V. Malakhov. The Effect of Alloying with Aluminum and Silver of the System Bi-Sr-Ca-Cu-O, SPCT, vol. 3, Issue 11 (1990), pp. 2608-2615.
7. A.G. Sargsyan, V.M. Arutyunyan,R.S. Hakobyan, R.S. Vartanyan, E.V. Putnin, N.M. Dobrovolskii, S.G. Gevorkyan,. On Superconductivity at the Temperature above 100K in the System of Bi-Ca-Sr-Cu-O. Letters to JETP, vol.49, Issue 2, (1989), pp.93-95.
8. M.P. Volkov, B.T. Melekh, V.I. Bakharev et al., The Influence of Doping With Lithium on the Critical Temperature of the Glass Formation of the System Bi-Sr-Ca-Cu-O, Physics of Solid State, vol. 41, Issue 1, (1999), pp. 18-21.

9. A.G. Shneider, Yu.S. Bulishev, A.I. Sedyakov. The Influence of the Heat-Treatment Modes and the Component Composition on the Phase Ratio in the System of Bi-Sr-Ca-Cu-O, SPCT, vol.4, Issue. 7, (1991), pp. 1003-1005.
10. S.K.Nikoghosyan, A.A. Sahakyan, V.A. Grigoryan, G.N. Yeritsyan, The Features of Irreversibility Lines in Y- and Bi-Based Superconductors, Phys. Stat. Sol. (a) 174, (1999), pp. 459-465.
11. S.K. Nikoghosyan, A.A.Sahakyan,G.N. Yeritsyan, V.A. Grigoryan, The Influence of the Bulk Density on the Intergranular Superconducting Properties of $YBa_2Cu_{3-x}Fe_xO_y$ ($0 \le x \le 0.01$), ceramics, Physica, C, 317-318, (1999), pp.607-610.
12. B.A. Aronzon, Yu.V. Gershanov, E..Z. Meilikhov, V.G. Shapiro. The Influence of the Magnetic Field on the Current-Voltage Characteristics of the Resistive State of the Ceramics $YBa_2Cu_3O_{6.9}$, SPCT, vol.2. Issue 10 (1989), pp. 83-88.
13. A.N Kopchikov. The Current-Voltage Characteristics of HTS. The Superconducting Glass sample, SPCT, vol.3, Issue 1 (1990), pp.47-51.
14. J.C. Soret, Scaling Behaviour and Crossover of Resistive Transition in YBa2Cu3O7-x, Phisika, C 177 (1991), pp. 45-51.
15. T.V. Sukhareva, V.A. Finkel. The Vortex Structure and the Magnetoresistance of Granular HTSC $YBa_2Cu_3O_{7-\delta}$, Physics of Solid State, vol.52. (2010), pp. 424-429.
16. M.I. Petrov, D.A. Balaev, K.A. Shaikhutdinov, The Influence of Thermal Fluctuations on the Resistive Properties of the Composites of HTSC+CuO, Physics of Solid State, vol.11 (1997) 1956-1957.
17. D.A. Balaev, A.A. Bikov, S.V. Semeunov, A.A. Dubrovskii, K.A. Shaikhutdinov, M.I. Petrov. General Laws on the Magnetoresistive Effects in Polycrystalline Yttrium and Bismuth Systems of HTSC, Physics of Solid State, vol. 53,Issue 5 (2011), pp. 865-874.
18. K.A. Shaykhutdinov, D.A. Balaev, D.M. Gokhfeld, Yu.I. Kuzmin, S.I. Popkov, M.I. Petrov. Study of Current-Voltage Characteristics of Bi-basd High-Temperature Superconductors with Fractal Cluster Strucure, Phisica C 435 (2006), pp. 19-22.
19. D.A. Balaev, K.A. Shaykhutdinov, S.I. Popkov, D.M. Gokhfeld, A.A. Dubrovskii, M.I. Petrov. The Comparative Study of the Magnetic Effect in the Semi-crystalline High-Temperature Superconductor $Y_{3/4}$ $Lu_{1/4}$ $Ba_2Cu_3O_7$ and Composites of $Y_{3/4}$ $Lu_{1/4}$ $Ba_2Cu_3O_7$ and Dielectric CuO., Condensed Matter Physics, http:// library.krasu.ru/ft/ft-articles/0089581.pdf
20. I.G. Gorlova,Yu. Latishev. The Equivalent Effect of the Weak Magnetic Field and the Current on the Resistivity of Single Crystals $Bi_2S_2CaCu_2O_x$ Lower than the Berezinskii- Kosterlitz-Thouless Transition Temperature, Letters to JETP, vol. 51, Issue 4 (1990), pp. 197-200.
21. D.D. Prokofev. The Destruction of the Bond between the Two Layers of the Film (YBCO) by the Transport Current. The Proceedings of the II International Conference "The Fundamental Problems of High-Temperature Superconductivity". (FPS- 06), Zvenigorod, 9-13 October, 2006, (FPS- 06). Section P. The Physical properties of HTSC, pp. 156-157.
22. S.R. Curras, P. Wagner, M. Ruibal, J. Vina, M.R. Osorio,M.T. Gonzalez,J.A. Veira, J. Maza and F. Vidal, Transition to the Normal State of superconducting Yba Cu O Thin Films Induced by High Current Densities, Supercond. Sci.Technol. V.14 (2001) 748-753.
23. K.A. Shaykhutdinov, D.A. Balaev, S.I. Popkov, M.I. Petrov, The Possible Occurrence of the Area With Negative Magnetoresistance, Physics of Solid State, vol. 51, Issue 6 (2009), pp. 1046-1050.
24. A.V. Krevsun, S.I Bondarenko, W.P. Koverya, L.V. Gnezdilova. The Influencet of the Magnetic State of Granular Ceramics $YBa_2Cu_3O_{7-x}$ on the Magnetoresistive Properties. Problems of Atomic Science and Technology, Series: Vacuum, Pure Materials, Superconductors, Vol. 18, Issue 6 (2006), pp. 97-104.

Radiation from a Charged Particle Rotating Outside a Dielectric Ball in its Equatorial Plane

Svetlana R. Arzumanyan

NAS Institute of Applied Problems in Physics, Yerevan Armenia

Abstract

The radiation from a relativistic charged particle rotating outside a dielectric ball in its equatorial plane is investigated. Analytical expressions for spectral distributions of the radiated energy are derived and numerical results are given. It is shown, that the ball-vacuum interface may strongly effect on Cherenkov radiation generated by the particle in the substance of ball.

1. Problem statement and basic formulas

The presence of matter may essentially influence the characteristics of high energy electromagnetic processes, generating new types of phenomena [1]. The synchrotron radiation from a charged particle rotating in a homogeneous medium is considered in [2] (see also [3,4]). It has been shown that the interference between synchrotron radiation and Cherenkov radiation (CR) leads to interesting consequences. New interesting phenomena occur in the case of inhomogeneous media.

The influence of spherical and cylindrical interfaces between media on CR from relativistic particles has been investigated in [5-8]. In the present work a case of circular rotation of a particle (e.g., of electron) in the equatorial plane of a dielectric ball at some distance from its surface (Fig.1) is considered.

In spherical coordinates r, θ, φ with origin in the center of ball the current density may be written as

$$\vec{j}(\vec{r},t) = \frac{q\vec{\mathrm{v}}}{r_0^2(t)}\delta(r - r_0(t))\delta(\theta - \theta_0)\delta(\varphi - \varphi_0(t)), \qquad (1)$$

where q and v are the charge and linear velocity of the particle, and $r_0(t)$, $\varphi_0(t)$, θ_0 are the coordinates of particle in the spherical system of coordinates.

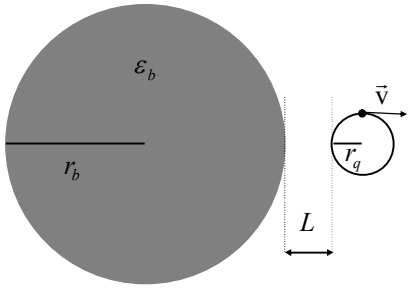

Fig.1. A charged particle rotating outside a dielectric ball in its equatorial plane.

The rotation of particle entails radiation at some discrete frequencies (harmonics)

$$\omega_k \equiv k\omega_0 \ , \quad k = 1;2;3... \qquad (2)$$

that are multiples of the rotation cyclic frequency ω_0 of particle. We assume that an exterior force would make up for the braking of particle due to the radiation, by forcing the particle to uniformly rotate outside the ball.

The total energy losses of particle during one revolution period may be written as

$$\sum_k (E_k^{(d)} + E_k^{(r)}) = \sum_k W_k \ . \qquad (3)$$

Here $E_k^{(d)}$, $E_k^{(r)}$ are the dielectric losses of energy and the energy losses due to radiation respectively.

It is convenient to introduce a dimensionless quantity

$$E_k^{(r)} / \hbar\omega_k \equiv n_k , \qquad (4)$$

where $\hbar\omega_k$ is the energy of corresponding electromagnetic wave quantum. So, n_k is the "number of electromagnetic field quanta" emitted during one period of particle revolution. We shall assume that the ball material is a loss-free dielectric and therefore $W_k = E_k^{(r)}$.

We have solved the Maxwell equations for the case under consideration and obtained the following final formula for

$$n_k = -\frac{icq}{\hbar k^2 \omega_0^2} \sum_{l=1}^{\infty} \sum_{m=-l}^{l} \int_0^T \Bigg(Z^{lm}(r_0(t)) \mathrm{v}_r(t) Y_{lm}(\pi/2,0) + \frac{im\mathrm{v}_\varphi(t)}{\sqrt{l(l+1)}} Y_{lm}(\pi/2,0) \times$$
$$\times \left(\frac{\omega^2}{c^2} A_2^{lm}(r_0(t)) + \frac{\sqrt{l(l+1)}}{r_0(t)} D^{lm}(r_0(t)) \right) + \frac{\omega^2}{c^2} A_3^{lm}(r_0(t)) \frac{\mathrm{v}_\varphi(t)}{\sqrt{l(l+1)}} \frac{\partial}{\partial\theta} Y_{lm}(\pi/2,0) \Bigg) e^{-i(k\omega_0 t - m\varphi_0(t))} dt. \qquad (5)$$

Here $Y_{lm}(\theta,\varphi)$ are the spherical harmonics. We introduce the following notations:

$$Z^{lm}(r) = \frac{\omega^2}{c^2} A_1^{lm}(r) + \frac{\partial D^{lm}(r)}{\partial r}, \qquad D^{lm} = \left(\frac{2}{r} + \frac{\partial}{\partial r} \right) A_1^{lm} - \frac{\sqrt{l(l+1)}}{r} A_2^{lm},$$

$$A_1^{lm}(r) = \frac{4\pi}{cr_b^2(2l+1)} \Big(l u_{l-1}^{lm}(r,1) + (l+1) u_{l+1}^{lm}(r,1) + \sqrt{l(l+1)} \left(u_{l-1}^{lm}(r,2) - u_{l+1}^{lm}(r,2) \right) +$$
$$+ \gamma_l \Big(l B_{l-1}^{lm}(1) - (l+1) B_{l+1}^{lm}(1) + \sqrt{l(l+1)} \left(B_{l-1}^{lm}(2) + B_{l+1}^{lm}(2) \right) \Big) \left(l P_{\underline{l-1}}(r,r_b) + (l+1) P_{\underline{l+1}}(r,r_b) \right) \Big),$$

$$A_2^{lm}(r) = \frac{4\pi}{cr_b^2(2l+1)} \Big(\sqrt{l(l+1)} \left(u_{l-1}^{lm}(r,1) - u_{l+1}^{lm}(r,1) \right) + (l+1) u_{l-1}^{lm}(r,2) + l u_{l+1}^{lm}(r,2) +$$
$$+ \gamma_l \sqrt{l(l+1)} \Big(l B_{l-1}^{lm}(1) - (l+1) B_{l+1}^{lm}(1) + \sqrt{l(l+1)} \left(B_{l-1}^{lm}(2) + B_{l+1}^{lm}(2) \right) \Big) \left(P_{\underline{l-1}}(r,r_b) - P_{\underline{l+1}}(r,r_b) \right) \Big),$$

$$A_3^{lm}(r) = \frac{2q\omega_0}{cr_b^2 \sqrt{l(l+1)}} \frac{\partial}{\partial\theta} Y_{lm}(\pi/2;0) \int_0^T \mathrm{v}_\varphi(t) P_{\underline{l_1}}(r, r_0(t)) e^{i(k\omega_0 t - m\varphi_0(t))} dt ,$$

$$u_{l_1}^{lm}(r;1) = \frac{q\omega_0 Y_{lm}(\pi/2;0)}{2\pi} \int_0^T \mathrm{v}_r(t) P_{\underline{l_1}}(r, r_0(t)) e^{i(k\omega_0 t - m\varphi_0(t))} dt ,$$

$$u_{l_1}^{lm}(r;2) = -\frac{imq\omega_0 Y_{lm}(\pi/2;0)}{2\pi\sqrt{l(l+1)}} \int_0^T \mathrm{v}_\varphi(t) P_{\underline{l_1}}(r, r_0(t)) e^{i(k\omega_0 t - m\varphi_0(t))} dt ,$$

$$B_{l_1}^{lm}(1)=\frac{q\omega_0}{2\pi r_b}Y_{lm}(\pi/2;0)uj_l(u)\int_0^T \mathrm{v}_r(t)h_{\underline{l}_1}(u_b r_0(t)/r_b)e^{i(k\omega_0 t-m\varphi_0(t))}dt\,, \qquad (6)$$

$$B_{l_1}^{lm}(2)=-\frac{imq\omega_0}{2\pi\, r_b\sqrt{l(l+1)}}Y_{lm}(\pi/2;0)uj_l(u)\int_0^T \mathrm{v}_\varphi(t)h_{\underline{l}_1}(u_b r_0(t)/r_b)e^{i(k\omega_0 t-m\varphi_0(t))}dt\,,$$

$$P_l(r;r')=h_l(u_b r/r_b)b_l^2(r')\,,\quad b_l^2(r)=iu_b r_b\left(\{j_l(u_b);h_l(u)\}j_l(u_b r/r_b)+\{j_l(u_b);j_l(u)\}h_l(u_b r/r_b)\right),$$

$$\{a_l(u_b);\ b_l(u)\}\equiv u_b a_{l+1}(u_b)b_l(u)-a_l(u_b)ub_{l+1}(u)\,,\quad f_{\underline{l}}(\tau)\equiv f_l(\tau)/\{j_l(u_b);h_l(u)\}\,,$$

$$u=k\frac{r_b\mathrm{v}}{r_q c}\,,\qquad u_b=k\frac{r_b\mathrm{v}}{r_q c}\sqrt{\varepsilon_b}\,,\qquad \gamma_l=\frac{1-\varepsilon_b}{\varepsilon_b\left(lz_{l-1}^l+(l+1)z_{l+1}^l\right)},$$

$$z_\nu^l\equiv\frac{\varepsilon_b j_\nu(u_b)uh_l(u)-u_b j_l(u_b)h_\nu(u)}{j_\nu(u_b)uh_l(u)-u_b j_l(u_b)h_\nu(u)}$$

($j_l(\tau)$ and $h_l(\tau)$ are the spherical Bessel and Hankel functions of the first kind respectively). Eventually,

$$r_0(t)=\sqrt{d^2+r_q^2+2dr_q\cos\omega_0 t}\,,\qquad \varphi_0(t)=\mathrm{Re}\left(-i\ln\left(\frac{d+r_q e^{i\omega_0 t}}{r_0(t)}\right)\right),$$

$$\mathrm{v}_r(t)=-\frac{r_q\omega_0 d\sin\omega_0 t}{r_0(t)}\,,\qquad \mathrm{v}_\varphi(t)=\frac{r_q\omega_0\left(r_q+d\cos\omega_0 t\right)}{r_0(t)}\,. \qquad (7)$$

Here $d=r_b+L+r_q$ is the distance between the center of ball and that of particle orbit.

2. Numerical results

We have calculated the number of quanta n_k emitted by the rotating particle and have found the values of system parameters r_q/r_b and L, for which n_k has maximum (for given k, v and ε_b).

In Fig.2 we give the number of electromagnetic field quanta n_1 emitted at the first harmonics versus the orbit radius r_q for an electron rotating in vacuum at $L=0.1cm$ distance from the surface of dielectric ball having permittivity $\varepsilon_b=3.78$ (molten quartz in $\sim 10^{10}Hz$ frequency range [9]), and radius $r_b=3cm$. As the electron energy is $1MeV$, the Cherenkov condition for the particle speed and the ball material is satisfied:

$$\mathrm{v} > \mathrm{c}/\sqrt{\varepsilon_b}\,. \qquad (8)$$

As is seen from the plot, the height of sharp peaks observed at definite values of the orbit radius r_q is by one order of magnitude higher than that in case of uniform rotation of particle in vacuum for the same values of the problem parameters (dashed line in Fig.2). This witnesses to the strong effect that the ball-vacuum interface has on CR generated by the particle in the substance of ball.

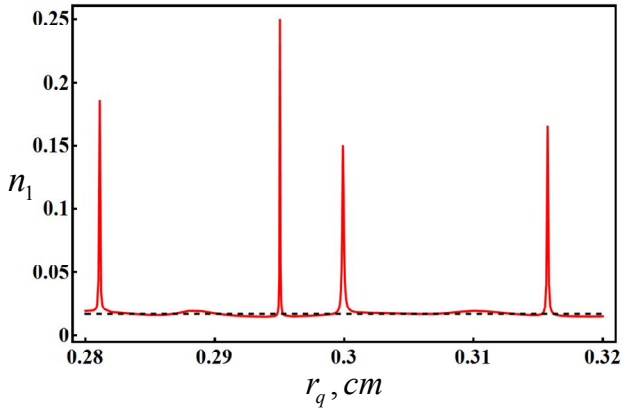

Fig.2. The number of electromagnetic field quanta n_1 emitted at the first harmonics versus the orbit radius r_q. For explanation see the text.

In Fig.3 the number of quanta n_1, is shown as a function of distance L between the ball surface and particle orbit in case when the orbit radius $r_q = 0.29503\,cm$ (see the corresponding peak in Fig.2). The remaining parameters are being the same as those in Fig.2. The exponential reduction in the number of electromagnetic field quanta (for increasing L) is an additional evidence in favor of the fact that the peaks in the radiation intensity in Fig.2 are precisely due to CR produced in the ball substance.

Acknowledgements

The author is grateful to L.SH. Grigoryan, H.F. Khachatryan for stimulating discussions and continued interest to this work, A.A. Saharian for assistance.

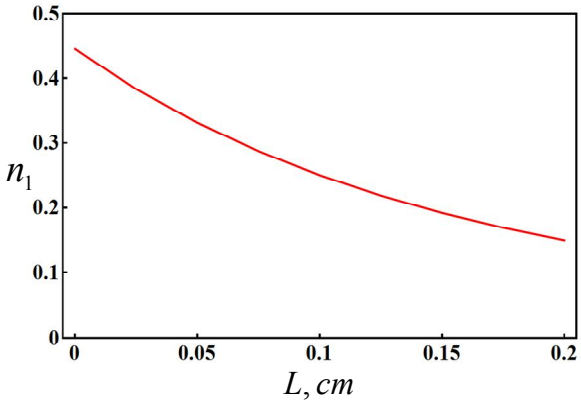

Fig.3.The number of electromagnetic field quanta n_1 emitted at the first harmonics versus the distance L between the ball surface and particle orbit. For explanation see the text.

References

1. P. Rullhusen, X. Artru, P. Dhez, Novel Radiation Sources Using Relativistic Electrons, Singapore: World Scientific, 1998.
2. V. N. Tsytovich, Westnik MGU 11, 27 (1951) (in Russian).
3. K. Kitao, Prog. Theor. Phys. 23, 759 (1960).
4. V.P. Zrelov, Vavilov-Cherenkov Radiation (and its Applications in High Energy Physics), Moscow: Atomizdat, 1968 (in Russian).

5. L.Sh. Grigoryan, H.F. Khachatryan, S.R. Arzumanyan, Izv. Nats. Akad. Nauk Arm. Fiz., 33, 267 (1998); 37, 327 (2002) (in Russian). L.Sh. Grigoryan, H.F. Khachatryan, S.R. Arzumanyan, M.L. Grigoryan, NIMB 252, 50 (2006).
6. L.Sh. Grigoryan, H.F. Khachatryan, S.R. Arzumanyan, M.L. Grigoryan, Microwave Radiation from a Particle Revolving Along a Shifted Equatorial Orbit About a Dielectric Ball, Proc. of the 35th Intern. Conf. on Infrared, Millimeter and Terahertz Waves (IRMMW-THz 2010), Rome, Italy, 05-10 Sept. 2010, Mo-P.27; arXiv: 1007.2776.
7. A.S. Kotanjyan, H.F. Khachatryan, A.V. Petrosyan, A.A. Saharian, Izv. Nats. Akad. Nauk Arm. Fiz., 35, 115 (2000); A.S. Kotanjyan, A.A. Saharian, ibidem, 36, 310 (2001) (in Russian). A.S. Kotanjyan, A.A. Saharian, Mod. Phys. Lett. A17, 1323 (2002).
8. A.A. Saharian, A.S. Kotanjyan, J. Phys. A38, 4275 (2005); A40, 10641 (2007); A42, 135402 (2009). A.A. Saharian, A.S. Kotanjyan, M.L. Grigoryan, J. Phys. A40, 1405 (2007).
9. E. M. Voronkova, B. N. Grechushnikov, G. I. Distler, I. P. Petrov, Optical Materials for Infrared Technology, Moscow: Nauka, 1965 (in Russian).

Stimulated excitation of resonant Cherenkov radiation at a large number of neighbouring waveguide modes

L. Sh. Grigoryan[1], S. R. Arzumanyan, H. F. Khachatryan, M. L. Grigoryan

NAS Institute of Applied Problems in Physics, Yerevan Armenia

Abstract. The resonance Cherenkov radiation generated from a train of equally-spaced unidimensional electron bunches travelling along the axis of a hollow channel inside an infinite cylindrical waveguide filled with (weakly dispersing) transparent dielectric has been investigated. It was shown that its excitation might be stimulated at a large number of neighboring modes of the waveguide. A visual explanation of this effect is given and the possibility of its observation in the range of terahertz radiation is discussed.

Keywords: Waveguide, train of bunches, resonant Cherenkov radiation, stimulated excitation of radiation.

1. Introduction

With the advent of modern accelerators it became possible to generate small size ($<1mm$) relativistic monoenergetic bunches with large number of electrons ($>10^9$) to produce high power quasi-coherent terahertz radiation that is of considerable interest for applications in physics, chemistry and biology [1]. Direct observation of the record power, narrow-band and coherent terahertz Cherenkov radiation (CR) generated by such a bunch travelling through a hollow channel inside the dielectric-filled waveguide was reported in [2] (2009). As was clarified later on (2010–2011), the radiated power of CR attained in [2] could have been essentially increased, if the filler dielectric in the waveguide were cut into plates and spaced at some distances one from the other [3,4].

There is another theoretical opportunity for considerable increase of the power of CR attained in [2] that is connected with the fact that in accelerators it turns possible to generate the trains of bunches spaced at small distances d ($<1mm$). Based on this fact high power resonant [6] (the so-called parametric [7]) coherent THz CR has been generated in [5] (2011) at a separate waveguide mode ω_{s_0} by selecting d distance according to the well-known formula

$$d = 2\pi \mathrm{v} / \omega_{s_0} \tag{1a}$$

(v is the velocity of bunch train travel and s_0 is the number of emitted mode).

Another choice of the value of d suggested in [8] (2006) provided the generation of resonant CR at larger number of neighboring modes of the waveguide, that proved to be higher power than in the case of (1a). Ibidem a visual explanation of this effect has been also given. However, the study in [8] was concerned with the case of CR from *a train of point charges* travelling along the axis of *a waveguide completely filled with a dielectric*. In reality (i) a train of electron bunches, not that of separate electrons is generated and (ii) the ionization losses are diminished when this train is directed in the hollow channel inside the dielectric. The presence of a hollow channel undoubtedly reduces the power of CR (see [9]) and complicates theoretical analysis of the problem. In the present work both these facts have been taken into account to construct a more adequate model of the situation.

2. The problem formulation

Let us consider a train of equidistant unidimensional electronic bunches traveling along the axis

of hollow channel in the central part of dielectric-lined waveguide[3]. In case of electron velocity

$$\mathrm{v} > \mathrm{c}/\sqrt{\varepsilon\mu} \tag{2}$$

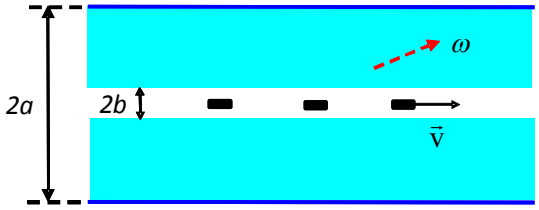

Fig.1. A train of three equidistant unidimensional electronic bunches traveling along the axis of hollow channel in the central part of dielectric-lined waveguide.

(ε and μ are the permittivity and permeability of the substance of waveguide filler respectively) the CR is generated inside the waveguide at discrete frequencies ω_s determined from the following dispersion equation

$$k\varepsilon\varphi_0 I_0(kb) = \chi\varphi_1 I_1(kb) \tag{3}$$

(see, e.g., [9]), where

$$\varphi_0 = J_1(\chi b)N_0(\chi a) - J_0(\chi a)N_1(\chi b)$$
$$\varphi_1 = J_0(\chi b)N_0(\chi a) - J_0(\chi a)N_0(\chi b) \tag{4}$$
$$k = \frac{\omega_s}{\mathrm{v}}\sqrt{1-\mathrm{v}^2/c^2}\,, \qquad \chi = \frac{\omega_s}{\mathrm{v}}\sqrt{\varepsilon\mu\mathrm{v}^2/c^2 - 1}\,.$$

Here a and b are respectively the radii of waveguide and of the hollow channel in its center (Fig.1), $J_n(x)$ and $N_n(x)$ are the Bessel functions of the first and second kind of order n, and $I_n(x)$ is the modified Bessel function of the first kind of order n.

The energy of CR generated in unit time is determined by the sum

$$\sum_{s=1}^{\infty} P(s) = \sum_{s=1}^{\infty} P_1(s)\,F(s)\,, \tag{5}$$

where [9]

$$P_1 = 2\frac{q^2}{\mathrm{v}}(1-\mathrm{v}^2/c^2)\frac{\omega_s[\chi\varphi_1 K_1(kb) + k\varepsilon\varphi_0 K_0(kb)]}{d[\chi\varphi_1 I_1(kb) - k\varepsilon\varphi_0 I_0(kb)]/d\omega_s} \tag{6}$$

is the radiation power of a single electron at the s-th waveguide mode ($K_n(x)$ is the modified Bessel function of the second kind of order n). In (5)

$$F = n_q(1-f_q)n_b + n_q^2 f_q n_b^2 f_{tr} \tag{7a}$$

is the structural factor [6,10-12] of the train of bunches. Here n_q is the number of electrons inside a bunch,

$$f_q = \exp(-\omega_s^2\sigma^2/\mathrm{v}^2) \tag{7b}$$

[3] Hereinafter we shall assume that the waveguide is filled with a transparent substance.

is the coherence factor of CR from electrons in a single bunch (admittedly distributed according to Caussian law with standard deviation σ), n_b is the number of bunches, and

$$f_{tr} = \sin^2(\omega_s d n_b / 2\mathrm{v}) \big/ n_b^2 \sin^2(\omega_s d / 2\mathrm{v}) \qquad (7c)$$

is the coherence factor of radiation from bunches in the train.

According to (7c) the train of bunches coherently generates parametric [7] (or, so called, resonant [6]) CR at the separately taken mode s_0: $f_{tr}(s_0) = 1$, if

$$d = 2\pi m \mathrm{v} / \omega_{s_0}, \quad \text{where} \qquad m = 1;2;3\ldots . \qquad (1b)$$

The novelty of *our work* consists in the other choice of the distance between bunches:

$$d \cong m d_0, \quad \text{where} \qquad d_0 = 2(a-b)\sqrt{\varepsilon\mu\mathrm{v}^2/c^2 - 1} \qquad (8)$$

(and in a visual derivation of the above equality) in case of which the CR from the train of bunches is practically resonant at a large number of neighboring modes:

$$f_{tr}(s) \approx 1, \; s_1 \le s \le s_2, \qquad (s_2 - s_1) >> 1. \qquad (9)$$

3. Numerical results

In our calculations we have used (3) – (8), $b = 0.1a$, and

$$d = 2(1+\alpha)d_0, \quad \text{where} \qquad \alpha = 0.011. \qquad (10)$$

The energy of electrons was taken to be $10MeV$, $n_q e = 200pC$, $\varepsilon = 3.8$, $\mu = 1$ [2]; $\sigma = 0.02a$ and $n_b = 5$.

The values of $P(s)/P_*$ are shown by blue dots in the lower part of Fig.2, where

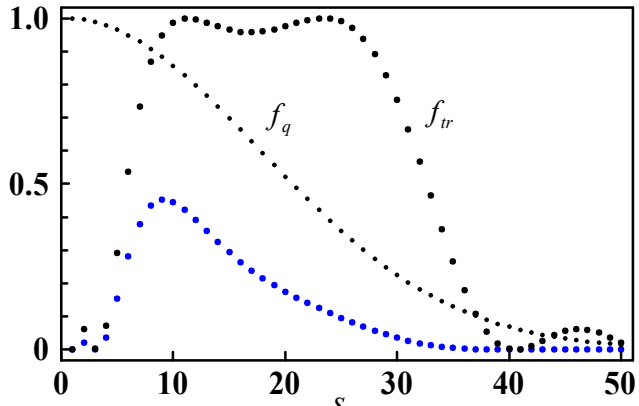

Fig.2. With blue points the power $P(s)/P_*$ of CR from a train of $n_b = 5$ unidimensional electron bunches was plotted depending on the number s of the radiated waveguide mode, $P_* = 10\mathrm{v}(en_q n_b)^2 / a^2$. The calculations were made using formulae (3)-(8). Black points represent the coherence factors $f_q(s)$ (for the radiation generated by a separate bunch) and $f_{tr}(s)$ (for the radiation generated by the train as a whole).

$P_* = 10\mathrm{v}(en_q n_b)^2 / a^2$. On comparing the values of $f_{tr}(s)$ and $f_q(s)$ in the upper part of Fig.2 one makes certain that

$$f_{tr}(s) \approx 1 \qquad \text{and} \qquad f_q(s) \geq 0.5 \qquad \text{at} \quad 10 \leq s \leq 20. \tag{11}$$

In this relatively wide range of waveguide modes *the energy of CR from the train of bunches is* $\approx n_b^2 = 25$ *times as large as that from the separate bunch* (see (5),(7a),(9)). Here in case of $a = 2mm$ the power of CR is

$$\sum_{s=6}^{24} P(s) = 36.3MW\,. \tag{12}$$

The radiation is generated within the range of $273 \leq \omega_s / 2\pi \leq 960\ GHz$.

4. Visual explanation

Equality (8) admits a visual interpretation. Now let us consider the instant when the first bunch (the rightmost one in the direction of train travel) was in the vicinity of point A (see Fig.3a) and observing the laws of ray optics follow the propagation of (the dotted) CR pulse generated by this bunch in the vicinity of point A. The angle θ in Fig.3a specifies the direction of radiation propagation in an infinite homogeneous medium: $\cos\theta = c / \mathrm{v}\sqrt{\varepsilon\mu}$. At some moment of its propagation the CR pulse would come closest to the trajectory of bunches (the waveguide axis) in the vicinity of point *C*. By this time the pulse would lag behind its faster-than-light source which will be found rightwards in the vicinity of A_C point. The second bunch stays leftwards in the vicinity of point B at the distance d from the first one (see Fig.3b, in Fig.3a it is not shown), and if

$$CB = 0 \qquad \Leftrightarrow \qquad d = d_0 \tag{13}$$

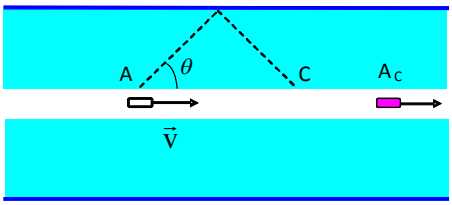

Fig.3a

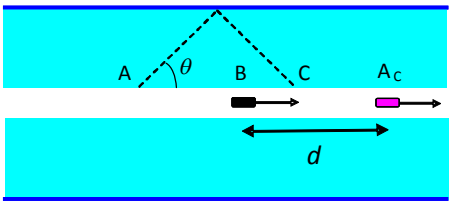

Fig3.b

Fig.3a. In the vicinity of point *C* the propagating Cherenkov wave (dotted line), emitted by the first bunch of train in the vicinity of point A, would most closely approach the trajectory of bunches. By this moment of time the faster-than-light bunch will be found rightwards, in the vicinity of point A_C.

Fig.3b. At the same moment the second bunch of the train (it is not seen in Fig.3a) will be located leftwards, - in the vicinity of point B, at d distance from the first one.

then it will traverse the vicinity of point *C* simultaneously with the pulse. In this case *an exceptional situation* is realized when the CR pulse emitted by the second bunch in point B is formed and simultaneously superimpose on the pulse that was emitted earlier by the first bunch in flight in the vicinity of point A. The situation with all d that are multiples of d_0:

$$d = md_0 \tag{14}$$

is similar.

One may conclude by analogy that in areas immediately adjacent to each of bunches (except for the first one), i.e., in the radiation formation zone the processes of emission and superposition of pulses occur simultaneously. In case of weak dispersion the condition (14) is practically independent of the number of generated waveguide mode and, hence, *the superposition of pulses will occur on the larger number of neighboring modes*. As a result of interference the pulses may be either suppressed or amplified depending on the specific value of phase difference. The in-phase superposition of electromagnetic oscillations would go with an amplification of field in the zone of radiation formation. As a result, the force retarding the motion of bunches also increases, and an additional work performed by the external force constraining the uniform motion of bunches shall be used for formation of higher power resonant CR stimulated on the larger number of neighboring modes. This case is illustrated in Fig.2 for $m = 2$.

The second equality in (13) is valid in the frameworks of geometrical optics laws, when the wavelength of the emitted wave is much less than b. This method for determination of d requires a more accurate definition for modes with $s \le a/b$. It is not surprising, hence, that in case of $a/b = 10$ the resonant CR, the excitation of which is stimulated on modes with $6 \le s \le 20$ (see Fig.2), occurs for d that somewhat differs from (14), namely for d that is determined according to (10).

5. Discussion

The coherent terahertz CR generated by a subpicosecond bunch of relativistic electrons travelling along the axis of a waveguide filled with a hollow dielectric has been experimentally studied in [2]. Here the value of $b/a \approx 0.23$ was chosen so that CR were generated only on the first waveguide mode. Later on it became possible [5] to generate the resonant (and coherent) THz radiation of a train of subpicosecond electronic bunches on a separate mode of the waveguide by proper choice of d distance by formula (1a).

We propose another choice of d (see (10)) providing an emission of resonant (and coherent) THz radiation, the excitation of which is stimulated on the larger number of neighboring waveguide modes. An increase in the number of resonantly emitted modes is stipulated by the fact that in areas immediately adjacent to each bunch (except for the first one) both the processes, - the emission and constructive interference of CR waves emitted earlier by those bunches flying ahead, occur simultaneously.

Similar stimulation for transition radiation was observed experimentally in [13-15]. In these works the total energy of radiation has been measured (confer with (12)) in the far infrared range. The radiation was generated by a train of electron bunches at the SUNSHINE setup (Stanford University, USA). The observed stimulation effect of transition radiation was explained by the interference of waves nearby the radiator, i.e., in area immediately adjacent to the emitting bunches. For implementation of such an interference a special system of mirrors and reflectors was constructed and adjusted to direct the transition radiation from one bunch of electrons to the other (confer with Fig.3b).

6. Conclusions

1) In the present work the Cherenkov radiation from a train of equally-spaced unidimensional electron bunches travelling along the axis of a hollow channel inside an infinite cylindrical waveguide filled with (weakly dispersing) transparent dielectric has been investigated.
2) It was shown that if the distance between the bunches is determined by equality (10), then the excitation of resonant CR from a train of bunches may be stimulated on the larger number of neighboring waveguide modes (Fig.2).

3) A visual explanation of this effect was given (Section 4) based on the fact that in case of weak dispersion the equality (10) is practically independent of the number of generated waveguide mode.
4) It is proposed to use the effect of stimulated excitation of the resonant CR on the larger number of neighboring modes for an additional increase of the power of experimentally observed resonant and coherent THz radiation [2,5].

Acknowledgments

One of the authors (L.Sh.G.) is thankful to B.M. Bolotovskii for stimulating discussions, P.A. Alexandrov, N.F. Shulga, S.I. Zaicev and L.A. Gevorgian for valuable comments.

References

1. G.P. Williams, Reports on Progress in Physics, 69 (2006) 301.
2. A.M. Cook, R. Tikhoplav, S.Y. Tochitsky, G. Travish, O.B. Williams, J.B. Rosenzweig, Phys. Rev. Lett., 103 (2009) 095003.
3. L.Sh. Grigoryan**,** H.F. Khachatryan, S.R. Arzumanyan, Proc. of the Intern. Conf. on "The Technique of Microwave and THz Waves and its Application in Biomedical and Radar Technologies and in Remote Sensing" (IRPhE 2010), Sept. 23-25, 2010, Ashtarak-Aghveran, Armenia, pp.32-37.
4. L.Sh. Grigoryan, A.R. Mkrtchyan, H.F. Khachatryan, S.R. Arzumanyan, W. Wagner, Self-amplification of Cherenkov radiation from a relativistic electron inside the waveguide partially filled with a laminated material, IX Intern. Symposium on "Radiation from Relativistic Electrons in Periodic Structures" (RREPS-11), Sept. 12-16, 2011, Egham, UK, Book of Abstracts, p.24.
5. G. Andonian, O. Williams, X. Wei, P. Niknejadi, E. Hemsing, J. B. Rosenzweig, P. Muggli, M. Babzien, M. Fedurin, K. Kusche, R. Malone, V. Yakimenko, Appl. Phys. Lett. 98 (2011) 202901.
6. M.L.Ter-Mikaelian, High Energy Electromagnetic Processes in Condensed Matter, New York, Wiley, 1972.
7. Y.B. Fainberg, N.A. Khizhniak, Zh. Eksp. Teor. Fiz., 32 **(**1957) 883 (in Russian).
8. L.Sh. Grigoryan, H.F. Khachatryan, A.A. Saharian, Kh.V. Kotanjyan, S.R. Arzumanyan, M.L. Grigoryan, Izv. Nats. Akad. Nauk Arm., Fiz., 40 (2005) 155 (in Russian).
9. B. M. Bolotovskii, Physics-Uspekhi, 62 (1957) 201; 75 (1961) 295 (in Russian).
10. N.A. Korkhmazian, L.A. Gevorgian, M.L. Petrosian, Zh. Tekh. Fiz., 47 (1977) 1583 (in Russian).
11. G.M. Garibian, Yan Shi, X-Ray Transition Radiation, Yerevan, AN Arm. SSR Press, 1983 (in Russian).
12. M.M. Nikitin, V.Ya. Epp, Undulator Radiation, Moscow, Energoatomizdat Press, 1988 (in Russian).
13. H.C. Lihn, P. Kung, C. Settakorn, H. Wiedemann, Phys. Rev. Lett., 76 (1996) 4163.
14. C. Settakorn, M. Hernandez, H. Wiedemann, SLAC-PUB-7587, August, 1997.
15. C. Settakorn, M. Hernandez, K.Woods, H. Wiedemann, SLAC-PUB-7812, May, 1998; SLAC-PUB-7813, May, 1998.

Synchrotron Radiation inside a Dielectric Waveguide

A.A. Saharian[1], **A.S. Kotanjyan**[2]

[1]*Institute of Applied Problem in Physics, NAS RA 25 Nersisyan Street, 0014 Yerevan, Armenia*
[2]*Department of Physics, Yerevan State University, 1 Alex Manoogian Street, 0025 Yerevan, Armenia*

1. Introduction

Unique characteristics of the synchrotron radiation have resulted in its extensive applications. Related to this, the investigation of mechanisms for the control of the radiation parameters is of great interest. Particularly important is the study of the influence of a medium on the spectral and angular characteristics. It is well-known that the medium can essentially change the characteristics of the high-energy electromagnetic processes. Moreover, new types of phenomena arise, such as the Cherenkov and transition radiations.

In [1]-[3] we have investigated the synchrotron radiation from a charge rotating around/inside a dielectric cylinder enclosed by a homogeneous medium. It has been shown that under the Cherenkov condition for the material of the cylinder and the particle velocity, strong narrow peaks appear in the angular distribution of the radiation intensity in the exterior medium. At these peaks the radiated energy exceeds the corresponding quantity in the case of a homogeneous medium by several orders of magnitude. Similar features for the radiation generated by a charge moving along a helical orbit have been discussed in [4,5].

In the previous investigations the radiation intensity is considered in the exterior region at large distances from the cylinder. In addition to this part there is radiation which propagates inside the cylinder and it is of interest to investigate the relative contribution of these modes to the total intensity. Here we discuss the radiation intensity inside a dielectric cylinder emitted by a charge rotating inside the cylinder.

2. Radiation intensity inside a dielectric cylinder

Consider a dielectric cylinder of radius ρ_1 and with dielectric permittivity ε_0 and a point charge q rotating inside a cylinder (see Figure 1). The radius of the rotation orbit and the velocity of the charge will be denoted by $\rho_0,\ \rho_0<\rho_1$ and v respectively. We assume that the system is immersed in a homogeneous medium with permittivity ε_1. In the cylindrical coordinate system (ρ,ϕ,z) with the z-axis directed along the cylinder axis, the only nonzero component of the current density is given by the expression

$$j_\phi=\frac{q}{\rho}v\delta(\rho-\rho_0)\delta(\phi-\omega_0 t)\delta(z), \qquad (1)$$

where $\omega_0=v/\rho_0$ is the angular velocity of the charge.

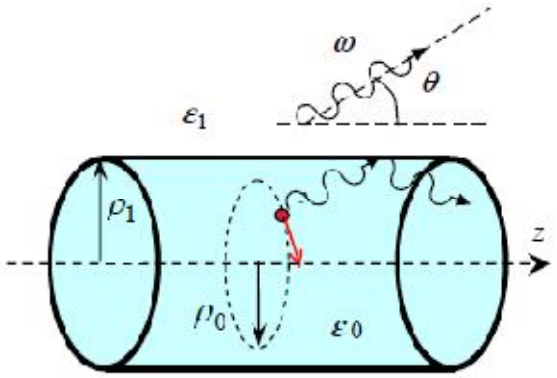

Figure 1: The geometry of the problem

Inside the cylinder the radiation fields can be expanded over the eigenmodes of the dielectric cylinder. The latter are the solutions of the equation

$$U_m \equiv V_m V_{\varepsilon,m} - m^2 \frac{\lambda_0^2 + |\lambda_1|^2}{\lambda_0^2 |\lambda_1|^2} \left(\varepsilon_1 \lambda_0^2 + \varepsilon_0 |\lambda_1|^2 \right) = 0, \qquad (2)$$

where $J_m = J_m(\lambda_0 \rho_1)$ and $K_m = K_m(|\lambda_1| \rho_1)$ are the Bessel and MacDonald functions, the prime means the derivative with respect to the argument of the function, and

$$V_m = \left(|\lambda_1| \rho_1 \frac{J'_m}{J_m} + \lambda_0 \rho_1 \frac{K'_m}{K_m} \right), \quad V_{\varepsilon,m} = \left(\varepsilon_0 |\lambda_1| \rho_1 \frac{J'_m}{J_m} + \varepsilon_1 \lambda_0 \rho_1 \frac{K'_m}{K_m} \right). \qquad (3)$$

In (2) we use the notations

$$\lambda_j^2 = m^2 \omega_0^2 \varepsilon_j / c^2 - k_z^2, \quad j=0,1. \qquad (4)$$

with k_z being the projection of the wave vector on the $z-$axis. For the modes propagating inside the cylinder one has $\lambda_1^2 < 0$. We denote by $k_z = \pm k_{m,s}$, $k_{m,s} > 0$, $s = 1, 2..., s_m$, the solutions to the equation (2) and define

$$\lambda_{m,s} = \rho_1 \sqrt{m^2 \omega_0^2 \varepsilon_0 / c^2 - k_{m,s}^2}, \quad \lambda_{m,s}^{(1)} = \rho_1 \sqrt{k_{m,s}^2 - m^2 \omega_0^2 \varepsilon_1 / c^2}. \qquad (5)$$

The radiation intensity propagating inside the dielectric cylinder can be computed in two different ways. In the first one we evaluate the work done by the radiation field on the charged particle:

$$I = -\int \rho j_\phi E_\phi d\rho d\phi dz, \qquad (6)$$

with E_ϕ being the azimuthal component of electric field. This leads to the result (details can be found in [6])

$$I = \sum_{m=1}^{\infty} I_m = \frac{q^2 v^2}{2\varepsilon_0 \omega_0} \sum_{m=1}^{\infty} \sum_{s=1}^{s_m} \frac{\lambda_{m,s}^{(1)} J_m^{-2}}{m \alpha'_m(k_{m,s}) K_m} \sum_{l=\pm 1} \frac{J_{m+l}(\lambda_{m,s} \rho_0 / \rho_1)}{V_m - lmu} \times$$
$$\sum_{p=\pm 1} J_{m+p}(\lambda_{m,s} \rho_0 / \rho_1) \left[\left(\frac{m^2 \omega_0^2}{c^2} \varepsilon_0 + k_{m,s}^2 \right) \frac{K_{m+p}}{V_m - pmu} - \frac{\lambda_{m,s}^2}{\rho_1^2} \frac{K_{m-p}}{V_m + pmu} \right], \qquad (7)$$

where

$$\alpha_m = \frac{U_m}{(\varepsilon_1 - \varepsilon_0)\left(V_m^2 - m^2u^2\right)}, \quad u = \frac{\lambda_0}{|\lambda_1|} + \frac{|\lambda_1|}{\lambda_0}, \tag{8}$$

with $\lambda_0 = \lambda_{m,s}$ and $|\lambda_1| = \lambda^{(1)}_{m,s}$. In the limit $\rho_1 \to \infty$, from (7) we find the intensity for the synchrotron radiation in a homogeneous medium with dielectric permittivity ε_0. Alternatively, the radiation intensity inside the dielectric cylinder can be obtained by evaluating the energy flux through the cross-section of the dielectric cylinder:

$$I_f^{(in)} = \int_0^{\rho_1} d\rho \int_0^{2\pi} \rho \boldsymbol{n}_z \boldsymbol{S} d\phi \tag{9}$$

where $\boldsymbol{n}_z$ is the unit vector along the $z-$axis and $\boldsymbol{S}$ is the Poynting vector. This leads to the

$$I_f^{(in)} = \sum_{m=1}^{\infty} I_{f,m}^{(in)} = \frac{q^2v^2\rho_1^2}{8\varepsilon_0\omega_0} \sum_{m=1}^{\infty} \sum_{s=1}^{s_m} \frac{k_{m,s}\lambda^{(1)2}_{m,s} J_m^{-4}}{m\alpha_m'^2(k_{m,s})K_m^2} \left[\sum_{l=\pm 1} \frac{J_{m+l}(\lambda_{m,s}\rho_0/\rho_1)}{V_m - lmu} \right]^2 \times$$
$$\sum_{p=\pm 1} \frac{K_{m+p}}{V_m - pmu} \left[\left(\frac{m^2\omega_0^2}{c^2}\varepsilon_0 + k^2_{m,s} \right) \frac{K_{m+p}}{V_m - pmu} - \frac{\lambda^2_{m,s}}{\rho_1^2} \frac{K_{m-p}}{V_m + pmu} \right] \left[J'^2_{m+p} + \left(1 - \frac{(m+p)^2}{\lambda^2_{m,s}} \right) J^2_{m+p} \right]. \tag{10}$$

This formula gives the flux in the region $z > 0$. By the symmetry of the problem we have the same flux in the region $z < 0$ and the total flux will be $2I_f^{(in)}$. Again, it can be seen that in the limit $\rho_1 \to \infty$, from (10) the expression for the radiation intensity in a homogeneous medium is obtained.

In Figure 2, by the black points we present the number of the radiated quanta at a given harmonic m per period of the charge rotation,

$$N_m = \sum_s N_{m,s} = \frac{TI_m}{\hbar m\omega_0}, \quad T = \frac{2\pi}{\omega_0}, \tag{11}$$

for the electron energy $E_e = 2MeV$ and for the values of the parameters $\varepsilon_1 = 1$, $\varepsilon_0 = 3$, $\rho_1/\rho_0 = 1.2$. The red points correspond to the number of the radiated quanta evaluated by the flux through the cylinder cross-section:

$$N_{f,m}^{(in)} = \frac{2TI_{f,m}^{(in)}}{\hbar m\omega_0}. \tag{12}$$

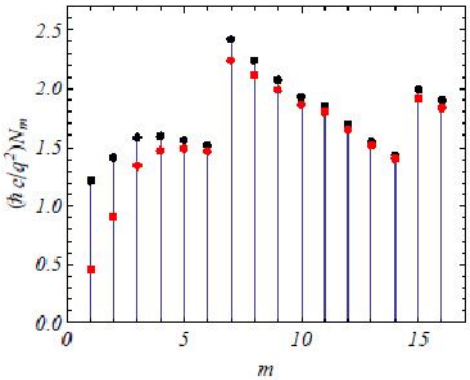

Figure 2: The number of the radiated quanta, per period of the rotation, on a given mode m for the electron energy $E_e = 2MeV$ and for the values of the parameters $\varepsilon_1 = 1$, $\varepsilon_0 = 3$, $\rho_1/\rho_0 = 1.2$. The black/red points correspond to the number of the quanta evaluated by formula (11), (12).

The factor 2 in the last expression corresponds to that we have the same amount of the energy flux in the region $z<0$. The number of the radiated quanta increases with the appearance of new modes. The numerical data in figure 2 show that $N_m \neq N_{f,m}^{(in)}$, i.e., the number of the radiated quanta evaluated by the energy flux through the cross-section of the cylinder and by the work done by the radiation field differ. As it will be shown in the next section, the reason for this difference is that for the eigenmodes of the dielectric cylinder there is also energy flux in the exterior region located near the surface of the cylinder.

3. Radiation intensity outside a cylinder

For a charge rotating inside a dielectric cylinder, in Ref. [2] we have evaluated the average energy flux per unit time through the cylindrical surface of large radius $\rho(\rho >> \rho_1)$ coaxial with the cylinder. The expression for the angular density of the radiation intensity on a given harmonic m with the frequency $m\omega_0$ is given by the expression

$$\frac{dI_m^{(ex)}}{d\theta}=\frac{q^2\nu^2m^2\omega_0^2\sqrt{\varepsilon_1}}{\pi^2c^3\rho_1^2}\sin\theta\left[\left|C_m^{(1)}-C_m^{(-1)}\right|^2+\left|C_m^{(1)}+C_m^{(-1)}\right|^2\cos^2\theta\right], \qquad (13)$$

where we have defined

$$C_m^{(p)}=\frac{J_{m+p}(\lambda_0^{(ex)}\rho_0)}{W_{m+p}^J}+p\lambda_1^{(ex)}H_m(\lambda_1^{(ex)}\rho_1)\frac{J_{m+p}(\lambda_0^{(ex)}\rho_1)}{2\alpha_m W_{m+p}^J}\sum_{l=\pm1}\frac{J_{m+l}(\lambda_0^{(ex)}\rho_0)}{W_{m+l}^J}, \qquad (14)$$

and

$$\lambda_0^{(ex)}=\frac{m\omega_0}{c}\sqrt{\varepsilon_0-\varepsilon_1\cos^2\theta},\quad \lambda_1^{(ex)}=\frac{m\omega_0}{c}\sqrt{\varepsilon_1}\,\sin\theta, \qquad (15)$$

with θ being the angle between the radiation direction and the axis of the cylinder. In (14),

$$W_m^J=\lambda_1^{(ex)}J_m(\lambda_0^{(ex)}\rho_1)H_m^{'}(\lambda_1^{(ex)}\rho_1)-\lambda_0^{(ex)}H_m(\lambda_1^{(ex)}\rho_1)J_m^{'}(\lambda_0^{(ex)}\rho_1). \qquad (16)$$

and $H_m(x)=H_m^{'}(x)$ is the Hankel function of the first kind.

The properties of the radiation corresponding to (13) are described in detail in [2] (see also [4] for a more general case of helical motion inside a dielectric cylinder). In particular, it was shown that under the Cherenkov condition for dielectric permittivity of the cylinder and the velocity of the particle image on the cylinder surface, strong narrow peaks are present in the angular distribution for the number of radiated quanta. At these peaks the radiated energy exceeds the corresponding quantity for a homogeneous medium by several orders of magnitude. The angular density of the number of the quanta radiated in the exterior region per period of the charge rotation is determined by the relation

$$\frac{dN_m^{(ex)}}{d\theta}=\frac{T}{\hbar m\omega_0}\frac{dI_m^{(ex)}}{d\theta}, \qquad (17)$$

with the radiation intensity given by (13).

In addition to the radiation corresponding to (13), in the exterior region there are also radiation fields localized near the surface of the dielectric cylinder. These fields are the tails of the

eigenmodes for the dielectric cylinder and exponentially decay in the exterior region for $\rho/\rho_1 >> 1/\lambda_{m,s}^{(1)}$. For a fixed value of $\rho > \rho_1$ and in the limit $z \to \infty$ the corresponding energy flux through a plane perpendicular to the axis of the cylinder is given by the expression

$$I_f^{(ex)} = \sum_{m=1}^{\infty} I_{f,m}^{(ex)} = \frac{q^2 v^2 \rho_1^2}{8\varepsilon_1 \omega_0} \sum_{m=1}^{\infty} \sum_{s=1}^{s_m} \frac{k_{m,s} \lambda_{m,s}^{(1)2} J_m^{-4}}{m\alpha_m'^2(k_{m,s}) K_m^2} \left[\sum_{l=\pm 1} \frac{J_{m+l}(\lambda_{m,s}\rho_0/\rho_1)}{V_m - lmu} \right]^2 \times$$
$$\sum_{p=\pm 1} \frac{J_{m+p}}{V_m - pmu} \left[\left(\frac{m^2\omega_0^2}{c^2} \varepsilon_1 + k_{m,s}^2 \right) \frac{K_{m+p}}{V_m - pmu} - \frac{\lambda_{m,s}^{(1)2}}{\rho_1^2} \frac{J_{m-p}}{V_m + pmu} \right] \times \qquad (18)$$
$$\left[K'^2_{m+p} - \left(1 + \frac{(m+p)^2}{\lambda_{m,s}^{(1)2}} \right) K_{m+p}^2 \right].$$

Now it can be explicitly checked that

$$I_m = 2(I_{f,m}^{(in)} + I_{f,m}^{(ex)}).$$

In Figure 3 we have plotted the number of the radiated quanta per period of the rotation on a given mode m for different values of m. The values of the parameters are as follows: $E_e = 2MeV$, $\varepsilon_1 = 1,\ \varepsilon_0 = 3,\ \rho_1/\rho_0 = 1.2$. The black points correspond to the radiation in the exterior region at large distances from the cylinder, $N_m^{(ex)} = \int_0^{\pi/2} d\theta (dN_m^{(ex)}/d\theta)$ (see (17)), and the red points are for the radiation on the eigenmodes of the dielectric cylinder, $N_m^{(in)} = \sum_s N_{m,s}$ (see (11)). For the comparison with the synchrotron radiation in the vacuum, in Figure 4, for the same values of the parameters, we plot the total number of the radiated quanta, $N_m = N_m^{(in)} + N_m^{(ex)}$, in the presence (black points) and in the absence (red points) of the dielectric cylinder. As it is seen from these graphs, the presence of the cylinder essentially increases the radiation intensity.

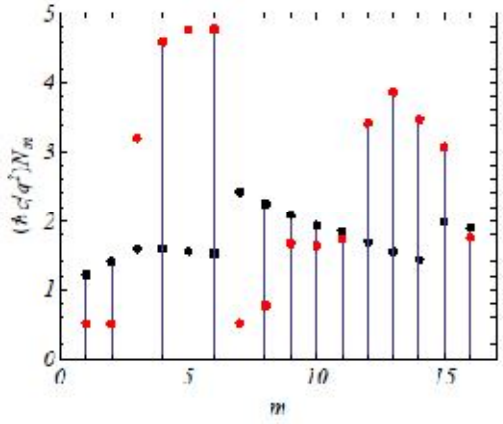

Figure 3: The number of the radiated quanta per period of the rotation on a given mode m for different values of m and for the values of the parameters $E_e = 2MeV$, $\varepsilon_1 = 1,\ \varepsilon_0 = 3,\ \rho_1/\rho_0 = 1.2$. The black points correspond to the radiation in the exterior region and the red points are for the radiation emitted on the eigenmodes of the dielectric cylinder.

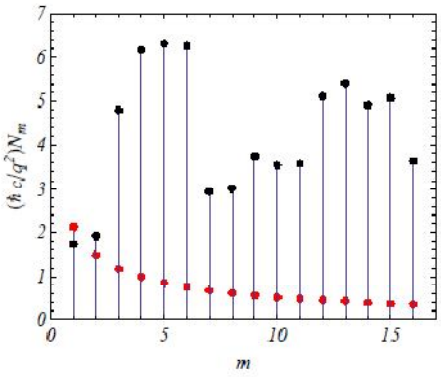

Figure 4: The total number of the radiated quanta, $N_m = N_m^{(in)} + N_m^{(ex)}$, in the presence (black points) and in the absence (red points) of the dielectric cylinder. The values of the parameters are the same as those for Figure 3.

4. Conclusion

We have investigated the synchrotron radiation from a charged particle rotating inside a dielectric cylinder surrounded by a homogeneous medium. Firstly we have evaluated the work done by the radiation field on the charged particle. Further, we have computed the energy flux through the cross-section of the cylinder and it is shown that these quantities differ.

The radiation field in the exterior region consists of two parts. The first one corresponds to the radiation propagating at large distances from the cylinder. The angular density of the corresponding radiation intensity on a given harmonic m is given by formula (13). For large values of m and under the Cherenkov condition for dielectric permittivity of the cylinder and the velocity of the particle image on the cylinder surface, strong narrow peaks appear in the angular distribution for the radiation intensity. The second part of the radiation field in the exterior region corresponds to the modes of the dielectric cylinder. The corresponding fields are located near the surface of the cylinder. These fields exponentially decay at distances from the cylinder surface larger than the radiation wavelength. The energy flux in the exterior region corresponding to the eigenmodes of the cylinder is given by the expression (18). We have explicitly checked that the radiation intensity evaluated by the work done by the radiation field on the charged particle is equal to the radiation intensity evaluated by the energy flux through the plane perpendicular to the cylinder axis if we take into account the contribution of the radiation field in the exterior region.

References

1. Grigoryan L.Sh., Kotanjyan A.S., Saharian A.A., J. Contemp. Phys. **30**, 1 (1995); Kotanjyan A.S., Khachatryan H.F., Petrosyan A.V., Saharian A.A., J. Contemp. Phys. **35,** 1 (2000); Kotanjyan A.S., Saharian A.A., J. Contemp. Phys. **36**, 7 (2001).
2. Kotanjyan A.S., Saharian A.A., J. Contemp. Phys. **37**, 263 (2002).
3. Kotanjyan A.S., Saharian A.A., Mod. Phys. Lett. A **17**, 1323 (2002); Kotanjyan A.S., Nucl. Instrum. Methods **B 201**, 3 (2003).
4. Saharian A.A., Kotanjyan A.S., J. Phys. **A 38,** 4275 (2005).
5. Saharian A.A., Kotanjyan A.S., Grigoryan M.L., J. Phys. **A 40**, 1405 (2007); Saharian A.A., Kotanjyan A.S., J. Phys. **A 40**, 10641 (2007); Arzumanyan S.R., Grigoryan L.Sh., Khachatryan H.F., Kotanjyan A.S., Saharian A.A., Nucl. Instrum. Methods **B 266**, 3703 (2008); Saharian A.A., Kotanjyan A.S., J. Phys. **A 42**, 135402 (2009).
6. Saharian A.A. and Kotanjyan A.S., Int. J. Mod. Phys. **B 26**, 125003 (2012).

Coherent X-Ray Radiation Produced by Microbunched Beams (Invited talk)

K.A. Ispirian

Yerevan Physics Institute, Br. Alikhanian 2, Yerevan, 0036, Armenia

Abstract

A review of the coherent bremsstrahlung (CXBR), X-ray transition (CXTR), resonance transition (CXRTR) and diffraction (CXDR) radiation produced by microbunched beams passing through radiators without the accompanying intense monochromatic beams of X-ray FELs is given. It is discussed the possibility of using these types of radiation for production of additional beams of intense monochromatic X-ray beams and for the study of the parameters of the electron beam microbunching which is important for the effectiveness of X-ray FELs.

1. Introduction

Just as after the proposals and experiments [1-4] the optical transition radiation (OTR) of relativistic particles has found wide application in high-energy particle beam diagnostics, recently following the proposal [5] and experiments [6,7], the coherent optical and softer transition radiation produced by microbunched particles at an interface of two media has found application for the study of particle grouping or microbunching (MB). At the end of the new X-ray FELs [8] (see, also [9]) the femtosecond electron bunches have subattosecond structures due to MB. It has been shown [10] that just as in optical and softer regions, the coherent X-ray transition radiation (CXTR) produced by these microbunched beams is monochromatic with frequency equal to the MB frequency, while the angular and spectral distributions are much narrower than the angular and spectral distributions of not microbunched electron beams. According to [10] CXTR also can be used for FEL diagnostics purposes at X-ray FELs. However, even though there are published a proposal [11] and a preparatory work [12] how one can measure and use CXTR at SLAC, nevertheless, nothing is known about the corresponding experiment.

After the prediction [13] and theoretical and experimental study of the parametric X-ray radiation (PXR) of single charged particles, PXR also has found application for solving various problems and production of monochromatic beams [14]. In the work [15] it has been studied the properties of the bunch coherence of PXR produced by microbunched electron beams as an alternative to CXTR for MB diagnostics. It has been proposed to use coherent X-ray parametric radiation (CXPXR), having the advantage of production under large angles, for the study of the process of MB. At present the existing at LCLS, SLAC beam of 14 GeV electrons microbunched with a period λ=10-0,15 nm as well as the other FELs are sent to dumps.

In Table 1 the main parameters of the electron beams of the existing SLAC LCLS [8] and of other XFELs under construction [9] are given. On the other hand, since the coherent radiation of the microbunched electron beams is monochromatic and proportional to the square of the number, N_b, of electrons in the bunches it can be used for production of intense monochromatic X-ray beams as the monochromatic radiation SASE from long undulators at XFELs. In the past great efforts have been devoted to the construction of small size sources of intense quasimonochromatic X-ray photons. Theoretically it has been shown that in order to have a PXR FEL [14] or a channeling radiation FEL [16] it is necessary to have high, not realistic, density of electron beams of the order

and higher than $\sim 10^9$ A/cm^2. In the works [17,18] it has been shown theoretically that resonance transition radiation (RTR) mechanism is suitable for constructing a RTR FEL.

Table 1. Some parameters of the microbunched electron beams of X FELS.

Parameter	ota- ions	nits	CLS USA)	CSS Japan)	E urXFEL (Germany)	Swi ssFEL (Swi tzerland)
Electron energy		eV	3.6		1 7.5	5.8
Bunch charge		C	.25			
Repetitio n rate		z	0	0	1 0	100- 400
Bunch length (rms)	$.36\sigma_z$	m	-8			
Projected emittance	$\varepsilon_{x,y}$	m	.5-1.6			
Photon wavelength		m	.15	.1	0. 1	0.1

However, at present as it has been mentioned above only the X-ray stimulated SASE radiation, which following the above terminology one can call coherent X-ray undulator radiation, CXUR, produced in long undulators has been detected and found application [8,9].

Let us note that the microbunched electron beams at the end of long undulators of the X-ray FELS are accompanied by intense X-ray photon beams of SASE (CXUR) of XFELs. The production of the below discussed types of coherent radiation do not need in such intense photon accompaniment if one does not consider the processes of stimulated radiation as in [19]. As it has been shown in [20, 21] using complicated magnetic systems one can conserve the MB and obtain pure microbunched beams by deflecting the microbunched the high energy electron beam after the long undulators with the help of especial magnetic systems. Since the required radiators for the production of the new radiation are much shorter than the XFEL undulators it is not necessary to use such magnetic systems if one can neglect the contribution of stimulated radiation. Compared with long (100 m) undulators of XFELs, the radiators of these radiations are very short ((10-100) μm), so that these types of additional beams of monochromatic radiation will be produced if the MB of the beam is not damaged.

Taking into account the above said in this work we shall consider the theory of the spontaneous coherent bremsstrahlung (CXBR), transition (CXTR2), resonance transition (CXRTR), and diffraction radiation (CXDR) produced by a microbunched beam in an amorphous radiator, in a plate with two interfaces, in a stack of layers and when the beam flies close to a slab, respectively.

2. Properties of the Microbunched Beams and Method of Calculations

As it has been mentioned above at the end of the long undulators of XFELs the electron beam initially having chaotic density longitudinal distribution will be grouped or microbunched with period $\lambda_r \approx d_{und}/2\gamma^2$ where d_{und} is the undulator period and $\gamma = E/mc^2 = (1-\beta^2)^{-1/2}$ is the Lorentz factor of the electrons. If the electron pulse with electron number in the bunch has Gaussian transversal and longitudinal density distributions with σ_r and σ_z rms or standard deviations, then the density distribution of the electrons in the microbunched pulse is given by the expression [10]

$$f(r,z) = \frac{N_b}{A}\frac{\exp(-r^2/2\sigma_r^2)}{2\pi\sigma_r^2}\frac{\exp(-z^2/2\sigma_z^2)}{(2\pi)^{1/2}\sigma_z}[1+b_1\cos(k_r,z)], \qquad (1)$$

where N_b is the number of electrons in the pulse, $k_r = 2\pi/\lambda_r$, $A = 1 + 2b_1\exp\left(-k_r^2\sigma_z^2/2\right)$ is a normalization factor, very close to 1 since usually $k_r\sigma_z >> 1$, and $0 \le b_1 \le 1$ is the MB parameter or modulation depth of the first harmonic (the higher harmonics are smaller and neglected). The larger is the value of b_1, the better is the MB and the higher is the radiation yield of the FEL. So that the measurement of b_1 is important for increasing the effectiveness of the XFELs.

The method of the calculation of the angular-spectral distributions of any type of coherent radiation $d^2N_{CXR}/d\omega d\theta$ with the help of known incoherent radiation corresponding distributions $d^2N_{XR}/d\omega d\theta$ of single electrons consists in substitution of $d^2N_{XR}/d\omega d\theta$ into the following formula the derivation of which is given in [22].

$$\frac{d^2N_{CXR}}{d\omega d\theta} \cong N_b^2 F(\omega,\theta)\frac{d^2N_{XR}}{d\omega d\theta} \qquad (2)$$

where [10]

$$F(\omega,\theta) = \exp\left(-(k\sigma_r\sin\theta)^2\right)\left[\exp\left(\frac{-\omega^2\sigma_z^2}{2v^2}\right) + b_1\exp\left(-\left(\frac{\omega}{v}-k_r\right)^2\frac{\sigma_z^2}{2}\right) + b_1\exp\left(-\left(\frac{\omega}{v}+k_r\right)^2\frac{\sigma_z^2}{2}\right)\right]^2, \qquad (3)$$

is the bunch form factor corresponding to the distribution (1), v is the velocity of the electrons and θ is the polar angle of the radiation.

As in the works [5-7,10] in this work to derive $d^2N_{CXR}/(d\omega d\theta)$ we substitute the known expression of the corresponding $d^2N_{XR}/(d\omega d\theta)$ and (3) into (2) and further consider only the intense part of the coherent radiation around $\omega \approx \omega_r$ when the contribution of the first and third terms of (3) is negligible. The coherent radiations obtained in this way 1) have intensity proportional to $(N_b b_1)^2$, 2) very narrow, diffraction-limited spectral distributions, due to the second factor in (3) which rapidly vanishes when ω slightly differs from the microbunched beam resonance frequency, $\omega_r = k_r/c$ and 3) narrower angular distribution around forward direction due to the common factor $\exp\left(-(k\sigma_r\sin\theta)^2\right)$ in (3). The results of theory on coherent X-ray bremsstrahlung are presented in Section 3. Section 4 is devoted to the results on coherent transition radiation including the radiation produced by microbunched beams at single boundary between two

media (subsection 4a), in a slab with two boundaries (subsection 4b) and in a stack of layers (subsection 4c). In Section 5 the results on coherent X-ray diffraction radiation are given. The numerical results on all the types are given in Section 6. Finally in Section 7 a short discussion on the theory and possible experimental setup is given.

3. Coherent Bremsstrahlung Produced by Microbunched Beams (CXBR)

Since the microbunched electrons have GeV energies, and one expects that CXBR will take place in the photon energy interval (1-10) keV corresponding to the MB ω_r of XFELs, for $d^2N_{BR}/(d\omega d\theta)$ it is necessary to use relativistic formulae for bremsstrahlung taking into account the density or medium polarization effect [13,23], the spectral distribution of which as that of the Landau-Pomeranchuk-Migdal effect has been studied in cosmic ray [24] and accelerator experiments [25,26]. In [27] formulae for the necessary $d^2N_{BR}/(d\omega d\theta)$ have been obtained which are very complicated and experimentally not verified, especially, what concerns the angular distribution. For this reason in this first work we shall use more transparent formulae obtained by the method described in [13,23] and [28]. In [28] the corresponding doubly differential cross section is obtained as product of the cross sections of the angular distribution of the Rutherford electron scattering and of the probability of the relativistic quantum mechanical, Born approximation (without screening) spectral distribution (see the formula (15.35) of [28]). Following [28] here using again the Rutherford formula in combination with the probability of the spectral distribution for bremsstrahlung taking into account the density effect (see the formula (15.25) of [13]) one obtains

$$\frac{d^2N_{XBR}}{d\omega d\theta} = \frac{A_{BR}}{A_{norm}} F(y) F1(\omega), \tag{4}$$

where $A_{BR} = 12N_0\bar{\sigma}L_{rad}L$, N_0 is the number of atoms in unit volume of the radiator with thickness L, $\bar{\sigma} = Z^2\alpha r_e^2 = Z^2 5.8x10^{-28}\ cm^2$, Z is the atomic number, $L_{rad} = \ln\{183Z^{-1/3}\}$, A_{norm} =1/3 is determined by the requirement that the integral of (4) over angles must give the spectral distribution of bremsstrahlung taking into account the density effect [13],

$$F(y) = \gamma \frac{y(1+y^4)}{(1+y^2)^4} \quad , \tag{5}$$

$y = \gamma\theta$, $\gamma = E/mc^2 = 1/\sqrt{1-\beta^2}$,

and after introduction $\omega_P = (4\pi N_e e^2/m_e)^{1/2}$, the plasma frequency

$$F1(\omega) = \frac{1}{\omega}\left[\left(\frac{\hbar\omega}{E}\right)^2 + \frac{4}{3}\left(1-\frac{\hbar\omega}{E}\right)\right]\frac{1}{1+\gamma^2(\omega_P/\omega)^2}. \tag{6}$$

Substituting (3) and (4) into (2), considering CXBR in the frequency region neighboring ω_r where the contribution of the first and third terms in (3) is negligible, after introducing the notations

$\tau = \gamma / q_{dif}$, where $q_{dif} = \omega\sigma_r / v$ [10], one can write the spectral-angular distribution of CXBR in the form

$$\frac{d^2 N_{CXBR}}{d\omega d\theta} = 3N_B^2 b_1^2 A_{BR} \exp\left[-\left(q_{dif}\theta\right)^2\right] F(y) F1(\omega) F2(\omega), \tag{7}$$

where,

$$F2(\omega) = \exp\left[-\left(\frac{\omega}{v} - k_r\right)^2 \sigma_z^2\right]. \tag{8}$$

The parameter q_{dif} determines the diffraction limited nature of CXBR since as it is seen from (7) CXBR vanishes when $q_{diff}\theta$ becomes greater than 1.

As in [10] the angular distribution of CXBR photons is obtained by integrating (7) over ω in an interval around ω_r, where we expect coherence enhancement:

$$\frac{dN_{CXBR}}{dy} = N_B^2 b_1^2 C \exp[-(y/\tau)^2] y \frac{1+y^4}{(1+y^2)^4}, \tag{9}$$

where $C = A_{BR} v\sqrt{\pi} F1(\omega_r) / \sigma_z$.

The spectral distribution of CXBR obtained integrating (7) over angles has the form

$$\frac{dN_{CXBR}}{d\omega} = 3N_B^2 b_1^2 A_{BR} D(\tau) F1(\omega) F2(\omega), \tag{10}$$

where

$$D(\tau) = \frac{\tau^2 + 2\tau^4 + 2\tau^6 - \exp(\tau^2)[1 + 3\tau^2(1+\tau^2)]E_1(\tau^{-2})}{6\tau^6}, \tag{11}$$

$E_1(x)$ is integral exponential function. For $\tau << 1$ the expansion of (11) into series gives $D(\tau) \approx \tau^2 / 2$.

The total number of CXBR photons obtained by integration of (9) over θ or of (10) over ω is given by the expression

$$N_{CXBR} = N_B^2 b_1^2 C D(\tau). \tag{12}$$

4. Coherent X-Ray Transition Radiation (CXTR)

4a) CXTR produced at an interface

(The main results of [10] will be given)

Using the formula [29] for XTR produced by a single particle on one interface

$$\frac{d^2N_1}{d\omega d\theta}=\frac{2\alpha\omega_P^4}{\pi\omega^5}\frac{\theta^3}{(\gamma^{-2}+\theta^2)^2(\gamma^{-2}+\theta^2+\omega_P^2/\omega^2)^2}, \qquad (13)$$

and the methods described above and in [10] one obtains for CXTR from one interface

$$\frac{d^2N_{XTR1}}{d\omega d\theta}=\frac{2\alpha N_b^2 b_1^2}{\pi}\frac{\omega_P^4}{\omega^5}\frac{\theta^3}{(\gamma^{-2}+\theta^2)^2(\gamma^{-2}+\theta^2+\omega_P^2/\omega^2)^2}\exp\left[-(\frac{\omega}{v}\sigma_r\theta)^2\right]\exp\left[-(\frac{\omega}{v}-k_r)^2\sigma_z^2\right] \qquad ,(14)$$

$$\frac{dN_{CXTR}}{d\theta}=\frac{4\alpha N_b^2 b_1^2}{\sqrt{\pi}}\frac{v\omega_p^4}{\sigma_z\omega_r^5}\frac{\theta^3}{(\gamma^{-2}+\theta^2)^2(\gamma^{-2}+\theta^2+\omega_P^2/\omega^2)^2}\exp\left[-(\frac{\omega_r}{v}\sigma_r\theta)^2\right]. \qquad (15)$$

For spectral distribution when $\tau<<1$, $\omega_\gamma=\omega/(\gamma\omega_P)<<1$ and $\xi=\omega_P\sigma_r/v>>1$ (These conditions are satisfied for all XFELs) one obtains

$$\frac{dN_{CXTR}}{d\omega}=\frac{\alpha N_B^2 b_1^2\tau^4}{\pi\omega}\exp\left[-\left(\frac{\omega}{v}-k_r\right)^2\sigma_z^2\right]. \qquad (16)$$

And for the total number of photons for CXTR

$$N_{CXTR}\approx\frac{\alpha N_B^2 b_1^2 v}{\sqrt{\pi}\sigma_z\omega_r}\frac{\tau^4}{(1+\omega_\gamma^2)^2}. \qquad (17)$$

4b) CXTR2 produced in a foil with two interfaces

Now using the following formula [29] for XTR produced in a slab with two interfaces and with thickness a

$$\frac{d^2N_2}{d\omega d\theta}=\frac{2\alpha\omega_P^4}{\pi\omega^5}\frac{\theta^3}{(\gamma^{-2}+\theta^2)^2(\gamma^{-2}+\theta^2+\omega_P^2/\omega^2)^2}\sin^2\left[\frac{a\omega}{4v}(\gamma^{-2}+\theta^2+\omega_P^2/\omega^2)\right], \qquad (18)$$

one obtains the following formula for CXTR2

$$\frac{d^2N_{CXTR2}}{d\omega dy}=N_b^2b_1^2\frac{8\alpha\omega_P^4\gamma^4}{\pi}\frac{y^3}{\omega^5}\frac{\sin^2\left[\frac{a}{4}\left(\frac{\omega}{c\gamma^2}\right)\left(1+y^2+(\gamma\omega_P/\omega)^2\right)\right]}{\left(1+y^2\right)^2\left(1+y^2+(\gamma\omega_P/\omega)^2\right)^2}\exp\left[-\left(\frac{\omega}{c\gamma}\sigma_r y\right)^2\right]\times$$
$$\times\exp\left[-\left(\omega-\omega_r\right)^2\left(\frac{\sigma_z}{c}\right)^2\right] \qquad . (19)$$

In (18) and (19) the squares of the sins oscillate rapidly at small variations of ω and y and when the thickness of the slab is much larger than the formation zones of XTR one can take ½ for the squares of the sins. For small angles the expression (19) is two times greater than (14) because no absorption was taken into account. However, if the slab is more than 3 times thicker than the absorption length as it happens in practice then CXTR produced at the first boundary will be absorbed. For this reason no numerical results on the radiation produced in a slab will be given.

4c) CRTR produced in a stack

Now taking $d^2N_X/d\omega d\theta=d^2N_{RTR}/d\omega d\theta$, the spectral-angular distribution of RTR which for a radiator consisting of M pairs of two layers with thicknesses $l_{1,2}$, linear absorbtion coefficients $\mu_{1,2}$ and plasma frequencies $\omega_{p1,2}$ is given by the formula [29,30]

$$\frac{d^2N_{RTR}}{d\omega d\theta} = F_1F_2F_3, \tag{20}$$

where

$$F_1 = \alpha\omega\theta^3(Z_1 - Z_2)^2 / 8\pi c^2,$$
$$F_2 = 1 + \exp(-\mu_1 l_1) - 2\exp(-\mu_1 l_1/2)\cos(2l_1/Z_1),$$
$$F_3 = \frac{1 + \exp(-2M\sigma) - 2\exp(M\sigma)\cos(2MX)}{1 + \exp(-\sigma) - 2\exp(-\sigma/2)\cos(2X)},$$
$$\sigma = \mu_1 l_1 + \mu_2 l_2,$$
$$X = l_1/Z_1 + l_2/Z_2,$$

and

$$Z_{1,2} \approx \frac{4\beta c}{\omega\left[\gamma^{-2} + \left(\omega_{p1,2}/\omega\right)^2 + \theta^2\right]}.$$

are the formation lengths of RTR.

Substituting (20) and (3) into (2) and considering RTR in the region neighboring resonance frequency, $\omega \approx \omega_r$, one obtains the spectral-angular distribution of CXRTR

$$\frac{d^2N_{CXRTR}}{d\omega d\theta} = N_B^2 b_1^2 F_1(\omega,\theta)F_2(\omega,\theta)F_3(\omega,\theta)\exp[-(\omega\sigma_r\theta/v)^2]\exp[-(\omega/v - \omega_r/v)^2\sigma_z^2]. \tag{21}$$

In order to derive angular distribution of CXRTR it is necessary to integrate (21) over ω. As it has been mentioned above and described in details in our work devoted to CXTR [10] the integration over ω of (21) will be carried out in the following way. Since it is expected that a strong enhancement will take place at ω_r over the pedestal of RTR spectral distribution one can draw out all the parts from the integral sign replacing all ω by ω_r considering them as weakly varying, besides the last rapidly varying exponent factor, the integral of which from 0 to infinity gives $v\sqrt{\pi}/2\sigma_z$. In this way one obtains the angular distribution of CXRTR in the form

$$\frac{d\ N_{CXRTR}}{d\theta} = N_B^2 b_1^2 \frac{v\sqrt{\pi}}{2\sigma_z} F_1(\omega_r,\theta)F_2(\omega_r,\theta)F_3(\omega_r,\theta)\exp[-(\omega_r\sigma_r\theta/v)^2]. \tag{22}$$

To obtain the spectral distribution, SD, of CXRTR it is necessary to integrate (21) over θ numerically, since it is impossible to find an analytical expression for the spectral distribution due to the complicated dependences of $F_i(\omega,\theta)$ $(i = 1,2,3)$. Similarly to obtain the total number of the produced CXRTR photons the integration of (22) over ω will be performed numerically. These results will be given and discussed in the Section 6.

5. Coherent X-Ray Diffraction Radiation (CXDR)

For soft photons, say, in the optical region the theory and experiment of diffraction radiation (DR), a phenomena relative to the TR, have been developed many years ago (see [13]). However, in the X-ray region the theory of XDR has been developed only recently [30,31]. To our knowledge there is no XDR experimental result. The interest to X-ray DR and SPR produced by high energy microbunched beams is conditioned by the following facts. First the corresponding beams have very small cross section, which in spite of photon beams can be further reduced by quadrupoles. Second the dangerous distance between the electron beam and radiator edge increases linearly with the increase of γ. Finally in the cases of DR there are no damages of the beam and radiator.

In contrast to TR, before the work [30] DR has not been studied in X-ray region. In [32] on the basis of some considerations given in [13] it has been shown that the XDR can be produced only for

ideal, not existing beams. However, the authors of [30] have shown theoretically that XDR can be produced by usual beams too. However, if XTR intensity decreases sharply after the critical frequency $\omega_{crit}^{XTR} \approx \gamma\omega_P$ proportional to $1/\omega^4$, the critical frequency of XDR is equal to $\omega_{crit}^{XDR} \approx c\gamma/H$, where H is the impact parameter, the minimal distance between the particle trajectory and radiator edge (see the insertion of Fig. 3). According to [30] the intensity of XDR after ω_{crit}^{XDR} decreases sharply, proportionally to $\exp(-2\omega/\omega_{crit}^{XDR})$. If the electron beam cross section is less than 3μm, one can take H=3μm. Assume also that $\hbar\omega_r = 8.3\,keV$, $E = 13.6\,GeV$. Therefore, the decreasing factor $\exp(-2\omega/\omega_{crit}^{XDR})$ is equal to $10^{4.1}$. Remembering that the coherence gives an increase of intensity by a very large factor N_b, one can hope that despite to large intensity decrease it will be possible to detect X-ray CDR.

Let a thin beam of electrons flies at a distance H and perpendicularly to a slab with thickness a , height b and length much more than the characteristic size $\gamma\lambda$ (see the insertion of Fig. 3). According to [30,31] in this case the spectral-angular distribution of XDR intensity is given by the formula

$$\frac{d^2W(\mathbf{n},\omega)}{d\Omega d(\hbar\omega)} = \frac{\alpha}{\pi^2}\left(\frac{\omega_p}{\omega}\right)^4 \frac{\sin^2\left[\frac{a\omega}{4c}\left(\theta^2+\gamma^{-2}+\omega_p^2/\omega^2\right)\right]}{\left(\theta^2+\gamma^{-2}+\omega_p^2/\omega^2\right)^2\left(\theta^2+\gamma^{-2}\right)} \frac{1+2\gamma^2 n_y^2}{1+\gamma^2 n_y^2} \exp\left\{-\frac{2h\omega}{c\gamma}\sqrt{1+\gamma^2 n_y^2}\right\}, \quad (23)$$

where $\rho = \frac{\omega}{c\gamma}\sqrt{1+\gamma^2 n_y^2}$, $\hat{n}$ is a unit vector with projection n_y.

Using this expression for XDR [30] as well as the above described method of calculation of radiation of MB beams one can obtain the following expressions for CXDR angular-spectral distribution

$$\frac{d^2N_{CXDR}}{d\omega dy} = N_b^2 b_1^2 \frac{\alpha\omega_P^4\gamma^4}{\pi}\frac{y}{\omega^5}\frac{\sin^2\left[\frac{a}{4}\left(\frac{\omega}{c\gamma^2}\right)\left(1+y^2+(\gamma\omega_P/\omega)^2\right)\right]}{\left(1+y^2\right)\left(1+y^2+(\gamma\omega_P/\omega)^2\right)^2} F(y,\omega)\exp\left[-\left(\frac{\omega}{c\gamma}\sigma_r y\right)^2\right]\times \quad (24)$$

$$\times\exp\left[-(\omega-\omega_r)^2\left(\frac{\sigma_z}{c}\right)^2\right].$$

where

$$F(y,\omega) = \int_0^{2\pi}\frac{1+2y^2\cos^2\phi}{1+y^2\cos^2\phi}\exp\left[-\frac{2H\omega}{\gamma c}\sqrt{1+y^2\cos^2\phi}\right]d\phi \quad (25)$$

is an integral over the azimuth angle ϕ, which can be calculated only numerically.

The sine square factor in (24) oscillates rapidly with small changes of ω and y and for $\omega \approx \omega_r << \gamma\omega_P$ one can take its mean value 1/2 if $aH\pi^2 >> \gamma\lambda_P^2$ [30], where $\lambda_P = 2\pi c/\omega_P$ is the plasma wavelength.

6. Numerical Results

The below given numerical calculations are made for the following parameters of LCLS [8]; E=13.6 GeV, $\hbar\omega_r = 8.3$ keV, σ_z=9. 10^{-4} cm (FWHM length equal to 2.1 10^{-3} cm or 70 fs), σ_r

=6.12. 10^{-4} cm (this value can be obtained taking the given values of the normalized emittance $\gamma\varepsilon_r = 0.5\,\mu m$ and angular spread $\sigma_{r'} = 1\,\mu rad$), and N_B =1.56x10^9. The radiators for CXTR, CXBR and CXDR are made of Ti with $\hbar\omega_P$=4.16x10^{-2} KeV. In the case of CXTR and CXBR the thickness of the radiator is equal to $L_R = a = 35\,\mu m$, while in the case of CXDR a=35 μm, b=2000 μm and it is taken H=3 μm. The radiator for CXRTR presents a stack of M=268 foils of Be with thickness a=50 μm and distance between each other b=2000 μm.

Figs. 2 and 3 show the angular and spectral distributions of the above considered types of radiation calculated with the help of the above formulae for the above given parameters of LCLS and radiators, respectively.

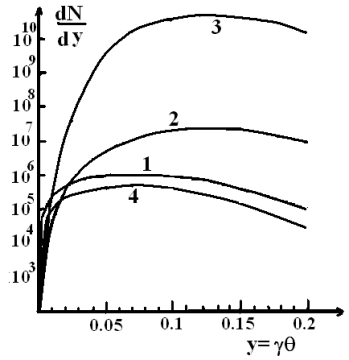

Fig.1. The angular distribution of CXBR, CXTR, CXRTR and CXDR (curves 1,2,3 and 4, respectively).

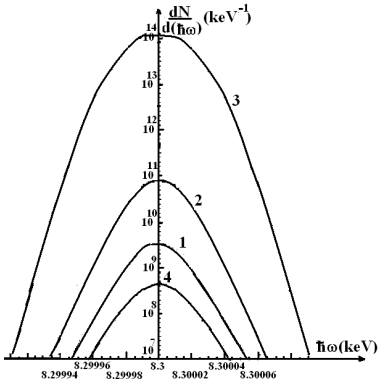

Fig. 2 The spectral distributions of CXBR, CXTR, CXRTR and CXDR (curves 1,2,3 and 4, respectively).

7. Experimental Arrangement and Discussion

The experimental setup shown in Fig. 3 can serve for the study of the above discussed types of radiation. The microbunched electron beam after the ~100 m long undulator of

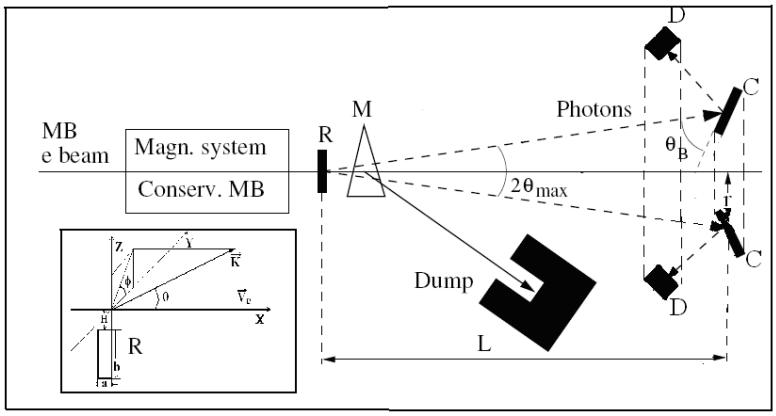

Fig.3. Possible arrangement for study of CXBR , CXTR, CXRTR and CXDR at LCLS.

the XFEL is separated from the XFEL SASE radiation with the help of magnetic system existing at LCLS instead of sending to the dump. Using a new magnetic system conserving MB of the type described in [33,34] the microbunched beam is sent to the radiators R of CXBR , CXTR, CXRTR and CXDR and then after deflecting magnet M it is absorbed in a dump. A part of the radiation produced in radiator emitted around θ_{max} is detected with the help of a Bragg spectrometer with annular conical crystal or a set of crystals. Varying L and/or r, one can choose $\Delta\theta_{opt}$, the optimal angle interval for the radiation type under investigation. Let us note that one can detect these types of radiation also without sending the electron beam in the accompaniment of the XFEL SASE radiation to the radiators R placed close to the end of long undulator when MB is still not spoiled, if the contribution of the XFEL SASE radiation is negligible compared to the CXBR , CXTR, CXRTR and CXDR produced in the radiators placed close to the end of undulator. However, the contribution of the stimulated radiations of electron beam under the influence of accompanying intense XFEL radiation remains unknown until the end of our calculations of these stimulated radiations, similar to the radiation considered in [19].

Finally one comes to the following conclusions. 1) Though many factors, such as multiple scattering, instabilities, etc, were not taken into account, nevertheless, all these types of radiation, especially CXTR and CXRTR, can serve for the study of MB in XFELs, e.g. for measuring the MB parameter b_1 and increasing the XFEL effectiveness. 2) The CXBR background is small while measuring CXTR and CXRTR. 3) For the first time it has been shown that X-ray DR can be observed due to the fact that CXDR is proportional to N_b^2. 4) The calculations have been performed assuming b_1=1. Therefore, even in the case of CXRTR, the total number of the photons N of coherent monochromatic photons is less or equal to the number of photons of the incoherent parametric X-ray radiation (PXR) with production efficiency ~($10^{-6} \div 10^{-5}$). This fact does not mean that coherent radiation is not proportional to N_b^2: The enhancement occurs for a narrow band where the number of photons of usual XTR, BR and DR is much less than . In this connection it is of interest to consider the coherent PXR (CXPXR) of microbunched beams which has been already considered in the work [15] without numerical evaluations. Assuming ~N^2 law one must expect $N_{CXPXR} \sim 10^{13} - 10^{14}$ for a bunch. This is a very high number. That is why we now are studying CXPXR, especially taking into account that it is emitted under large Bragg angles.

References

1. A.I. Alikhanian, K.A. Ispirian, A.G. Oganesian, Zh. Eksp. Teor. Fiz. 56 (1969) 1796.
2. R. Wartski et al, EEEE Trans. Nucl. Sci. NS, 20 (1973) 544.
3. R. Wartski et al, J. Appl. Phys. 46 (1975) 3644.

4. R. Wartski et al, Proc. Intern. Symp. on Transition Radiation of High Energy Particles, Yerevan, Armenia, 1977, p. 561.
5. J. Rosenzweig, G. Travish, A. Treimane, Nucl. Instr. And Meth. A 365, (1955) 255.
6. Y.Liu et al, Phys. Rev. Lett. 80 (1998) 4418.
7. A. Treimane et al, Phys. Rev. Lett. 81 (1988) 5816.
8. P. Emma et al, a) Proc. FEL2009,p 397; b) Nature Photonics, 4, 641, 2010*;* c) LCLS, Design Study Report, 1998 SLAC-R-521.
9. B.D. Patterson et al, New Journal of Physics, 12, 035012, 2010.
10. E.D. Gazazian, K.A. Ispirian, R.K. Ispirian, M.I. Ivanian, Pisma Zh. v Eksp. Teor. Fiz. 70, 664, 1999; Nucl. Instr. And Meth. B173 (2001) 160.
11. A.H. Lumkin, W.M. Fawley, D.W. Rule, Proc. FEL2004, p.515.
12. A.H. Lumkin, J.B. Hastings, D.W. Rule, SLAC-PUB-12451, 200????.
13. M.L. Ter-Mikaelian, The Influence of the Medium on High Energy Processes at High Energies, Publishing House of Academy of Science of Armenia, Yerevan, 1969; High Energy Electromagnetic Processes in Condensed Media, Wiley Interscience, New York, 1972.
14. V.G. Barishevski, I.D. Feranchuk, A.P. Ulyanov, Parametric X-Ray Radiation in Crystals: Theory, Experiments and Application, Springer Tracts in Modern Physics, Heidelberg, 2005.
15. X. Artru, K.A. Ispirian, Proc. NATO Workshop Electron-Photon Interaction in Dense Media,Nor-Hamberd, Yerevan, Armenia 25-29 June, 2001, p, 191: ArXive ph/0208018, 2002.
16. M.A. Kumakhov, Izluchenie kanalirovannikh chastits v kristallakh, Moscow, Energoatomizdat, 1986.
17. M.A. Piestrup, P.F. Finman, IEEE J.Quantum Electron. 19, 357, 1983.
18. M.B. Reid, M.A. Piestrup, IEEE J. Quantum Electron, 27, 2440, 1991.
19. E.G. Bessonov et al, Proc. of the conference CHANNELING2010, to be publ. in Nuovo Cimento; Journ. of Instrumentation, 12, PO510, 2010; ArXiv-1003.3747; ArXiv-1009.3724.
20. Y.Li, W. Decking, B. Faatz and J.Pflueger, Phys. Rev. STAB, 13, 080705, 2010.
21. G. Geloni, V. Kocharyan, E. Saldin, Arxiv 1106.1776, 2011.
22. N.A. Korkhmazian, L.A. Gevorgian, M.P. Petrosian, Zh. Tekh. Fiz. 47, 1583, 1977.
23. M.L. Ter-Mikaelian, Dokladi Akad. Nauk SSSR, 94, 1033, 1954.
24. A.A. Varfolomeev, D.M. Golenko and I.A. Svetlolobov, Dokladi Akad. Nauk SSSR, 122, 785, 1958.
25. F.R. Arutiunian, K.A. Ispirian, A.G. Oganesian and A.A. Frangian, Dokladi Akad. Nauk Arm. SSR, 44, 65, 1967.
26. P.L. Anthony et al, Phys. Rev. Lett. 75, 1949, 1995: S. Klein, Rev. Mod. Phys. 71, 1501, 1999.
27. V.E. Pafomov, Zh. Eksp. Teor. Fioz. 49, 1222, 1965; Trudi FIAN v.44 p. 28,1969.
28. J.D. Jackson, Classical Electrodynamics, John Wiley & Sons, Inc, New York, 1998 (Third edition).
29. G.M. Garibian, Y.Shi, Rentgenovskoe Perekhodnoe Izluchenie, Publ. House of NAS of Armenian Republic, Yerevan, 1983 (in Russian).
30. A.A. Tishchenko, A.P. Potilitsin, M.N. Strikhanov. Phys. Rev. E, 70, 088501 (2004).
31. A.P. Potilitsin, M.I. Ryazanov, M.N. Strikhanov, A.A. Tishchenko, Diffraction Radiation from Relativistic Particles. Springer tracts in modern physics, v. 239, 2010.
32. M.J. Moran. Phys. Rev. Lett., 69, 2523 (1992).
33. Y.Li, W. Decking, B. Faatz and J.Pflueger, Phys. Rev. STAB, 13, 080705, 2010.
34. G. Geloni, V. Kocharyan, E. Saldin, Arxiv 1106.1776, 2011.

Proposal on Unruh Radiation Experiment with the Help of X-Ray Photon Beams from XFELs

K.A. Ispirian, M.K. Ispiryan

Yerevan Physics Institute, Br. Alikhanian 2, Yerevan, 0036, Armenia

Abstract

Using the collision between the already available SASE X-ray photons of XFELs and relatively not very high electrons it is shown that at present one can study the production of entangled photon pairs in order to test the concepts of the Unruh effect and corresponding radiation.

1. Introduction

1a. Unruh effect (UE)

According to quantum field theory, general relativity with curved coordinates [1,2] in its instantaneous rest frame every body (or particle), undergoing acceleration a', is immersed in a «thermal bath» of Planckian photons with a temperature

$$T_U = \frac{\hbar a'}{2\pi kc}. \tag{1}$$

1b. Unruh and Hawking radiation (UR, HR)

The interaction (say, Compton scattering) of these photons with an accelerated Unruh detector (say an electron) should result in the laboratory frame of the observation in production of the so-called Unruh radiation, UR, [2] which is a relative to the Hawking radiation, HR, [3] of black holes with mass M having a temperature at the surface (or at Schwarzschild radius $R_S=2GM/c^2$) equal to

$$T_H = \frac{\hbar c^3}{8\pi kGM} \Rightarrow \frac{\hbar g}{2\pi kc} \tag{2}$$

(One can obtain formally (1) from (2) by substituting a' instead of g).

1c. Larmor Radiation (LR)

According to Larmor mechanism of the classical field theory (J.D. Jackson, 3-th Ed., or L.D. Landau, M.E. Lifshits, Field Theory) a charge e undergoing acceleration $\vec{a}$ radiates power

$$P^L = \frac{2}{3}\frac{e^2}{c^3}a^2 \Rightarrow 5.7x10^{-51}a^2 \qquad \text{(in CGSE)} \tag{3}$$

If $\gamma = E/mc^2 = 1/\sqrt{1-\beta^2} >> 1$ then

For $\vec{v} \coprod \vec{a}$ the angular distribution of this Larmor radiation, LR, has the form

$$\frac{dP_{II}}{d\Omega} \approx \frac{8e^2a^2\gamma^8}{\pi c^3}\frac{(\gamma\theta)^2}{(1+\gamma^2\theta^2)^5} \tag{4}$$

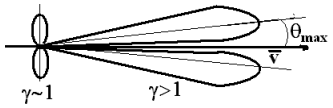

For $\vec{v} \perp \vec{a}$

$$\frac{dP_{\perp}^{L}}{d\Omega} \approx \frac{2}{3}\frac{e^2a^2}{c^3}\gamma^6\frac{1}{(1+\gamma^2\theta^2)^3}\left[1-\frac{4\gamma^2\theta^2\cos^2\phi}{(1+\gamma^2\theta^2)^2}\right] \qquad (5)$$

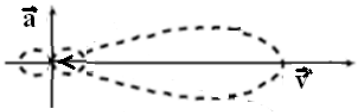

1d. Comparison of UR and LR

As one can understand the UR in IRF arises due to absorption an emission of a thermal bath photon by Unruh detector (or due to scattering on electron). In LF following [5] one can roughly estimate UR power.

$$P^{Un} = \int \frac{dP_{Pl}}{cd\nu}\sigma_{Th}d\nu = \frac{\hbar r_0}{90\pi c^6}a^4 \Rightarrow 4.1x10^{-118}a^4 \quad (in\ \ CGSE). \qquad (6)$$

Therefore, Unruh and Larmor radiation powers become equal to each other for $a_{eq} \sim 3x10^{33}$ cm/s^2 ~$3x10^{30}$g. If a_{eq} is achieved by E_{eq} then $E_{eq} \sim 2x10^{17}$ V/cm >> $E_{cr} \sim m^2c^3/2\pi eh \sim 1.3x10^{16}$ V/cm.

Here we shall not discuss theoretical problems of Unruh effect (see [6,7] and references therein).

1e. More accurate interpretation of UR [2,4,8-10]

According to [2,4] due to UR two photons, γ_1 and γ_2, are produced (see Fig. 1) with opposite momenta and polarizations. For some processes the second "idler" photon can be neglected. As it has been shown in [8-10] the quantum numbers of these photon pairs can be entangled.

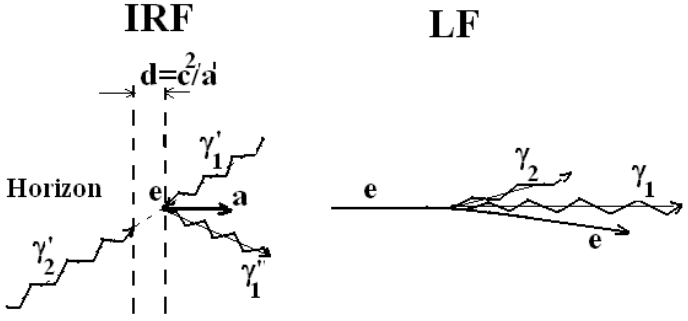

Fig.1

For some processes the second «idler photon can be neglected. Further without discussing the explanations [11-13] "and observation" [14] of UE and omitting proposed low energy and other type experiments (see [6,7]) we shall discuss only proposed experiments with high energy electrons for «testing» the UE.

1f. High Energy Experimental Proposals

According to modern theoretical approaches (see the review [7]) to UE, it «does not need experimental confirmation any more than free Quantum Field Theory does». Nevertheless, having no, say, accurate contribution of radiation reaction, etc, it is of interest to observe experimentally the difference between the predictions of modern theories, say, QED, as background, and those predicted for some processes taking into account UE.

Table. 1 Proposals on production of UR and LR by high energy electrons.

	Processes	Reactions	References
	Channeling radiation	e+cryst→ e+cryst+	S.M.Darbinian et al, Preprint YerPhI 1188(65)-88, 1989 [15]
	Magnetic and laser fields	e+H→e+H+ γ, e+(LB) →e+(LB)+γ	S.M.Darbinian et al, Pisma JETP 51,97,1990 [16]
	$e^+ e^-$ pair production colliders	e+Bunch→ e+Bunch+e^++e^-	S.M.Darbinian et al, Pisma JETP 54,235,1991 [17]
	Laser standing waves	e+(SW) → e+(SW)+ γ	P.Chen, T.Tajima, PRL, 83,256,1999 [18]
	Coherent X-ray beam	e+X-Photon → e+ γ	P.Chen,Workshop LCLS,1999 [19]
	2 LB with circular polarization	e+(2LB) → e+(2LB)+ γ	G.Brodin et al, Class. Quantum Gravitation, 25,45005, 2008 [20]
	LB or X-ray photons with production of 2 entangled photons	e+ħω →e+γ_1+ γ_2	R. Schutzhold et al, PRL 97, 121302, 2006: 100, 091301, 2008: P. Thirolf et al, Eur. Phys. J. D55, 379, 2009 [8-10]

It is worthy to discuss briefly the experiments 5 and 7, the schemes of which are shown below.

a) Experiment 5. It is proposed [19] to detect the UR photon produced due to the scattering of SASE X-ray photons with λ=2.5 A^o on 14 GeV electron beam. For SASE beam power P=20 GW one obtains a=6.10^{26} m/s^2, E=3.3x10^{13} V/cm, KT=200 eV . According to [19] The signal to noise ratio, SNR, is $P_{UR}/P_{LR} = (\hbar\omega/mc^2)\eta\ln(\eta/\pi)$, i.e. is proportional to λ^{-1}, giving a 10^4 gain for LCLS X-ray photons compared to optical photons. For realistic values of the parameters of the beams SNR=10^{-4}. Therefore, it is necessary to use angular discrimination in order to improve SNR. Without discussing technical and theoretical problems (It is not taken into account that the electron and SASE beams are microbunched) let us only note that since the scattering angle is very small it will be difficult to carry out the angular discrimination and coincidence the UR scattered photons.

b) Experiment 7a. It is proposed (see Fig. 5 of [10]) to detect the coincidence and polarization of the 2 produced entangled photons emitted in a cone with opening angle ~0.1^o in collision of 300

MeV electrons with laser photons with $\hbar\omega_L = 2.5\,eV$. Following [10] let us note that the main difficulty is connected with the smallness of the scattering angle.

c) Experiment 7b. It is proposed (see Fig. 6 of [10]) to detect the coincidence and polarization of the produced 2 entangled photons emitted in a cone with opening angle ~15^o in the collision of 300 MeV electron beam with X-ray beam with photon number in a bunch equal to 10^{13}, produced with the method of reflection of laser photons from a relativistic mirror. Let us only

note that, probably, the main difficulty is connected with the production and focusing of intense 20 keV photon beam by the still not sufficiently studied method of relativistic mirror [21].

1) Theoretical results on entangled and not entangled photon pair production in collision of electron-photon beams

It has been carried out nonlinear QED calculations for production of Unruh entangled photon pairs assuming $\eta<1$ for a'=const in [8] and for periodic a' perpendicular to $\vec{v}$ in [9]. In IRF for the Unruh $\gamma\gamma$-pair $k'_1+k'_2=\omega'=2\gamma\omega_L<<m$ (Thomson), while for Larmor 1 photon $k'=\omega'=\gamma\omega_L$.

According to [9] the probabilities of production of an Unruh entangled photon pair and a Larmor photon by an electron are equal to

$$P_U^{\gamma\gamma} = \frac{\alpha^2}{4\pi}\left[\frac{E_{\text{int}}}{E_{cr}}\right]^2 O\left(\frac{\omega T}{30}\right), \qquad P_L^{\gamma} = \alpha\left[\frac{eE_{\text{int}}}{m\omega}\right]^2 O\left(\frac{\omega T}{2}\right) \qquad (7)$$

In these expressions $E_{\text{int}} = 2\gamma E_{lab}$ is the electrical field of the photon beam in IRF.

The authors of [9,10] give the 3D dependence of the Unruh (entangled $\gamma\gamma$) pair and Larmor (γ) single photon production upon ω_1 and θ_1 in collision of a 150 MeV electron with laser photon pulse with $\hbar\omega_L$ =2.5 eV, $I=10^{18}$ W/cm^2 and length equal to 100 wavelength. Unfortunately, the cross sections are given only qualitatively without giving the values of the colors and the expression with the help of which one can calculate, say, similar results.

2. The Parameters of the Proposed Experiment

In this work it is proposed (see Fig. 2) to detect the coincidence and polarization of 2 produced entangled photons emitted in a cone with opening angle $\sim 1/\gamma$ in collision of 2.5 MeV ($\gamma \approx 5$) electrons with XFEL photons with energy $\hbar\omega_L = 8\ keV$. Let us note that the main advantage of this proposal is connected, as in the experiment 7b [10], with the large entangled photon production angles, as well as the availability of the electron [22] and X-ray beams [23].

As it is schematically shown in Fig. 2 the 14 GeV, ~100 fs electron pulses with particle number $N=1.6\text{x}10^9$ pass the ~100 m long undulator of the SLAC LCLS and after producing 8.3 keV SASE monochromatic X-ray beam with $N_\gamma=2.\text{x}10^{12}$ per bunch are deflected by the magnet M to a dump [23]. The produced X-ray photons with energy 1.5 mJ per pulse and peak power $P=2.66\text{x}10^{10}$W [23] are focused with the help of Snigirev lenses to a waist diameter ~1μm (S ~10^{-8} cm^2) at the interaction point IP. According to [24] it is possible to focus the LCLS SASE beam to focuses less than 1μm, however taking the difficulties connected with the SASE beam position

instabilities as well as with the focusing of 2.5 MeV electron beam. Therefore, the LF photon beam intensity is equal to $I = P/S$ =2.66x10^{18} W/cm^2. while the

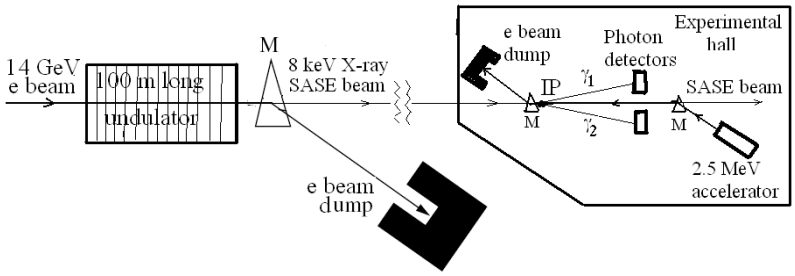

Fig. 2. Schematical view of the experimental setup in which 2.5 MeV electrons collide with SASE coherent X-ray photons with $\hbar\omega_L = 8\,keV$ after the deflection of 14 GeV electron beam.

electric field in the laser is equal to $E_{LF}(V/cm) \approx 20\sqrt{I(W/cm^2)}$ =3.26x10^{10} V/cm = 3.26x10^{12}V/m and $E_{ERF} = E_{\text{int}} = 2\gamma E_{LF} = 9.16\text{x}10^{14}$ V/cm=3.26x10^{13} V/m.

As in the case of [10] it is assumed that with the help of a Ge strip Compton polarimeter-spectrometer of the type of that already constructed and described in [25] it will be carried out the following discriminations: 1) angular discrimination between LR and UR photons, 2) coincidence 3) polarization and 4) energy measurement between the Unruh entangled photons.

3. Results and Discussion

Now using the formulae (7) one can calculate the probabilities $P_{\gamma\gamma}^U$ and P_{γ}^L of emitting an Unruh entangled photon pair and a Larmor photon by an electron. The results are given in the 8-th and 9-th columns of the third row of the Table 2 in which the parameters and results of the first and second experiments (Fig. 5 and 6 of the work [10], respectively) proposed in [10] are also given for comparison.

Table 2. Some parameters and the probability (per electron) of the production of one UR 2 entangled photons and LR one photon for the setups of Figs 5 and 6 of [10] and Fig.3 of this work (rows 2, 3 and 4, respectively).

γ/ unch	kin MeV)	I_{LF} (W/cm^2)	$\hbar\omega_L$ (keV)	$\hbar\omega_{IRF}$ (keV)	E_{LF} (V/m)	E_{IRF} (V/m)	P_U	P_L
						1		

$x10^{15}$	50	$1.x10^{18}$	.0025	1.5	$1.9x10^{12}$	$.2x10^{15}$	$.x10^{-11}$	$.x10^{-1}$
0^{13}	1	$2.x10^{25}$	20	80	$8.7x10^{15}$	$.5x10^{16}$ 3		
$x10^{12}$	2.5	$.7x10^{18}$ 2	8.3	83	$3.3x10^{12}$	$.3x10^{13}$ 3	$.1x10^{-10}$	$.1x10^{-4}$

As it follows from Table 3 for the case c) $SNR=P_U/P_L=10^{-6}$ is better than for the case a). Therefore, taking into account that the emission angles of the entangled photons are large, of the order of the not realistic case b), and using the above described discriminations the number of the detected events per electron-laser collision will be sufficient to carry out the experiment c). Indeed, having 100 pC charge per 2.5 MeV electron bunch [22] colliding with LCLS SASE photons with 8.3 keV photon number per bunch $\sim 2x10^{12}$ and with frequency 30 Hz [23] one expects ~0.3 entangled photon pair production per second which is sufficient for collecting reasonable number of events with enough statistics.

The expected results will be important since "Understanding the structure of the quantum vacuum is one of the key challenges of contemporary fundamental physics, since theoretical efforts to describe the observed energy density of the vacuum amounting to 5 GeV/m^3 drastically fail by 10^{124} microscopic approach via string theory) and 10^{-121} (via cosmological considerations), respectively". In more details one can find the discussion of the recent theoretical and experimental problems connected with possibility of study of Unruh radiation with the help of the high energy electrons and photon beams in [26].

References

1. W. Unruh, Phys. Rev, D14, 870, 1976.
2. W.G.Unruh, R.M.Wald, Phys. Rev. D29, 1047,1984.
3. S. Hawking, Nature, 248, 30, 1974; Commun. Math. Phys. 43, 199, 1975.
4. Ya.B. Zeldovich, L.V. Rojinskii, A.A. Starobinskii, Pisma Zh. Eksp. Teor. Fiz. 43, 407, 1986.
5. K.T. McDonald, Princeton preprint DOE/ER/3072-38, 1986.
6. H.C. Rosu, Gravitation Cosm. 7, 1, 2001; Arxiv:gr-qc, 9406012, 2001.
7. L.C.B. Crispino, A. Higuchi, G.E.A. Matsas, Rev. Mod. Phys.80, 787, 2008.
8. R. Schutzhold, G. Schaller, D. Habs, Phys.Rev. Lett. 97, 121302, 2006.
9. R. Schutzhold, G. Schaller, D. Habs, Phys.Rev. Lett. 100, 091301, 2008.
10. P.G. Thirolf et al, Eur. Phys. J. D 55, 379, 2009.
11. J. Bell, J.M. Leinaas, Nucl. Phys. B212, 131, 1983 (Spin).
12. S.Barshay, W. Troost, Phys. Lett. B73, 437, 1978 (Strong interactions).
13. K.A. Ispirian, A.T. Margarian, Yad. Fiz. 54, 600, 1991 (Quarks UR).
14. I.I. Smolyaninov, ArXiv Cond. Matt./0510743, 2008 (Fs IR Photoluminescence of a tips).
15. S.M. Darbinian, K.A. Ispirian, A.T. Margarian, Preprint YerPhI-1188(65)-89, 1989.
16. S.M. Darbinian, K.A. Ispirian, M.K. Ispirian, A.T. Margarian, Pisma Zh. Eksp. Teor. Fiz.51, 97, 1990.
17. S.M. Darbinian, K.A. Ispirian, M.K. Ispirian, A.T. Margarian, Pisma Zh. Eksp. Teor. Fiz. 54,235, 1991.

18. P. Chen, T. Tajima, Phys. Rev. Lett. 83, 256, 1999.
19. P.Chen,Workshop LCLS,1999 (unpublished).
20. G.Brodin, M.Marklund, R.Bingham, R.G.Evans Class. Quantum Grav. 25, 145005, 2008.
21. D. Habs et al, Appl. Phys. Let. B 93, 349, 2008.
22. H. Wiedemann et al, Phys. Rev. Lett.73, 967, 1994; J. Nucl. Mater. 248, 374, 1997; NATO Science Series, Math. Phys. Chem, v. 49, p. 320, Kluwer Publ. Dordrecht, 2002.
23. P. Emma et al, a) Proc. FEL2009, p 397; b) Nature Photonics, 4, 641, 2010.
24. A. Snigirev, I. Snigireva, Proc. of the Intern. Conf. on Electron, Positron, Neutron and X-Ray Scattering under External Influences, Yerevan-Megri, Armenia, October 2009. Publisher Institute of Applied Problems of Physics, Yerevan, 2010. p. 137.
25. T. Stohlker, J. of Phys. Conf. Series, 58, 411, 2007.
26. K.A. Ispirian, invited talk to QEDSP 2011, Kharkov, August 29-September, To be published in Problems of Atomic Science and Technology in 2012.

Defining of the Marginal State of a Quantum System at Its Conditionally Cyclic Evolution

Karayan H. S.

Yerevan State University

Summary

Quantum cyclic conditional dynamics of a coherently correlated combined system of three cubits is considered. A principle of forming of the cycle repetition for finding of the marginal state vector that is presented through a unitary transformation is offered. The expression of the iteration operation is found and the corresponding quantum scheme is made up that carries out the iteration for finding the marginal state vector.

Introduction

Classically correlated combined physical systems have been widely used for associative and parallel information handling and calculation and for physical modeling. In particular, the only way of creating an artificial intellect has been based on the use of such systems – which have been also called *neuron nets* [1-2].

But the classically correlated combined physical systems can be used to carry out the polynomial algorithms only, and to create an artificial intellect it is necessary much higher efficiency of information handling.

It was shown in many papers (see [3-6] and references in them) that the coherently correlated combined quantum systems are at least exponentially able to increase the efficiency of information handling.

Now a new and more complicated problem is actual, namely, the *non-formal* ***simulation*** *(not imitation) of intellect and thinking*. But if it is necessary that a physical system could "think" (i.e. it could make up an algorithm of its action on its own, and not to operate under the algorithms externally input into the system) it must carry out such logic algebra, which is not narrower than the non-distributive quantum logic algebra that is inherent to quantum systems and most probably only to them (for as Feynman put [3, 4], all natural processes take place according to the quantum logic).

At least one of the ways of solution of the mentioned problems is connected with combining the possibilities of classical neuroinformatics with quantum informatics, i.e. it is connected to creation of quantum neuroinformatics, but such combination is not trivial owing to incompatibility of the methods of classical neuroinformatics with those of quantum dynamics of a closed system.

One possible way of carrying this out was offered in [7] where a formal principle was chosen for such combination. One of the central problems is the non-formal definition of the marginal state of the quantum system at its conditionally cyclic evolution, and the aim of the present paper is this.

Description of the Quantum Iteration Layout

We consider embedding of a cyclic process of the conditionally tunable iteration of knowledge formation. To create conditions for repetition of each iteration cycle the following operations must be carried out.

Comparison of the physical system state with its state in the previous cycle or with some given state (the expert state.)

Taking into account the comparison results, to form the conditions of varying of the system dynamics through the feedback.

Creating the conditionally tuning iteration operator. Creating an operator of projecting to project the physical system state vector into the "knowledge codes" subspace.

To carry out these tasks it is only necessary to carry out the programme operators through the induced algorithm, for the state of the physical system can be known at any moment [1-2]. Iteration is going on as far as the established state is found, or some condition of proximity of the two output (or exit) states is established. The output state of the macroscopic system is described by the values of the characteristic parameters, and the mentioned proximity means the proximity (or coincidence) of these characteristic values. It is to be mentioned that this procedure is not physically reciprocal (reversible) and, generally, it is not connected with the physical system properties. The physical system is only responsible for the efficiency (performance speed, energy waste, reliability, stability, etc.) of carrying out the mathematical operations, according to the programme.

This way is not applicable to the quantum tunable systems. First, the difficulties are connected with the fact it is impossible to know the state of a quantum system without violating it or its coherence.

This prevents the use of the classical methods of comparison of different states through their proximity and, consequently, prevents formation of the dynamics variation conditions [7]. Moreover, the comparison is to be carried out through the unitary operations to provide physical (and then mathematical, as well) reciprocity. Finally, the notion of the state proximity itself becomes non-trivial in the quantum case. A quantum state is presented by a function (an infinite dimensional vector) in the complex unitary functional space, and it is impossible to establish equality or proximity of two states through one (or more but of finite number) numerical values, without an essential loss of information. In contrast to the classical case, one can hardly define a convenient unitary operation for comparison of the quantum states without applying to the properties of the physical system.

A good candidate for this aim can serve the coherently correlated combined quantum system, particularly, the system of three cubits. The basis in the space of states of the coherently correlated combined quantum system of a few cubits, Ai, is formed through the tensor product of the bases of all cubits. If the coefficients of two superpositions coincide in the same basis in the mentioned space of states of the combined system, $\mathcal{H}_{\text{к}}$, then these superpositions present the same state of the system to within the global phase. This well-known fact [8-11] makes possible to compare the quantum states' components (i.e. compare their numerical values) through unitary operations in the given basis.

Then, in $\mathcal{H}_{\text{к}}$, it is easy unitarily produce comparison of the quantum states through the separate cubits. Indeed, $\mathcal{H}_{\text{к}}$ includes spaces of all states of all cubits, and the space, $\mathcal{H}_{\otimes \text{A}_\text{i}}$, includes the tensor products of all states of all cubits. Besides, $\mathcal{H}_{\text{к}}$ includes the space $\mathcal{H}_{\text{e}}$, of all entangled states, which are absent in $\mathcal{H}_{\otimes \text{A}_\text{i}}$, and have no classic analogue and carry no information of the states of two and more cubits, that is:

$\mathcal{H}_{\text{к}} \equiv \otimes_{\text{i}} \mathcal{H}_{\text{i}} = \mathcal{H}_{\otimes \text{A}_\text{i}} \oplus \mathcal{H}_{\text{e}}$.

The last condition is the base of the unitary operation of the logic scheme, "if…, then; if…, then…," and the comparison operation of the quantum states is led to the latter with further formation of the condition of the iteration cycle for the cycle number displacement operator, $\widehat{\text{T}}_{\text{n}}(\text{U})$ presented in Fig. 1, where $|\psi_{\text{n}}(0)\rangle$ and $|\psi_{\text{n}}(\tau)\rangle$ are the initial and evolved states of the n-th cycle, $\psi_{\text{e}}\rangle$ is the state of the expert cubit (of the "teacher").

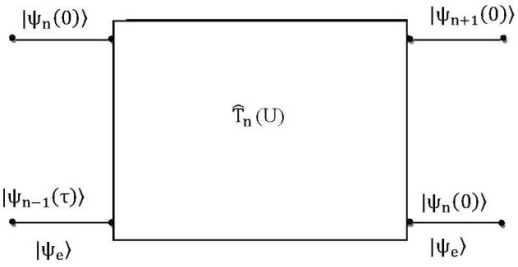

Fig. 1

Let $\hat{C}_N$ be the operator, *conditional NOT* (*controlled NOT*), and $\Delta_{ab} \equiv ||a\rangle - |b\rangle|$ is the symmetric difference of the basis states, $|a\rangle$ *and* $|b\rangle$. Then, according to the identity, $\hat{C}_N \begin{pmatrix} |a\rangle \\ |b\rangle \end{pmatrix} \equiv \begin{pmatrix} |a\rangle \\ \Delta_{ab} \end{pmatrix}$, the condition of repetition of the iteration cycle can be formed through the symmetric difference as follows:

$\Delta_n \equiv \left||\psi_n(\tau)\rangle - |\psi_{n-1}(\tau)\rangle\right|$ (or $\Delta_n \equiv \left||\psi_n(\tau)\rangle - |\psi_e\rangle\right|$, if there is an expert state).

Indeed, if the cubit with the state, Δ_n , is used as controlling, the transformation of the similarity, $\hat{C}_N\ \Delta_n \hat{C}_N$, will not change the states of the two participating cubits (because $\hat{C}_N$is a self-converting operator). But the cubit, Δ_n, can intermediately carry out controlling (Fig. 2), combining with the third cubit to carry out conditional operations. In particular, usingΔ_n, we form the operator, $\hat{U}_\varphi$, which displaces the phase of the controlled cubit by the angle φ , if the cubit with Δ_n is in the state $|1\rangle$ (for instance, with eigen value 1); Otherwise, it does not change the state of the third cubit. The quantum sketch of the operator, $\hat{T}_n$, for the n-th iteration cycle is presented in Fig. 2.

Here the operators, $\hat{1}$, $\hat{U}_\tau$, $\hat{S}_w$ and $\hat{I}$, are the operators of: identical operator, the evolution of the

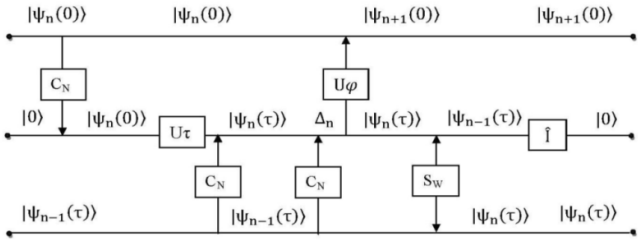

Fig. 2

cubit, change of the states of cubits, and the initialization, respectively (operations in the figure are carried out from the left).

If Δ_n=0 for some number, n_{marg}, then Δ_n=0 for all $n \geq n_{marg}$ and the corresponding state is the marginal state, $|\psi_{marg}\rangle$. In this case, $\hat{T}_n$ becomes and stays an identical operator. Then, if $n \geq n_{marg}$, the whole iteration process is presented through the following operator:

$$\hat{T}_{it}=\hat{1}\ \hat{1}\ldots..\hat{T}_{n_{marg}}\ \hat{T}_{n_{marg}-1}\ \ldots\hat{T}_2\ \hat{T}_1 \equiv \left(\hat{T}\right)^{n\geq n_{marg}}, \qquad (1)$$

i.e. the structures of the operators, $\hat{T}_n$, of all cycles are the same and are denoted by $\hat{T}$:

$$\hat{T} \equiv \hat{I}(2)\,\hat{S}_w(2,3)\,\hat{C}_N(3,2)\,\hat{U}_\varphi(2,1)\,\hat{C}_N(3,2)\,\hat{U}_\tau(2)\,\hat{C}_N(1,2). \qquad (2)$$

Here to avoid the matrix writing form the cubit number is written in the brackets of each operator on which the operator acts and, for the binary operators, the first number is for the controlling cubit and the second is that for the controlled one.

For the given coherently correlated combined system of cubits in expressions (1) and (2) and in Fig. 2, all the operators can be principally physically carried out through establishing of the operator, $\widehat{U}_{\varphi}$, and the unitary phase convertor operator as well (the latter is the logic negation) [3-7]. Physically, the binary operator, $\widehat{U}_{\varphi}$, is carried out through the tunable conditional dynamics of the closed system of two (and more) coherently correlated cubits.

From the application point of view, it is expedient to carry out each operator in (2), as well as the Adhemar operator that transforms the basis states into the equi-probable ones, independently and optimally. Physical and mathematical methods worked out at present (see [3-6, 8-15] and references in them) compose a complete foundation for this aim.

Discussion 1

The marginal state considered above can be trivial or it can have no existence, which means that there is no new information (knowledge). Existence of the marginal state is equivalent to the convergence of the iteration process. Besides the existence of n_{marg}, it is necessary that the iteration process be finite. In this case for the given finite values of n_{marg}, the above quantum sketch and formulas (1) and (2) make possible to find the marginal state and the unitary operator corresponding it and, consequently, the dynamics of the quantum system, after n_{marg} steps. Moreover, this algorithm can be strengthened (i.e. the convergence speed can be increased) if we combine the Grover algorithm through the quantum oracle [4, 5]. These lead to the desired marginal state after $\sqrt{n_{marg}}$ steps.

But the above algorithm does not contain either an indication for establishing the existence of the marginal state, or for finding the value of n_{marg}. This narrows the region of application of the algorithm and decreases the efficiency of looking for the marginal state. The probability of finding of the marginal state can be increased if the phase, φ, in the operator, $\widehat{U}_{\varphi}$, is varied chaotically, but this does not exhaust the problem of finding the n_{marg}.

It seems that the most consistent way of handling the problem is widening the algorithm of the marginal state to its invariance. In short, an algorithm is necessary, which led to the nearest state of the marginal one after the steps of the given number, N, independent of the existence of the marginal state and its convergence character. In its turn, to do these it is necessary to "widen" the size of the proximity of the quantum states based on the identity: $\hat{C}_N \begin{pmatrix} |a\rangle \\ |b\rangle \end{pmatrix} \equiv \begin{pmatrix} |a\rangle \\ \Delta_{ab} \end{pmatrix}$. And to do this one has to generalize the $\hat{C}_N$ and Δ_{ab}. For instance, let the operator, $\hat{C}_N$, be replaced for $\widehat{K}_N$, which converts the phase of the state $|b\rangle$ when the eigen values of the states, $|a\rangle$ and $|1\rangle$ differ by a non zero δ. This means that we use a " δ-worn on" entangled state, $|a\rangle$, with the state, $|b\rangle$, instead of the "naked" entangled states of the operators, $|a\rangle$ и $|b\rangle$, from the sub-space, $\mathcal{H}_e$.

Mathematically, it is equivalent to replacing $\mathcal{H}_e$ by some of its non-orthogonal " δ-worn on" extension, and this can be done, but the author does not know at the moment an appropriate quantum system for establishing the operator, $\widehat{K}_N$, physically.

References

1. Osovski S. A. – *Neuron Circuits For Information Handling* (in Russian), Moscow, Finacies and Statistics, 2002. p.344.
2. Kruglov, V. V., Borisov V. V. – *Artificial neuron circuits* (in Russian), 2002, p 388.

3. Feynman R. Ph. –Quantum Mechanical computers, Foundation of Phys. 1986, vol. 16, № 6, pp. 507-531.
4. Feynman R. Simulating Physics with Computers// Inter. Jour. Theor. Phys. 1982, vol. 21, # 6/7, pp. 467-488.
5. Valiev K. A., Kokin A. A. – *Quantum Computers: Hopes and Reality* // Regular and Chaotic Dynamics (in Russian), Izhevsk, 2001. p. 352.
6. Deutsch D. Quantum Computational networks // Proc. R. Soc. Lond.,-1985, vol. A425, - pp.73-90.
7. Karayan H. S. – *On Quantum neuron Computation* (in Russian), Izv. NAS RA, series Tech. S. vol. LX, Iss. IV, 2007. pp. 608-615.
8. Di Vincenzo – *Quantum Computation,* Regular and Chaotic Dynamics (in Russian), Izhevsk, 1999. pp. 35-55.
9. Fridman J.R., Patel V., Chen W., Tolpygo S.K., Lurens J.E. Quantum Superposition of Distinct Makroscopic States//Nature, 2000, v. 406, 6 July, pp 43-46.
10. M. A. Nielsen, I.L. Chuang, Quantum Computation and Quantum Information, Cambridge Universiti Press, 2000, 2001.
11. Shor P. In Proc. of the 35 the Ann. Synp. Of the Foundations of Computer Sci// (Ed. S. Goldvasser), Los Alamitos, CA., IEEE Computer Society, 1994, p.124.
12. Openov L. A. Resoant Elektron Transfer between Quantum Dots//Phys. Rev. 1999, v. B60, #12, pp 8798-8803.
13. Burkard G., Loss D., DiVincezo D. Coupled Quantum Dots as Quantum Gates// Phys. Rev. 1999, v. B59, pp 2070-2078.
14. Molotkov S. N., Nazin S.S. Single-Electron Computing: Quantum Dot Logic Gates// ЖЭТФ, 1996, т. 110, вып. 4(10), pp. 1439-1452.
15. Valiev K. A., Kokin A. A. – The semiconductor NMR Quantum Computers with Individual and assembly Conduct of Cubits, Microelectronika, 1999, vol. 28, No 5, pp 326-337.

Cholesteric Liquid Crystals with Isotropic Defect Inside

A. H. Gevorgyan[1,2], M. Z. Harutyunyan[1], K. B. Oganesyan[3], E. M. Harutyunyan[2], S. O. Harutyunyan[2]

[1]*Department of Physics, Yerevan State University, 1, Str. Al. Manoogian, Armenia, 025 Yerevan, E-mail: agevorgyan@.ysu.am*
[2]*Institute of Applied Problems of Physics, Academy of Sciences of Armenia, 014 Yerevan, Armenia*
[3]*Yerevan Physics Institute, Alikhanyan Br.2, 036, Yerevan, Armenia*

The peculiarities of the defect modes of cholesteric liquid crystals (CLCs) with an isotropic defect inside are investigated. The influence of the defect layer thickness and the system thickness and of the defect layer position in the system, as well as the influence of the dielectric borders on the defect modes are investigated. It is shown that it is possible to change the reflection at the defect modes in wide intervals and change the defect mode wavelength, through tuning the defect location and its thickness. Such a system possesses transmission asymmetry. Also, the CLC system thickness and the refraction coefficient of the medium (bordering the CLC layer on its both sides) have essential influence on the reflection at the defect mode and on the reflection frequency.

Key Words: Cholesteric liquid crystals, defect modes, diffraction, photonic band gap, tunable reflection.

I. Introduction

In recent years, considerable interest has been attracted to the photonic crystals (PCs) [1-4], which are a special class of artificial and self organizing structures with periodic changes of spatial dielectric properties in the scale of optical order of wavelength. Such media are also called *media with photonic band-gap* (PBG), since there is a zone of frequency in their transmission spectra, where light undergoes diffraction reflection on their periodical structure.

The interest in PCs is conditioned both by their interesting physical properties and wide practical applications. As these structures are designed artificially or in a self assembled manner, they can be prepared with given properties, which lead to many challenging problems of theoretical and applied character. The optical elements constructed on the basis of PCs result in intelligent, multifunctional tunable optics, which possess such favorable traits, such as their compactness, small losses, high reliability and compatibility with other devices.

Cholesteric liquid crystals (CLCs) are the most important representatives among the one dimensional (1D) chiral PCs, because they can spontaneously self organize their periodic structure and their PBG (that exists only for circularly polarized light with the same handedness of the CLC helix), and they can be easily tuned over wide frequency intervals.

Recently, CLCs have drawn great interest to them due to their possibility of low-threshold laser generation at the edges of their PBG. Dowling et al. predicted [5] lasing at the band edge of photonic band gap materials based on the argument that light slows down near the band edge and due to it a spontaneous emission would be enhanced. The Dowling mechanism of lasing only applies to infinite or very long systems.

In [6], it was discovered that CLCs are photonic band gap materials. In the same work it was discovered the lasing in finite systems, such as CLCs, where the lasing occurs in specific modes, which have very different lifetimes depending on how close they are to the band edge, and this gives the selectivity of lasing in long lived modes. And it should be noted that it is not the light with a low velocity that is involved, but essentially, the standing waves associated with standing

resonances. Vigorous investigations in this area have been going on up to now (see [7] and references cited therein).

Besides, recently the CLC having various types of defects have been considered from the point of view of generating additional resonance modes in them and of investigating the possibilities of low-threshold laser generation at these modes. It is to be noted that CLCs with a defect in their structure possess a number of peculiarities, which the isotropic 1D PCs lack (see below). Recently, CLCs with an anisotropic (isotropic) defect were considered [8-25].

In this paper, we investigated (by numerical simulations) some new peculiarities of the defect modes in the CLC with an isotropic defect and found out different features of such system. To investigate the influence of the dielectric borders, we study two cases: a) the system is sandwiched between the two half-infinite isotropic spaces with the refractive indices, n_s, equal to the CLC average refractive index given by $\overline{n} = \sqrt{\left(n_o^2 + n_e^2\right)/2}$ ($n_o = \sqrt{\varepsilon_1}$ and $n_e = \sqrt{\varepsilon_2}$ are the ordinary and extraordinary refractive indices of the local anisotropic structure; in this case the dielectric borders influence is minimum) and $\alpha = \overline{n}/n_s = 1$; and b) the system is in the vacuum and $\alpha = \overline{n}$.

II. The method of analysis

The problem is solved by Ambartsumian's layer addition modified method [13, 19] adjusted to solution of such problems. A ***CLC layer*** with a defect can be treated as a multi-layer system: ***CLC(1)-Defect Layer (DL)-CLC(2***.

According to Ambartsumian's layer addition modified method, if there is a system consisting of two adjacent (from left to right) layers, A and B, then the reflection transmission matrices of the system, $A+B$, viz. $\hat{R}_{A+B}$ and $\hat{T}_{A+B}$, are determined in terms of similar matrices of its component layers by the matrix equations:

$$\hat{R}_{A+B} = \hat{R}_A + \tilde{\hat{T}}_A \hat{R}_B \left[\hat{I} - \tilde{\hat{R}}_A \hat{R}_B\right]^{-1} \hat{T}_A,$$
$$\hat{T}_{A+B} = \hat{T}_B \left[\hat{I} - \tilde{\hat{R}}_A \hat{R}_B\right]^{-1} \hat{T}_A, \qquad (1)$$

where the tilde denotes the corresponding reflection and transmission matrices for the reverse direction of light propagation, and $\hat{I}$ is the unit matrix. The exact reflection and transmission matrices for a finite ***CLC layer*** (at normal incidence) and the defect (isotropic) layer are well known [26, 27]. First, we attach the ***DL*** to the ***CLC Layer (2)*** from the left side, using the matrix Eqs (1). In the second stage, we attach the ***CLC Layer (1)*** to the obtained ***DL-CLC Layer (2)*** system.

III. Results and discussion

We investigate reflection (transmission) spectra for either orthogonal linear or orthogonal circular polarizations. The refractive index of the ***DL*** is taken to be $n^d = 1.7$. The ordinary and extraordinary refractive indices of the ***CLC layer*** are taken to be $n_o = 1.4639$ and $n_e = 1.5133$, the ***CLC layer*** helix is right handed and its pitch is: p = 0.42 μm. These are the parameters of the ***CLC cholesteryl-nonanoate–cholesteryl chloride–cholesteryl acetate*** (20 : 15 : 6) composition, again at the temperature $T = 25^{\circ}$C. So, the light normally incident onto a single ***CLC layer*** – with the right circular polarization (RCP) – has a PBG, and the light with the left circular polarization (LCP) does not.

Below we investigate the effects of defect thicknesses and defect locations in the system on the reflection.

Fig. 1 shows the wavelength dependences of the reflectance *R*, in the presence of an isotropic defect in the mid-plane of the CLC layer. The light incident on the system is right-handed (the solid line) and left-handed (the dashed line) circularly polarized. As can be seen in Fig. 1, the presence of the defect in the CLC structure leads to the occurrence of defect modes in the PBG (indicated by an arrow). It manifests itself in the form of a hole in the reflection spectrum (in the PBG) for the light with the RCP, and in the form of a peak in the reflection spectrum for the light with the LCP. The defect mode has either donor or acceptor character, depending on the optical thickness of the defect layer.

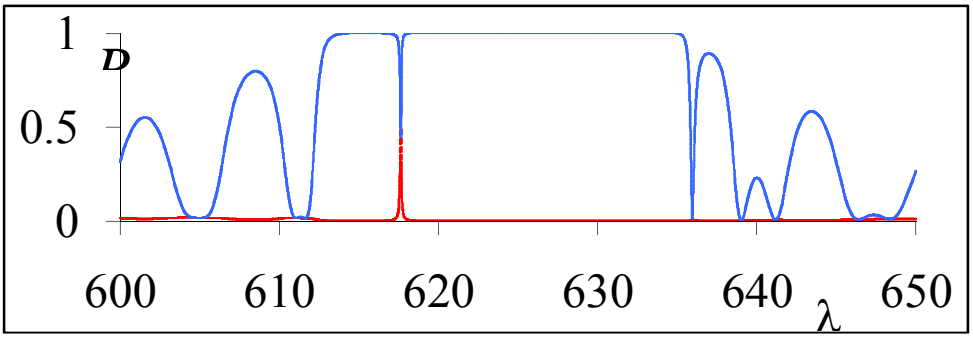

Fig. 1. The Spectra of reflectance for a CLC layer with an isotropic defect in the midplane. Light incident on system is right_handed (solid line) or left_handed (dashed line) circularly polarized. CLC helix is right_handed. CLC thickness d = 70p, defect_layer thickness d^d = 1.86 μm, and refractive index of the medium around $n_s = \bar{n} + 0.1$ system.

In Fig. 2 the density plot of the reflection spectra as a function of the ***DL*** thicknesses are presented. Incident light has the LCP (a), and the RCP (b). The defect mode wavelength increases from a minimum to a maximum band gap value if the defect layer optical thickness increases, and at the borders of the PBG two defect modes appear, then the longer wavelength mode leaves the PBG and the shorter wavelength mode moves into the PBG, as the defect layer thickness increases further. The reflection/transmission coefficient changes with oscillations (at the defect mode) if the defect layer thickness increases. The defect mode for the light with the LCP is absent. I it is natural, because the ***CLC*** with a defect in its structure is a micro-resonator, and one needs multi-reflections to arouse defect modes.

In Fig. 3a we present the 3D plots of the reflectance coefficient, *R,* on the wavelength, λ, and on the reduced distance between the ***CLC*** right border and the ***DL*** (on *d/p,* where *d* is the distance between the ***CLC*** right border and the ***DL***); and in Fig. 3b the transmittance coefficient, *T,* on λ and on *d/p* are presented. The incident light has the LCP (a) and RCP (b). The defect is an isotropic one, and $\alpha = \bar{n}/n_s = \bar{n}$ that is $n_s = 1$. It is seen from Fig. 3, that if the defect layer goes near the system center, the PBG is significantly widened. If the defect layer is nearby the ***CLC*** borders, the defect modes practically do not appear, and the reflection is practically the same as for the case when there is no defect. The reflection at the defect mode increases for the light with the RCP if the defect shifts to the system center. However, there is an asymmetry in respect to the distance from the ***CLC*** left or right border, i.e. the system possesses structural non-reciprocity and can be used as an all-optical diode if there is absorption (or gain). Thus, the defect location change in the system has

essential influence on reflection, as well as on the other optical parameters at the defect mode. Some change of the defect mode wavelength takes place, too.

As our calculations show, practically the same dependences are observed in the case of the structure with a thin anisotropic defect layer.

The change of the index, n_s, of the medium surrounding the system on its both sides has essential influence on the system reflection and the reflection at the defect modes. In Fig. 4 the dependences of the reflection coefficient, R, on the wavelength, λ, and on n_s are presented. The incident light has the LCP (a) and the RCP (b). The defect is isotropic. As it is seen from the figure, the increase of the n_s leads to strong reflection both inside and outside the PBG, as well as at the defect mode. This change is especially strong for the LCP light. The increase in $|\overline{n} - n_s|$ also leads to a change in frequency of the defect mode in a significant interval. For an anisotropic defect and at $\overline{n} = n_s$, the defect mode for the LCP light is absent, and it is natural, because a ***CLC*** with a defect in its structure is a micro-resonator, and one needs multi-reflections to arouse defect modes. As our calculations show, practically the same dependences are observed in the case of the anisotropic layer defect. In this case, the defect mode exists at $\overline{n} = n_s$, as well.

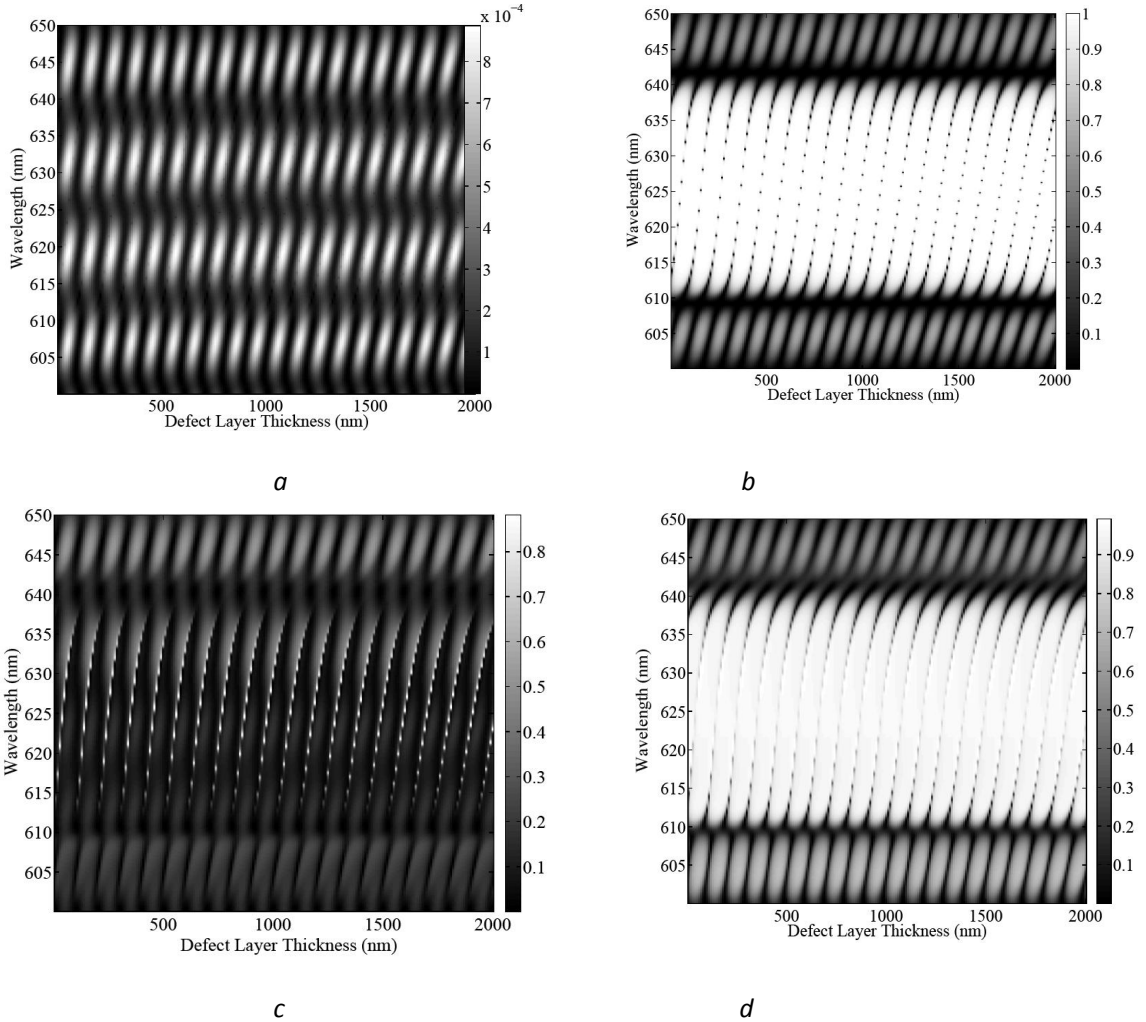

Fig. 2. The density plot of the reflection spectra as a function of defect layer thicknesses. The incident light is of the LCP (a, c) and RCP (b, d). $\alpha = 1$ (a,b) and $\alpha = \overline{n}$ (c, d). CLC layer thickness: d=50p.

As it is mentioned earlier, the defect mode for the LCP incident wave reveals itself in the form of a peak in the reflection spectrum inside the PBG, but that for the RCP substantially reveals itself in the form of a hole in the reflection spectrum. Additionally, both polarizations have practically the same wavelength and the same reflection coefficient at the center of the peaks. As it is shown in [22], for the case of a small ***CLC*** thickness the defect mode with the RCP is strongly excited, and it vanishes in the case of very large ***CLC*** thicknesses. The case for a defect mode with the LCP behaves the other way round; it is excited very little for small thicknesses, and appears very strongly at large thicknesses. In the case of the intermediate thicknesses they are excited almost equally. Let as note that an analogous behavior is observed for the ***CLC*** with a twist defect [28]. Here we present the results of a more detailed analysis of the behavior of the defect mode of various thicknesses in the ***CLC*** layer. In Fig. 5a we present plots of the reflectance coefficient, *R,* on the wavelength, λ, and on the reduced thickness of the ***CLC*** layer (on *d/p,* where *d* is the ***CLC*** layer thickness); and in Fig. 5b the transmittance coefficient, *T*, on λ and on *d/p* are presented. The incident light has the LCP (a), and the RCP (b). The defect is anisotropic. The same regularities are also observed for isotropic defects.

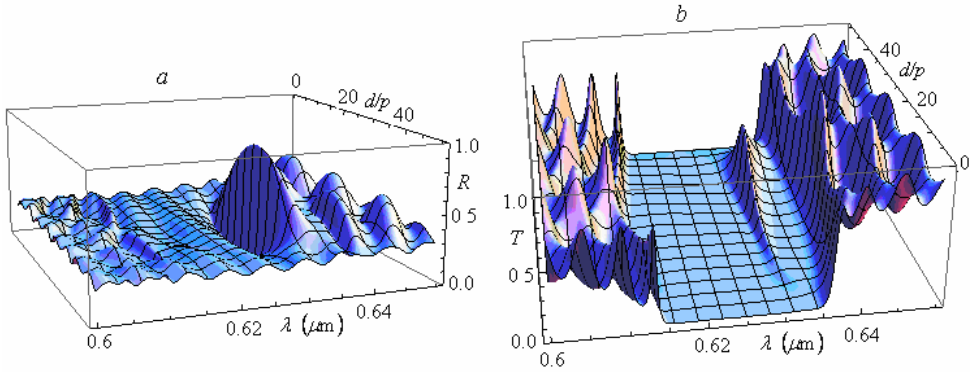

Fig. 3. The 3D plots of the reflection coefficient, R, (a) and the transmission coefficient, T, (b) on the wavelength, λ, and on the reduced distance between the CLC right border and the defect layer (on d/p, where d is the distance between the CLC right border and the DL). The incident light is of the LCP (a) and RCP (b). The defect is isotropic with the thickness: $d^d = 0.1\mu m$, and $\alpha = 1$. CLC layer thickness: d=50p.

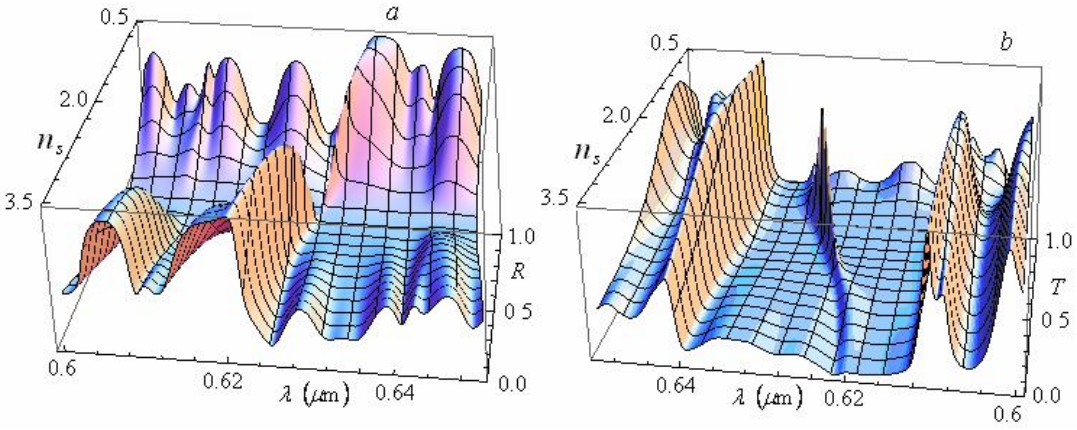

Fig. 4. (Color online). The 3D plots of the reflection coefficient, R, (a) and the transmission coefficient, T, (b) on the wavelength, λ, and on ns. The incident light is of the LCP (a) and RCP (b). The defect is isotropic with the thickness: $d^d = 0.1\mu m$. CLC layer thickness: d=50p.

IV. Conclusion

We showed that, in contrast to the anisotropic defect case, if the defect thickness changes, the changes of the defect mode half-widths become insignificant for the isotropic defect. This can enable strong light accumulation and low-threshold laser radiation at the defect mode for comparatively larger defect layer thicknesses, which can easier be carried out experimentally than for a thinner defect.

Indeed, as it is well known, the ***CLC*** doped with laser dyes (resonance molecules) can be used for designing feedback lasers without any mirror use. In an amplifying media (for instance, in ***CLCs*** doped with fluorescent guest-molecules, but in the way that the fluorescent peak is either in the PBG, or covers it), the PBG has significant influence on the radiation spectrum. The wave is evanescent (decreases exponentially) in the PBG and, consequently, the spontaneous radiation vanishes. The explanation is that the photonic density of states (PDS) vanishes and, as the spontaneous radiation intensity is proportional to PDS, the spontaneous radiation intensity also vanishes. At the PBG borders, the spontaneous radiation life time, τ_s, sharply increases (τ_s decreases oscillating outside it) and makes the stimulated radiation strongly go up. Laser generation threshold energy essentially decreases, and the radiation essentially increases. And, as the ***CLC*** helix pitch can be changed, as well as tuned, a possibility of the laser radiation wavelength tuning arises, which can have most important practical significances. Yablonovitch has predicted that a low-threshold lasing will occur at the defect modes inside the band gap of PCs, too, since the excitation energy is not drained by spontaneous emission into the modes other than the lasing mode [29]. Lasing is further facilitated at the wavelength of the defect mode since the photon dwelling time is enhanced, giving ample opportunity for amplification by the stimulated emission.

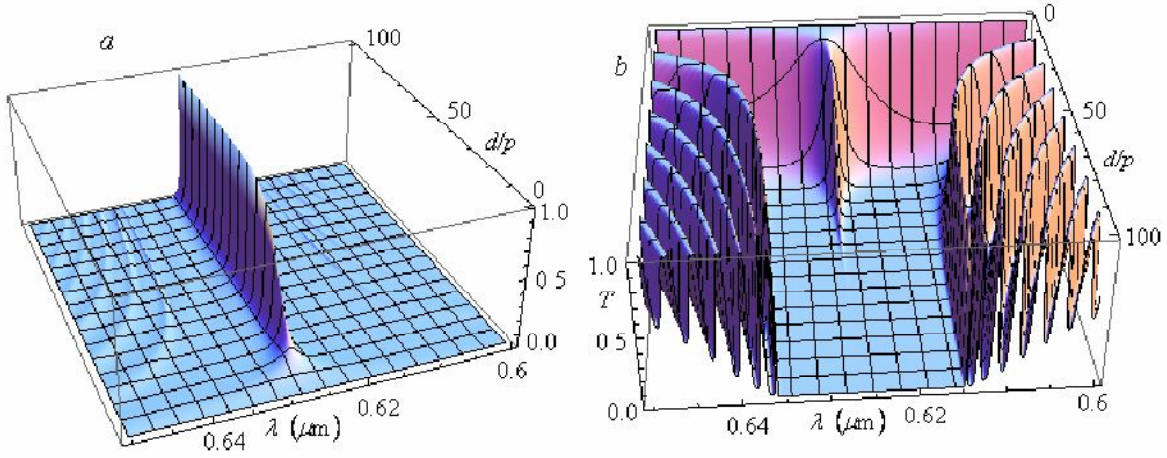

Fig. 5. The 3D plots of the reflection coefficient, R, (a) and the transmission coefficient, T, (b) on the wavelength, λ, and on the reduced thickness of the CLC layer (on d/p, where d is the CLC layer thickness). The incident light is of the LCP (a) and RCP (b). The defect is anisotropic with the thickness: $d^d = 0.1\mu m$. $\alpha = 1$.

We showed that the change of the refraction coefficient of the medium bordering the system on both sides leads to a significant change of the reflection at the defect mode, as well as to a defect mode wavelength change in a significant wavelength interval.

Also, let us note that the results obtained in this paper can be used for designing: narrow-band filters and mirrors, optical diodes, etc.

References

1. J. Joannopoulos, R. Meade, J. Winn. Photonic Crystals, Princeton: Princeton Univ. (1995).
2. K. Sakoda Optical Properties of Photonic Crystals, Berlin: Springer (2001).
3. S. G. Johnson, J. Joannopoulos. Photonic Crystals: The Road from Theory to Practice, Boston: Kluwer (2002).
4. Soukoulis, C. M. (Ed.). Photonic Crystals and Light Localization in the 21st Century. NATO Science Series C: Vol. 563. 2001, 616 p.
5. Dowling J. P., Scalora M., Bloemer M.J., Bowden C. M. The photonic band edge laser: a new approach to gain enhancement. *J. Appl. Phys.,* **75**, 1896-1899 (1994).
6. V. I. Kopp, B. Fan, H. K. M. Vithana, and A. Z. Genack. Low-threshold lasing at the edge of a photonic stop band in cholesteric liquid crystals. Opt. Lett. **23**, 1707-1709 (1998).
7. M-Y. Jeong, J. W. Wu. Continuous spatial tuning of laser emission with tuning resolution less than 1 nm in a wedge cell of dye-doped cholesteric liquid crystals. Opt. Express. **18**, 24221-24228 (2010).
8. Y.-C. Yang, Ch.-S. Kee, J.-E. Kim, and H.Y. Park. Photonic defect modes in cholesteric liquid crystals. *Phys. Rev. E.* **60**, 6852-6854 (1999).
9. V. I. Kopp, A. Z. Genack. Twist defect in chiral photonic structures. *Phys. Rev. Lett.* **89**, 033901-4 (2002).
10. I. J. Hodgkinson, Q. h. Wu, M. Arnold, M. McCall, A. Lakhtakia. Chiral mirror and optical resonator designs for circularly polarized light: suppression of cross-polarized reflectances and transmittances. *Opt. Commun.* **210**, 201-211 (2002).
11. J. Schmidtke, W. Stille. Photonic defect modes in cholesteric liquid crystal films. Eur. Phys. J. E. **12**, 553-564 (2003).
12. I. J. Hodgkinson, Q. h. Wu, L. De Silva, M. Arnold, M. McCall, A. Lakhtakia. Supermodes of chiral photonic filters with combined twist and layer defects. *Phys. Rev. Lett.,* **91**, 223903-4 (2003).
13. A. H. Gevorgyan, A. Kocharian, G.A. Vardanyan, Accumulation and Transmission of the Light Energy in Nonreciprocal Multilayer Systems. *Opt. Commun.,* **259**, 455-564 (2006).
14. J. Schmidtke, W. Stille, H. Finkelmann. Defect Mode Emission of a Dye Doped Cholesteric Polymer Network. Phys. Rev. Lett. **90**, 083902-4 (2003).
15. M. Becchi, S. Ponti, J. A. Reyes, C Oldano. Defect modes in helical photonic crystals: An analytic approach. *Phys. Rev. B.* **70**, 033103 (2004).
16. T. Matsui, M. Ozaki, K. Yoshino. Tunable photonic defect modes in a cholesteric liquid crystal induced by optical deformation of helix. *Phys.Rev.E.* **69,** 061715-4 (2004).
17. M. H. Song , N. Y. Ha, K. Amemiya, B. Park, Y. Takanishi, K. Ishikawa, J. W. Wu, S. Nishimura, T. Toyooka, H. Takazoe. Defect-Mode Lasing with Lowered Threshold in a Three-Layered Hetero-Cholesteric Liquid-Crystal Structure *Adv. Mater.* **18**, 193-197 (2006).
18. A. H. Gevorgyan. The Loss of the Polarization Dependence of Diffraction Reflection in Chiral Photonic Crystals in the Presence of Anisotropic Defects. *Tech. Phys. Lett.*, **32**, 698 (2006).
19. A. H. Gevorgyan, M. Z. Harutyunyan. Chiral photonic crystals with an anisotropic defect layer. *Phys. Rev. E.* **76**, 031701-9 (2007).
20. A. H. Gevorgyan, K. B. Oganesyan, E. M. Harutyunyan, S. O. Arutyunyan. The peculiarities of radiation of chiral photonic crystals with isotropic defect layer. *Opt. Communn.* **283**, 3707-3713 (2010).
21. A. H. Gevorgyan. Chiral photonic crystals with anisotropic defect layer. Oblique incidence. *Opt. Commun.*, **281**, 5097-5103 (2008).
22. A. H. Gevorgyan, and M. Z. Harutyunyan. Tuning of Emission Wavelength in Chiral Photonic Crystals with an Anisotropic Defect Layer. *J. Mod. Opt.,* **56**, 1163-1173(2009).

23. F. Wang, A. Lakhtakia. Defect modes in multisection helical photonic crystals. *Opt. Express*., **13**, 7319-7335 (2005).
24. C. J. Avendaño, S. Ponti, J. A. Reyes, C. Oldano. Multiplet structure of the defect modes in 1D helical photonic crystals with twist defects. . *J. Phys. A: Math. Gen.,* **38**, 8821-8840 (2005).
25. A. H.Gevorgyan. Tunable reflectance of a two-defect-layer cholesteric liquid crystal. Phys. Rev. E., **83,** 011702(1-12) (2011).
26. A. H. Gevorgyan. Reflection and Transmission of Light for a Layer with Dielectric and Magnetic Helicities. I. Jones Matrices. Natural Polarizations. *Opt. Spectrosc*., **89**, 631-638 (2000).
27. H. Wohler, M. Fritsch, G. Hass, D. A. Mlynski. Characteristic matrix method for stratified anisotropic media: optical properties of special configurations *J. Opt. Soc. Am. A*, **8**, 536-540 (1991).
28. F. Wang, A. Lakhtakia. Specular and nonspecular, thickness-dependent, spectral holes in a slanted chiral sculptured thin film with a central twist defect. *Opt. Commun.*, **215,** 79–92 (2003).
29. E. Yablonovitch. Inhibited spontaneous emission in solid-state physics and electronics. *Phys. Rev. Lett.* **58**, 2059-2062 (1987).

Nanoobject Sizes of Defects in Porous Systems and Defective Materials According Adap Method

Y A Chaplygin[1], V.I.Grafutin[2], O.V.Ilyukhina[2], G.G.Myasischeva[2], E.P.Prokopev[2], S.P.Timoshenkov[1], G.I..Savelev[2], Yu.V.Funtikov[2]

[1]Moscow state institute of electronic technology (MIET), Zelenograd, pas. 4806, bld. 5, 124498, Moscow, Russia
[2]Alikhanov Institute for Theoretical and Experimental Physics (ITEP), B.Cheremushkinskaya street 25, 117218 Moscow, Russia

Abstracts. - It is shown, that positrons effectively probe free nanoobject volumes (basically vacancies, divacancies and pores) with the sizes ≤ 1-10 nm both in metals and alloys, and in semiconductors and porous systems.

It is known [1-3], that positrons effectively probe free nanoobject volumes (basically vacancies, divacancies and pores) with the sizes $\leq$1-10 nanometer both in metals and alloys, and in semiconductors and porous systems. We receive on the basis of model of movement of a particle in a plane limited by round cylindrical absolutely impenetrable wall [4], more correct formulas for definition of radiuses R_c cylindrical (symbol) c and the specified formulas of radiuses spherical (symbol) sp of nanopores in the width a component of angular distribution of annihilation photons (ADAP) $\theta_{1/2}$ and energies E_{1c} and E_{sp} of the basic parapositronium state, annihilated in pores in porous silicon and aluminum dioxide

$$R_c[\overset{0}{A}] = \frac{21{,}1}{\theta_{1/2}[mrad]}, R_c[\overset{0}{A}] = \left(\frac{30{,}58}{E_{1c}(eV)}\right)^{1/2}, \quad (1)$$

$$R_{sp}[\overset{0}{A}] = \frac{16{,}6}{(\theta_{1/2})[mrad]}, R_{sp}[\overset{0}{A}] = \left(\frac{18{,}85}{E_{1sp}(eV)}\right)^{1/2}, \quad (2)$$

where R and $\theta_{1/2}$ are expressed in Å and $mrad$ accordingly. Let's note, that in formulas (1), (2) and further in (5), (6) numbers 16,6, 18,85, etc. have dimensions [Å] while value $\theta_{1/2}$ in $[mrad]$ actually is size dimensionless.

In tab.1 shown parameters of investigated samples of porous silicon, features of their production and characteristic of ADAP spectra [1].

A. Table 1

Parameters of investigated samples of porous silicon, features of their production and characteristic of ADAP spectra [1]

ample	Sample characteristics	$Ig_2=S_{g1}/S_{sum}$	$I_{g1}=S_{g1}/S_{sum}$	$I_p=S_p/S_{sum}$	Note
64(1)	Monocrystall		0.335±0.031	0.665±0.035	
R86	Pore Si, <111>, SDB-0,03, h=360-370 mc, HF:C_2H_5OH=2:1, J=20 mA/sm^2	0,015 ± 0,003	0,493± 0.052	0,492± 0,044	Porosity 45%±3%

Notes: h – thickness of silicon plates, <111> - them crystallographic orientation, SDB – 0,03 – mark of silicon plates alloyed by B with specific resistance 0,03 om·sm, Ig = S_{gi}/S_{sum} (i=1,2) – intensity of gauss components, and I_P = = S_p/S_{sum}-intensity of parabolic component in ADAP spectra (the S_{sum}-total area of experimental ADAP spectrum, and S_{gi} and S_p – respectively areas of gauss and parabolic components in this spectrum). J – current density.

Consideration of the kinetic scheme of annihilation disintegrations and transformation of a positron and positronium states in a porous layer enables to receive communication between their speed of capture k_{tr} by pores and intensity components I_{g2} [1-3]

$$k_{tr} \cong I_{g2}\lambda_{cr},\ \text{s}^{-1} \qquad (3)$$

Here $\lambda_{cr} \approx \lambda_s = 0{,}8\cdot 10^{10}$ s^{-1} - speed of annihilation disintegration of parapositronium (p - *Ps*), value $I_{g2} \approx 0{,}015$ (see table 1) in [1] and λ_{cr} in the formula (3), we receive average speed of p - *Ps* capture by pores $k_{tr} = 1{,}2\cdot 10^8$ s^{-1}. The size of speed of capture k_{tr} can be in turn certain on the basis of known expression

$$k_{tr} = \sigma_{tr}\upsilon N_{tr},\ \text{s}^{-1} \qquad (4)$$

Here σ_{tr} - average value of section of capture by pores (defects) of positronium and a positron; v - speed of thermal positronium or a positron; N_{tr} - average concentration of pores (defects) (in

porous (defective) area of a crystal), sensitive to thermal volumetric positronium and a positron states. Thus, from the resulted expressions it is possible to define sizes k_{tr}, N_{tr} and R_{tr} if such parameters are known, as well as $\lambda_1, \sigma_{tr}(i), \upsilon$. Average thermal speed of positronium and a positron at a room temperature $T = 293K$ was estimated under the formula $\upsilon = \left(8k_0T / \pi m_+^*\right)^{1/2} \approx 7{,}52 \cdot 10^6$ cm/s, for a positron $\upsilon \approx 1{,}05 \cdot 10^7$ cm/s, where k_0 – Boltzmann constant, $m_+^* \approx 2m_0$ - effective mass of positronium, $m_+^* \approx m_0$ - effective mass of a positron, $m_0 = 9{,}1 \cdot 10^{-28}$ г - mass of a free positron. We assume, that section of capture of positrons and positronium by pores to equally average value of geometrical section of pore (defect) $\sigma_{tr} \approx \pi R_{tr}^2 = 1{,}26 \cdot 10^{-13}$ cm^2. Having certain by us above value $R_{tr} \approx 2 \cdot 10^{-7}$ cm, k_{tr} and υ, have defined under the formula (3) average value of the centers of p - Ps capture in a porous layer of silicon $N_{tr} \approx 1{,}27 \cdot 10^{14}$ cm^{-3}.

Thus for experimental value in porous silicon $\theta_{1/2} = 0{,}8$ мрад (see tab.1), have received average value of radius of cylindrical pores $R \approx 26{,}4$ Å ≈ 3 nm. Their concentration in a porous layer has appeared equal $\sim 5{,}6 \cdot 10^{13}$ cm^{-3}. Approach of spherical pores gives size $R_{sp} \approx 20{,}75$ Å ≈ 2 nm and $N_{sp} \sim 1{,}3 \cdot 10^{14}$ cm^{-3}.

Experiments have shown [1-3], that the basic part of positrons is in porous silicon from positron states no positronium type in volume of pores annihilated. We shall consider, that such type positron states are the positrons localized in volume of pores in the same way, as well as positronium atoms. In this case formulas (1) and (2) will be transformed in

$$R_c[\overset{0}{A}] = \left(\frac{61{,}1}{E_{1sp}(eV)} \right)^{1/2}, \qquad (5)$$

$$R_{sp}[\overset{0}{A}] = \left(\frac{37{,}7}{E_{1sp}(eV)} \right)^{1/2}, \qquad (6)$$

Investigated by a method by positron annihilation spectroscopy (PAS) samples of porous silicon in the sizes 10×20×10 mm^3 have been cut out from the whole plates of silicon p – type with orientations <111>. For researches two samples designated by us as 164 (1) (the initial monocrystal sample), PR 86, PR16, PR17 (the sample of porous silicon received by a method of electrochemical processing in solution HF:C_2H_5OH have been chosen, at force of current J=20 mA/cm^2). Parameters of investigated plates of silicon and the basic characteristics of ADAP spectra are resulted in tab.1.

Table 2

Characteristics of ADAP spectra of investigated samples of porous silicon of p-type and parameters of cylindrical pores

№ образца	$I_g=S_g/S_{sum}$	$I_p=S_p/S_{sum}$	$k_{tr} \cdot 1$, с$^{-1}$	R_{tr}, Å	$N_{tr} \cdot 10$, см$^{-3}$
164(1)	0.335± 0.031	0.665±0.035			

P R86	0.493± 0.052	0.492±0.044	7.21	13	1.31
P R16	0.483 ± 0.045	0.517±0.041	6.76	13	1.23
PR17	0.511 ± 0.051	0.489±0.044	8.00	13	1.55

From tab.2 the difference between intensities of gauss components I_g(oxidized), that is the oxidized plates of silicon, and I_g (not oxidized) (the initial not oxidized plate) in ADAP spectra, can be written down in the form of

$\Delta I_g = I_g$ (oxidized) - Ig (not oxidized) = $k_{tr}\tau_1$ (7)

That is average value of speed of capture by pores makes size

$k_{tr} = \Delta I_g / \tau_1$, (8)

Let's estimate value k_{tr}, under the formula (8), for value $\Delta I_g = 0{,}665 - 0{,}493 = 0{,}172$ [1-3]. With this value ΔI_g under the formula (8) $k_{tr} \cong I_{g2}\lambda_{cr} = 7{,}9 \cdot 10^8$ s^{-1} for value $\tau_1 = 2{,}19 \cdot 10^{-10}$ s it is received $k_{tr} \approx 7{,}9 \cdot 10^8$ s^{-1}. The size of pores and energies in a annihilation place on external valent electrons E can be found also, using only ADAP data. Thus, on energy in a annihilation place on external valent electrons E it is possible to find also radiuses of pores, using only ADAP data. For this purpose we shall result the expression connecting energy of annihilated electron-positron pair with $\theta_{1/2}$ (*FWHM* (full width half-maximum)) [1-3]

$E = 6{,}9 \cdot 10^{-2} (\theta_{1/2})_g^2$ (9)

Here *E*-energy in eV, and $(\theta_{1/2})_g$ - (*FWHM* (full width half-maximum)) full width of ADAP curve in мрад. So for samples of silicon the measured size $(\theta_{1/2})_g$ has made 11,1 mrad and to it there corresponds average energy of annihilation electron-positron pairs, equal $E = 8{,}5$ eV and caused by average energy of electrons an external environment of atom of silicon on a wall of a pore which can be accepted equal energy of electron on an external environment of the isolated atom of silicon. Thus it is considered, that up to annihilation a positron and positronium are in pore thermal and the measured energy is defined, basically, energy of electron. Tabulated value of energy for $Si(3p^2\ ^3P_0)$ an electronic external environment of silicon $E(Si) = 8{,}1517$ эВ [5]. As we see, the consent of these sizes energies E and $E(Si)$ quite satisfactory. Thus, positrons are basically on external electrons of silicon atoms of "wall" of a pore annihilated. It is possible to believe, that the difference of sizes $E - E(Si) = 0{,}35$ эВ is caused by the contribution of energy of bond of the positron which is being a pore in energy of annihilated electron-positron pairs. In this case for definition of the size of cylindrical pores it is rational to use expression (3)

$$R_c = \left(\frac{61{,}1}{E - E(Si)} \right)^{1/2}, \qquad (10)$$

Thus, at value $E = E - E(Si) = 0{,}35$ eV for the size of pores is equal 13,2 Å.

Further with value $R_{tr} \approx 13{,}2$ Å have defined average value of section of positron capture by defects $\sigma_{tr} \approx 5{,}5 \cdot 10^{-14}$ of cm^2. For estimations of average values of concentration of pores have accepted $k_{tr} \approx 7{,}9 \cdot 10^8$ s^{-1}, $\sigma_{tr} \approx 5{,}5 \cdot 10^{-14}$ cm^2 and $v \approx 10^7$ cm/s. Have received value of concentration of pores $N_{tr} = k_{tr} / v \cdot \sigma_{tr} \approx 1{,}4 \cdot 10^{15}$ cm^{-3}.

Knowing the general porosity (45 %) [1-3] and average volume of a pore, we can estimate concentration of pores from simple geometrical reasons and, having compared it with calculated N_{tr} to check up reliability of accepted assumptions. Certain by us under the formula (2) average size of pores $R_{tr} \approx 3$ nm there corresponds their average volume $V_{tr} = \pi R_{tr}^2 \cdot h \approx 2{,}8 \cdot 10^{-16}$ of cm^{-3}, here h - thickness of a layer of porous silicon. For a case of "dense packing» such pores their concentration proceeding from size of the general porosity 0,45 could be equal $N_{tr}^G \sim 0{,}45 / (V_{tr} = 2{,}8 \cdot 10^{-16}) = 1{,}6 \cdot 10^{15}$ cm^{-3}. Divergences of size N_{tr}^G with us the certain concentration $N_{tr} = 1{,}4 \cdot 10^{15}$ of cm^{-3} it is not so great. Thus, the samples of porous silicon studied by ADAP method is represent microporous cylindrical nanoobjects with the sizes of the order 1 - 3 nanometers and concentration ~ 10^{15} of cm^{-3}.

References

1. Y A Chaplygin, S A Gavrilov, V I Grafutin, E P. Svetlov-Prokopiev, S. P. Timoshenkov, Proc. Imeche. Part N: J. Nanoengineering and Nanosystems. 221, 125 (2007).
2. Yu.A. Chaplygin, V.I. Grafutin, E.P. Svetlov-Prokopiev, S.P. Timoshenkov. Positronics And Nanotechnologies: Possibilities Of Studying Nano-Objects In Technically Important Materials And Nanomaterials. In Book: Advances In Nanotechnology. Volume 1, 2010. Editors: E. J. Chen And N. Peng. Nova Science Publishers, New York, 2010. P.191-208.
3. R.Burcl, V.I. Grafutin, O.V. Ilyukhina, G.G. Myasishcheva, E.P. Prokop'ev, S.P. Timoshenkov, Yu.V. Funtikov. Physics of the Solid State, 2010, Vol. 52, No. 4, pp. 700–705.
4. I.E.Irodov. Collection Of Problems On The Nuclear Physics (Rus.). Moscow: Gosatomizdat, 1960.
5. Physical Sizes: Directory, Moscow. Energoatomizdat, 1991.

Some Features of Phase Transition Kinetics in Liquid Crystal System in the Presence of External Electric and Acoustic Fields

L.Bezhanova

Institute of Applied Problems of Physics NAS Armenia

The peculiarity of the LC behavior in electric and acoustic fields is stipulated by the high mobility of molecules of mesophase and elasticity of the medium. Three-dimensional compressions (tension) or shear deformation created by acoustic waves distort the thermodynamic balance of the medium. This causes shears, turns of molecule and their groups and consequently their new distribution to which corresponds the alteration of all structure-sensitive properties of the mesophase. This reorientation takes place not instantly but has a relaxational character. It is in the range of phase transitions where the mesophase is especially labile that anomalies in the behavior of its viscous-elastic features are evident, and practical application of mesophase in several cases is based on the employment of these properties in the pretransition condition.

From the point of view of kinetics of phase transitions liquid crystalline medium differently reacts to the influence of electric and acoustic fields.

In this paper we report the results of study of the influence of an acoustic and electric fields on the process of formation of the interface boundary and its advance speed during nematic liquid crystal (NLC) ↔ isotropic liquid (IL) phase transitions, as well as the results of the calculation of the isotropic liquid nucleus critical radius in a NLC ↔ IL phase transition in the presence of ultrasonic field.

The mesophases and the interface advance speed during the LC↔ IL phase transition have been examined by the combination of optical polarized light microscopy and designed plant for the velocity measurement of interface advancement (Fig. 1).

Laser beam is focused with the lens and passes through a slit which is designed for making the incident beam after the output have =7mm of height and 1mm of width. After the output the laser beam falls on the mirror system, which consists of a semitransparent and a full rate mirror, and bifurcates. The bifurcated beam passes through a heat chamber regulating the temperature of the cell with LC inside it. "Sandwich" type cells with the thickness of the observable LC layer of 20mcm, 50mcm, 100mcm. The cell is located in the way that the distance between the incident beams is 10mm. At the output from the cell pencils are focused in one point at the photodiode with the help of a lens and it is signaled from the photodiode to the recorder.

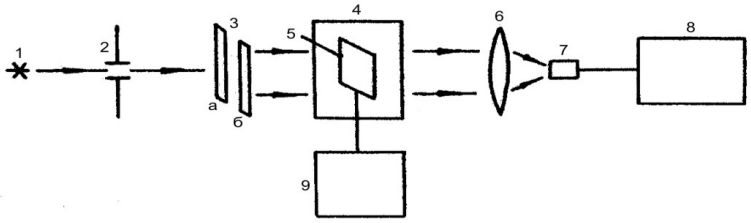

Fig.1 Arrangement flowchart for LC interface advancement speed measurement during LC-IL transition: 1-light source, 2-split, 3-mirrors (a, b), 4-heat chamber, 5-cell with a liquid crystal, 6-lens, 7-photodiode, 8-recorder, 9-generator

During the phase transition the interface at first ($t = t_1$) passes through the propagation place of the first beam in the cell which results in the alteration of beam intensity. After some time ($t = t_2$)) the interface propagates through the location of the second beam. As a result of that the intensity of the second beam changes as well. All this is registered by the recorder. Knowing that $\Delta t = t_2 - t_1$ and the distance between the two beams it is possible to determine interface advance speed. During the experiment an electric field of various frequency and amplitude is impressed at the cell with LC. The electric signal is received by the cell from the generator. Current amplitude and frequency are controlled by an oscillograph.

Dependences of NLC↔ IL phase transition speed from the magnitude of the electric field under the frequencies of 20, 100, 500, 1000Hz are given at the Fig.2,3. Under the frequency of 100Hz interface advance speed declines with the increase of the voltage of electric field. Under these conditions slight monotonic decrease of the first stage of NLC-IL phase transition speed is being observed when the frequency is 20Hz. Under the frequency of 100Hz interface advance speed decreases with the increase of electric field voltage. Under these conditions slight monotonic decrease of the first stage of NLC↔ IL phase transition speed is being observed when the frequency is 20Hz. At the frequencies of 1000 and 500Hz depending on the electric field voltage this phase transition speed has a complex form (fig.4). These effects are stipulated by a number of reasons connected with the behavior of LC in an electric field as a simple dielectric with electrohydrodynamical instability of liquid-crystal state and the influence of the electric field on the spontaneous phase nucleation.

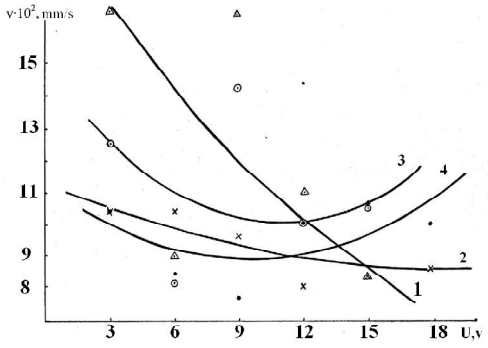

Fig.2. Dependence of destruction rate of distant orientational order in NLC from electric field voltage during NLC-IL phase transition: 1-20Hz; 2-100Hz; 3-500Hz; 4-1000Hz.
Stage of distant orientational order destruction.

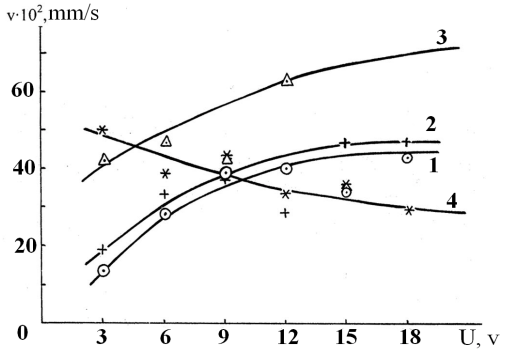

Fig.3 Dependence of short-distance orientational order in NLC from electric field voltage during NLC-IL phase transition: 1-20Hz; 2-100Hz; 3-500Hz; 4-1000Hz.
Stage of short-distance orientational order destruction (cluster destruction).

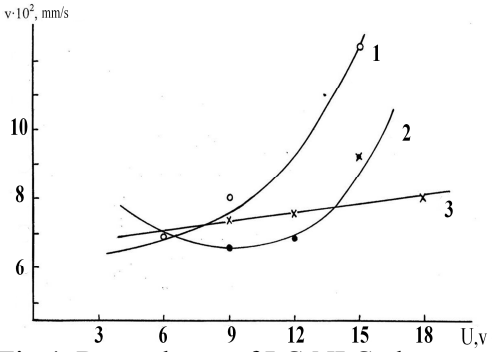

Fig.4. Dependence of LC-NLC phase transition speed during NLC from electric speed voltage: 1-100Hz; 2-500Hz; 3-1000Hz.
Corresponds to the entire phase transition.

Cited results were obtained for the planar orientation of the LC layer, $\Delta\varepsilon < 0$ and phase

transition in an electric field is accompanied by electrohydrodynamical instability.

Under voltages above the threshold voltage instability mode characterized by vortex motion is being observed in NLC with $\Delta\varepsilon < 0$.These vortexes, undoubtedly, change the defect picture in NLC and influence the possibility of IL phase nucleation and, consequently, the speed of phase transition.

Under the frequencies of 20, 100 and 500Hz polarization effects are essential (for example, frequency of low-frequency polarization disappearance of etoxibenzil is equal to -10^4Hz, and the value of dielectric conductivity ε under t=56,^{0} C and frequencies of $5\cdot10^2$ and 10^3Hz are correspondingly equal to 11,8 and 4,7). As it is

known, polarity effects stipulate an additive term $\Delta F_E = -\int \frac{1}{2}\vec{P}\vec{E}dV$ to the thermodynamic potential of supercooled isotropic liquid.

Not only the nucleus polarization but also the polarization of the ambient medium generally change during a new phase nucleation in an electric field which in the final analysis results into alteration of possibility of liquid-crystal nucleation in comparison with its spontaneous nucleation. Thermodynamic profitability of liquid-crystal phase nucleation in an electric field will be characterized by the decrease of free energy of the system.

It deserves mentioning that cited results go with our microscopic investigations. These observations show that in cells made of conducting glass measuring 2smx1sm where the thickness of LC layer is 50mcm LC-NLC transition under temperature alteration speed of 0,5 grades/minute takes place in -10seconds .In an electric field with the frequency of 25Hz and voltage of 10-12V this time is increase to -100seconds.

Experimental studies of the influence of an acoustic field on the process of formation of the interface boundary and its advance speed during nematic liquid crystal (NLC) - isotropic liquid (IL) phase transitions were carried out in acoustically “soft” and acoustically “stiff” sandwich type cells, one of the paddings of which was an X-cut piezoelectric quartz plate with the thickness of 0.7mm, as well as in a drop. LCs of planar and homeotropic orientation were examined in cells with 20, 50, 100μm thickness. The frequency of ultrasonic field was 3,77- 4MHz. The temperature of the sample was controlled to within $\pm0,1^0$C. The mesophases and the interface advance speed have been examined by the combination of optical polarized light microscopy and designed plant for the velocity measurement of interface advancement (Fig.1). Preliminary studies indicate the existence

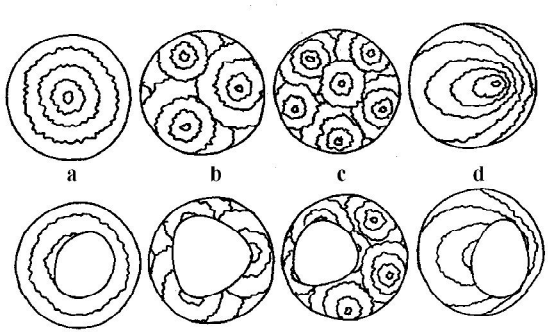

Fig.5a Development of phase boundary during NLC-IL phase transition in LC-440 in ultrasonic field when thickness of the observed layer is a-20mcm; b-50mcm; c-100mcm; d-drop.

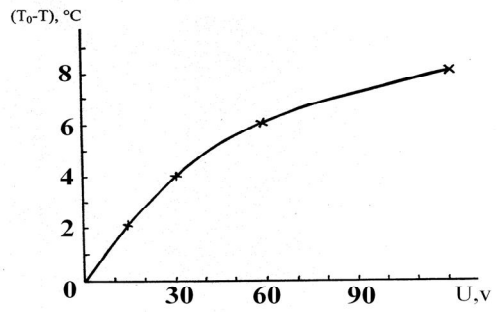

Fig.5b Dependence of NLC-IL phase transition temperature in LC-440 from

of vortex motion of LCs in acoustic streams. The presence of vortex motions of LCs in acoustic streams in our studies was ascertained by mixing slight amount of dies difficultly solving in the examined samples with LC. In all cases the motion of LC is directed from the center of a cell or a drop to the edges. In an isotropic phase such motions are not observed. As a rule, phase transition starts at the strips of the sample where the speed of vortex motion is maximal. In the neighborhood of point where the phase transition starts turbulence disappears, emerges the interphase boundary whose displacement speed depends on intensity of ultrasonic field. And phase transition starts at that, as a rule, at the strip of the sample (nearer to the center), where the speed of vortex motion is maximal. With the acoustic damping decreases the amount of current lines, the speed of vortex motion and simultaneously rises the time of phase transition. The typical picture of interphase boundary development in an ultrasonic field during the NLC-IL transition which is observed under a microscope is displayed on the Fig 5a.

It deserves mentioning that the intensity of ultrasound influences the temperature of phase transition (Fig. 5b).

The most interesting part of this study concerns the following: liquid crystalline medium reacts differently to the influence of electric and acoustic fields. First of all, electric field increases by several grades the temperature of LC↔IL phase transition, while ultrasonic field decreases the temperature of phase transition. Secondly, electric field improves the linear form of LC↔IL interphase boundary, whereas this interface has a form of closed curve in an ultrasonic field. The influence of ultrasound on the formation of isotropic phase nucleus in NLC phase during NLC-IL phase transition was also examined. The significance of isotropic phase nucleus radius r was determined from the condition $\partial(\Delta\Phi)\big/_{\partial r} = 0$, where $\Delta\Phi$ is the alteration of thermodynamic potential during the phase transition. $\Delta\Phi$ contains terms determined by the heat of transition, surface tension, as well as terms conditional on elastic energy of NLC and ultrasonic field. Supposed that NLC→IL phase transition occurs at the constant external pressure P_0 the state of the system is possible to depict with the help of thermodynamic potential Φ. The expression $\Delta\Phi$ has the following appearance for the spheric liquid nucleus with the volume V :

$$\Delta\Phi = -\frac{4}{3}\pi r^3 \frac{q}{T}\left(T - T_c\right) + \frac{4}{3}\pi r^3 \rho \Delta F_{elast.} + \frac{20}{3}\pi\alpha r^2 \qquad (1)$$

q -heat of transition calculated to the unit of value under the $T = T_c$, T- actual temperature of NLC phase, T_c- NLC→IL phase transition temperature under the pressure P_0 . In order to establish the influence of the ultrasound on the critical radius of isotropic phase nucleus, (1) must be supplemented with the corresponding summands stipulated by the ultrasonic field in LC.

Under ultrasonic oscillations behavior of the liquid crystal concerning the sound transmission is similar to the solid, and the density of the free elastic energy comprises the following terms [1]:

$$F_{us} = \frac{1}{2}C_{11}\left(U_{xx} + U_{yy}\right)^2 + C_{22}\left(U_{xx} + U_{yy}\right) + \frac{1}{2}C_{33}U_{zz}^2, \qquad (2)$$

where C_{ij} - elastic constants, , U_{ij} - deformation tensor. Director is chosen lengthwise the z axis. Under the frequency of ultrasound ω , sufficing $\omega\tau << 1$ condition (τ -Maxwell relaxation time), U_{ij} - can becan be expressed in terms of strain tensor $\sigma_{ij} = 2\mu U_{ij}$ [2], where shear modulus $\mu = \eta/\tau$ (η- NLC volume viscosity). Adding $\Delta F_{us} = 4\pi r^3 \rho F_{us} - 4\pi r^2 G\Delta t$ to the (1), where $G = \frac{U_0^2}{2}\left(\frac{\omega\rho\eta}{2}\right)^{1/2}$ energy dissipation in isotropic liquid in a unit time rated to a unit of area of an

oscillating plane, which generates ultrasonic oscillation in medium, Δt-nucleation time, we will obtain for critical radius r_c:

$$r_c = \frac{10\alpha + 6G\Delta t}{3\left[\left(T - T_c\right)q/T + \rho\left(\Delta F_{us} + \Delta F_{elast}\right)\right]} \qquad (3)$$

Let's discuss the phase transition in acoustically "stiff" sandwich type cells with the homeotropic orientation of NLC layer. Construction of the cell doesn't admit LC to spread and doesn't oppose to uniform compression. System of motion equations in NLC has the following appearance [3-5]:

$$\rho\frac{\partial v_i}{\partial t} = -\frac{\partial P}{\partial t} + \frac{\partial \sigma_{ki}}{\partial U_k}, \qquad \left[\vec{n}\left(\gamma_1\vec{N} + \gamma_2\hat{A}\vec{n}\right)\right] = \left[\vec{n}\varphi\right]_y \qquad (4)$$

where $\vec{n}$- director ($n_x \sin\theta, n_y = 0, n_z = \cos\theta$); ρ - density; P - pressure; $\hat{A}\vec{n}$- vector with $A_{ij}n_{ij}$; $\varphi = \partial f / \partial \vec{n}$ components, f -frank's energy; U_k - components of shift vector; $\gamma_1 = \alpha_3 - \alpha_2$ и $\gamma_2 = \alpha_6 - \alpha_5, \alpha_2, \alpha_3, \ldots$ - Leslie's constants; σ_{ki}- viscous stress tensor with a glance volume viscosity [1,5]: The inertial terms are omitted in (4) whereas they are infinitesimal in megahertz range.

$$\sigma_{ki} = \alpha_2 n_k N_i + \alpha_3 N_k n_i + \alpha_4 A_{ki} + \alpha_5 n_k n_j A_{ij} + \alpha_6 n_i n_j A_{jk} + \mu_1 A_{jj}\delta_{ki} + \mu_2 A_{jj} n_k n_i,$$

$$A_{mj} = \frac{1}{2}\left(\partial \mathrm{v}_j / \partial U_m + \partial \mathrm{v}_m / \partial U_j\right), \qquad (5)$$

$$\vec{N} = \frac{\partial \vec{n}}{\partial t} + \frac{1}{2}\left[\vec{n} rot \vec{v}\right],$$

μ_1, μ_2 -coefficients of volume viscosity.

For the diagonal elements of viscous stress tensor from (5) we obtain:

$$\sigma_{xx} = (\alpha_2 + \alpha_3)\sin\theta\left[\ \partial n_x/\partial t - \frac{1}{2}\cos\theta(\partial v_x/\partial z - \partial v_z/\partial x)\ \right] + \left[\alpha_4 + \mu_1 + (\alpha_5 + \alpha_6 + \mu_2)\sin^2\theta\right]\frac{\partial v_x}{\partial U_x},$$

$$\sigma_{yy} = 0, \qquad (6)$$

$$\sigma_{zz} = (\alpha_2 + \alpha_3)\cos\theta\left[\ \partial n_z / \partial t + \frac{1}{2}\sin\theta(\partial \mathrm{v}_x/\partial z - \partial \mathrm{v}_z/\partial x)\ \right] + \left[\alpha_4 + \mu_1 + (\alpha_5 + \alpha_6 + \mu_2)\cos^2\theta\right]\frac{\partial \mathrm{v}_z}{\partial U_z}.$$

Under the assumption that $k_s h \ll l$ (k_s-sound wave's wave number, h-LC layer's thickness) in [6] it was obtained that: $v_x = \theta = 0, \quad v_z = \frac{2}{h}\left(z - \frac{h}{2}\right)\omega U_0 \cos(\omega t)$, ($U = U_0\cos(\omega t)$ in the acoustic field). It follows from this solution that in (6) $\sigma_{xx} = 0, \sigma_{zz} = \beta\left(\partial \mathrm{v}_z / \partial U_z\right)$, where $\beta = \alpha_4 + \alpha_5 + \alpha_6 + \mu_1 + \mu_2$.

In considered case $U_z = U_0 \exp(\omega t - kz)$ and for σ_{zz} we will have:

$$\sigma_{zz} = \frac{2}{h}\left(\frac{h}{2} - z\right)\beta\omega\left[2ctg(kz - \omega t) - \cos(kz)\right]\exp(kz). \qquad (7)$$

Calculations have shown that in (3) terms $6G\Delta t$ and $\rho\Delta F_{elast}$ can be neglected. Then with the help of (2), (3) and (7) for the r_c we can obtain:

$$r_c = \frac{10}{3}\alpha\left\{\frac{q(T - T_c)}{T} - \frac{3\rho C_{33}\tau^2\beta^2\omega^2}{2\eta^2 h^2}\left(\frac{h}{2} - z\right)^2 \times\left[2ctg(kz - \omega t) - \cos(kz)\right]^2 \exp(2kz)\right\}^{-1} \qquad (8)$$

The quantity of critical radius of isotropic phase nucleation in the presence of ultrasonic field in NLC, as it is obvious from the obtained expression, is a complex function of z coordinate. It being

known that in the plane $z = h/2$ ultrasound does not influence r_c . Calculating the nucleus critical radius with the help of (8) in NLC→IL phase transition it has been obtained for n-etoxianizol that $r = 3,8 \cdot 10^{-5} sm$ in the absence of ultrasound and $r = 4,3 \cdot 10^{-5} sm$ in an ultrasonic field with the frequency of 4 MHz (parameters required for the calculation are taken from [7-9]).

These design results conform well to experimental data mentioned above, namely to the decrease of phase transition temperature in the presence of ultrasound.

Since during the description of sonic wave propagation through liquid crystalline medium it can be assumed that the system is in quasithermodynamic equilibrium (i.e. after alteration of external parameters the system instantly comes to a new equilibrium condition), regulation of phase transition kinetics must be possible with the help of choice of temperature mode and the acoustic field after some time from the start of phase transition.

Further work is in progress to estimate the efficiency of the ultrasonic field influence on the kinetics of phase transition and to determine the possibility of kinetics regulation.

References

1. Stephen M.J., Straley J.P. Physics of Liquid Crystals // Rev. Mod.Phys. 1974.V.46. №4. P.617-704.
2. Landau L.D., Lifshits E.M. Theory of elasticity. M.: Nauka,1965.p.202
3. Erikson I.L. Continuum Theory of Liquid Crystal of Nematic Type // Mol. Cryst. Liq. Cryst. 1969. V7.P.153-164.
4. Leslie F.M. Some Thermal Effects in Cholesterical Liquid Crystals // Pros. Roy. Soc. L. 1968. V. A307. № 1490.P.359-372.
5. Chaban I.A. Vibro-hydrodynamic Instability of Liquid Crystals // Asoustic J. 1978. V.24. №2. P.260-270.
6. Chaban I.A. Acousto- hydrodynamic Instability of Nematic Liquid Crystals // Asoustic J. 1979. V.25. №1. P.124-134.
7. Blinov L.M. Electro-and magnetooptics of Liquid Crystals. M.: Nauka,1978.p.386
8. Kapustin A.P. Acoustic of Liquid crystals. M.: Nauka,1986. p.368.
9. Jpma J.G., Vertogen G. Short Range Order in Nematic Liquid Crystals // Solid State Comm.1976. V.18. P.475-478.

The Molecular Dynamics Study of Coagel and Lamellar Liquid Crystalline Phases of Sodium Pentadecyl Sulfonate (SPDS)/Water System

L. H. Arsenyan[a], A. H. Poghosyan[b] and A. A. Shahinyan[b]

[a] *Institute of Applied Problems of Physics NAS RA*
[b] *International Scientific Educational Center NAS RA*

Abstract

We have performed molecular dynamics (MD) study of sodium pentadecyl sulfonate (SPDS)/water system above and below the Krafft point, at T=300K (coagel phase), T=323K, T=333K temperatures. The parallel molecular dynamics simulation was done using GROMACS software package. After 500 ns of overall MD run some structural parameters of system in coagel and lamellar liquid crystallie phases were calculated. Particularly, the received results for the interlayer spacing of the system, SPDS lamella thickness, average area per SPDS molecule head group on the surface of lamella, SPDS molecules hydrophobic chains orientation parameter in the hydrophobic core of lamella, etc. are in good agreement with real experiment findings.

Results

For detailed analysis of SPDS/water system some structural parameters was examined. The first one is the average of interlayer spacing of the system (Fig. 1). One can see from the figure that the increase of the temperature leads to the growth of average interlayer spacing. After increasing of the temperature from 300K to 323K the average parameter grows slightly from ~4.94 nm to ~4.97 nm, meanwhile the further increase of the temperature up to 333K influences more significantly, and finally, the average interlayer spacing reaches 5.05 nm. According to [1], the value of interlayer spacing for surfactant/water systems, received from experiment, is in the range of 2.7-5.3 nm.

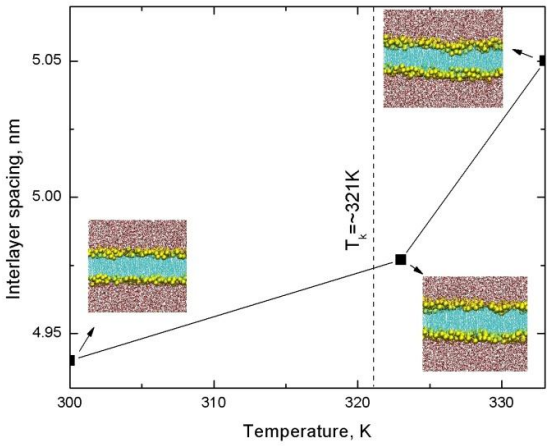

Fig. 1. The average interlayer spacing of the system depending on temperature.

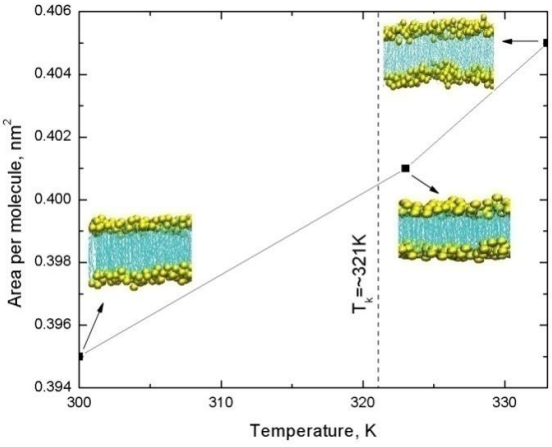

Fig. 2. The average area per SPDS molecule headgroup depending on temperature.

The next parameter which can be extracted from real experiment is the average area per headgroup. Fig. 2 represents the dependence of average area per SPDS molecule headgroup on the temperature. As one can see the area grows with the temperature increase reaching ~0.405 nm^2 which is in good agreement with the real experiment findings [2]. The growth of the average area per SPDS molecule headgroup means that the lamella surface enlarges at higher temperature points and the compactness of SPDS molecules packing is reduced.

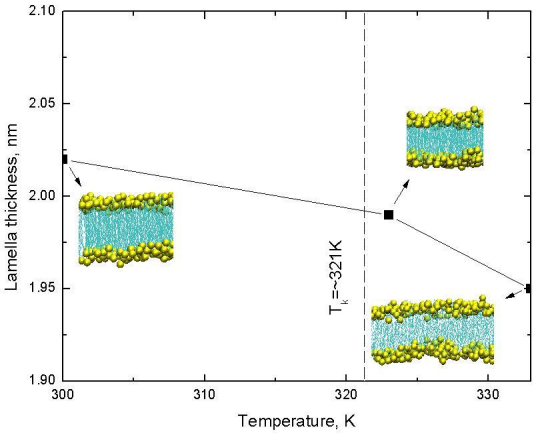

Fig. 3. The average area lamella thickness depending on temperature.

In Figure 3 the average lamella thickness changes depending on temperature is shown. From the plot we see that the continuous increase of temperature brings to a bit decrease of SPDS lamella thickness from 2.02 nm at 300K to 1.95 nm at 333K. Comparing this result with the interlayer spacing plot data one can see that the growth of interlayer spacing occurs mainly due to the water layer swelling. The decrease of lamella thickness is due to some factors including the behavior of SPDS molecules hydrocarbon tails.

In this aspect we have estimated the orientation order parameter of SPDS molecules alkyl chains (Fig. 4) which was calculated by the following formula:

$$S_{zz}^{mol} = \frac{3}{2} < \cos^2 \alpha_i > -\frac{1}{2} \qquad (1)$$

assuming

$$-S_{CD} = S_{zz}^{mol} \qquad (2),$$

where α_i is the angle between z-axis of the simulation bo x and the molecular axis defined as a

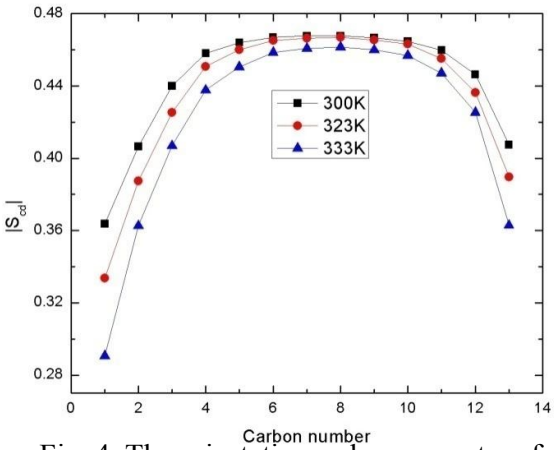

Fig. 4. The orientation order parameter of SPDS molecules alkyl tails.

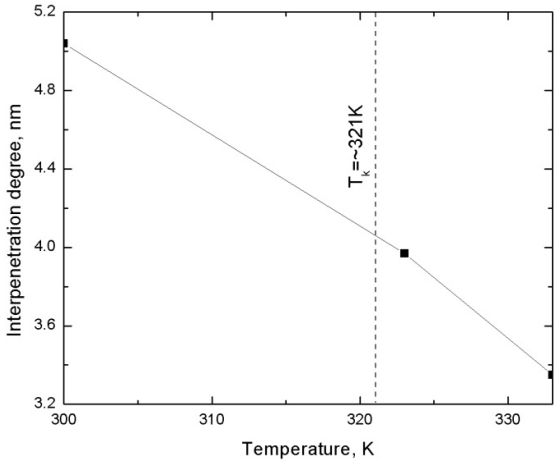

Fig. 5. The interpenetration degree of SPDS molecules alkyl tails.

vector from C_{i-1} to C_{i+1} carbon atom and the brackets denote the ensemble and time average. As it can be seen from the plot at the 300K the order parameter value shows plateau region for C_4 to C_{11} carbon atom, which refers to strongly ordered conformation of mentioned atoms, while at 333K after simulation the mentioned region was observed only for C_6 to C_{10} atoms. Hence, one can see that the increase of temperature leads to the disordering of SPDS molecules hydrocarbon chains.

Another parameter describing conformational structure of alkyl tails inside the bilayer is the interpenetration degree of SPDS molecules hydrocarbon chains (Fig. 5) which is the mean distance between C_{15} terminal atoms of monolayers. Due to the higher temperature the interpenetration degree decreases from ~5.05 nm to 3.35 nm which also shows that the packing of hydrocarbon chains inside the bilayer becomes more disordered.

Conclusion

The MD study of SPDS/water system in given range of the Krafft point shows that below the Krafft point temperature region (in coagel state) the lamella has compact packing both at the surface and inside the bilayer. Further increase of the temperature above the Krafft point leads to the reducing of the system compactness, particularly, average area per SPDS molecule headgroup increase, SPDS alkyl tails disordering and extrusion from each other. Summarizing the received results one can say that above the Krafft point (in lamella liquid crystalline phase) some structural changes of the system are observed. However, the further increase of temperature and longer MD run would be very important for the deep insight the nature of such kind of changes.

References

1. A.A. Shahinyan. The role of structural organization of ionic micelles in the mechanism of macromolecules formation in the emulsions (*in Russian*). *NAS RA,* **1985**.
2. M.K. Minasyants, V.A. Zakaryan, A.A. Shahinyan, I.G. Chistyakov. X-ray analysis of sodium dodecyl sulfate (SDS)/water system. *Kristallografiya (in Russian)*, **1979,** XXIV, 319-323

Structural Analysis of Glycophorin A, Transmembrane Protein of Erythrocyte

P.K. Hakobyan, A. H. Poghosyan, A. A. Shahinyan

International Scientific Educational Center NAS RA

Abstract

Molecular Dynamics (MD) simulation of human erythrocyte asymmetric membrane model has been performed. CHARMM27 force field and NAMD software package has been used for parallel calculations. We have estimated some features of embedded protein (Glycophorine A) and have disscused some important problems concerning the mutual orientation of separate parts of protein molecule inside the membrane. The nature of interaction between protein and neighboring phospholipid hydrocarbon chains are dominant forces governing to association of protein molecule helices in membrane.

Introduction

At present time the computational research and study of biological membranes is widely spread and is very actual. There are different types of simulation methods for research of biological membranes and one of them is Molecular Dynamics (MD) [4-5]. Most of the studied biological systems were consist of phospholipids bilayers, proteins and all these in aqueous medium. Among the different lipids found in biomembranes, phospholipids play a very important role. Phospholipids can be neutral but zwitterionic like phosphatidylcholine (PC) or phosphatidylethanolamine (PE) and charged as in the case of phosphatidylserine (PS) [1-3]. A lot of successful phospholipid membrane MD simulations have recently been carried out, e.g. for saturated DPPC [5-7] and monounsaturated POPC systems [8]. There are also done some simulations on research of influence of Cholesterol on monophospholipid`s, e.g. Sphingomyelin bilayer [9]. In this work we mainly discuss the conformation properties of Glycophorine A protein transmembrane helices in erythrocyte membrane and also the influence of surrounding media (phospholipids and cholesterol molecules) on structural properties of protein.

Construction and simulation details

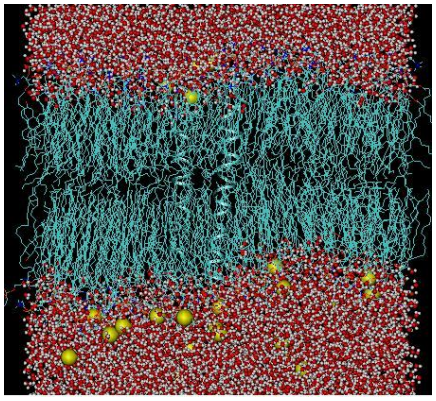

Figure 1: Erythrocyte membrane model in water environment

The construction of model membrane was implemented by using of MDesigner software [8]. First the molecules of POPE, POPC, SAPE, SOPC, SAPS, SDPS, LSM, HSM, and Cholesterol were created and we have received a system consisting of 256 molecules of phospholipids, cholesterol, and 27 Sodium counter ions by random replication making allowance for asymmetry of model membrane and final concentration of phospholipids and cholesterol. The GpA protein transmembrane part were inserted into the system ready from previous simulation. The investigated model was solvated: inserted into water bulk with 8572 water molecules of TIP3P [9] model. The membrane model was hydrated at about 33 water per phospholipid so in order to assure that the system is at fully hydrated. The initial membrane model size

was about 10.5×9×9 nm^3 so the rough estimation for area per phospholipid was about 0.89 nm2. The initial configuration of was stabilized by an energy minimization using conjugate gradient method for 15000 steps and was subjected to short (about 1000 ps) MD simulation in NVT ensemble .The Langevin dynamics [10] with 5 ps−1 damping coefficient was used. The constant temperature and pressure were set correspondingly to 310 K and normal 1 atm. The constant temperature and pressure were controlled by using the Langevin piston Nose-Hoover method [11]. For the non bonded full electrostatic interactions between atom pairs cutoff parameter was set to 14 Å. The coordinates and velocities were saved with 2 stages first, each 0.001 ns for calculation of MSD and diffusion coefficient values of phospholipids and cholesterol and second 0.01 ns for calculation of other parameters of the system. The visual representation performed by using VMD package. System MD simulation run (in NPT ensemble) was done with 2 fs time step, using NAMD software code with CHARMM27 all-atom force field on parallel Linux cluster. The simulation was performed for 80 ns on 12 nodes (24 Intel Xeon 3.06 GHz processors) of the cluster with the duration of about 60 days. The force field parameters of Cholesterol

molecule were generated using Dundee PRODRG server. The ready for MD simulation system consists of 57640 atoms.

Results and discussions

It is known from NMR experiment that Gly79 amino acid residue plays an important role in GpA

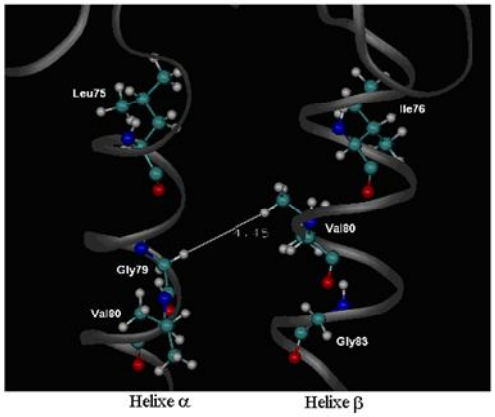

Fig 4. The last simulation point. The Gly^{79}, Gly^{83}, Val^{80}, Leu^{75}, and Ile^{76} are pointed in VDW mode.

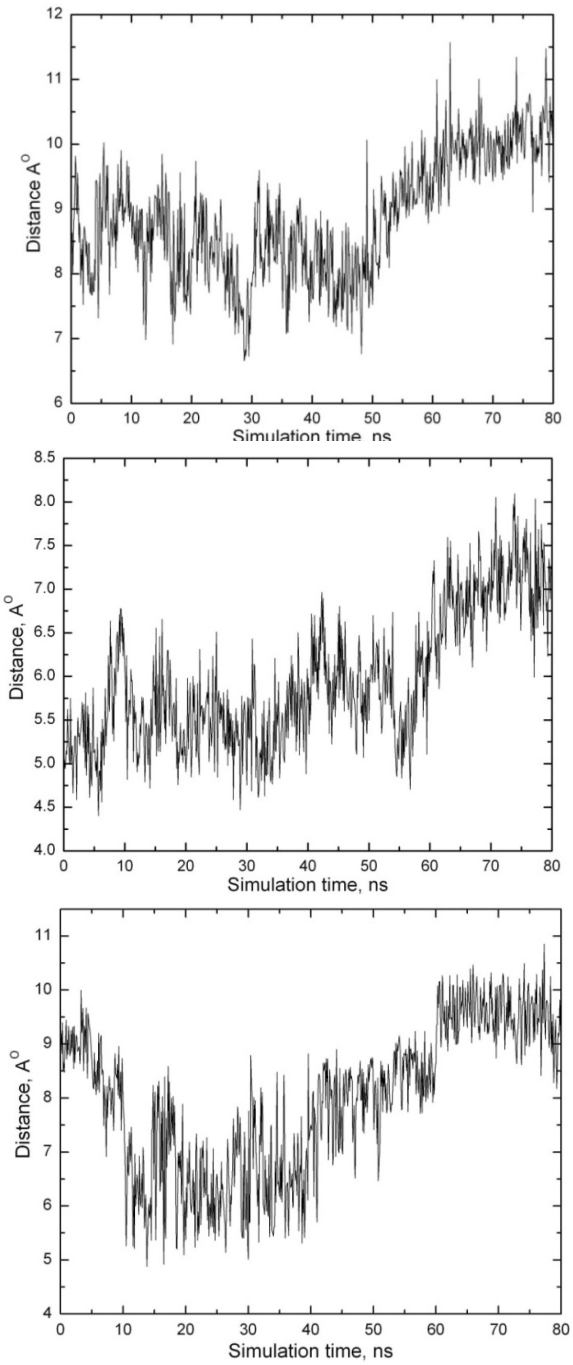

Fig. 2. Ieu^{75}-Ile^{76}, Gly^{79}-Val^{80} and Gly^{79}-Gly^{83} distances between α and β helices depending on simulation time.

helices dimerization, and hydrogen bonds between Gly79, Val80, Gly83 of two helices stabilize the dimmer inside of GpA molecule [12]. We have estimated the distances of above mentioned amino acids and represented the distance changes during the whole simulation time (Fig. 2(a),(b),(c)). In addition we have also examined the contact distance between Leu75 and Ile76 in order to explain the effect of this contacts in dimerization. The Gly79 - Val80 distance fluctuates in the range of 5 Å± 1 and 7 Å± 1 during whole simulation time. Indeed, we can see the strong and close contacts over the whole simulation time. In comparison with experimental data (NMR refinements) we can see a shift (about 3

Å) of Gly79–Val80 distance. The NMR data of Gly^{79} – Val^{80} distance is 3.5 Å, which is almost the starting point of our simulation (fig. 3(b)). During the 80ns of MD simulation one can see the increasing of the distance up to 7 Å and as well equilibrium since 60ns of the simulation.

The increasing is due to presence of surrounding media, namely phospholipids and cholesterol molecules. Changing the media, for instance, the presence of surfactants (SDS micelle) [9] lead to the decrease of Gly^{79} – Val^{80} distance to the value of 3.5 Å which means that the surrounding media influences on the GpA structure inside of membrane. For explanation, we have also visualized and presented the snapshots extracted from the last point of simulation (80 ns last point). We have measured the hydrogen – hydrogen distance in mentioned amino acid residues. From the structural parameters which we have calculated the equilibrium state reaches after 60 ns of simulation and therefore the Gly^{79} – Val^{80} distance is estimated to be about 7 Å. The Hydrogen- hydrogen distance is about 4.5 Å as shown in fig. 3.

References

1. Yeghiazaryan G.A., Poghosyan A.H., A.A. Shahinyan. Physica A., 362, 197, (2006)
2. Tieleman D.P., Berendsen H.J.C. J. Chem. Phys. 105, 4871, (1996).
3. Chiu S.W., Clark M., Balaji V., Subramaniam S., Scott L.H., E. Jakobsson. Biophys. J. 69, 1230 (1995).
4. Poghosyan A.H., Gharabekyan H.H., Shahinyan A.A. IJMPC 18 (1), 73, (2007).
5. Mori K., Hata M., Neya S., Hoshino T. Chem-Bio Inf. J., 4, 15, (2004)
6. Robinson A. J., Richards W. G., Thomas P. J., Hann M. M.. Biophys. J. 67(6), 2345, (1994)
7. Berkowitz M. L. Biochimica et biophysica acta. Biomembranes , 1788, 86, (2009)
8. White S.H. , Wimley W.C. Annu. Rev. Biophys. Biomol. Struct. 28, 319, (1999).
9. Braun R., Engelman D.M., Schulten K. Biophys. J. 87, 754, (2004).
10. Soumana O. S., Garnier N., Genest M. Eur.Biophys. J. 36, 1071, (2007).
11. Zhang J., Lazaridis T. Biophys. J. 96 (11), 4418, (2009).
12. Eilers M., Patel A.B., Liu W., Smith S.O.. Biophys. J. 82, 2720, (2002)

A Common Ellipsometry with an Arbitrary Orientation of Polarization Angle of Analizer and Polarizer with an Amplifier

[1]A.M. Sedrakyan, [2]V.N. Agabekyan, [1]A. Petrosyan

1) State Engineering University of Armenia, asedrakyan@seua.am
2) *Institute of Applied Problems of Physics of NAS RA, Hr. Nersisyan str. 25, Yerevan, 0014, Armenia*

We submitted an investigation scheme of an ellipsometry for measurement of super small rotations of polarization plane (when an electromagnetic wave interacts with a medium with an arbitrary orientation of polarization angle of the ellipsometry optical element in respect to the amplifying medium). We obtained an analytical expression for measurement of the wave intensity in the inlet and outlet of the device.

Key words: ellipsometery, amplifying medium, polarization parameters, ellipsometer.

Introduction: As it is known, the measurement of a light beam polarization is the basis of the modern physics because the investigation of atomic and molecular effects of non-conservation of special parity is connected to the weak interactions between electrons and the atomic nucleus. One of the macroscopic expressions of these interactions is the appearance of optic activity for substances, which don`t posses natural optic activity. For the revelation of this effect, an experiment for measurement of rotation of light polarization plane has been done in the vapors of bismuth. Despite the fact that the expected effects are very small, during the experiments we succeeded to measure the rotation angel, which well coincided with the predictions of the united theory of electromagnetic and weak interactions suggested by Winberg, Glashon and Salam. The effect of rotation of the polarization plane of a flat electromagnetic wave as well as a circular diachronism has been used for investigation of the optic properties of gyro tropic media for a long time. Particularly, many experimental works dealing with dependences of the spectra upon the angle of reflection and propagation of the waves are made to reveal the dispersion dependence of these media upon the optic properties. The optic activity of a substance is very sensitive of the changes in the molecule spatial structures of the inter molecule interaction. These investigation results of polarization plane rotation in the infra red range of the spectrum act as an important information for understanding of the inner molecular structure of different chemical and biological objects.

The phenomenon of light polarization and the peculiarities of polarized light interaction with a substance have found particularly wide application in the scientific investigation of crystal-chemical and magnetic structures of the solid bodies, the optical properties of crystals, the state nature and structures of biological object, the behavior character of gas, liquid and solid bodies, as well as for obtaining information about hardly reachable objects (particularly, in anisotropic). For this purpose, recently, a significant achievement has, been made in the areas of polar metric and spectra polar metric measurements, which enable to enhance the measurements of super small rotations of a polarization plane [1-8] (also see the cited literature there). The actuality is mainly conditioned by the following circumstances. Theoretically, there are predicted effects, the experimental approval of which requires the measurement of very small rotations of polarization plane [2, 3]. On the other hand, the ability of measuring of small rotations of a polarization plane and light polar metric sensitivity enable to reveal new physical effects experimentally [4].

On the overhand, the capability of measuring of very small polarization plane rotations and high polar metrical sensitivity are enabled. To experimentally observe a new effect, which is principally small in value for macroscopic ensembles,-the magnetic resonance in the spectrum of Faradey

rotation, etc.,- the laser polarometer was successfully applied for the revelation of the "Rotational Increase of Ether predicted by Tomson,- i.e. the light polarization plane rotation, when light propagates through a rotating medium, to measure weak rotations of polarization planes they are preliminary amplified. For amplifying the rotation of a polarization plane, frequently, it is used the phenomenon of the optical azimuth inhomogeneity.

In work [3], it is presented the supersensitive universal polarometer (SSUP), which is recently widely used and allows us to measure simultaneously the parameter of optical activity and double-reflection. The improvement of resolving power of SSUP is obtained by maximal simplification of the polarimeter, maximal decreasing of the element number in the polarometer.

In our works [5-8] we have studied and compared different mechanisms of rotation of a polarization plane and stabilization of the polarization azimuth in the case of the light reflection from a non isotropic half-space, the light propagation through a non isotropic plate and the light reflection from such a plate.

In works [5, 6], it is presented the methods of amplification or reflection or propagation of light though the half-space of anisotropic (non-isotropic) plate. It was considered the probability of existence of practically ideal stabilizators of azimuth polarization. It was considered the probability of improvement of resolving power of the amplifier of polarization plane rotation at the maximal value of amplification. It was studied the influence of isotropic and non-isotropic absorption on the amplification of polarization plane rotation. The analytical formula for the amplification and stabilization while the propagation and reflection of light from

(4) such a plate (the problem geometry is submitted in fig. 1)

Indeed, it is easy to show that, for instance, in the case of light reflection from half-space of an isotropic medium, the electric vector azimuth in the incident beam, (φ), and the reflected one (ψ), are connected by the relation:

$$tg\psi = \frac{r^s}{r^p} tg\varphi = k tg\varphi \tag{1}$$

And for the lower values of φ and those of not very large k we have

$$\psi = k\varphi \tag{2}$$

but due to $k \geq 1$, polarization plane rotation angle is enhanced. The precise analytical solution of this problem in the case of enrich went with molecules of an absorbing (amplifying) medium is well-known [6]. The azimuth amplification coefficients $f^{T,t}$, are the derivatives of $\psi^{\Gamma,t}$ by φ. Then from (7) we obtain for $f^{r,t}$.

$$f^{r,t} = \frac{d\psi^{r,t}}{d\varphi} = -\frac{\mathrm{Re}\left(k^{r,t}\right)\left(1+\left|k^{r,t}\right|^2 tg^2\varphi\right)}{\cos^2\varphi\left[\left(1-\left|k^{r,t}\right|^2 tg^2\varphi\right)^2 + 4\left(\mathrm{Re}\left(k^{r,t}\right)\right)^2 tg^2\varphi\right]} \tag{3}$$

The polarization characteristics of reflected and propagated fields past through amplifier are determined by polarization functions, that can be presented in the form [6].

$$\chi^{r,t} = \frac{E^y_{r,t}}{E^x_{r,t}} = k^{r,t} tg\varphi, \tag{3}$$

where $k^r = r^y / r^x, k^t = t^y / t^x$, considering

$$k^r = \frac{r^y\left(1-\exp(2i\beta_y)\right)\left(1-r^{y2}\exp(2i\beta_y)\right)}{r^x\left(1-\exp(2i\beta_x)\right)\left(1-r^{x2}\exp(2i\beta_x)\right)}, \tag{4}$$

$$k^t = \frac{\left(1-r^{y2}\right)\left(1-r^{y2}\exp(2i\beta_y)\right)\exp(i\beta_y)}{\left(1-r^{x2}\right)\left(1-r^{x2}\exp(2i\beta_x)\right)\exp(i\beta_x)}, \tag{5}$$

where $r^{x,y} = (1-n_{x,y})/(1+n_{x,y}),\ \beta_{x,y} = 2\pi n_{x,y} d/\lambda$.

(5) In works [5–8] the schemes of an ellipsometer (polarometer) with such an amplifying plate are considered for a particular case when the analyzer and polarizer are crossed with each other (have only one orientation $\theta_1 = 90^\circ, \theta_2 = 0^\circ$)

In this work we suggest to use the amplifying non-isotropic and isotropic media enriched with resonance atoms as an amplifier of the polarization plane rotation of electromagnetic waves, in the case of linear polarization conservation and arbitrary polarization geometry of the polarometer (analyzer and polarizer).

The ellipsometr scheme: Ellipsometry (polarometry) is substance study method based on the measurement of radiation polarization level of optically active transparent and homogeneous media, solutions (sugarometery), liquids. Substance optical activity is very sensitive to the changes of molecule spatial structure and their inter molecule interaction. As the polarization of atom, ions and molecules the left of inter molecule interaction and its influence on the optical activity of a medium, so the polarometry submits valuable information about the substances in organic molecules and about the structure of complex organic compounds. Polarometers are used in analytic and structural chemistry. With help of optical polarometers, the value of rotation of light polarization plane is being determined while its reflection (propagation) through optically active media (solid bodies or solutions). The value of optical rotation in solutions depends upon their concentration in solutions upon their concentration and specific properties of optically active substances. There for the polarometers are widely used in analytic chemistry for fast measurement of the concentration of optically active substances, for identification of ether oils and for other studies. The determination of rotational dispersion of light, the measurement the rotation angle while the change of electromagnetic wave lengths enable to study the matter structure.

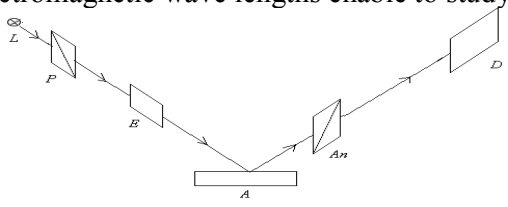

Fig.1. The scheme of the ellipsometer with amplifier of polarization plane rotation wile the reflection from non-isotropic amplifying media. L-source of light, P-polarizer, E-sample, A-amplifying media, An-analyzer, D-detector.

Now let's discuss a real ellipsometer with a polarization plane rotation amplifier with an amplifying medium (fig.2) and the same ellipsometer without an amplifier. For this problem solution, let's apply the method of matrix formalism of Johns while the light propagates though the ellipsometer. According to this formalism, the vector column of ingoing beam and Johns' matrix of the ellipsometer elements are connected through the equation.

$$\vec{E}_{out} = T_A \cdot T_S \cdot T_P . E_i, \tag{8}$$

In the first case, and through equation

$$\vec{E}_{out} = T_A \cdot T_S \cdot T_{Amp} \cdot T_P . E_i , \tag{9}$$

In the second case

Here $T_A, T_p = \begin{bmatrix} \cos^2\theta_{1,2} & \sin\theta_{1,2}\cos\theta_{1,2} \\ \sin\theta_{1,2}\cos\theta_{1,2} & \sin^2\theta_{1,2} \end{bmatrix}$ – Johns matrix of polarizer (analyzer), which transmission plane makes angler θ_1 with axis OX (Johns matrix for analyzer has the same form, transmission plane make angle θ_2 with axis OX).

$T_{Amp} = \begin{bmatrix} e^{x} & 0 \\ 0 & e^{y} \end{bmatrix}^{Amplifier}$ – Johns matrix for the amplifying medium, where $x = -i\frac{2\pi d(n_x^{'} + in_x^{''})}{\lambda}$, $y = -i\frac{2\pi d(n_y^{'} + in_y^{''})}{\lambda}$,

$n_{x,y} = n_{x,y}^{'} + in_{x,y}^{''}$ - crystal refraction coefficient.

For the intensity of the outgoing signal in the first and second cases Maxwell Vector equals

$$\vec{E}_{out} = \begin{bmatrix} E_x \\ E_y \end{bmatrix} = \begin{bmatrix} \cos^2\theta_1 & \sin\theta_1\cos\theta_1 \\ \sin\theta_1\cos\theta_1 & \sin^2\theta_1 \end{bmatrix} \begin{bmatrix} \cos\alpha & \sin\alpha \\ -\sin\alpha & \cos\alpha \end{bmatrix}^{Sample} \begin{bmatrix} e^{-x} & 0 \\ 0 & e^{-y} \end{bmatrix} \begin{bmatrix} \cos^2\theta_2 & \sin\theta_2\cos\theta_2 \\ \sin\theta_2\cos\theta_2 & \sin^2\theta_2 \end{bmatrix} \begin{bmatrix} 1 \\ 1 \end{bmatrix}, \tag{10}$$

In the first case

$$\vec{E}_{out} = \begin{bmatrix} E_x \\ E_y \end{bmatrix} = \begin{bmatrix} \cos^2\theta_1 & \sin\theta_1\cos\theta_1 \\ \sin\theta_1\cos\theta_1 & \sin^2\theta_1 \end{bmatrix} \begin{bmatrix} \cos\alpha & \sin\alpha \\ -\sin\alpha & \cos\alpha \end{bmatrix}^{Sample} \begin{bmatrix} \cos^2\theta_2 & \sin\theta_2\cos\theta_2 \\ \sin\theta_2\cos\theta_2 & \sin^2\theta_2 \end{bmatrix} \begin{bmatrix} 1 \\ 1 \end{bmatrix}, \tag{11}$$

In the second case

Where α - rotation angle of polarization plane of the studied substance, for gyro tropic media $\alpha = \rho d$ (ρ -gyro tropic parameter). We obtain from (11):

$$\vec{E}_{out} = \begin{bmatrix} \cos\theta_1 \cdot (\cos\theta_2 + \sin\theta_2) \cdot [\cos\theta_2 \cos(\theta_1 + \alpha) + \sin\theta_2 \sin(\theta_1 + \alpha)] \\ \sin\theta_1 \cdot (\cos\theta_2 + \sin\theta_2) \cdot [\cos\theta_2 \cos(\theta_1 + \alpha) + \sin\theta_2 \sin(\theta_1 + \alpha)] \end{bmatrix} \tag{12}$$

We find the intensity of the propagated beam by multiplying the Maxwell vector of this beam on the left with the transposed vector of this beam on the left with the transposed vector complex conjugated to it. For the intensity of the outgoing signal for the first and second case, we obtain correspondingly:

$$I \propto \vec{E}_{out}\vec{E}^{*} = (\cos\theta_2 + \sin\theta_2)^2 [\cos(\theta_2 - \theta_1 + \alpha)]^2 \exp\left(-\frac{4\pi d n_x^{''}}{\lambda}\right) \tag{13}$$

For the first case:

$$I \propto \vec{E}_{out}^{2} = (\cos\theta_2 + \sin\theta_2)^2 [\cos(\theta_2 - \theta_1 + \alpha)]^2 \tag{14}$$

For the second case:

For the corresponding choice of amplifier parameters (thickness- d , refraction index of an amplifying medium- n as well as the polarizer transmission angle θ_1, and the analyzer θ_2), it is

possible to obtain much better results while the registration of super small rotation angle of a polarization plane of an electromagnetic wave.

References

1. R. M. A. Azzam, N. M. Bashara, Ellipsometry and polarized light. North-Holland, New York, 1977.
2. V. S. Zapasskii, J. Appl. Spectrosc., **37**, 181-196 (1982).
3. K. K. Svitashev, G. Khasanov, Opt. Spectrosc., **54**, 538-539 (1982).
4. Meekhof D.M., Vetter P., Majumder P.K., Lamoreaux S.K., Fortson E.N., High-precision measurement of parity nonconserving optical rotation in atomic lead Phys. Rev. Lett. 71, 3442 (1993).
5. Седракян А.М. Эффекты оптическая азимутальная неоднородности в одномерных фотонных кристаллах. Кандидатская диссертация. Ереван 2009., ст. 143.
6. Gevorgyan A.A.., Grigoryan A.A., Kocharian A., A.Zh.Khachatryan A.Zh, Mikaelyan L.O., Sedrakyan A.M., Vardanyan G.A. Polarization plane's weak rotation amplifiers and polarization azimuth stabilizers. //Optik. 2006, V. 117, p. 309-316.
7. A.H. Gevorgyan, A.M. Sedrakyan. J. Contemp. Phys. (Acad. Sci. Arm.), **41**, 25-31 (2006).
8. Геворгян А.А., Седракян А.М., Хачатрян А.Ж., Метод усиление поворота плоскости поляризации электромагнитных волн и устройство. Патент № AM20060077, 06.05.2006.